Temperature Reconstruction and Acoustic Time of Flight determination for Boiler Furnace Exit Temperature Measurement

Prepared by:

Geoff Raikes

RKSGEO001

Department of Mechanical Engineering

University of Cape Town

Supervisor:

A/Prof Hennie Mouton

A/Prof Wim Fuls

2017

Submitted to the Department of Mechanical Engineering at the University of Cape Town in partial fulfilment of the academic requirements for a Masters of Science degree in Mechanical Engineering

Key Words: Acoustic Pyrometry; Acoustic Pyrometer; Temperature reconstruction; Time of flight determination; Furnace exit gas temperature;

Abstract

The furnace exit gas temperature (FEGT) is one of the fundamental parameters necessary to determine the energy balance of the boiler in a coal-fired power plant, and is thus beneficial to the production of reliable thermo-fluid models of its operation and the operation of the systems down and upstream. The continuous measurement of the FEGT would also be a useful indicator to predict, prevent and diagnose faults, optimize boiler operation and aid the design of heat transfer surfaces.

Acoustic pyrometry, a technique that measures temperature based on the travel time of an acoustic wave in a gas, is investigated as a viable solution for continuous direct measurement of the FEGT. This study focuses specifically on using acoustic pyrometry to reconstruct the temperature profile at the furnace exit including methods for accurately determining the time of flight (TOF) of acoustic waves.

An improved reconstruction technique using radial basis functions (RBF) for interpolation and a least squares algorithm is simulated and its performance was compared to cubic spline interpolation, regression and Lagrange interpolation by evaluating its reconstruction accuracy in terms of mean and root-mean-squared (RMS) error when reconstructing set temperature profiles. Various parameters including transceiver positions, grid divisions and time of flight error, are investigated in terms of how they inform acoustic pyrometry implementation.

The improved RBF interpolation function managed to reconstruct complex temperature profiles and had a greater reconstruction accuracy than compared interpolation methods, improving on the accuracy of previous work done. Random acoustic path error was found to not be additive with reconstruction error however repeating acoustic TOF readings improved reconstruction accuracy to mitigate this effect. In general, it was also found that symmetrical transmitter/receiver positions produced more accurate reconstructions as well as positioning receivers/transceivers and grid lines closer to the furnace walls, where the greatest temperature change occurs.

In addition to testing reconstruction methods, a low-cost experimental set-up was constructed to measure the time of flight. The focus of this study was on using various signal processing methods to determine the time of flight and evaluating their accuracy in the presence of noise. Methods such as threshold detection with bandpass filtering, cross correlation, generalized cross-correlation (GCC) and a new method developed employing variable notch filters with locations and widths based on repetitive frequencies identified in the noise with cross correlation. The performance of methods was experimentally tested under varying signal to noise ratios (SNR) and noise conditions.

These SNR tests showed that cross-correlation methods produced more reliable TOF readings under lower SNRs than threshold detection methods. Under white noise the smooth coherent transform (SCOT) GCC variation proved to produce the most accurate results producing an average TOF error of 0.84 % up until a SNR of 1.4 before reducing in accuracy. In coloured noise (generated based on previous boiler recordings) the variable notch filter method with cross-correlation was able to identify repetitive noise frequencies filter them out and ultimately produced results with an average TOF error of 1.99 % up until a SNR of 0.67, where the noise level exceeds that of the signal.

Declaration

I know the meaning of plagiarism and declare that all the work in the document, save for that which is properly acknowledged, is my own. This thesis/dissertation has been submitted to the Turnitin module (or equivalent similarity and originality checking software) and I confirm that my supervisor has seen my report and any concerns revealed by such have been resolved with my supervisor.

Signed by candidate

GR Raikes

Acknowledgements

Firstly, I would like to acknowledge my supervisor, A/Prof Hennie Mouton for his tireless mentorship, guidance, support and feedback over the last two years.

Secondly, I would like to thank A/Prof Wim Fuls. Not only am I appreciative of his immense assistance and guidance throughout my project as a co-supervisor, but also for approaching me and giving me the opportunity to a pursue a master's degree.

Thank you, Prof Pieter Rousseau, for initially introducing me to the project topic, taking a keen interest in it and for providing constructive feedback along the way.

I would also like to thank the Eskom Power Plant Engineering Institute's (EPPEI) specialisation centre of Energy efficiency (or ATProM) and the National Research Foundation for funding this project. In addition to funding, I'd like to thank the staff at EPPEI for their willing assistance throughout the project.

Thank you to all my colleagues at Maintenance place for making these years thoroughly enjoyable, even through the most stressful periods. For the same reason, I would like to thank all of my friends.

Lastly, I would like to thank my immediate family and partner. Your emotional support, confidence in me and tendency to feed me was sincerely appreciated!

Table of Contents

List of Figures

List of Tables

List of Nomenclature

General symbols

d	Acoustic path distance	m
t	Acoustic time of flight	s
R_{x_1,x_2}	Cross correlation of two signals	-
G_{x_1,x_2}	Cross power spectrum of two signals	-
$\mathbf{L}$	Distance/Length matrix	m
$H(f)$	Filters	-
f	Inverse of velocity ‘slowness’	s/m
L	Lagrange polynomials	-
ΔL	Length of acoustic path segment	m
ma	Mass concentration of ash	%
E_{mean}	Mean reconstruction error	%
T_{mean}	Mean Temperature	K
$n(t)$	Noise signal	-
N_t	Number of acoustic paths	-
N_b	Number of blocks in grid	-

N_d	Number of interpolation divisions	-
e_{path}	Path error	%
p	Pressure	kPa
E_k	Reconstruction error estimation	%
E_{RMS}	Root mean square reconstruction error	%
$s(t)$	Signal	-
R_s	Specific gas constant	J/kgK
R_{fg}	Specific gas constant of flue gas	J/kgK
C_v	Specific heat at constant volume	J/kgK
C_a	Specific heat of ash	J/kgK
c	Speed of sound	m/s
T	Temperature	K
R	Universal gas constant	$J/molK$
v	Velocity	m/s

Greek symbols

α	Attenuation factor	-
ρ	Density	kg/m^3
ψ	GCC weighting	-
γ_{12}	Magnitude squared coherence	-
ϕ	Radial basis function	-
γ	Ratio of specific heats	-
γ_{fg}	Ratio of specific heats of flue gas	-
ω	Reconstruction weights	-
λ	Relaxation factor	-
ε	Shape factor	-
β	Shape factor	-
σ	Standard deviation	-

Acronyms and Abbreviations

ADC	Analog-to-Digital Convertor
ART	Algebraic Reconstruction Technique
ASR	Acoustic Receiver
AST	Acoustic Generator
CC	Cross-Correlation
CCD	Charge-Coupled Device
CMOS	Complementary Metal Oxide Semiconductor
DAC	Digital-to-Analog Converter
emf	Electromotive force
EPPEI	Eskom Power Plant Engineering Institute
FEGT	Furnace Exit Gas Temperature
FET	Furnace Exit Temperature
FFT	Fast Fourier Transform
GCC	Generalised Cross-Correlation
HT	Hannon-Thompson
HVT	High Velocity Thermocouple
IFT	Inverse Fourier Transform
IG	Interpolation Grid
IRP	Integrated Resource Plan
IRR	Infinite-Impulse-Response
LSM	Least Squares Method

LSM-MQ	Least Squares Method Multiquadratic
ML	Maximum Likelihood
MWe	Megawatt electric
PHAT	Phase Transform
PSD	Power Spectral Density
PVC	Polyvinyl Chloride
RBF	Radial Basis Function
RMS	Root mean square
SCOT	Smoothed Coherence Transform
SNR	Signal to Noise Ratio
SPL	Sound Pressure Level
STFT	Short Time Fourier Transform
SVD	Singular Value Decomposition
TOF	Time of Flight
USB	Universal Serial Bus
VI	Virtual Instrument

1. Introduction

1.1 Background to the study

Currently, the vast majority of electricity available in South Africa is generated by coal-fired power plants with boiler furnace and heat exchanger layouts[1]. At the Eskom Power Plant Engineering Institute (EPPEI) centre for energy efficiency at the University of Cape Town, the main aim is to build accurate process and thermo-fluid models for application in these systems. In a boiler system, furnace exit gas temperature (FEGT) is one of the fundamental parameters necessary to determine the energy balance of the boiler, and thus would be beneficial to produce reliable models for the systems downstream from the furnace exit. In addition to this, continuous measurement of the FEGT would be a useful indicator to predict, prevent and diagnose faults, ensuring the safe operation of the boiler; a crucial task for ensuring energy security with South Africa's aging power plant fleet.

Subsequently, temperature measurement techniques are being considered for the furnace exit region. FEGT measurement devices are split up into two groups, namely contact and non-contact methods. The most popular contact method is the use of high velocity thermocouples, "high velocity" referring to the high speed of the gas whose temperature is measured. This method is advantageous as it allows for accurate readings, however only provides single point readings, require impractically long probe lengths to reach the centre of the boiler and due to the harsh conditions of the boiler, has a short lifespan. As a result, this technique does not lend itself to continuous monitoring and is rather used for short term measurement.

Radiation pyrometry is an alternate non-contact solution that uses the emitted radiation from the flue gas to determine the temperature. It does not physically come into contact with the boiler and is more suitable for continuous measurement. However, this solution is also a single point measurement, and due to the properties of flue gas, it is depth limited.

Consequently, devices that are based on measuring the acoustic properties of flue gas are being investigated as a possible solution. The acoustic pyrometer is a non-contact device that uses time of flight measurements of a generated sound wave as well as the properties of the medium through which it is travelling through to determine an average temperature along its path of travel. When multiple of these devices are installed, these average path temperatures can then be used to reconstruct a spatial temperature profile at the furnace exit. These devices are currently developed internationally; but they are not yet implemented in Eskom's power plants.

1.2 Goals and objectives of the study

The overall goal of this research is to gain an in-depth understanding of the operation of the acoustic pyrometer and to determine the implementation guidelines of an acoustic pyrometer system for FEGT measurement in a South African context. Subsequently, the objectives of the research are as follows:

1. **To provide a review of the current methods of FEGT measurement**. This will discuss current measurement techniques and their limitations, with a focus on acoustic pyrometry.

2. **Model acoustic pyrometry temperature reconstruction with multiple acoustic paths.** Based on this model recommendations can be drawn up guiding implementation for the case of multiple acoustic pyrometer transmitter and receiver pairs.

3. **Demonstrate recording an acoustic time of flight reading with its associated signal processing**. The goal here is to identify significant factors that affect acquiring the time of flight and compare the performance of various methods in different noise scenarios.

1.3 Scope and limitations

To meet the objectives of the study, the approach taken is to develop simulations to predict the performance of a multi-path acoustic pyrometer system when reconstructing given temperature profiles. The reconstruction problem will not be validated experimentally. On the other hand, an experimental approach is taken for single path acoustic measurements.

The work done on this master's seeks to compliment the work already done by Tootla[1] on investigating methods for the calculation and measurement of flue gas furnace exit temperature. As a result, aspects already well documented in his work will not be investigated in this dissertation, such as a detailed analysis of flue gas properties.

The multi-path reconstruction simulation is limited to rectangular or square boiler cross sections with acoustic pyrometer transceivers placed on a fixed horizontal plane. Most boilers do fit this description, but due to accessibility issues, observations ports might not always be on a horizontal plane.

The furnace exit temperature distribution is reconstructed also using set of temperature profiles based on what might be expected from literature. In addition, the acoustic paths are assumed to be straight paths and the number of acoustic transceivers simulated is constrained by what is practically feasible for physical implementation. A variety of transceiver layouts are tested in a step by step fashion rather than numerically optimised, since the aim is to draw up a set of guidelines for implementation rather than finding the exact best implementation, as this would vary between power plants.

The experimental set-up considers single path acoustic time of flight readings and is limited to a small-scale set-up. Thus, the experimental set-up will not be applied to an active power plant boiler with the associated elevated temperature ranges but rather applied in the spatial and temperature limitations of the EPPEI laboratory. The focus is on measuring the time of flight rather than the temperature and factors affecting the translation of the TOF to temperature are not a priority. The time of flight is considered over 6 m and the signal processing methods are limited to cross-correlation, generalised cross-correlation variable filtering and threshold detection. The experimental set-up will not aim to accurately replicate the physical conditions within a coal-fired power plant boiler, but will rather focus on the signal processing methods and their effectiveness at varying signal to noise ratios to draw up recommendations for consideration in later application. Repeatability under the same conditions will be the main factor to determine the success of the experimental method.

1.4 Format of report

The proceeding chapter acts as a more detailed introduction to the problem, giving an overview of the coal fired power plant and the subsystems neighbouring the acoustic pyrometer. This chapter also discusses and reviews various other temperature measurement techniques and introduce the core concepts of acoustic pyrometry.

Most of the content of the dissertation is presented in two self-contained chapters. Chapter 3 will then focus on temperature profile reconstruction, surveying the various methods that have been applied before and detailing the development of the reconstruction model. This chapter will also present the methodology, the results obtained, a discussion and conclusion for each test undertaken.

The fourth chapter follows the same format; however, the content is based on experimental time of flight determination. Therefore, literature regarding noise and attenuation in the boiler and signal processing methods to overcome this is presented. Also, the LabView model and experimental

design are described. Each experimental test methodology is then presented along with its results, discussion and conclusions following.

The concluding chapter then summarises the prominent conclusions from the two preceding chapters and makes recommendations for future work.

2. General literature survey

2.1 Overview of the coal fired power plant

Currently Eskom remains the largest electricity provider in South Africa, producing 95% of electricity as of 2016, of which the majority (85.5%) is generated by coal-fired powerplants[1]. While there are plans to introduce more renewables into the energy mix, the last accepted Integrated Resource Plan (IRP) still forecasts that coal-fired power plants will be the dominant electricity supply in the next 20 years[2]. Thus, from an economic and availability perspective, it is imperative that the existing generating plants are maintained in good operating health.

The typical coal-fired powerplant found in Eskom's fleet has a layout as shown in Figure 1, which produces electricity using a steam turbine and generator. The steam used for this process is produced by the combustion of pulverised coal in the boiler and the complex manipulation of steam thereafter[2]. The process works by transferring energy between multiple flow cycles, as represented by distinct colours in Figure 1. The red and blue lines refer to steam and water respectively in the steam cycle and the black lines refer to the fuel, air and the by-product of combustion known as flue gas.

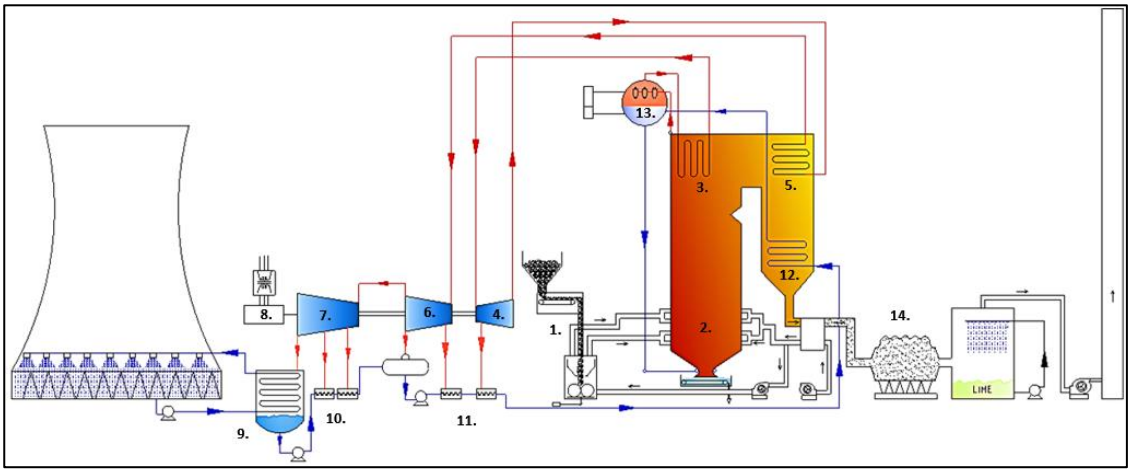

Figure 1 Typical coal-fired powerplant

While many coal-fired power plants have different layouts, a generic plant can be described as follows. The cycle starts with the fuel supply system where coal is first transported from the coal bunker to the mills at 1 to be pulverised and conveyed to the boiler via a draft created by primary air fans. The air/fuel mixture enters the boiler at the bottom region, known as the furnace, where combustion takes place, and the chemical energy of the fuel mixture is converted to thermal energy

in the form of hot flue gas. The flue gas then travels upstream of the boiler, where it exchanges thermal energy with the pressured water in pipes in the walls alongside of the boiler and the heat exchangers upstream. The first heat exchanger it encounters at 3, is known as the superheater where the steam inside is heated to superheated levels and transported to the high-pressure turbine at 4. At this point the steam is expanded, which results in the rotation of the turbine, converting the thermal and pressure energy to mechanical energy. The steam/mixture at the outlet of the high-pressure turbine is then pumped back to the boiler and into the boiler where it is reheated at 5 (known as the reheater). The heated steam is then sent back to an intermediate pressure turbine at 6 where more energy is extracted, before being sent to the final turbine stage at 7, known as the low-pressure turbine. The mechanical energy extracted at 4,6 and 7 is used to turn the same shaft, which rotates the generator at 8, which in turn converts the mechanical energy to the electrical energy that is sent out for consumption.

Following the removal of energy from the steam, the mixture exiting the low-pressure turbine is then sent to the condenser at 9, where it is then condensed to water, by removing excess energy and transferring it to the atmosphere. The water exiting the condenser is heated again at the feedwater heaters at 10 and 11, which increase the cycle efficiency by bleeding hot steam from the turbines to heat the water, effectively reducing the heat ejected to the atmosphere at the condenser. The now heated water is pumped back to the boiler through the economiser at 12, where more energy is added to the water before entering the steam drum at 13. The steam drum acts as a collection point, where water is sent down to the water walls, where it is heated by the hot flue gas, only to eventually return as a water/steam. The steam portion in the drum is tapped of from the top and enters the superheater tubes to complete the steam cycle. The remainder of the flue gas exits after the economiser for scrubbing at 14, before it is ejected into the atmosphere.

2.1.1 The boiler and furnace exit

The primary system that is pertinent to this study is the boiler (or steam generator) which has the vital function of converting the thermal energy from coal combustion to the steam used for electric power generation later on in the cycle[2].

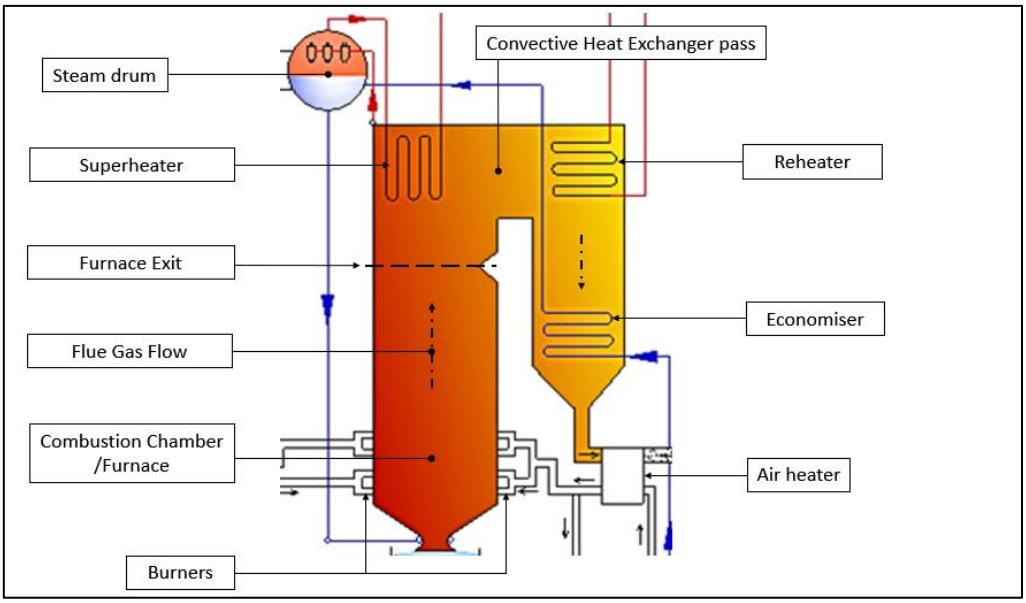

Figure 2 Boiler Schematic showing location of furnace exit and relative components

The typical boiler is designed having a large open furnace volume where combustion can take place near the bottom of the boiler as fuelled by multiple coal burners. The result of this, it the production of hot flue gas that exchanges heat radiatively with the water-cooled pipes that enclose the whole boiler. The water in these pipes is typically still a liquid, so instead of the heat drastically increasing the pipe temperature, it results in a change of phase in the water before it is fed into the steam drum[3].

The specific region of the boiler that is of interest to this study in is the furnace exit, which is located upstream, after the radiative combustion chamber or furnace and before a region known as the convective pass. The primary source of heat transfer in the region is via convection, and accordingly, tubular heat exchangers such as superheaters, reheaters and economisers are placed in the flow path to absorb heat from the flue gas. While the location furnace exit varies between boilers it is generally accepted that it occurs before the first superheater as shown in Figure 2.

2.1.2 Impact of burners on furnace exit temperature

While knowledge of the furnace exit temperature might have great implications for the components upstream, and by extension the operation of the plant, much of the properties of this region are determined by the combustion downstream of the furnace exit. Primary fuel combustion takes place near the bottom of the furnace at the outlet of the burners as shown in Figure 3 and fuel continues to combust higher into the furnace region completing before the furnace exit[3].

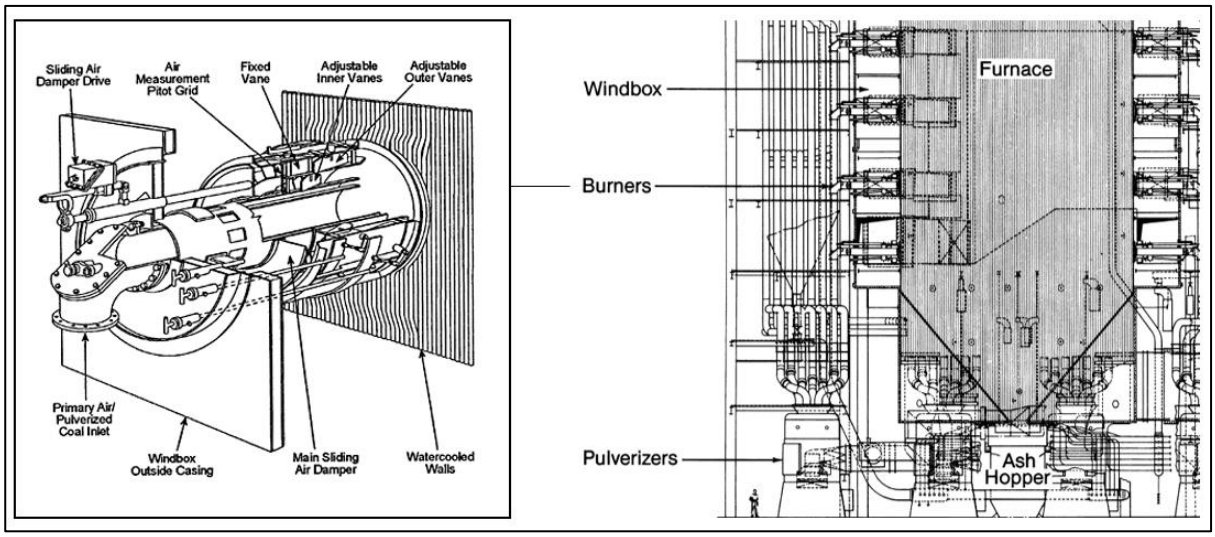

Figure 3 Low NOx coal burner and its location in the furnace. adapted from [2]

The fuel burning system is responsible for facilitating a controlled and efficient conversion of chemical to heat energy in this region. This is dependent to a considerable extent on the burners used. The performance of these burners are dependent on (and thus the efficacy of combustion) their ability to effectively mix the reactants (air and coal), reduce the amount of excess oxygen and unburnt combustibles and to ignite the combustible mixture and distribute the flame envelope and the products[4]. More modern units also have the environmental requirement of producing low NO_x emissions[5], the burner shown in Figure 3 is of this variety. Furthermore, since multiple burners are used, the furnace exit temperature and the temperature distribution are also dependent on the layout and firing of these burners. Typical burner firing arrangements as shown in Figure 4 including vertical, horizontal and tangential firing.

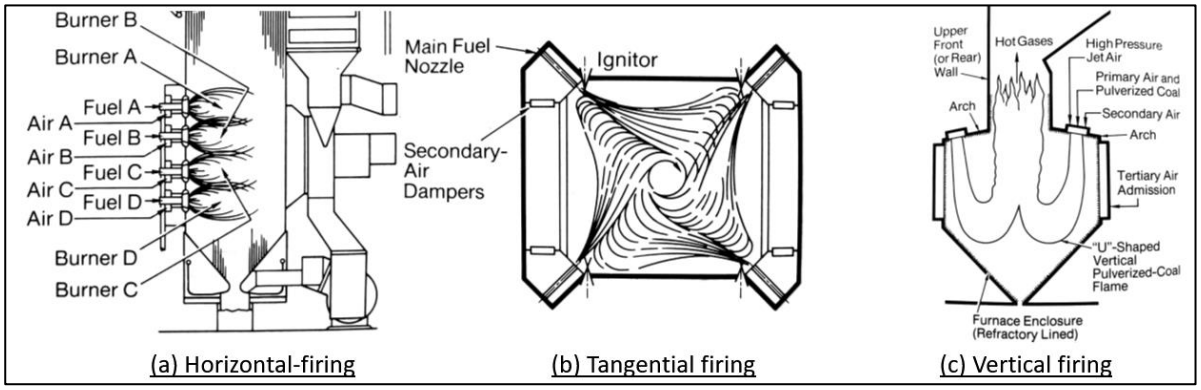

Figure 4 Fuel firing systems (a) Horizontal firing, (b) Tangential firing (c) vertical firing. adapted from[4]

Horizontal firing systems mix the fuel and air in individual burners and fire them tangentially to the burner nozzles imparting a swirl as it exits horizontally into the furnace for combustion. Multiple

burners are usually used and when burners are located at both front and rear walls, it is referred to as opposed firing[4]. The tangential firing (or corner firing) burner layout instead has burners located at each corner of a square furnace. For these burners fuel mixing and combustion take place in the furnace, where the nozzles in the same plane are directed slightly off centre to create a rotating fireball as seen in Figure 4 (b)[3]. Vertical firing as seen in Figure 4 (c) involves placing the burners in the arch of a furnace facing vertically down, producing a long flame that loops around with hot gases rising through the centre of the furnace. This method is typically used to fire solid fuels that are harder to ignite, such as coals with high moisture content and low amounts of volatile content[4]. In Eskom's fleet, opposed firing is the most popular firing system, followed by tangential firing and lastly front wall firing.

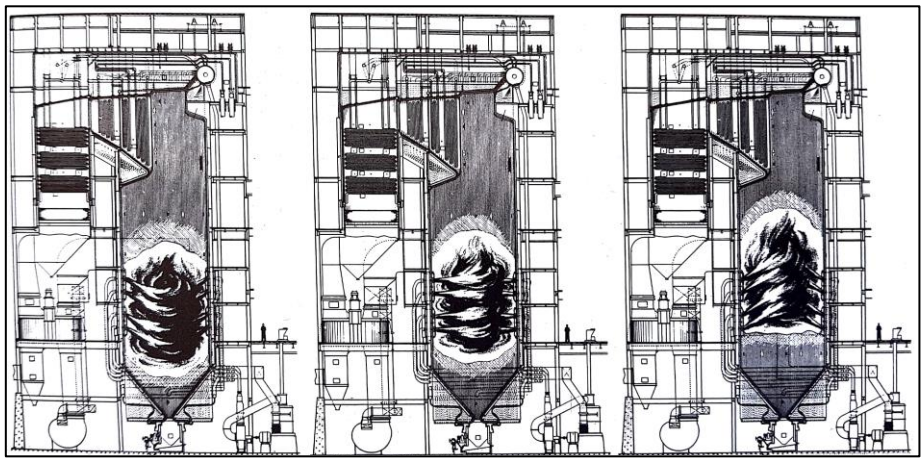

Figure 5 Temperature control with tilting burner nozzles[6]

In addition to the temperature field being determined by the firing arrangement, it is also determined by the vertical tilt on the burners as shown in Figure 5. For furnace exit temperature control, and thus steam temperature control in the superheaters and reheaters , the burners can be tilted to raise and lower the fireball created at lower loads[3].

2.1.3 Benefits of furnace exit temperature measurement

Since the heat exchanging components are located upstream of the furnace exit, knowledge of the flue gas exit temperature would be very beneficial to predicting the heat exchange upstream as well as providing an indication of the heat transfer to the water wall piping below. Thus, this would be advantageous from a research perspective, as furnace exit temperature data would be useful to produce and validate more reliable component and mass energy balance models, which in turn would be useful to improve plant operation for the fleet.

In addition to this, the boiler is subjected to inhibiting phenomena due to the type of fuel used. By-products of coal combustion such as ash and inorganic elements contained in coal are prone to deposition on heat exchanging elements, resulting in slagging and fouling. Fouling refers to the deposition of high-temperature inorganic elements that have bonded with ash in the process of vaporisation, which typically occurs deeper into the convective pass at relatively lower temperatures. Slagging on the other hand refers to the molten fused, or solidified solids exposed to radiation produced in combustion and typically occurs in the furnace and on the first heat exchangers in the convective path.

Both slagging and fouling reduce heat transfer and thus to meet the same operation point, temperatures are increased, resulting in premature failure of heat transfer tubes. The slagging classification also establishes a limit on the temperature at the furnace exit[3], since beyond this, ash is more likely to fuse. From this perspective, knowledge of the furnace exit gas temperature would be beneficial to reduce temperatures and prevent slagging, but also diagnose poor heat transfer due to slagging and fouling.

Furthermore, furnace exit temperature readings could be used to inform different operating actions either to control the furnace exit temperature or to correct undesirable operation. For example, combustion can be altered by changing fuel quality, adjusting burner settings, changing burner fire distribution, cleaning heat transfer surfaces using sootblowing[1] and in some cases changing burner tilt to compensate for the reduction of absorption due to ash deposition[4].

2.2 Temperature measurement methods

As outlined previously, the temperature measurement of combustions gases within the boiler is beneficial from both a design and operating perspective, and subsequently this section details the measurement methods that are applicable for directly measuring flue gas temperature in the furnace. The first section will detail the use of contact temperatures methods (specifically thermocouple variants) followed by a review of non-contact methods such as radiation and acoustic pyrometry. Temperature measurement methods are generally considered as contact methods when the sensor used is in contact with the medium and essentially measures its own temperature once it is in thermal equilibrium with that medium and in contrast non-contact methods measure temperature without needing to be in thermal equilibrium with the medium[7].

2.2.1 Thermocouples

While there are a wide variety of contact temperature measurement techniques available, most of them are not suitable for the high temperatures and particle laden nature of the flue gas at the furnace exit. Nevertheless, the most suitable contact temperature technology is the use of thermocouples[2].

A bare thermocouple comprises of two conductors of different material that are joined at a junction to form a circuit. The operating principle is based on the Seebeck effect, which produces and electromotive effect (emf) when one side of the junction is maintained at a temperature that is higher than the other. And if one side of the junction is at a known controlled “cold” temperature, the temperature at the other side can be determined from the emf measured at the junction and the relationship between this emf and the known materials used in the thermocouple.

Bare thermocouples however are not suitable for flue gas temperature measurement and are subject to several restraining factors. Firstly, thermocouples used to measure high temperatures (>535°C) are typically constructed from distinct metals and alloys, but these materials tend to deteriorate when exposed to high temperature contaminants in flue gas[2] and thermal shocks during start-ups and shutdowns[8]. This implementation also suffers from poor heat transfer due to gaseous convection between the probe and the flue gas, overestimation of temperature due to transfer of kinetic energy from the flue gas to the probe, the limitation of a response times [9] and most considerably, under estimation of temperature due to radiative heat transfer with the surroundings[10].

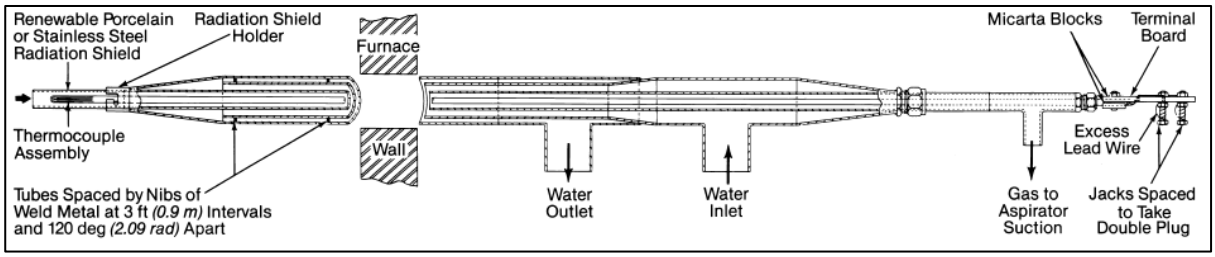

Figure 6 Water-cooled Suction Pyrometer/High Velocity Thermocouple (HVT) cross sectional view[2]

Because of these limitations, when measuring temperature in hot gases, high velocity thermocouples (HVT) or suction pyrometers[11] are used. The water-cooled HVT was developed for boiler testing and introduces extra complexity to the method to eliminate the sources of error associated with bare thermocouples. A schematic of this this thermocouple is shown above in Figure 6. The thermocouple is termed “high velocity” because it uses an aspirator to extract the flue gas at

a velocity much higher than the flue gas flow velocity to improve the convective heat transfer over the thermocouple. It addresses the issue of radiation losses by employing an insulating radiative shield and water cooling to regulate heat transfer between the shield and thermocouple junction. Furthermore, in high radiation environments multiple shield high velocity thermocouples (MHVT) can be considered, which adds extra shielding to reduce radiation effects.[2].

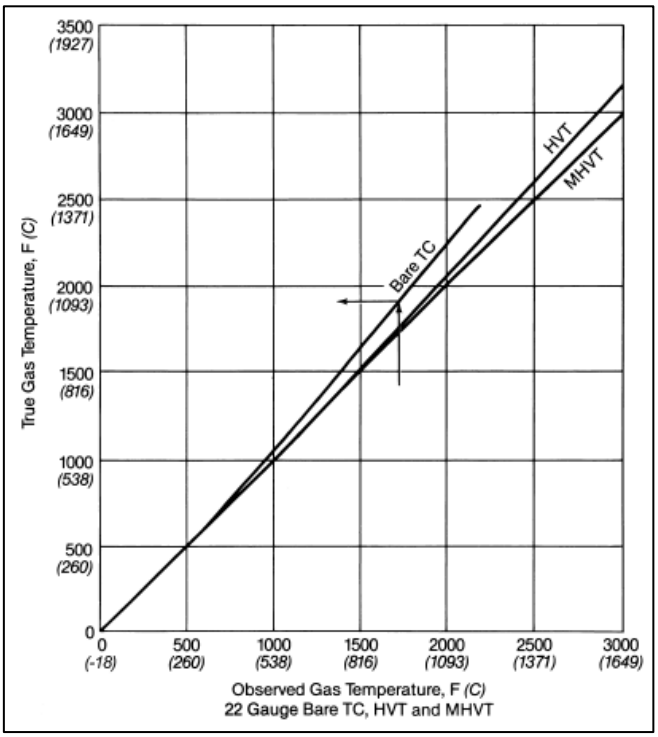

Figure 7 Error observed due to radiation effects between bare thermocouples, high velocity and multiple shield high velocity probes[2]

The improvement in reducing radiation effects can be seen in Figure 7, where there is a considerable deviation between methods upwards of 500°C. This result correlates well with a comparison study done in[11] where it was found that there was a nearly constant temperature deviation between suction and bare thermocouples during load due to radiation effects.

While HVT and MHVT probes are an improvement on bare thermocouples reducing radiation effects and time delay for temperature acquisition[8], they are by no means a complete solution for high temperature monitoring at the furnace exit, with considerable limitations for continuous monitoring. Its faced with the problems that small flow areas rapidly become filled with ash in flue gas environments, and requires considerable correction due to calibration drift[2]. Furthermore, with the increasing size of steam generators, the use of these probes has become difficult due to the unfeasible lengths required to get point measurements near the centre of the furnace, rendering

it expensive, impractical to support, and difficult to manoeuvre[12]. Slag formation and thermal shock also continues to be a problem over long periods without frequent replacement[8], rendering the method unfeasible for continuous monitoring.

2.2.2 Non-contact methods

The limitations and difficulties faced by contact techniques have encouraged the use of alternate non-contact temperature measurement techniques that avoid the harsh conditions of the flue gas.

2.2.3 Radiation pyrometry

A popular alternative to thermocouple temperature measurement is to the use of radiation pyrometry. This section will discuss the different implementations of radiation pyrometry and its applicability to the furnace environment.

Radiation encompasses a wide variety of devices with functioning based on the fact that every object with a temperature of above absolute zero (0 K), emits radiation. The intensity of the produced radiation is a function of the temperature of the body and this is measured either directly by a sensor or by comparison to a body of known temperature. Traditionally the radiation pyrometer consisted of an optical system to focus in on the target and collect energy emitted, a detector to convert it into an electrical signal and a compensation and calibration system to ensure that temperature variations and ambient conditions did not affect temperature readings[13].

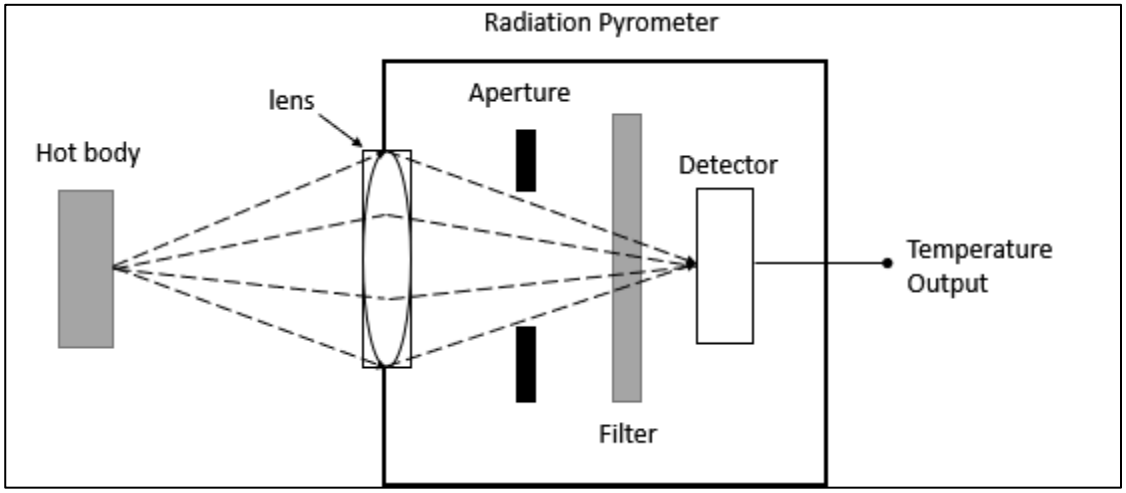

Figure 8 Simple radiation pyrometer configuration

The construction of a simple radiation pyrometer is shown in Figure 8, in this system the radiation measured by the device is gathered by the lens, which determines the focal point/field of view of the pyrometer. The aperture and filter and then used to block unwanted rays at the edges and permit the desired spectral range to enter to the detector respectively. Rays passing to the detector are then converted into an electrical signal, linearized and prepared to be displayed or further processed. Variants of this method also include focusing the radiation on a delicate thermocouple or a technique termed as optical pyrometry where the brightness of the hot body is visually compared to a reference source. However these are more suitable for solid objects and not gases where gases are relatively clear[2].

Radiation pyrometers are usually categorised by the spectral band over which it operates, where they are usually split up into narrow band pyrometers, focusing on a very narrow range of wavelengths, and broad or total wavelength pyrometers, which measure radiation in a much wider spectrum of wavelengths[14]. Narrow band pyrometers focused on the infrared range tend to produce reliable results for solids and flames[2].

The choice of pyrometer considered is largely dependent on the emissivity of the object being measured, and since a wide variety of radiation pyrometers have been developed, for this dissertation, only those applicable to the boiler furnace environment will be considered. Radiation pyrometers are widely used and are present in all Eskom boilers, however temperature measurement is a secondary function and it is primarily used to detect flames for combustion safety[1]. However, in a study comparing radiation pyrometry with thermocouple methods it was stated that the optical pyrometer and radiation pyrometer are not designed to measure gas temperature and encounter excessive error[2].

On the other hand, recent advances have seen the growth in popularity of colour-band pyrometry using digital imaging devices known as flame image detectors in narrower Chinese boiler furnaces[15]–[17]. Most commonly a colour charge-coupled device (CCD) or complementary metal oxide semiconductor (CMOS) digital camera is used. The colour camera can provide light intensity data filtered for specific frequencies from the image, and from this the radiative temperature can be inferred. A typical flame image detector, much like the simplified radiation pyrometer in Figure 8 consists of a focal lens, and an image guide to convey the radiation image to the CCD camera used. A schematic for the device used by Jiang et al. is shown in Figure 9.

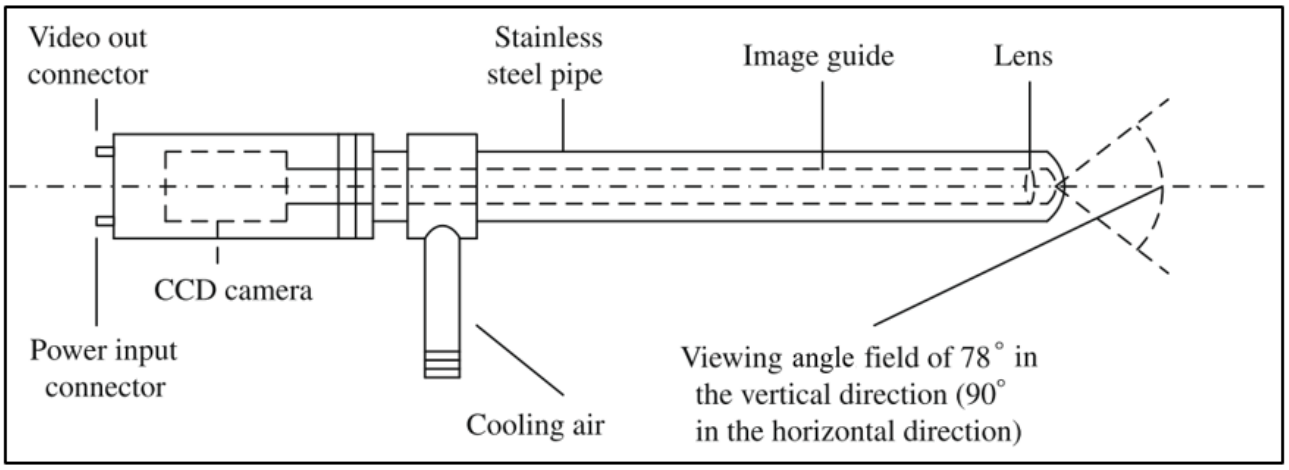

Figure 9 Schematic structure of flame image detector[15]

In this device, a commercial Samsung SCC-B2303P colour CCD camera is used. An image guide is fitted to the centre of a stainless-steel pipe and inserted into the water-wall of the furnace. Since this region is exposed to high temperatures and flue gas, the device is cooled by air and the lens surface is routinely purged to prevent fouling. Details on the lens angular range is shown, however the focal depth is not clearly stated.

Typically, multiple detectors are needed to image the cross-section of the furnace for this measurement method. In a study done by Jiang et al. as low as two detectors per level were used. The detectors were connected to a frame maker to combine the recorded images and send the combined video signal to an industrial computer with a frame grabber, where processing could be done.

Using this set-up, they were able create cross section temperature images of a relatively small 140 MW boiler having a maximum cross section of 7.5x15 m. The results were validated by comparing them with a thermocouple and the unit load. There was a clear correlation but there still existed a high temperature deviation of 10% and the cross-sectional position of the thermocouple and image comparison is not clearly defined[15].

Earlier work done by Lou et al. used a very similar experimental set-up, however the emphasis was placed on acquiring high spatial resolution of the cross-sectional temperature image. A Tikhonov regularisation method was used to reconstruct a 2-D temperature distribution in 100 discrete meshes above the burners of a 300MW unit using 4 image detectors as shown in Figure 10.

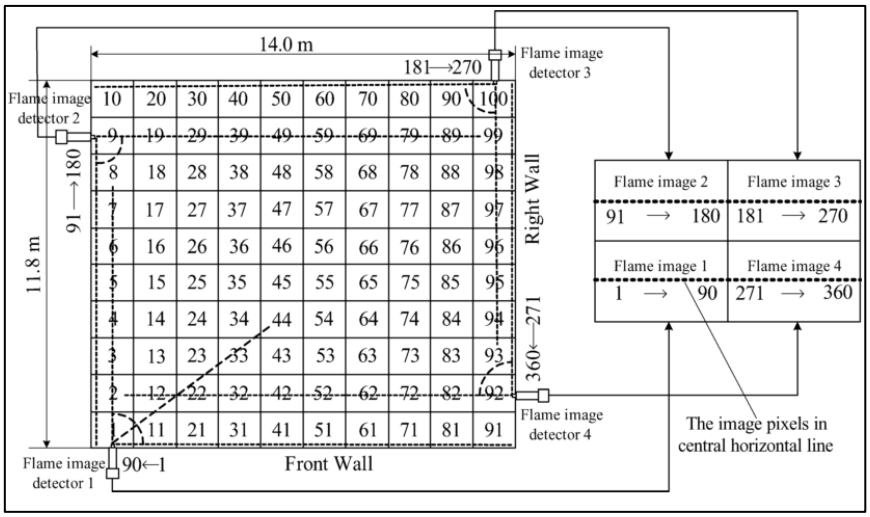

Figure 10 Cross section of furnace (14.0m x 11.8 m) with mesh and flame image detector locations[16]

As shown above, the positioning of the 4 detectors enabled the method to map the temperature over a 14.0 x 11.8 m cross section by measuring the temperature in some regions and applying a regularisation method to reconstruct the rest of the temperature. The use of a Tikhonov regularisation method was motivated by the need to have a more continuous and on-line measurement system, and when applied using the image detectors it could visually update within 2 seconds. The calculated 2-D reconstruction was compared to the measured radiation temperatures and although it was not numerically quantified it showed a close visual correlation. The method was not verified by another direct measurement device due to the limitations on the observation ports and the depth to which a thermocouple could be used. There was however a continuous on-line comparison over a 4 hour period between the average temperature measured and the furnace load, which showed that the average temperature did follow the furnace load[16].

The same research group also applied the technology to a smaller 200 MW generation unit to create a 3-D visualisation at multiple levels, shown in Figure 11.

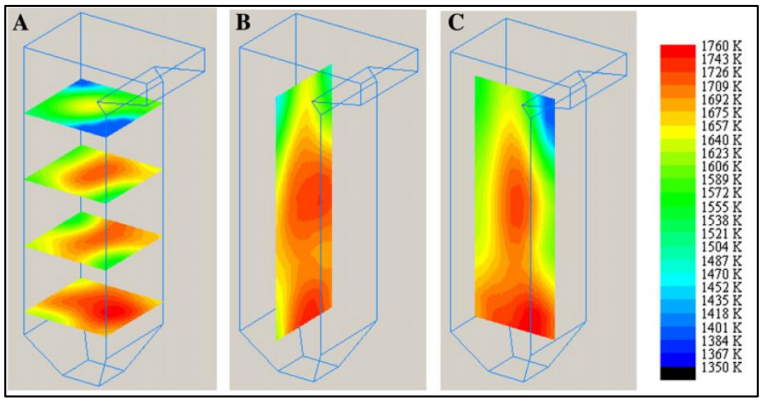

Figure 11 Example of 3-D temperature visualisation produced[17]

As expected, the temperatures decrease at the higher sections of the furnace with peak temperatures in the centre of the cross section and cooler temperatures at the water walls. The measured temperature was once again compared to the load, however an attempt to make a direct temperature comparison was made using a suction thermocouple. The thermocouple was placed in the numbered grey regions of the mesh as shown in Figure 12.

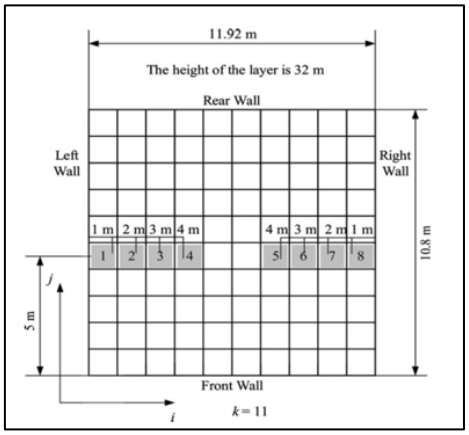

Figure 12 Grid showing temperature measurement locations[17]

The thermocouple measured temperatures at multiple locations up to a depth of 4 m and these measurements are compared to the temperature measured by the visualisation method at a height of 32 m. The results of the validation showed a maximum discrepancy of 5% over the spots directly measured however temperature in the centre could not be done. With the stated reason being that slagging occurred at the higher temperature locations close to the centre of the furnace. The comparison has shown validation for the method in some areas, however the accuracy of the method across the whole furnace cross section is not quantified[17].

In a later study done by Huajian et al[18]. the technology was applied to a much larger 660 MWe coal combustion furnace, with the goal of providing further validation for the measurement method. To overcome the obstacle of the increases size of the boiler, more detectors (20 in total) were used at the narrow section of the furnace.

Verification of the flame image detector method is done using a portable version of the flame image detector and a PT300B infrared pyrometer. Comparison of their readings is done at 12 different ports under 3 different loading conditions, 350, 500 and 600 MWe respectively. The infrared pyrometer and image detector are mounted in the same direction, but since the field of view of the infrared pyrometer is only 10% of the flame image detector, only the central 10% of the pixels of the image detector are used for comparison. Since the combustion process naturally fluctuates over time, 20 frames of the image detector are taken in 20 ms and the brightest (highest temperature) is selected for comparison. When the infrared pyrometer measures the same port, the highest temperature is taken during an unspecified time of measurement. The average temperature error ranged from 5.13-6.52% with maximum deviations of 8.87-10.32% for the load cases[18].

The justification given for this error lies in the fact that the two methods operate in different spectral ranges. The flame images work in the visible spectrum and infers the temperature from particulate matter, while the infrared pyrometer is also influenced by H_2O and CO_2, which results in varying blackbody temperature readings. Additionally, the 3-D reconstructed temperatures by the visualising system are compared with the portable system and show reasonable agreement, however the exact error is not quantified[18]. The 3-D reconstructed temperature is useful to get a general idea of the temperature distribution, however the direct comparison between the infrared pyrometer and flame image detector show relatively large discrepancies and the 3-D visualising system is compared to the portable system and not the infrared pyrometer readings, essentially only verifying the reconstruction and not the temperature obtained by the measurement method.

The technology as presented shows promise and has the advantages of a relatively fast response time. The non-contact nature avoids corrosion and with multiple radiation pyrometers, temperature reconstruction is possible. However, it still suffers from fouling over the lenses, requires calibration, has a dependency on the radiation or optical properties of the gas being measured, is depth limited , and for the more modern implementation, significant errors are still present and thorough research will be needed to validate the method as a truly viable commercial on-line monitoring temperature system.

2.2.4 Acoustic pyrometry

Acoustic Pyrometry is an alternate non-contact method for direct temperature measurement that improves on the limitations faced by conventional measurement techniques when used in the boiler. It is based on the well-known dependency of the sonic wave velocity (or speed of sound) on the temperature and fluid properties of the medium through which the wave travels[2]. Thus, with knowledge of the fluid properties of the medium and by measuring the transit time of an acoustic wave propagating through it, the temperature along the travel path can be determined[19]. Furthermore, if multiple paths are measured in the same plane, the temperature field in that plane can be reconstructed using a relevant reconstruction algorithm[20]. The operating principle has also extended beyond temperature measurement, and the use of transit time of acoustic waves is also being investigated to determine velocity flows[21] and furnace wall fouling[22].

Theory of operation for temperature measurement

The basic acoustic pyrometer can be described as having an acoustic transmitter positioned on the boundary at one end of the boiler and an acoustic receiver on the opposite end. The transmitter generates a distinct acoustic signal that propagates through the fluid along an acoustic path and is recorded at the acoustic receiver. Herein, both transmitters and receivers will be referred to as transducers. A schematic of this process is shown below in Figure 13, where the acoustic wave is traveling horizontally from left to right.

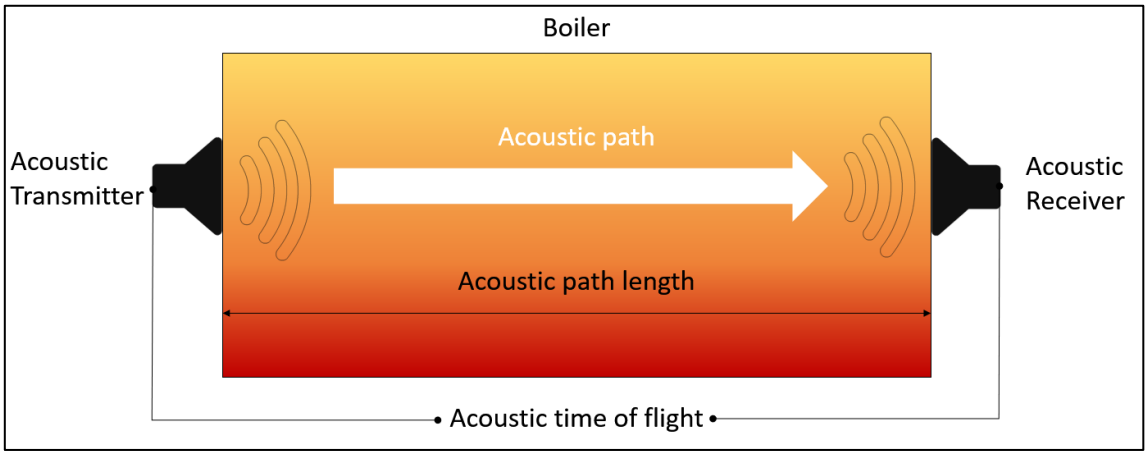

Figure 13 Basic Acoustic Pyrometer set-up

The acoustic wave is frictionless and adiabatic and acoustic pyrometry is usually applied in high temperature scenarios where the fluid through which it travels can be considered as ideal which can be considered using the ideal gas law.

$$\frac{p}{\rho} = R_s T \tag{1}$$

Where p is pressure, ρ is density, R_s is the specific gas constant and T is temperature.

It is known that for a frictionless and adiabatic (isentropic) sonic wave the following relationship is true, where c is the sonic velocity of the acoustic wave.

$$c^2 = \left(\frac{\partial p}{\partial \rho} \right)_s \tag{2}$$

The relationship between speed of sound and the ratio of pressure and density can then be derived as shown in (3) when considering an isentropic wave in an ideal gas, where γ is the ratio of specific heats.

$$c^2 = \gamma \frac{p}{\rho} \tag{3}$$

By considering equation (1) and (3) the sonic velocity can be represented as:

$$c = \sqrt{\gamma R_s T} \tag{4}$$

Note, R_s is the specific gas constant which is the quotient of the Universal gas constant R [8.314 J/molK] and the molar mass M of the fluid [kg/mol].

This velocity can also be expressed as the acoustic path distance/length d divided by the transit time t.

$$c = \frac{d}{t} \tag{5}$$

And by substituting (4) into (5) and rearranging the terms we can determine the average path temperature from the following.

$$T = \frac{d^2}{t^2 \gamma R_s} \tag{6}$$

Where,

γ is the ratio of specific heats

R_s is the specific gas constant [J/kgK]

t is the time of flight [s]

d is the path distance [m]

T is the path temperature [K]

Since γ, R_s, d are considered constant and can be obtained, the average path temperature can be calculated by measuring the time of flight.

Furthermore, if sufficient acoustic transducers are installed in the same plane, these average path temperatures can be used to estimate the temperature distribution at the furnace exit. These transducers will generally be spread around the furnace circumference to get greater coverage of the area, a depiction of the acoustic paths formed by having relatively evenly spaced transducers can be seen inFigure 14. In this figure, the red triangles depict acoustic transmitters, the blue arrow heads depict receivers and the dotted lines are paths between them in the same plane. By inputting the average temperatures obtained by these paths into an appropriate reconstruction algorithm and temperature profile can be constructed as shown on the right-hand side ofFigure 14.

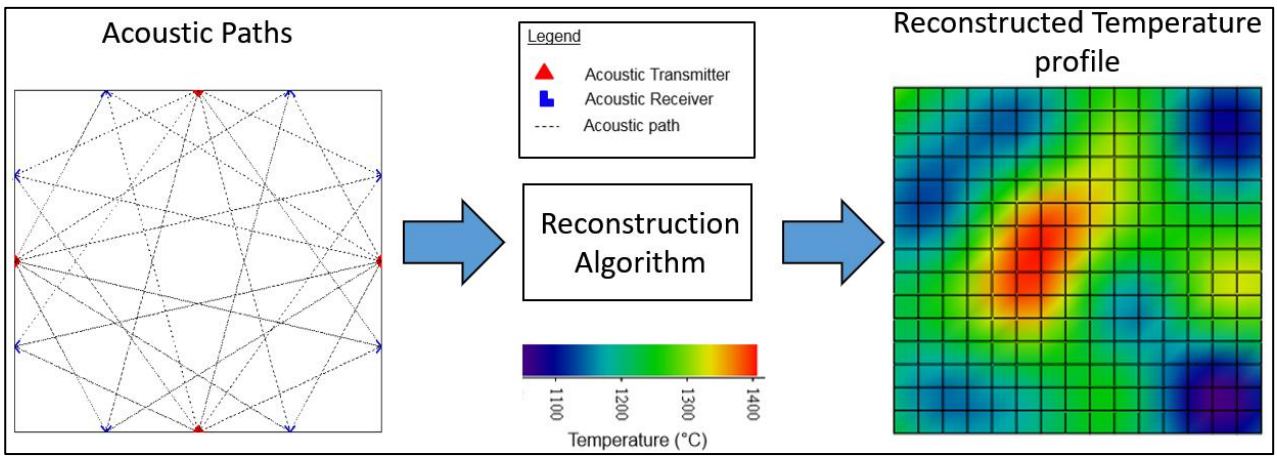

Figure 14 Acoustic paths and reconstructed temperature profile at the furnace exit

A greater number of acoustic paths covering more spatial area of the furnace exit will allow for more data points and thus a reconstruction of greater accuracy. However, this is not always feasible to implement from a practical and financial standpoint and thus a compromise must be made,

introducing a deviation from the actual temperature field and its reconstruction. Typically, reconstructions are made with few data points when compared to other inversion problems such as topography or imaging[23], placing emphasis on the type of reconstruction method used and the layout of these transducers to achieve a reliable temperature reconstruction. These factors amongst others will be discussed and investigated in greater detail in chapter 3.

Acoustic pyrometry application

As acoustic pyrometry is becoming more mature, the operating principle is finding application in more industrial fields. Acoustic Pyrometry methods have been applied to a wide variety of industrial systems including the measurement of furnace exit gas temperatures in coal fired power plants[24], validation of numerical CFD models[25], temperature measurement in energy from waste plants[26], cement kilns[8], oil refineries[27], and many other applications where the measurement medium is too harsh for conventional methods. The operating principle has also been extended beyond temperature measurement and been applied to monitoring fouling on the furnace walls[22] and reconstructing velocity fields in boiler furnaces[28].

Although there have been multiple commercially available acoustic pyrometers in the past, at present there are two main commercial acoustic pyrometers, the PyroMetrix™ device developed by Enertechnix Inc[29] and the Boilerwatch® MMP-II-SSX acoustic pyrometer from SEI[30]. These pyrometers operate on the same principle, but use slightly different approaches.

Acoustic Sound Generator (ASG) Acoustic Sound Receiver (ASR)

Figure 15 PyroMetrix™ Acoustic Sound Generator (ASG)(left) and Acoustic Sound Receiver (ASR)(right)[26]

The most distinct difference between the PyroMetrix™ and Boilerwatch® acoustic pyrometers is that the former employs a separate acoustic generator(ASG) and Acoustic receiver(ASR) for a single path measurement (which can be seen in Figure 15) while the latter has a singular unit that is a transceiver and acts as both a transmitter and a receiver (shown in Figure 16). They both use a pneumatic sound source requiring plant air supply to generate the acoustic signal, however the PyroMetrix™ is a much louder 170dB signal with a sharp rising peak, while the Boilerwatch® transceiver produces wide band signal at 126dB.

Figure 16 Boilerwatch® Hardware[30]

The signal processing methods used by these pyrometers are proprietary and thus not openly available. Nevertheless, despite the lower intensity signal generated by the Boilerwatch® acoustic transceiver, the accuracy is claimed to be lower than 0.5% compared to the 1% accuracy rating of the PyroMetrix™.

Figure 17 Temperature reconstruction for Pyrometrix™[29]

Both pyrometers also support the use of single and multiple acoustic paths.When multiple paths are used the temperature distribution can be reconstructed as shown in Figure 17 and have dedicated hardware for displaying and continuously monitoring these temperature distributions. Ultimately both devices are well developed and offer very similar functionality. The preferred product will largely be dependent on the application and characteristics of the furnace concerned.

2.3 Acoustic pyrometer sources of error

The basic Acoustic pyrometry principle makes certain assumptions about the how an acoustic wave travels, the medium through which it travels and the method of its application. All these assumptions are subject to either uncertainty or measurement error. Minimising these errors are of critical importance in developing a device that can reliably determine the FET and thus, in this section the possible sources of error and uncertainty are considered in order to reduce their affects where possible. Green released a comprehensive list of sources of error in[31] which was later republished in[19]. Moreover, a study was done by Young et al. where the focus was placed rather on the systematic errors of acoustic pyrometry[10]. The following list is a summary of these stated sources of errors.

2.3.1 Gas Composition

To obtain an accurate temperature reading, the properties of the acoustic medium should be known. The gas composition error manifests itself in the change of the acoustic constant as result of variation in mean molecular weight from not knowing the combustion gas composition and changes with temperature of the specific heat ratio. Young et al.[10] investigated this effect on a variety of fuel sources and found that in the worst case scenario when the combustion composition of coal is unknown, the systematic error is less than 2 %. However, this error is greatly reduced by knowledge of the furnace exit gas composition and could be accounted for by modifying the speed of sound versus temperature equation. In[31] Green estimated that the standard deviation of the molar mass of a given fuel is around 0.4 % and that when the specific heat ratio is linearized over the acceptable temperature range, the resulting standard deviation is 0.6 %. However in[1], Tootla noted that in South African power plants the coal composition is well known due to coal analysers and gas analysers in the flue gas stream.

2.3.2 Path Curvature and Length

Due to the fact that the speed of sound is dependent on temperature and time of flight readings are subject to Fermat's principle, the first acoustic signal to arrive at the receiving end might not necessarily be the straight-line path as one might expect and actually be a distorted acoustic path that has travelled faster in warmer regions. An amplification of this phenomenon is shown in Figure 18, where the red section represents the higher temperature region and the blue section represents the slower region.

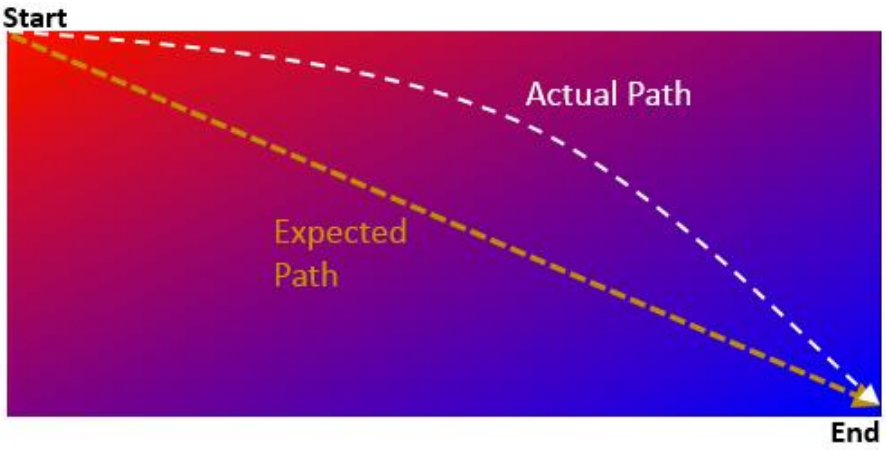

Figure 18 Path curvature due to temperature gradients

This problem is especially prevalent at regions near the furnace walls, where thermal gradients as high as 1000 $\frac{K}{m}$ can exist. Beyond around 0.5 m from the furnace walls this gradient is typically significantly decreased (less than 100 $\frac{K}{m}$). For typical path lengths, this error was estimated at around 0.2%, however in the worst-case scenarios it could be as high as 3.5 %[19]. As a result, for longer acoustic paths this effect is reduced, especially when the angle between the path and temperature gradient is reduced. This reasoning has been used in a few studies where the straight line assumption is implemented or treated as a systematic error [21], [23], [32]. In addition to this the actual straight-line path distance should be well known. Green suggested a standard deviation of less than 0.2 % for the shortest path is typically known and for shorter paths were bending is more likely to occur, a correction factor can be applied to compensate for this[31].

2.3.3 Gas Velocity

A further incurred error in the furnace is the components of gas velocity along the acoustic path. Usually the magnitudes of these velocities are relatively small when compared to the speed of sound (around 1-2%). However, this error can be easily mitigated by taking path readings in both directions and averaging the result. This method is easily applied when the acoustic pyrometer can act as a transmitter and a receiver (or transceiver)[23].

2.3.4 Particle content in gas

Another possible source of error involves the presence of solid particles within a flue gas. As is known, the speed of sound in a gas is very much dependant on the properties of that medium. In general, the speed of sound is determined by equation (4) which is based on the propagation of an adiabatic wave in an ideal gas. The assumption of an ideal gas is admissible at high temperatures, however at the furnace exit there is also a great likelihood that the gasses at the exit plane contain ash particles. In[33], Wallis gave an approximation for the change in speed of sound, by treating the flue gas, which is essentially a homogeneous 2 phase mixture, as a “pseudo gas” with modified gas properties. As a result, the universal gas constant and the ratio of specific heats was adjusted to include the mass concentration of ash and the specific heat of ash, as shown in equation (7) and (8)
.

$$R_p = \frac{R}{1+ma} \tag{7}$$

$$\gamma_p = \left(\gamma + \frac{C_a ma}{C_v}\right)\left(\gamma + \frac{C_a ma}{C_v}\right) \tag{8}$$

Where ma is the mass concentration of ash in the furnace gas, C_a is the specific heat of ash and C_v is the specific heat of the gas at constant volume. Since South African coals has a much higher ash content (as high as 30-40%), Tootla did a more detailed review of this effect in[1]. He compared two methods by Weber and Wallis for the operating conditions in South African boilers. He found that in the extreme (unlikely) worst case, if this effect was neglected an error of 3% would be associated with the speed of soundand 6% for the resulting temperature measurement. However, he also found that in most applications the solid particle concentration is so low that it need not be accounted for. In the case for South African power plants where there is high ash content, there is

sufficient information available to produce good estimates when using Wallis' correction. By accounting for this using the method proposed by Wallis, this effect could be easily mitigated.

2.3.5 Timing Error

The timing error arises from a difference between when a sound pulse arrives and when it is detected. This error is greatly dependant on the type of detection method used and is most easily shown using the threshold detection method. For this method time is captured when the amplitude of a filtered wave exceeds a set threshold. As seen in Figure 19 , the potential room for error is dependent on the rise time or frequency of the filtered wave, where higher frequency waves would result in a lower room for error. However due to the attenuation characteristics of flue gas this acceptable range is often limited. In order to reduce this error, the signal received should have a high signal to noise ratio with a sharp rise time (for the threshold detection method). In[31] Green estimated this error to have a standard deviation of around 0.3 % when using an older spark discharge transmitter.

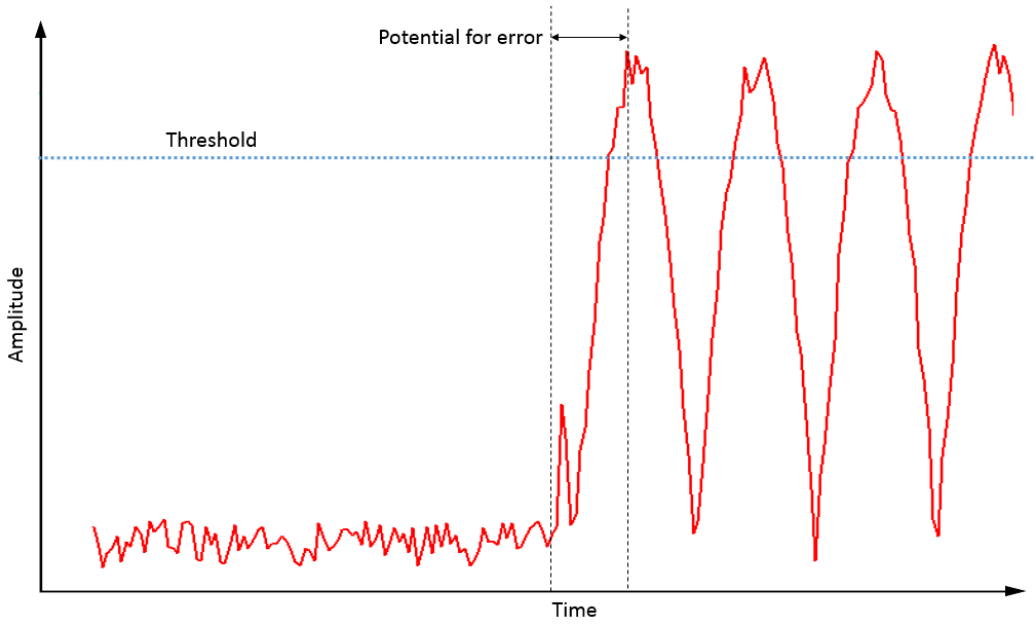

Figure 19 Potential for timing error when using threshold detection

2.3.6 Input and output of sound pulse

The method of inserting and extracting the acoustic signal from the furnace area is another source of potential error. This arises from the temperature change from the cooled mounting tubes to the hot furnace gas and the formation of particles in the transducer waveguides. The magnitude of this

error is greatly dependant on the furnace configuration used and Green's estimation for this error is around a 0.1 % for general configurations[31]. The temperature change from the transducer to furnace is a systematic one and can be compensated for[19] . More modern acoustic pyrometers also have automatic purging to prevent this from occurring, and consequently the error produced here is again greatly dependant on configuration.

2.3.7 Speed of sound pulse

Another source of potential error identified was the speed of the sound pulse. This is not true for all transmitter types, however for early acoustic pyrometers that used a spark gap discharge, the shock wave produced exceeded Mach 1 and resulted in an acoustic wave that travelled at different speeds in different directions. However, even with the technology used, the effect was negligible over typical path lengths. This has not been identified as a source of error on modern acoustic pyrometers.

2.3.8 Temperature variation with time

All acoustic path readings cannot be measured simultaneously, and thus there exists a time delay between these readings, during which the temperature in the furnace could have changed. This temperature change is approximated as oscillating at a frequency of 1 Hz with a variation of 20 K around the mean[31]. A simple model documented by Kleppe, assumed a sinusoidal temperature change, which resulted in a mean error of measured temperature of zero with a standard deviation of around 2 K. It was also calculated that fluctuating velocity affects would increase this deviation by 0.25 K[31].

3. Temperature profile reconstruction

3.1 Introduction to temperature reconstruction

One of the main advantages of acoustic pyrometry over conventional methods is that it does not only measure temperature at a single point, but rather measures average path temperatures, using properly positioned acoustic transmitters and receivers (or transceivers). If multiple path temperatures are measured in the furnace exit plane, it is possible to reconstruct a 2D temperature profile and get a spacial estimation of the temperature in that region. And because acoustic pyrometry is a non-contact technique, it is able to continuously monitor the temperature field at the furnace exit. An example of a reconstructed temperature profile can be seen below in Figure 20.

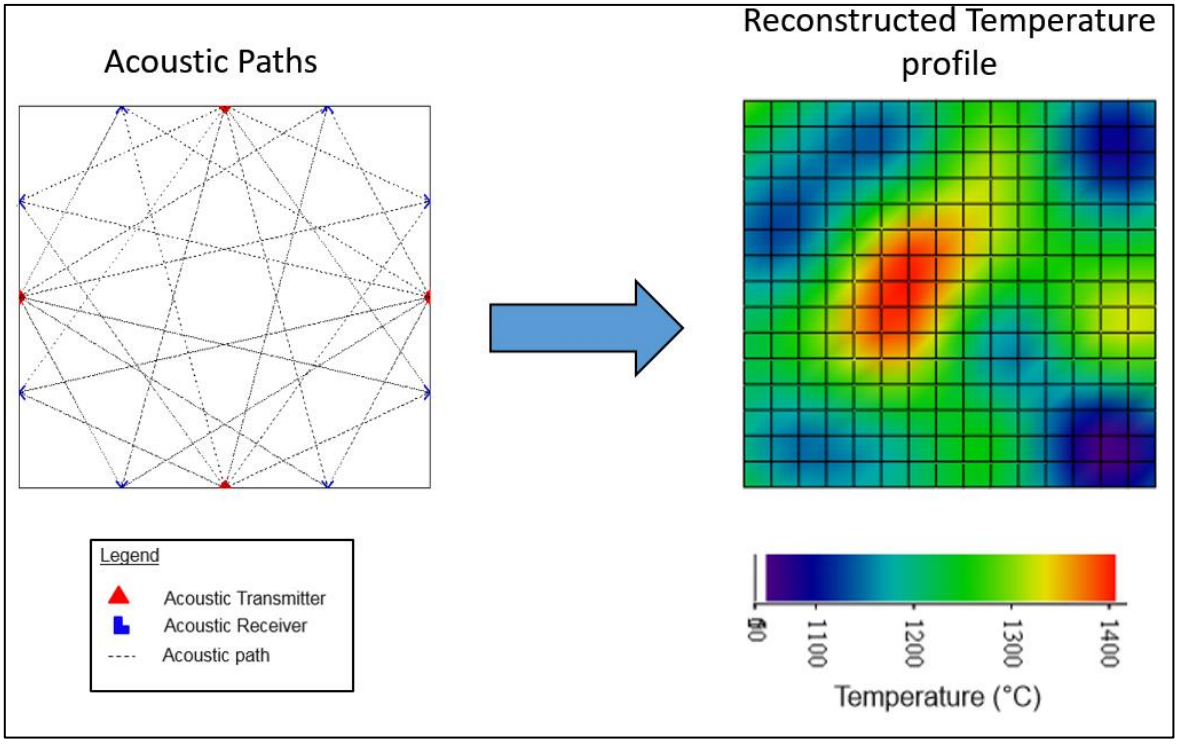

Figure 20 Acoustic Paths and Reconstructed Temperature Profile

The acoustic pyrometer system will have multiple acoustic transmitters and receivers placed around the perimeter of the furnace which will create several acoustic paths when fired as shown on the left side of Figure 20. Each of these paths will have a time of flight (TOF) and thus an associated average path temperature. By some reconstruction process, these average path temperatures are then used to estimate the special temperature profile as shown in the right of Figure 20.

Experimentally demonstrating temperature reconstruction would ultimately require multiple acoustic path measurements. This was not possible for this project due to equipment and time requirements and therefore did not fall under the scope of this study. Instead reconstruction is explored by simulating time of flight readings and then applying reconstruction algorithms.

3.2 Reconstruction methods applied in literature

Many approaches at temperature reconstruction have been attempted in the past, with the goal to produce the most accurate representation of the temperature field at the furnace exit. This section will present and review these methods, their contexts, as well as their advantages and disadvantages.

3.2.1 Fourier reconstruction method

An early attempt at temperature profile reconstruction involved representing the temperature distribution in a plane with a Fourier series. This method was first achieved by Green[31] and was characterised by determining the inverse of the temperature distribution, referred to as the "slowness" over the plane, which was approximated with a limited amount of terms as shown in equation (9).

$$F\left(X,Y\right) \approx \hat{F}\left(X,Y\right) = \sum_{k=0}^{sk} \sum_{l=0}^{sl} A_{kl} \cos\left(k\pi X\right) \cos\left(l\pi Y\right) \tag{9}$$

A – Matrix of Fourier coefficients

X, Y – Normalised coordinates

k, l – Index values for x and y direction respectively

sk, sl – Maximum number of Fourier terms in x and y direction respectively

The acoustic paths were described by normalised coordinates, where a single path is shown below in Figure 21.

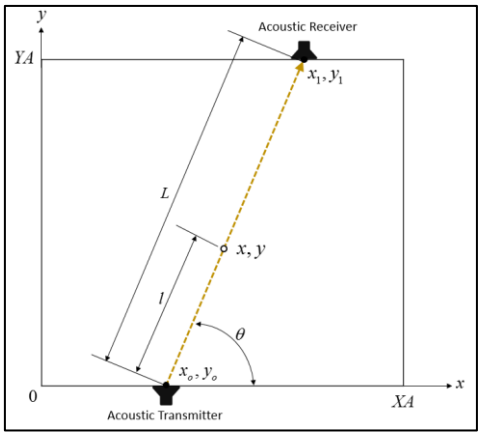

Figure 21 Acoustic paths with normalised coordinates

Where X, Y are expressed as follows.

$$X = \frac{x}{XA} = x_o + (x_1 - x_0)s \tag{10}$$

$$Y = \frac{y}{YA} = y_0 + (y_1 - y_0)s \tag{11}$$

XA, YA – Furnace dimension in x and y direction respectively

x_o, y_o – Starting coordinates in x and y direction

x_1, y_1 – End coordinates in x and y direction

$s = \frac{l}{L}$ – The fraction of distance along the total length of the path

The procedure is then to obtain an equation for the slowness of each path and solve for the Fourier coefficients by measuring the travel time of each acoustic path and knowing the positions of the transducers. This is done by representing them as a set of linear equations, however it was noted that it would only produce valid results if the number of acoustic paths (N_t) satisfied the following relationship.

$$N_t \geq (sk+1)(sl+1) \tag{12}$$

Since some redundancy might be necessary to produce a consistent set of results, a least squares fit is often used. Green[31] applied this method to produce contour plots as shown in Figure 22.

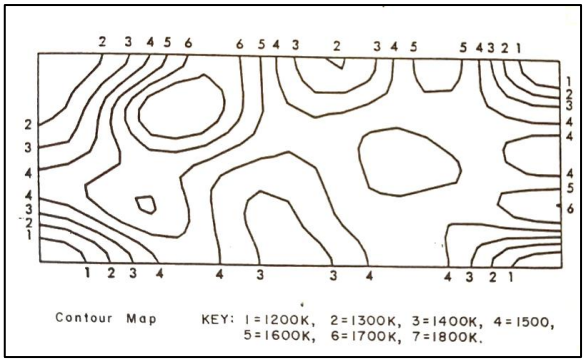

Figure 22 Temperature distribution reconstructed using Fourier technique[19]

Using randomly generated temperature distributions, Green could produce reconstructions that had a mean temperature error of less than 1 % between generated temperature distribution and the simulated reconstruction using only 6 transducers. However, this method of error analysis is somewhat misleading, since although there was great agreement for the mean temperatures, a comprehensive error analysis was not performed to evaluate the shape of the fit, which would give a much more reasonable indication of the performance.

Bramanti et al[32] also successfully applied this method, and found it to produce similar results to their section interpolation method. However, to avoid the limitation of equation(12), regularisation was used with sampling parameterization. This method was further verified numerically by comparison with a known temperature field. The fit of the reconstruction was evaluated by measuring the root-mean-squared (RMS) error.

$$E_{RMS} = \frac{\sqrt{\frac{1}{NM}\sum_{j,k=2}^{N,M}[T_{recon}(j,k) - T_{model}(j,k)]^2}}{T_{mean}} \times 100 \qquad (13)$$

Where, *NM* is the size of the sampling grid, $T_{recon}(j,k)$ and $T_{model}(j,k)$ are the reconstructed temperature and model temperature at index *j,k* respectively and T_{mean} is the mean temperature of the model temperature. It was found that the Fourier technique produced and RMS error of around 3.21 % for a temperature distribution with a mean temperature of 1330 °C and maximum temperature of 1400 °C. In addition to this it was validated experimentally by comparing the reconstruction with suction pyrometer readings reaching a depth of 2 m into a 5x5 m boiler at equally spaced locations along one of the walls, the results of this are shown in Figure 23.

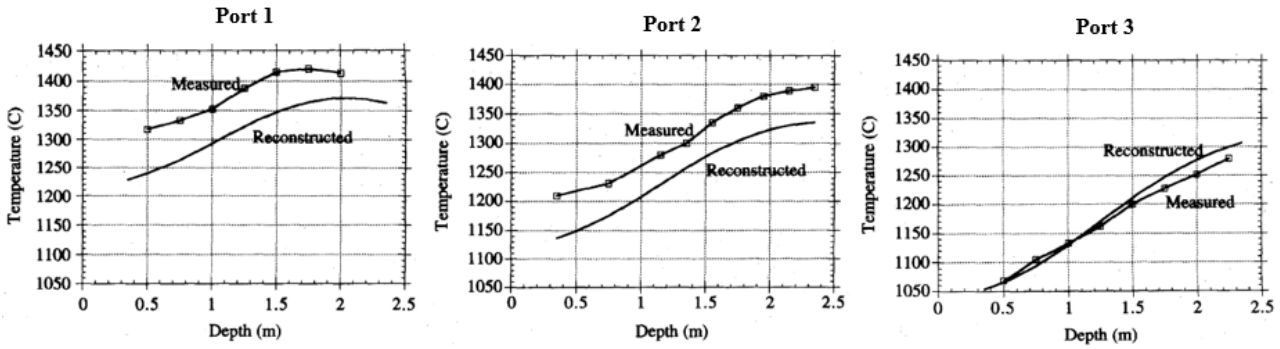

Figure 23 Thermocouple measurements compared to reconstructed temperature field with Fourier method for 3 different viewing ports[32]

The results show the discrepancy in this region is usually around 50 °C, nevertheless the correct temperature trend is observed. However, it should be noted that typical gas pyrometry temperature measurements are still prone to high error, as discussed in 2.2, and thus there is scope for improvement for validating temperature reconstruction methods. Bramanti further criticised the technique in noting that much like the reconstruction shown Figure 22 ,the Fourier technique was prone to producing reconstructions that intersect the boiler wall orthogonally, which is the opposite of what should occur.

3.2.2 Bi-Linear profile approximation

Another early approach to acoustic pyrometer temperature reconstruction was proposed by Kleppe et al.[19] where they proposed applying image processing to acoustic pyrometry in the form of 'numerical deconvolution methods' to create isothermal contours from time of flight readings (using multiple acoustic transceivers).

The method begins by taking the time of flight readings of all acoustic paths and converting these readings into mean path temperatures. A bi-linear profile is then used for each acoustic path as shown in Figure 24.

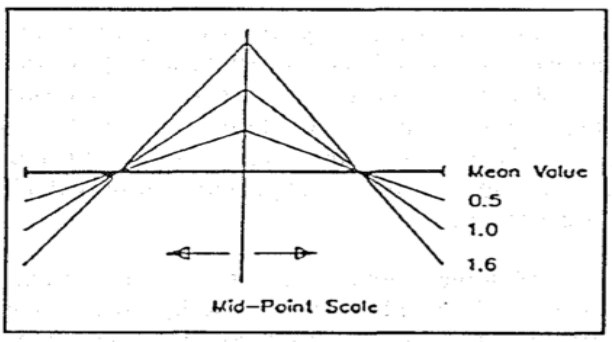

Figure 24 Bi-Linear Temperature Distribution[20]

This profile assumes that the peak temperature occurs at centre of each path and the minimum temperature is found at the ends of each path. In order to scale the bi-linear profile, the standard deviation of the path temperatures is taken and used to determine the deviation from the mean temperatures. They are then iteratively scaled to converge to the solutions that best fits all the measured path temperatures.

The estimated profiles are then plotted onto a two-dimensional grid representing the planar area of the boiler. Since the paths will not cover the entire area, the matrix will be sparse. The Bezier function is then used to interpolate between the known points using a polynomial approximation and creating discrete points on the grid. Once this is done, the curves are smoothed and line integrals are performed along the smoothed reconstruction. The results of these line integrals are then compared to the measured path temperatures and then used to adjust the scale factors for the next iteration to minimize the error between the measured readings and the reconstructed profile. The result of this is either an isothermal plot or 3D surface plot as shown in Figure 25.

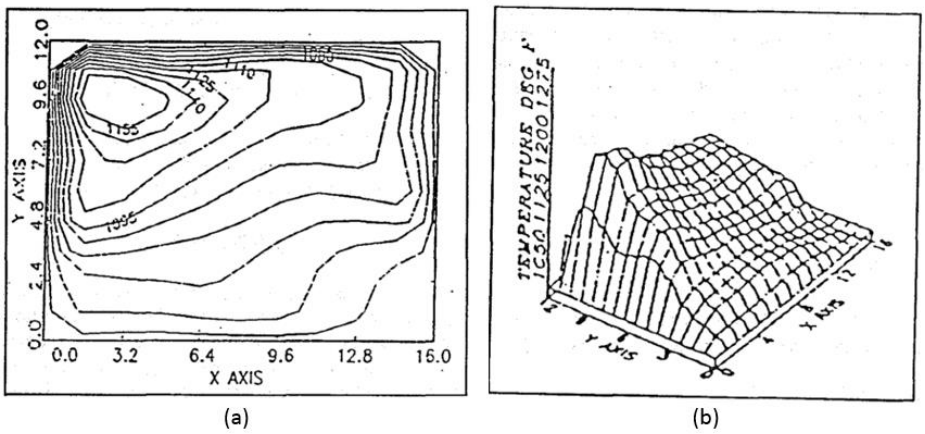

Figure 25 (a) Estimated Isothermal plot (b) Estimated 3D surface plot[20]

Kleppe et al. then go further to show the application of their method to correcting the temperature distribution in a waste-to-energy boiler. The temperature distribution was corrected applying control modifications of the secondary air distribution. The results as shown by the figure below, indicate that the peak location was moved from the edge to the centre of the boiler[20].

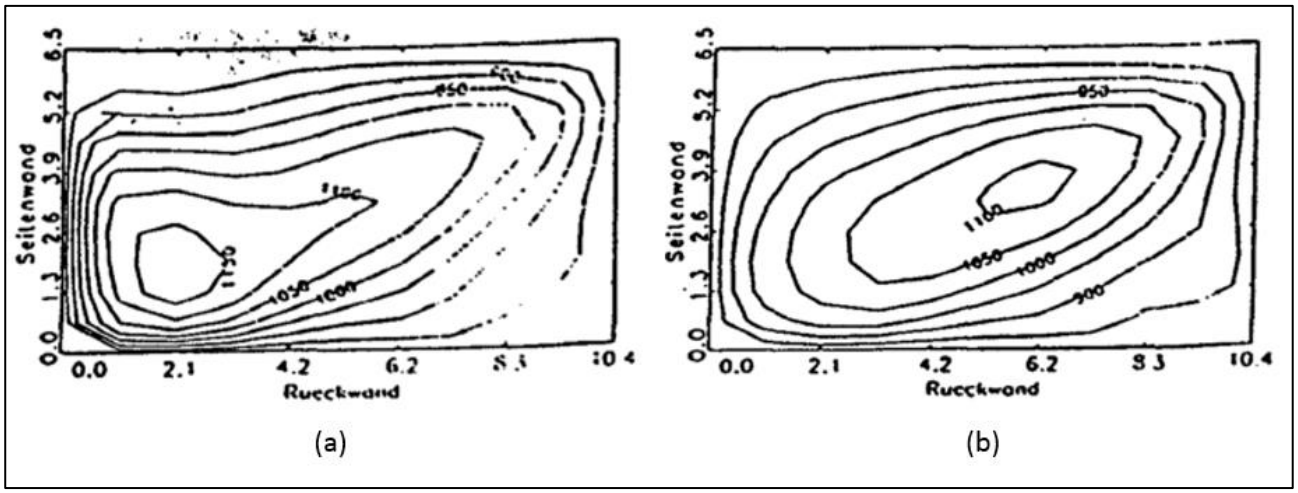

Figure 26 (a) Isothermal map generated (b) Isothermal map generated after control modifications[20]

While this paper does put forward a method that has been practically applied to continuous measurement, it does not provide any validation for the accuracy of this reconstruction method and was not tested against physical readings or simulated with known temperature distributions.

3.2.3 Least squares methods

Another popular reconstruction method is the least squares method[1], [24], [34]. The least squares method of reconstruction aims to achieve the minimum error between the time of flight readings obtained and the resulting reconstruction. This is done by considering the reconstruction region as a grid of discrete blocks as shown in Figure 27. In this particular example, a 4x4 grid is used and the shown acoustic path is discretised into 4 segments.

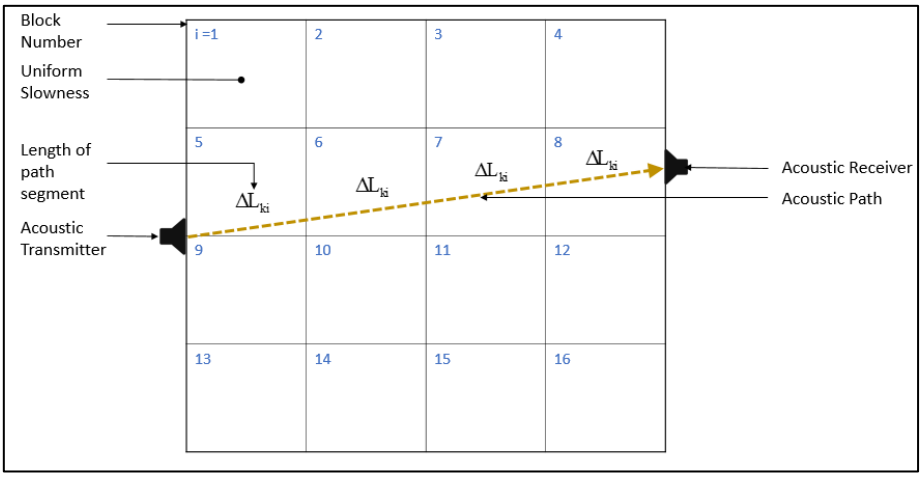

Figure 27 Temperature plane with a single discretised path

The time of flight of each path can then be expressed as a line integral of the slowness or reciprocal of velocity field in the direction of that acoustic path as shown in equation(14). This time of flight can be approximated by representing it as a sum of the product of the slowness in each block the path crosses and the length of the segment that passes through that block, shown below in equation(15). The assumption made here is that each block has a uniform temperature and therefore uniform slowness, so any sound wave travelling through that block with travel at the same speed.

$$t_k = \int_0^{L_k} f(x,y)\,dl \tag{14}$$

$$t_k{}' = \sum_{i=1}^{N_b} f_i L_{ki} \tag{15}$$

Where,

N – Total number of blocks

f_i – Slowness of i^{th} block [s/m]

L_{ki} – Length of the k^{th} path segment passing through the i^{th} block [m]

The error of this approximation can be considered as the difference between the measured time of flight for each path and the approximated time of flight when multiple acoustic paths are used.

$$error_k = t_k - t_k{}' = t_k - \sum_{i=1}^{N_b} f_i L_{ki} \tag{16}$$

The goal of the least squares method is then to minimise the sum of the squares of the path errors. This is achieved by taking the partial derivative of the error with respect of the slowness and equating it to zero.

$$\frac{\partial}{\partial f_i} \sum_{k=1}^{N_r} \left(t_k - \sum_{i=1}^{N_b} f_i L_{ki} \right)^2 = 0 \tag{17}$$

This reduces to the following canonical equation.

$$\mathbf{L}^{\mathrm{T}}\mathbf{L}\mathbf{f} = \mathbf{L}^{\mathrm{T}}\mathbf{t} \tag{18}$$

Where,

$$\mathbf{f} = \begin{bmatrix} f_1 \\ f_2 \\ \vdots \\ f_{N_b} \end{bmatrix},\ \mathbf{t} = \begin{bmatrix} t_1 \\ t_2 \\ \vdots \\ t_{N_t} \end{bmatrix}, \mathbf{L} = \begin{bmatrix} \Delta L_{11} & \Delta L_{12} & \cdots & \Delta L_{1N_b} \\ \Delta L_{21} & \Delta L_{22} & \cdots & \Delta L_{2N_b} \\ \vdots & \vdots & \ddots & \vdots \\ \Delta L_{N_t 1} & \Delta L_{N_t 2} & \cdots & \Delta L_{N_t N_b} \end{bmatrix}$$

The reciprocal of velocity or slowness can then be determined by trivial manipulations of equation(18).

$$\mathbf{f} = \left(\mathbf{L}^{\mathrm{T}}\mathbf{L}\right)^{-1}\mathbf{L}^{\mathrm{T}}\mathbf{t} \tag{19}$$

Since the layout of acoustic transducers and geometry of the furnace exit is known beforehand, matrix L can be calculated in advance. The vector t then becomes a collection of actual time measurements from which we can determine the slowness of each block. The limitation here is that for this calculation to be acceptable it must be well posed or overdetermined. To avoid an ill-conditioned problem the number of acoustic paths N_t must be the same or exceed the number of blocks N_b .

Once the slowness of each block is determined the temperature of each block can then be calculated by equation(20), knowing the properties of the flue gas.

$$T_i = \frac{1}{\gamma_{fg} R_{fg} f_i^2} \tag{20}$$

This temperature calculated for each represents a uniform temperature along that block. This process is shown in Figure 28, where the actual temperature profile is reduced to the least squares solution of uniform temperature blocks forming a 4x4 grid of pixels.

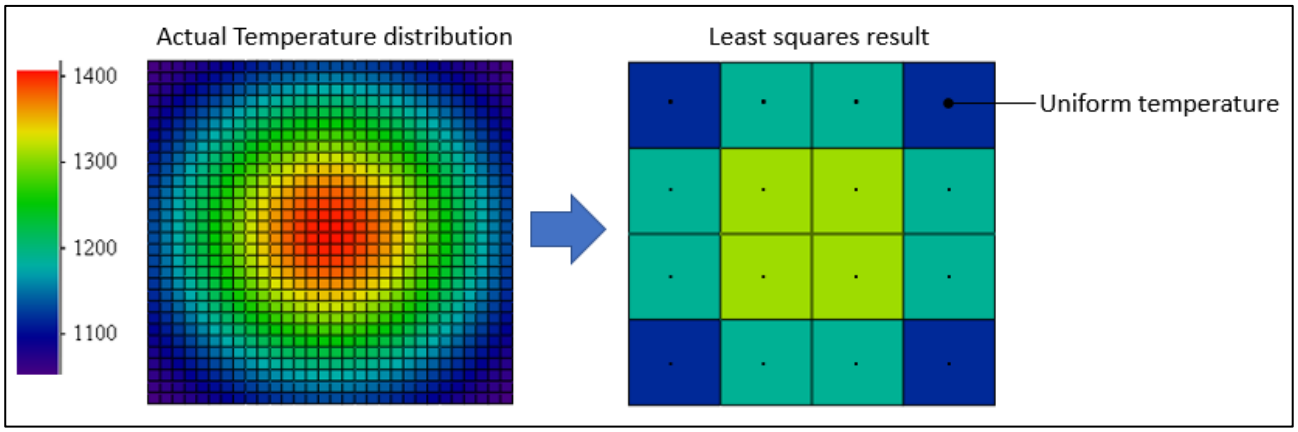

Figure 28 Least squares reconstruction from actual temperature distribution

This solution by itself is not that useful due to the limitation imposed that $N_t \geq N_b$, so in order to get a more useful solution with greater resolution an interpolation method is generally used. When doing this the assumption is made that the uniform temperature is the temperature at the centre of each block, and this becomes the temperature data point.

Recently Shen et al.[35] proposed a new algorithm to solve the ultrasonic thermometry reconstruction problem using the least squares method, and multi-quadratic radial basis functions (LSM-RBF) for interpolation. Their algorithm was not physically implemented but was rather implemented numerically in the Matlab environment.

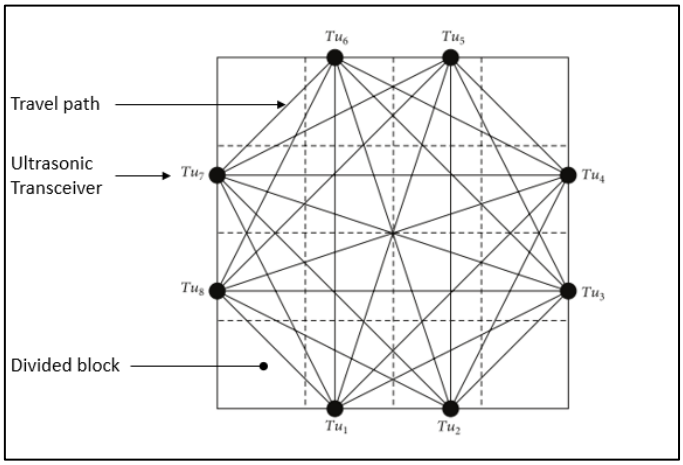

Figure 29 Schematic view of simulated measurement area used by Shen et al.[35]

In this study 8 transceivers were simulated and equally spaced apart as shown in Figure 29. This configuration allowed for 24 travel paths and to evaluate the temperature distribution the

simulated measurement area was divided into a 4x4 grid of blocks spanning over a total area of 12x12m.

For the interpolation stage, a multiquadratic nucleus function of the following form was used.

$$\phi_i(x,y) = \left(\left\| (x,y) - (x_i, y_i) \right\|^2 + \gamma^2 \right)^{\beta} \tag{21}$$

Where (x,y) is the interpolated point and (x_i, y_i) is the centre coordinate of the nucleus function and the centre of each divided block. The shape factor is represented by γ and is treated as a constant, experimentally predetermined as 2.35. β is also a constant chosen usually being either 0.5 or 1; for this algorithm, it is selected as 0.5, which corresponds to a multiquadratic nucleus function.

To evaluate the performance of the algorithm, four varying temperature functions were defined and reconstructed using the least squares with multiquadratic interpolation algorithm (LSM-MQ) and compared with a least squares model (LSM) curve fitting solution on Matlab. When reconstructing the profile, the assumption was made that the thermometry devices would protrude 1m into the boiler and thus the outside 1m of the area is excluded, thus as shown in Figure 30, the measurement area is from 1-11m. Another noticeable difference shown is that the LSM-MQ method is able to reconstruct the whole model area, while the LSM method loses the outside 1m of the area.

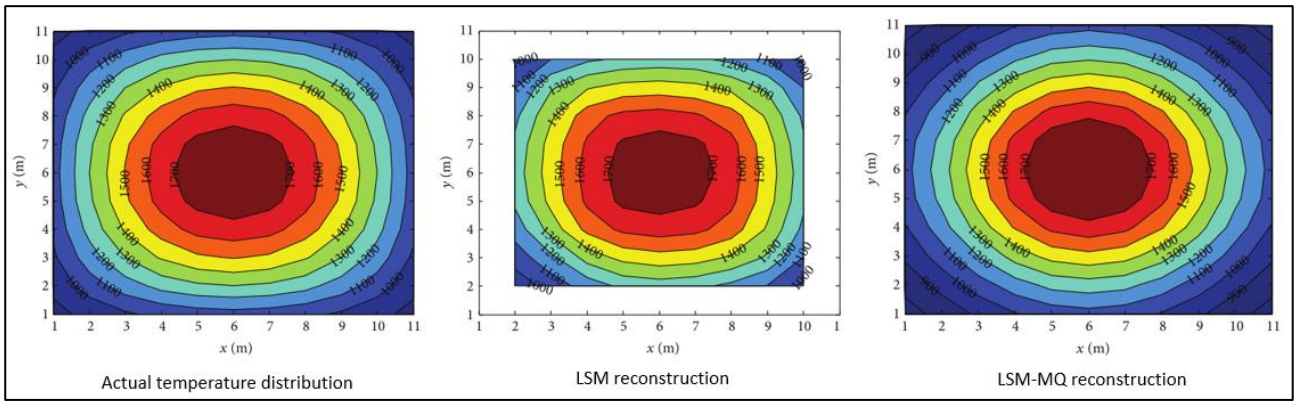

Figure 30 Comparison of reconstructed temperature profiles with actual temperature profile for first temperature function[35]

Nevertheless, for both reconstruction models, the first temperature distribution is closely recreated. In order to test the true versatility of the models, a total of 4 temperature distributions were tested. The formulas defining these distributions are shown in equations (22) - (25).

One-peak symmetrical temperature distribution:

$$T_1(x,y) = 800 + 1000 \cdot \sin\left(\frac{\pi}{12}x\right) \cdot \sin\left(\frac{\pi}{12}y\right) \tag{22}$$

One-peak asymmetrical temperature distribution:

$$T_2(x,y) = 600 + 1200 \cdot e^{-\left(\frac{(x-8)^2+(y-4)^2}{100}\right)} \tag{23}$$

Two-peak asymmetrical temperature distribution:

$$T_3(x,y) = 800 + 900 \cdot e^{-20\cdot\left(\left(\frac{x}{12}-\frac{1}{3}\right)^2+\left(\frac{y}{11}-\frac{2}{3}\right)^2\right)} + 800 \cdot e^{-\left(20\cdot\left(\frac{x}{12}-\frac{2}{3}\right)^2+15\cdot\left(\frac{y}{11}-\frac{1}{3}\right)^2\right)} \tag{24}$$

Three-peak asymmetrical temperature distribution:

$$T_4(x,y) = 1000 \cdot e^{-20\cdot\left(\left(\frac{x}{12}-\frac{1}{5}\right)^2+\left(\frac{y}{11}-\frac{5}{7}\right)^2\right)} + 1000 \cdot e^{-20\cdot\left(\left(\frac{x}{12}-\frac{4}{5}\right)^2+\left(\frac{y}{11}-\frac{4}{7}\right)^2\right)} + 800 \cdot e^{-\left(20\cdot\left(\frac{x}{12}-\frac{2}{5}\right)^2+15\cdot\left(\frac{y}{11}-\frac{1}{3}\right)^2\right)} + 800 \tag{25}$$

Since the study aims to approximate known temperature distributions, the accuracy of the reconstruction was determined by calculating the mean and root mean square error of the reconstruction. The errors were calculated using equation (26) and(27).

$$E_m = \frac{1}{n} \cdot \sum_{j=1}^{n}\left(\frac{TR_j - TM_j}{TM_j}\right) \cdot 100 \tag{26}$$

$$E_{rms} = \frac{\sqrt{\left(\frac{1}{n}\right)\sum_{j=1}^{n}\left(TR_j - TM_j\right)^2}}{TM_{mean}} \cdot 100 \tag{27}$$

TR_j and TM_j are the reconstructed and model temperatures at point (x_j, y_j) respectively and *n* is the number of calculated points. The LSM and LSM-MQ algorithms are compared for each tested temperature distribution and it was found that the accuracy of reconstruction varied greatly depending on the temperature distribution being reconstructed and that the accuracy of both algorithms were in a similar error range. The LSM-MQ algorithm showed a more accurate

reconstruction for the two more complex temperature distributions, namely T_3 and T_4, while the LSM algorithm was more accurate for T_1 and T_2. Both algorithms were also able to reconstruct the temperature profile within 0.15 s, showing that both algorithms are suitable for practical implementation[35].

Although radial basis functions are effective for solving the interpolation problem in acoustic pyrometry, its accuracy is strongly dependent on a shape parameter which has been largely overlooked in its application to reconstructing temperature profiles for acoustic pyrometry. Generally when these functions are used for interpolation, a single value for the shape parameter is chosen that is usually preselected using experimental results[35]. Several researchers have developed formulas to predict an optimum shape parameter for interpolation, solely on the distribution of data points. However, later research done by Rippa[36] found that these solutions were only approximate and the ideal shape parameter for the interpolation problem was dependant on more than just the distribution of data points.

Rippa concluded that an algorithm that effectively predicts the optimum shape parameter must consider the number and distribution of data points, the radial basis function Φ, the precision of computation and the data vector used.

$$S = S(x) = \sum_{j=1}^{N} a_j \Phi\left(\left\| x_j - x \right\|\right) \tag{28}$$

Thus, an algorithm was developed that determines a shape factor that minimises a cost function that imitates the behaviour of the RMS error between the interpolant and the unknown function from which the data vector was sampled, where the RMS error is taken as an indication of the quality of fit.

This is done by taking the norm of the error vector as calculated from equation(29).

$$E_k = f_k - S^{(k)}(x_k) \tag{29}$$

Where $S^{(k)}$ is the interpolant of a reduced data set obtained by removing x_k and corresponding value f_k from the data set. The interpolant $S^{(k)}$ is calculated a shown below.

$$S^{(k)} = S^{(k)}(x) = \sum_{j=1, j\neq k}^{N} a_j^{(k)} \Phi\left(\left\|x_j - x\right\|\right) \tag{30}$$

Thus, a cost value is obtained for each sampled data point. However, to determine the optimum smooth parameter, the error vector must be calculated by repeating the interpolation phase N (number of data points) times and then the norm of that error vector produced must be calculated for each smooth parameter tested, which would be extremely computationally expensive.

As a result, Rippa simplified the error vector calculation to the form in equation (31) . In this form, a_k is the kth element in the complete weighting coefficient vector and $x_k^{[k]}$ is the kth diagonal element in a matrix obtained by computing the inverse of the complete radial basis function matrix.

$$E_k = f_k - S^{(k)}(x_k) = \frac{a_k}{x_k^{[k]}} \tag{31}$$

This implementation greatly reduces the computational complexity of the algorithm as it does not require us to recalculate the interpolant in equation (30) N times for each shape value. This simplification reduces the algorithm's computational complexity to a level which is practicable.

The simplified algorithm was then used to compute the cost function for varying values of the shape parameter. The graph of the cost function is shown numerically to be very similar to the graph of the RMS error and thus indicates that computing the cost function is a great predictor for the optimal shape parameter if the interpolated function is not explicitly known.

Consequently, the algorithm was shown to consistently produce good values for the shape parameter for the multiquadratic, inverse multiquadratic and Gaussian interpolants for a range of different interpolated functions[36].

This algorithm has not yet been applied to the acoustic pyrometry problem, and if its accuracy extends to reconstruction problems with less data points, it could prove to be beneficial to achieving more accurate reconstructions when the temperature distribution is not known.

3.2.4 Computed tomography

More recently Zhang et al.[37] put forward the method of applying computed tomography to the acoustic pyrometry reconstruction problem. Computed tomography is an efficient image processing

method that has a wide variety of applications but is most commonly known for its use in medical imaging using x-rays.

In their application Zhang et al. set out to use this method for continuous online monitoring of the furnace exit temperature. This included the signal processing of the time-of-flight (TOF) readings as well as reconstructing the temperature field. This was achieved with 4 sound sources based on loudspeaker technology and 8 sound receivers arranged as shown in Figure 31, ultimately creating 24 acoustic paths.

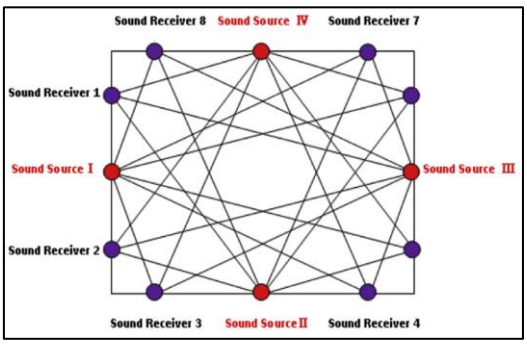

Figure 31 Schematic of measurement points[37]

Zhang et al. noted the high likelihood of the reconstruction to be overdetermined or ill-conditioned, and thus not having an exact solution. For their experimental setup, they split the cross section into a 4x4 grid, creating 16 pixels (data points) but had 24 acoustic paths. In an attempt to reduce the amplified effects of noise that would be incurred from direct matrix inversion or some iterative least squares methods, a computed tomography technique was attempted. The computed tomography method applied was the algebraic reconstruction technique (ART). The iterative equation for the ART process is shown in equation (32).

$$x^{k+1} = x^k + \lambda \frac{b_j - w_j \cdot x^k}{w_j^{\,2}} w_j \tag{32}$$

For this process, *k* is the iteration number, and λ is the relaxation factor (between 1.3-1.35), w_j is the j^{th} row of the weighting matrix used and x_o is the initialisation vector. In order to speed up the iteration process, the least squared solution can be used as x_o.

Once the pixel values were obtained the rectangular section was then interpolated into a 16x14 grid using bicubic interpolation, producing a temperature profile as shown in Figure 32.

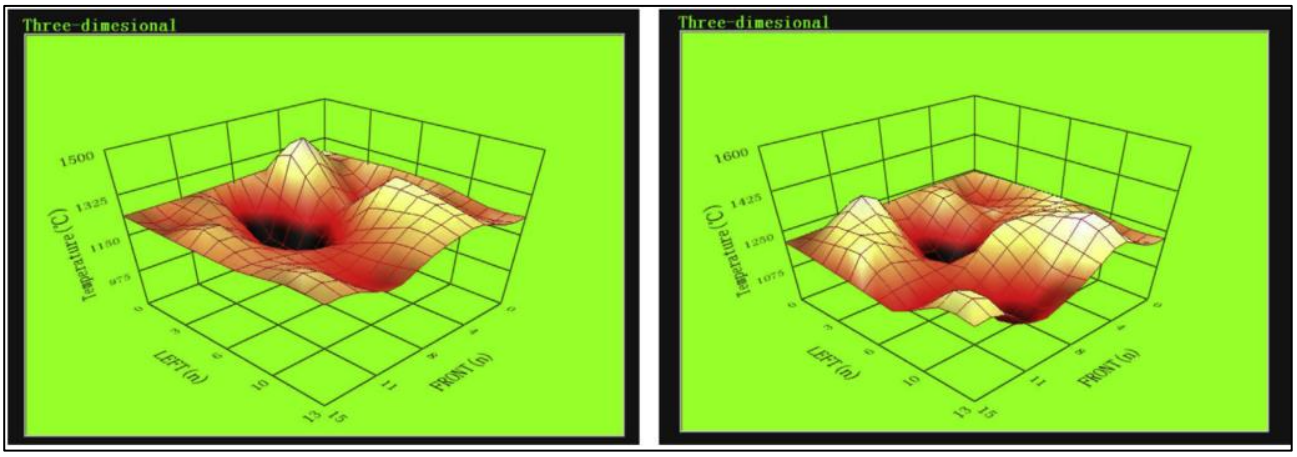

Figure 32 Three-dimensional reconstructions during hot state monitoring[37]

In the hot state results show the high temperature regions to be instable, however this was attributed to combustion instability.

The only validation done on the model was by measuring the temperature of the flue gas at four locations using thermocouples, and there was no comparison done using simulated data. These four thermocouples were placed as shown in Figure 33 and due to the limitations as to how deep a thermocouple can be placed, they were evidently located near the outer edges of the furnace.

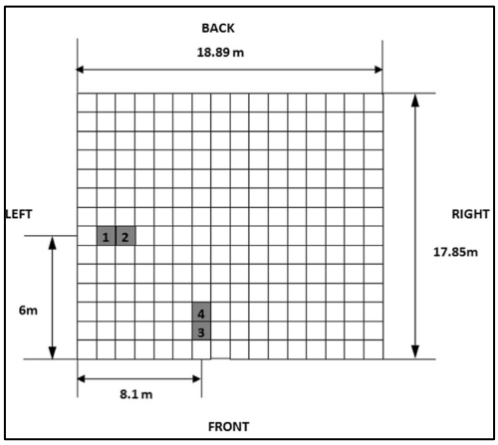

Figure 33 Schematic of temperature measurements using thermocouples[37]

The comparison between the reconstructed temperature and the measured temperature at these regions showed a relative error of around +-4.3 %. Although this error might be acceptable for some applications, this comparison is limited and the discrepancy near the high temperature regions, where there seems to be a large temperature fluctuation, is unknown. In addition to this the number of measurement repetitions is not given so there is no indication of whether there is a fluctuation

in this error and which regions were more affected. While the technique can produce three-dimensional reconstructions, the model is not comprehensively validated.

3.2.5 Regularisation Methods

The reconstruction problem is essentially an inverse problem, and in many applications, it is prone to be ill-posed, especially in the presence of noise. Consequently, to achieve a meaningful solution to the reconstruction problem, some researchers have attempted regularising the solution to compensate for these shortfalls.

Sielschott et al.[23] attempted the reconstruction problem placing emphasis on the use of few data points. Ideally to get an accurate reconstruction of the temperature field, more acoustic paths would be preferred, however this is not always feasible. A more realistic selection of 24 acoustic paths was used and compared with a more ideal scenario of having 96 acoustic paths. For this study acoustic transceivers were used (acting as both transmitters and receivers) the arrangement used is shown in Figure 34. By using transceivers, acoustic readings were taken in both directions to remove and cancel out the source of error associated with the flue gas velocity in a particular direction.

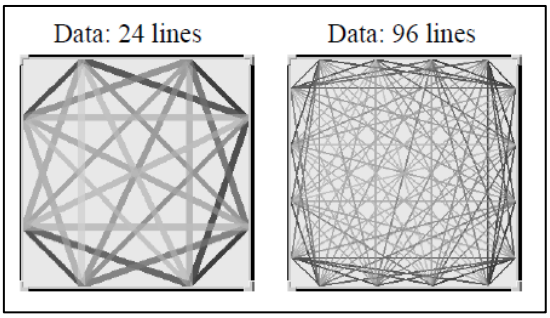

Figure 34 Acoustic transceivers layout with 24 lines (8 transceivers) and 96 lines (16 transceivers)[23]

The reconstruction method employed involved using “ansatzfunctions” or basis functions and solving the linear set of equations using Tikhonov-Phillips regularisation. Like most methods the time of flight for each path (g_l) was defined as a line integral of a slowness function *f(x)* along the path distance L_l , knowing the mean time of flight and path distance for each path.

$$g_l = \int_{L_l} f(x)\, ds \tag{33}$$

A collocation method is the used to describe the slowness function, defining the slowness as a sum of undermined coefficients ξ_k and basis functions $\varphi_k(x)$ for each reconstruction region. And ultimately the slowness of the plane is defined as a sum of these basis functions.

$$f(x) = \sum_{k=1}^{n} \xi_k \varphi_k(x) \tag{34}$$

$\varphi_k(x)$ – Basis Function

ξ_k – Undetermined coefficients

The basis functions used take the form as shown in (35). Although it is not explicitly referred to as such, the form of these equations resemble an exponential radial basis function, where λ can be thought of as a shape parameter controlling the shape of the function and x_k is the midpoint of the pixel concerned. A value of λ *=8.0* was selected by Sielschott et al.[23].

$$\varphi_k(x) = e^{-\lambda|x-x_k|^2} \tag{35}$$

The reconstruction region is divided into 10x10 pixels and thus *n*=100. By defining the integral of the basis function along each path as a_{lk} in equation(36). The equation for time of flight can be represented as a sum of ξ_k and a_{lk} as shown in equation(37).

$$a_{lk} = \int_{L_l} \varphi_k(x)\, ds \tag{36}$$

$$g_l = \sum_{k=1}^{n} a_{lk} \xi_k \tag{37}$$

This form can be easily converted to a linear set of equations as shown in(38). Where the goal now is to find vector ξ to solve the set of equations.

$$A\xi = g \tag{38}$$

In this example *A* is ill-conditioned, since we have 24 paths but require 100 pixels. In order to compensate for this, Tikhonov Phillips regularisation for digital filtering was used. The goal is then to minimise the following equation.

$$\|A\xi - g\|^2 + \gamma\|D\xi\|^2 \tag{39}$$

In this equation, $\gamma\|D\xi\|^2$ is the minimiser and γ exists as a parameter controlling the regularisation, where the minimiser can be computed using the singular value decomposition (SVD) of *A* and D is chosen as the identity matrix *I.* Once ξ is obtained, the slowness equation (34) is defined and the temperature of the region can be determined.

The artificial temperature distributions (referred to as 'phantoms') used by Sielschott et al.[23] cover a temperature range of 850-1250 °C which was deemed a realistic temperature range for the furnace exit. Moreover, based on suction pyrometry readings the phantoms were selected as having steep temperature gradients near the edges and a rather constant temperature in the centre.

An example of one of these profiles is shown in Figure 35. The quality of reconstruction was tested visually and no numeric metric for fit was considered, however they did consider path error and reconstructed for three path error conditions, 0% 1% and 2.5% respectively. Under these conditions the reconstructions with 96 paths were much more accurate and stable, however this number of paths would be unrealistic for actual application. Reconstructions with a more realistic 24 paths were not able to adequately represent the chosen temperature profile[23].

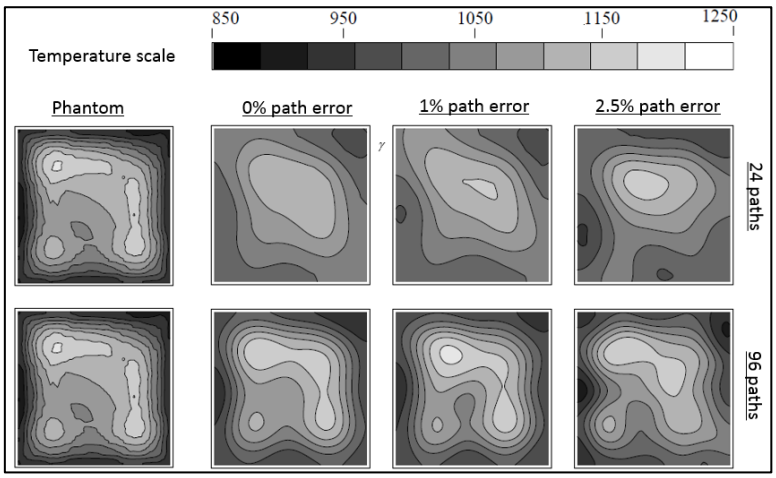

Figure 35 Reconstruction results when using 24 and 96 paths for 3 path error conditions, where γ =0.1[23]

In another study Sielschott[38] went further to try and incorporate a priori information into the reconstruction. Since the furnace exit region was well known for the ideal case based on suction pyrometer, a radiation pyrometer and theoretical considerations, they've attempted to incorporate starting pictures and smoothing into the reconstruction process. The goal behind this process was to get a more realistic reconstruction and remove the unrealistic peaks seen in previous attempts.

When starting pictures are used, the reconstruction process attempts to form the slowness function *f(x)* from a more realistic distribution *h(x)* which would form the 'starting picture' as shown in equation(40).

$$f(x) = \kappa h(x) + u(x) \tag{40}$$

Here κ, which is a scaling factor, is selected to minimise the difference between the time of flight readings obtained, and that which would be obtained with $\kappa h(x)$ as the slowness function. Once κ is determined, *u(x)* is computed as a reconstruction from the difference between the measured data and the time of flight readings which would be obtained with $\kappa h(x)$.

In addition to this smoothing is attempted, where a maximum value is selected based on the starting picture and if the $\kappa h(x)$ term exceeds this value it is limited to this maximum value. In summary the process involves computing the reconstruction, changing it to incorporate a priori information and then correcting it to fulfil the measured data. Using this process reconstructions were achieved as seen in Figure 36. Three different 'phantoms' were used, the starting picture was the rather flat 3rd phantom and time of flight data was given a 1 % error.

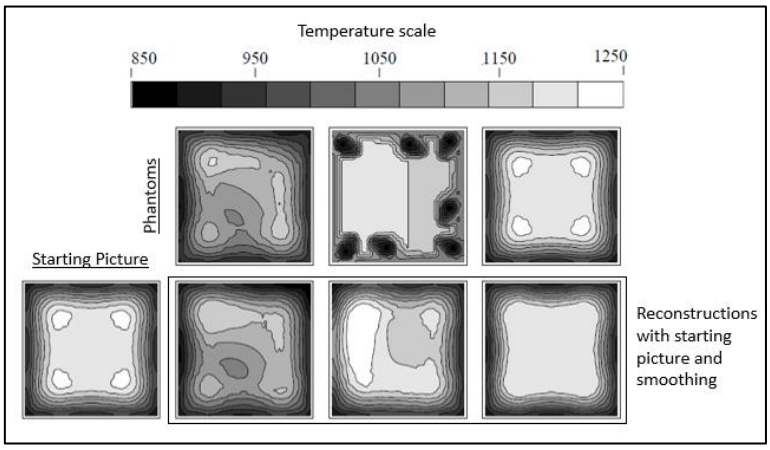

Figure 36 Reconstructions with starting picture, smoothing and time of flight errors of 1%[38]

Reconstructions incorporating a starting picture were much more accurate than previous reconstruction attempts. Although no error analysis was performed, visually two of the three phantoms showed great correlation. However, it was noted that the quality of the reconstruction was largely dependent on the starting picture chosen, which can be seen by the failed reconstruction of the second phantom. Simple starting pictures such as the one used in Figure 36 produced rather accurate reconstructions, while more complicated starting pictures were likely to

produce unfavourable reconstructions for simpler temperature profiles. This method proved to be very useful if you had a great knowledge of the shape of the temperature profile[38].

Another recent popular and similar method of temperature reconstruction involves the use of Markov radial basis functions in conjunction with Singular value decomposition(SVD RBF)[34], [39]–[41].

The form of radial basis functions used take the same form as that used by Sielschott et al. as shown in equation(41).

$$\varphi_m(x,y) = e^{-\theta\sqrt{(x-x_m)^2+(y-y_m)^2}} \tag{41}$$

Here θ is a shape parameter and (x_m, y_m) is the midpoint coordinate of the m^{th} block or pixel. If the temperature plane is divided into N blocks or pixels, the slowness function is then represented as a sum of the product of the undetermined coefficient and the radial basis functions

$$f(x,y) = \sum_{m=1}^{N} \varepsilon_m \varphi_m(x,y) \tag{42}$$

Then,

$$t'_k = \sum_{m=1}^{N} \varepsilon_m a_{km} \tag{43}$$

$$t = A\varepsilon \tag{44}$$

As in previous methods, this problem can be ill-conditioned, and singular value decomposition is used here as a form or regularisation to estimate the undetermined coefficient. According to this method a real or complex matrix can be decomposed as follows.

$$Q = USV^T \tag{45}$$

Where U and V are orthogonal matrices and S is defined as:

$$S = \begin{bmatrix} \Sigma & 0 \\ 0 & 0 \end{bmatrix} \tag{46}$$

Here, Σ is a diagonal matrix of singular values in descending order.

$$\Sigma = \begin{bmatrix} \sigma_1 & 0 & 0 & 0 \\ 0 & \sigma_2 & 0 & 0 \\ 0 & 0 & \ddots & 0 \\ 0 & 0 & 0 & \sigma_n \end{bmatrix} \tag{47}$$

By using the following definition:

$$S^+ = \begin{bmatrix} \Sigma^{-1} & 0 \\ 0 & 0 \end{bmatrix} \tag{48}$$

where

$$\Sigma^{-1} = \begin{bmatrix} \frac{1}{\sigma_1} & 0 & 0 & 0 \\ 0 & \frac{1}{\sigma_2} & 0 & 0 \\ 0 & 0 & \ddots & 0 \\ 0 & 0 & 0 & \frac{1}{\sigma_n} \end{bmatrix} \tag{49}$$

The generalised inverse of matrix A can be computed.

$$A^+ = VS^+U^T \tag{50}$$

And thus, the undetermined coefficient can be obtained since A can be computed.

$$\varepsilon = A^+ t \tag{51}$$

Once the undetermined coefficients are known, the slowness function can be constructed from equation (34) and thus the temperature field can be determined.

In a study done by Shen et al.[34] this method was applied numerically to a furnace with a square cross section and then later the same method was applied to reconstruct in a furnace with a circular cross section[40].

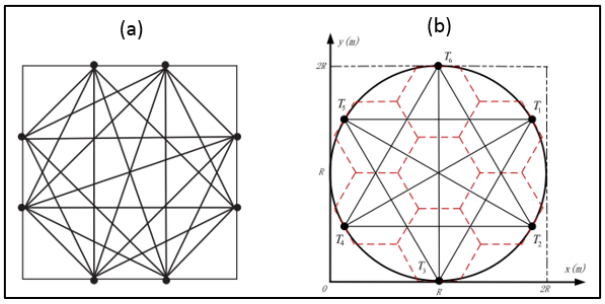

Figure 37 (a) travel paths and division for a square cross section (b) travel paths and divisions for a circular cross section[40]

These methods were tested against the temperature functions similar to those used by[35] and compared with a least squares method using multi-quadratic radial basis functions (LSM-MQ)[35]. In the study testing regularisation methods, Shen et al. go further than merely testing mean and RMS error as shown in equation (26) and (27), but also perform a hotspot analysis evaluating the position of the peak as shown in equation (52) as well as the temperature error at that peak as shown in equation (53) to evaluate the quality of the reconstruction.

$$P_E = \frac{\sqrt{\left(x_0 - x_{r0}\right)^2 - \left(y_0 - y_{ro}\right)^2}}{d} \times 100 \tag{52}$$

$$E_{Th} = \left| \frac{TM_h - TR_h}{TM_h} \right| \times 100 \tag{53}$$

In these equations, $\left(x_0, y_0\right)$ and TH_h are the coordinates of the hotspot and temperature at the hotspot on the temperature distribution model, while $\left(x_{r0}, y_{r0}\right)$ and TR_h are the coordinates and temperature of the hotspot on the reconstructed temperature field respectively. These similarities between the two studies ([34] and [35]) would suggest that the results between the two methods would be directly comparable, however on further analysis slight variances exist between the application of the two methods. The first being that the double peak model temperature distribution was altered between studies as shown below.

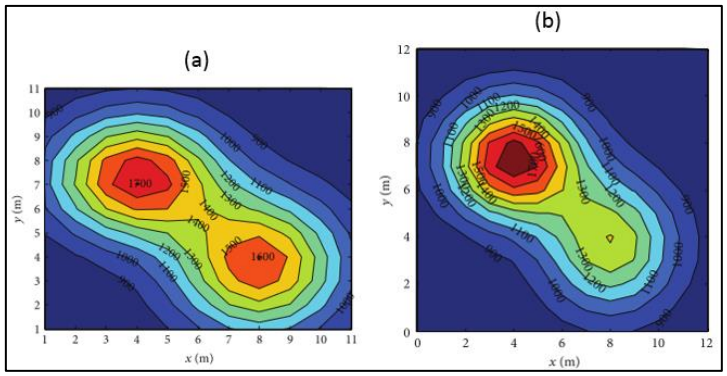

Figure 38 a) Double peak temperature distribution model used in[35] and b) double peak model used in[34]

A noticeable difference here is that although the peak locations in both models are the same, the actual temperature of these peaks were varied. Secondly the measurement area was changed across all distributions from 11 m x11 m to 12 m x12 m without changing the temperature distribution formulas to reflect this.

Nonetheless, the mean and RMS error results from both studies are still able to give an indication of the efficacy of both methods. When comparing the four temperature profiles, the LSM-MQ method produces results around the same accuracy as the SVD RBF method for the single peak functions. However, when comparing the results from the double and triple peak temperature distribution model, the SVD RBF method produced more accurate results.

Additionally, the method was tested with random travel path noise to evaluate the effect of noise on the final reconstruction. This was done by adding Gaussian noise with a mean of 0 ms and a standard deviation of 1 ms to each path travel time. This method showed strong noise resistance, and the mean reconstruction error changed by less than 0.5 %. The method shows great potential in the numerical environment, especially in its ability to reconstruct despite path noise, however has it not been validated in a boiler furnace environment.

The same method was tested numerically by Jia et al.[39] with very similar temperature distributions and compared their results with the least squares algorithm. The temperature distributions used in this study were slightly steeper and tested over a smaller 10 m x10 m grid. The result of this was that the mean error when evaluated with the same equation used by Shen et al.[34] produced comparable error results for the single peak distribution, however was less accurate for multiple peaks. In this study the least squares algorithm was more accurate for the single peak profile, but was less accurate for multiple peaks. In theory the algorithm used in this study was the same as that used by Shen et al.[34], however the results of the latter was much more accurate. This could suggest that changes in the temperature field and transmitter and receiver

layout is a great influencer of performance and care should be taken when directly comparing methods.

Jia et al. went further in [42] to validate the SVD RBF algorithm using a small experimental setup as shown in Figure 39 a. A heater source was used to create a temperature distribution and then moved to various locations to create asymmetrical peaks.

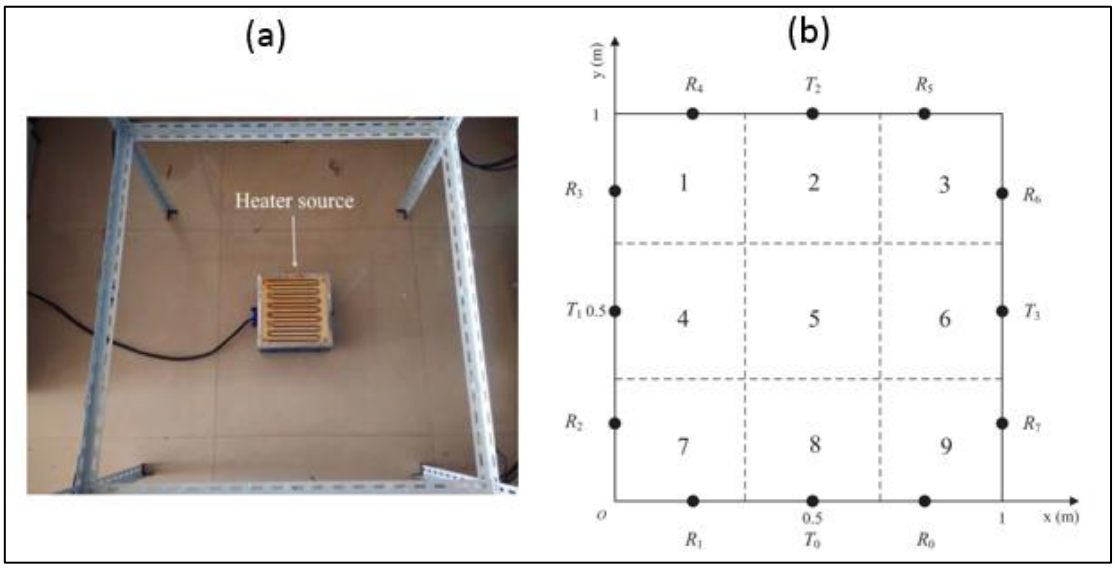

Figure 39 (a) Experimental frame with heat source (b) Transmitter and receiver locations with measurement grid[42]

Due to the small distances, 4 ultrasonic transmitters and 8 receivers were used, positioned as shown in Figure 39(b). To validate their method thermocouple measurements were taken at the centre of each of the 9 numbered blocks and compared with the temperature value at that point in the reconstruction.

Both the least squares method and the SVD RBF method was tested and evaluated at these points. Overall temperature errors varied significantly across blocks with some blocks having an error of 2.2 % while others were as high as 10.5 % for the same reconstruction. The mean accuracy of the two methods were very comparable and when the heater is placed in the centre the least squares method achieved a mean accuracy of 6.757 % while the SVD RBF method achieved a lower error of 6.11 %. When the heater was placed towards the corner the least squares method achieved a lower error of 6.34 % while the SVD RBF method achieved a higher 6.71 %. These results suggest that in practice these two reconstruction methods would produce comparable results.

3.3 Mathcad model development

This section discusses the Mathcad model developed for temperature reconstruction. It begins by providing and overview of the processes in the model, followed by a detailed report of each of these processes and how they were implemented.

3.3.1 Overall Process

At an abstracted level, the model has 5 main steps that can be broadly grouped into the sub processes shown in Figure 40. The model begins by specifying the inputs, after which the grid and length matrix is determined. The average TOF measurement for each acoustic path is then simulated, from which the data points are determined using a least squares algorithm. Each of these acoustic paths are assumed to be straight.

Once the temperature data points are determined, interpolation algorithms are applied. The result of that interpolation is then evaluated against the selected temperature profile and the results are plotted. Each of these sub processes will be described in greater detail below and the resulting Mathcad code can be found in Appendix A.

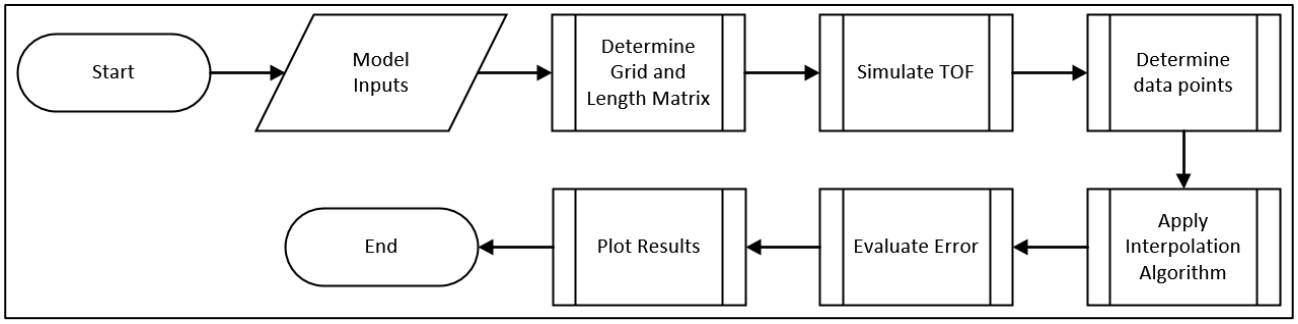

Figure 40 Overview of Mathcad process

The model takes a least squares approach to temperature reconstruction (further detailed in 3.3.5) after which multiple interpolation methods are applied, with an emphasis on a RBF interpolation with shape factor prediction, as documented in 3.3.6.

3.3.2 Model Inputs

In the implementation of this model, the goal was to include as many input variables as possible, such that temperature reconstruction could be attempted under multiple different scenarios with

relative ease. This section discusses inputs used by the model and how they are applied to reach this goal.

The model has a dedicated graphical input section at the top of the script as shown in Figure 41, where in this figure similar inputs are grouped by colour boxes.

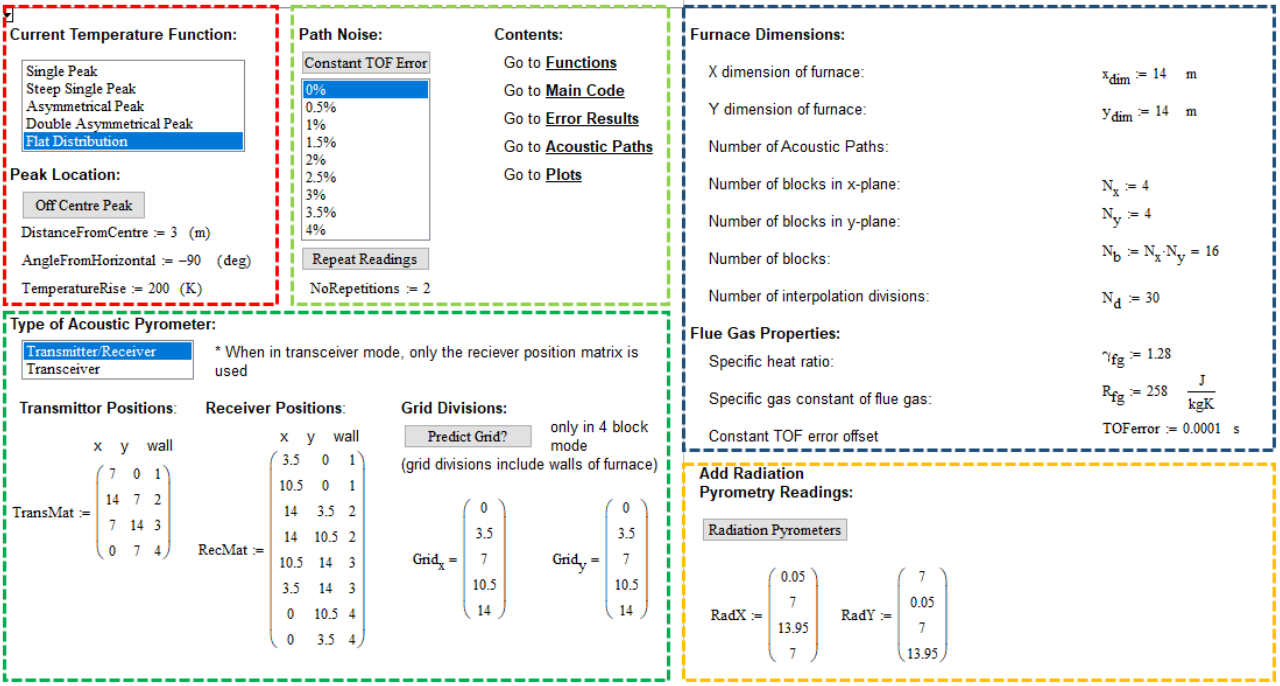

Figure 41 Reconstruction model Input section

The first section of inputs as contained within in the red box in Figure 41, pertain to the selection of the temperature profile to be reconstructed and any modifications if necessary. The lime box has settings pertaining to adding noise to time of flight (TOF) readings and a hyperlinked contents page for navigation through the script. The dark green box inputs relate to the positions of and the type of acoustic pyrometer transmitter used. In addition, there are options to control the grid used for the data points. On the right page, the blue box encloses constants such as the furnace dimensions and flue gas properties. Below this, the inputs in the yellow box, relate to adding radiation pyrometer readings to acoustic pyrometer readings to improve accuracy. The following sections will discuss how these inputs are implemented.

Temperature profiles

The temperature profile is chosen via a selection box as shown in Figure 41, where there is a selection of set profiles and a more variable profile that can be defined below this box. The first four

set temperature profiles used were from the precursor to this study done by [1] as adapted from [35]. The equations of these profiles are shown explicitly below and visually in Figure 42.

$$T_1(x,y) = 1100 + 300\sin\left(\frac{\pi}{14}x\right)\sin\left(\frac{\pi}{14}y\right) \tag{54}$$

$$T_2(x,y) = 800 + 800\sin\left(\frac{\pi}{14}x\right)\sin\left(\frac{\pi}{14}y\right) \tag{55}$$

$$T_3(x,y) = 1000 + 600e^{\frac{-\left((x-7)^2+(y-4)^2\right)}{100}} \tag{56}$$

$$T_4(x,y) = 800 + 800\cdot e^{-20\cdot\left(\left(\frac{x}{14}-\frac{1}{3}\right)^2+\left(\frac{y}{12}-\frac{2}{3}\right)^2\right)} + 800\cdot e^{-\left(20\cdot\left(\frac{x}{14}-\frac{2}{3}\right)^2+15\cdot\left(\frac{y}{12}-\frac{1}{3}\right)^2\right)} \tag{57}$$

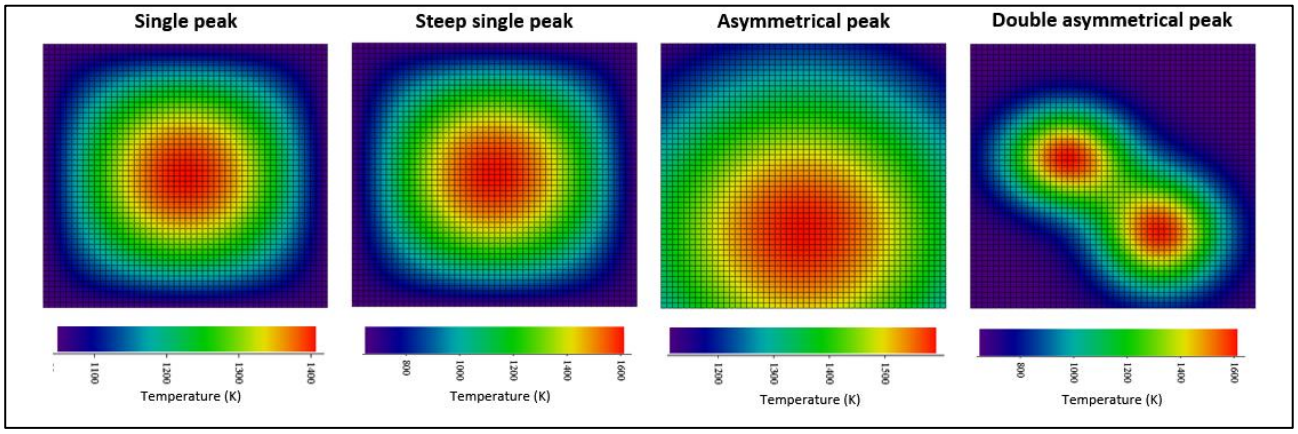

Figure 42 Set temperature profiles on 14x14m cross sectional area

The first two profiles are symmetrical single peak profiles, where the peak temperature is located at the centre of the furnace cross section. They have the same overall shape; however, the second profile is much steeper having an 800 K temperature change. The third profile is an asymmetrical profile where the peak is located towards the furnace wall. The last profile is the most complex, having two asymmetrical peaks and a high temperature change. These set profiles were the main ones considered for this study.

In addition to these set temperature profiles, a more variable temperature profile was developed, with the intention of determining accuracy when the peak location changes. The profile is mathematically similar to the third temperature profile, except the peak location and temperature change are variables and can be altered, as shown in (58).

$$T_5(x,y) = 1000 + T_{rise} e^{\frac{-\left((x-x_{peak})^2+(y-y_{peak})^2\right)}{100}} \quad (58)$$

Where T_{rise} is the temperature rise in Kelvin and x_{peak} and y_{peak} are the x and y cartesian coordinates (in m) of the peak. However when applied, these peak locations are inputted as polar coordinates with an origin at the centre of the furnace as shown in equation (59) and (60).

$$x_{peak} = \frac{x_{\dim}}{2} + r \cdot \cos(\theta) \quad (59)$$

$$y_{peak} = \frac{y_{\dim}}{2} + r \cdot \cos(\theta) \quad (60)$$

Here, r is the distance from the centre (in m) and θ is the angle from the horizontal plane. This implementation reduces the amounts of inputs required and is more intuitive when successively changing the location of the peak. An example of this is shown in Figure 43, where the angle and distance from the centre is changed. While the 3rd profile is called the asymmetrical profile, it is symmetric around one axis. The custom off-centre peak profile can be used during plant scale implementation to create a profile that is asymmetrical around all axes if and underdeveloped FEGT profile is suspected.

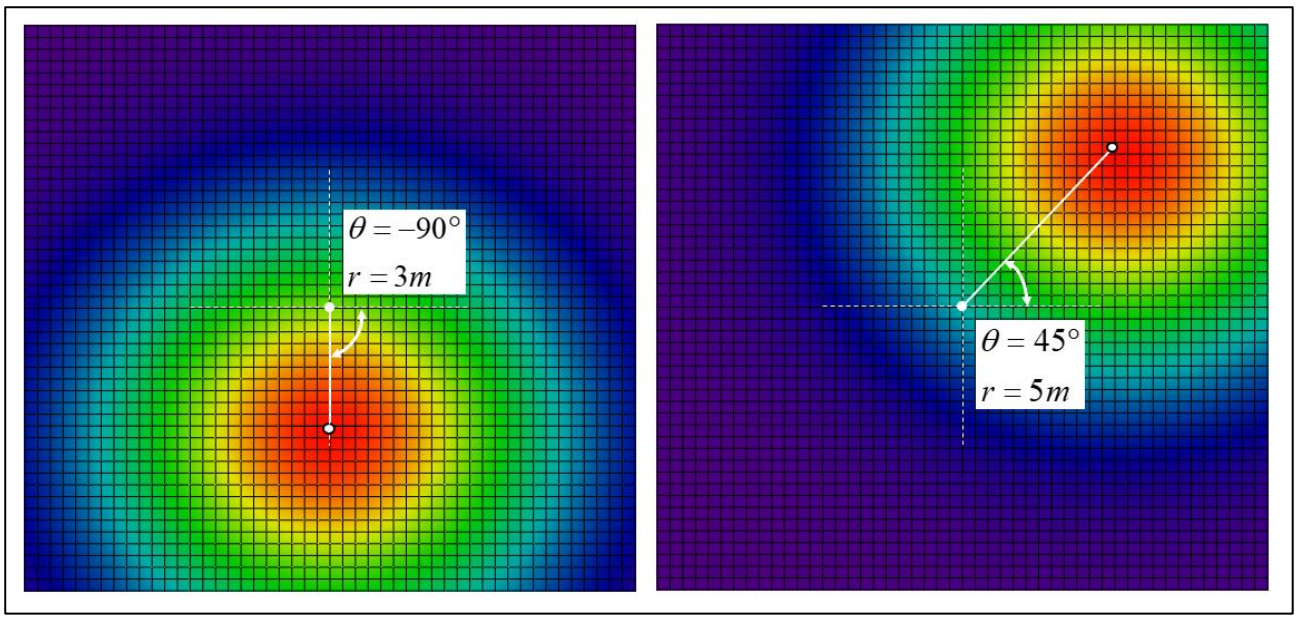

Figure 43 example of off centre peak temperature profile with different inputs

The last profile was developed as an extreme scenario where the flue gas is cooled rapidly by the water walls but remains fairly constant outwards from the walls, as seen in the reconstructions studies done by Sielschott et al.[38] on tangentially fired boilers. It is characterised by having and extremely flat top, with a very sharp temperature gradient at the walls as shown in Figure 44.

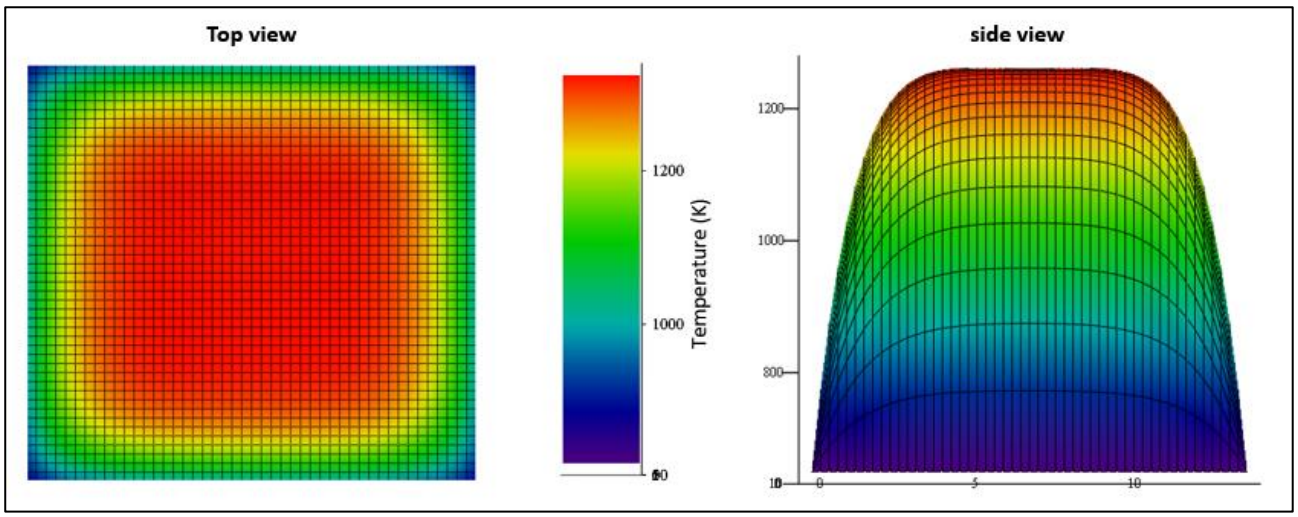

Figure 44 Flat temperature distribution with sharp temperature decline at walls

$$T_6(x,y)=\sum_{i=0}^{n}\sum_{j=0}^{n}B_{x,i}\left(\frac{x}{x_{\dim}},i\right)B_{y,j}\left(\frac{y}{y_{\dim}},j\right)P_{i,j} \tag{61}$$

$$B_{x,i}\left(\frac{x}{x_{\dim}},i\right)=\left[\frac{n!}{i!(n-i)!}\right]\left[\left(\frac{x}{x_{\dim}}\right)^{i}\left(1-\left(\frac{x}{x_{\dim}}\right)\right)^{n-i}\right] \tag{62}$$

$$B_{y,i}\left(\frac{y}{y_{\dim}},i\right)=\left[\frac{n!}{i!(n-i)!}\right]\left[\left(\frac{y}{y_{\dim}}\right)^{i}\left(1-\left(\frac{y}{y_{\dim}}\right)\right)^{n-i}\right] \tag{63}$$

To achieve this sharp drop of temperature but still maintain a flat top, the temperature profile was defined using a Bezier surface. The surface is defined by a two-dimensional set of control points ($P_{i,j}$) and basis-functions ($B_{x,i}$ and $B_{x,i}$). The resulting profile passes through the end control points but lies within the convex hull of the control points. The resulting temperature profile is described by equation (61), where n is the dimension of the control point matrix. To achieve the profile as shown in Figure 44 a 10x10 matrix of control points was used.

Transmitter and Receiver positions

In order to generate TOF data, the geometry of the acoustic maths must be established. This is primarily dependent on the inputs in the darker green box as shown in Figure 41 and Figure 45, which are related to the transmitter and receiver positions. The inputs for transmitter and receiver positions are placed into a matrix where the first two columns are the cartesian x and y coordinates and the last column is the wall on which that transmitter or receiver lies. In addition to this the grid that partitions the furnace exit area is defined by two vectors for the x and y coordinates of the partition lines. An example of the grid produced from these vectors is shown in Figure 45, along with the convention for the wall numbers. For the grid vectors edges of the wall are also included in the vector (a 5-element vector produces 4 blocks) and the wall numbers begin with 1 at the bottom wall and are numbered incrementally in an anti-clockwise fashion. The convention was also to enter the coordinates into the transmitter and receiver matrix in ascending wall number (i.e. anti-clockwise from the bottom). Likewise, this is the convention followed when paths are determined. When a 4x4 block grid is selected, there is also an option to try predicting the optimum grid based on the transmitter and receiver locations.

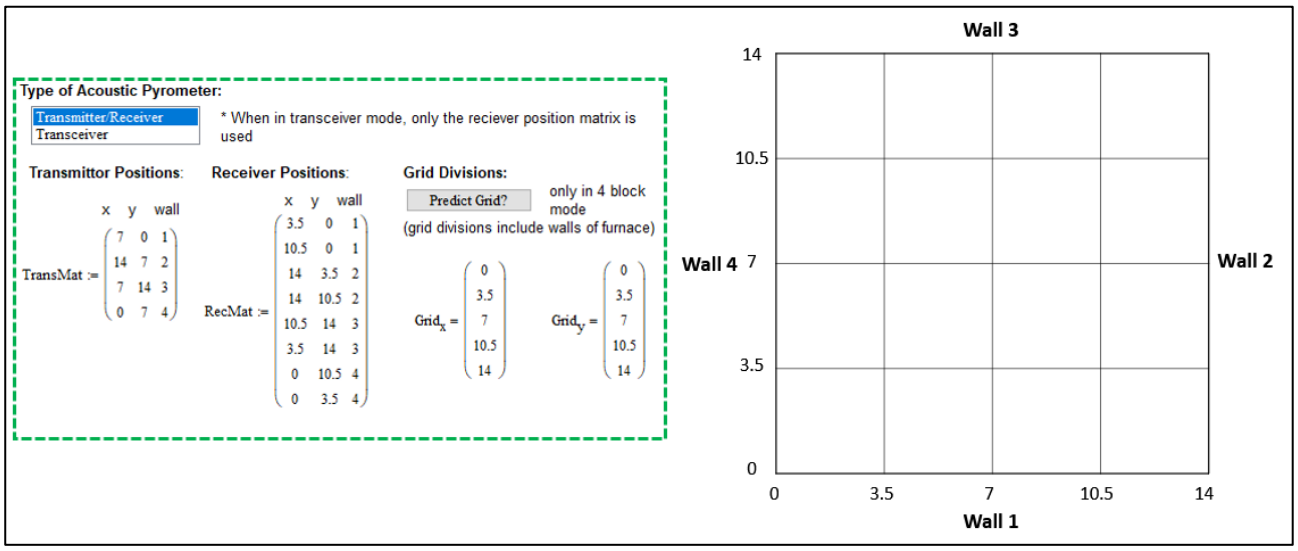

Figure 45 Transmitter and receiver position inputs and resulting grid

Since two types of acoustic pyrometer exist, one where the transmitters and receivers are separate and one where they act as one device known as a transceiver, the model has been developed to account for both. A selection box above the transmitter and receiver positions chooses which type is used. When the transceiver option is selected, the receiver position matrix is used and the transmitter matrix is disregarded.

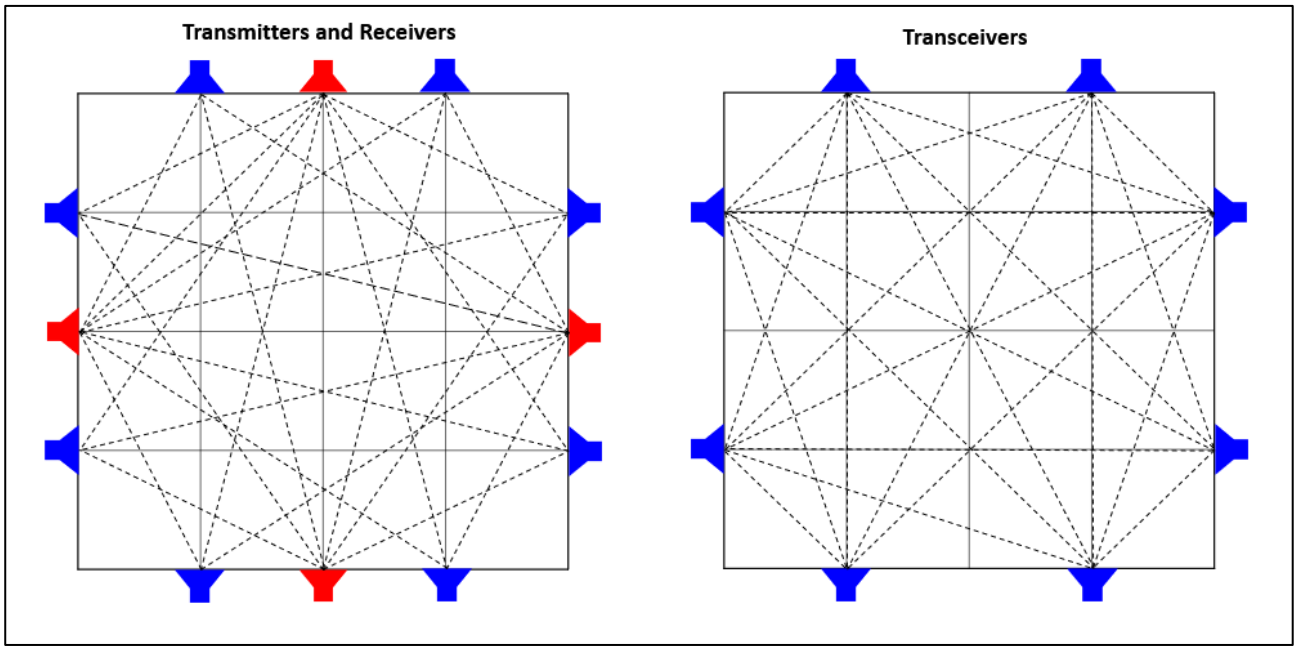

Figure 46 Resulting acoustic paths from example inputs for transmitter and receiver option and transceiver option

The result of the inputs of Figure 45 are shown in Figure 46, where the transmitter and receiver option is selected on the left; and where the transceiver option is selected on the right. The red icons represent transmitters and the blue ones represent receivers or transceivers. As illustrated by Figure 46, while both modes have the same number of acoustic paths, the direction and orientation of the paths differ. This allows for a more detailed study into how the type of acoustic pyrometer might benefit the reconstruction process.

Path noise

The settings in the lime green box pertain to dealing with path noise. These settings came about since commercial acoustic pyrometers have a rated TOF accuracy, with the Pyrometrix™ having a rated accuracy of 1 % and the Boilerwatch® acoustic pyrometer having a rating of 0.5 %. As a result, an option to include TOF error was added to the input section to study the effect it has on reconstruction. In the model, there is an input for random TOF error as selection from a drop-down box in 0.5 % increments from 0-4 %, or a constant TOF offset as a variable. In addition to this there is an option to repeat readings when high noise is expected.

Constants

On the right side of Figure 41, there is a section for inputting constants. These constants are inputted as variables in Mathcad. Specifically, this section includes the dimensions of the furnace region to be simulated and the properties of the gas within that area. Even though constants such as furnace

dimension are not critical, since this is a mathematical exercise, for consistency and means of comparison, furnace dimensions and flue gas properties were kept the same as the previous study done by Tootla[1].

Adding radiation pyrometer readings

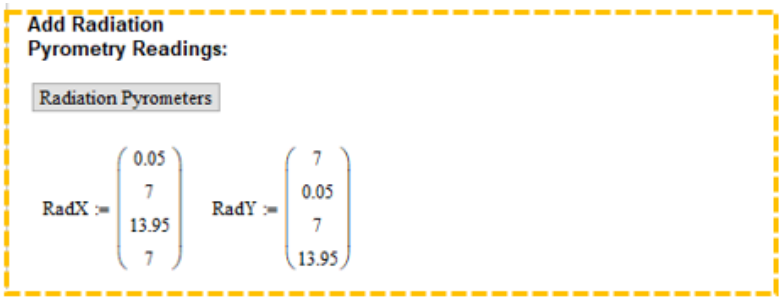

Figure 47 Radiation pyrometer inputs

The last section of the inputs pertains to a conceptual feature in which radiation pyrometry could be used to complement acoustic pyrometry. One of the limitations (as discussed in 2.2.3) of radiation pyrometry is that it is depth limited, however acoustic pyrometer is not and rather produces an average temperature over the path length. By combining these two measurement methods, a short-range temperature reading could be used to improve the accuracy of temperature reconstruction using acoustic pyrometry.

In this implementation, the radiation pyrometers are point temperature readings. Therefore, as shown in Figure 47, the inputs of this section are two vectors and a push button. The pushbutton is simply a selection to include radiation pyrometer readings and the vectors are the x and y coordinates of the points to be measured by the radiation pyrometer. It is implemented such that the radiation pyrometer data points are added to the acoustic pyrometer data points before interpolations, however more on its implementation will be discussed in the following chapters.

3.3.3 Populating distance matrix

One of the most important aspects of successfully applying the least squares method (as described in 3.2.3) is populating the L matrix (also referred to as the distance matrix). In this matrix the column index(i) is the block number and the row index(k) is the path number and the value stored within the matrix is the length of path k that passes through block i. An example of this is shown in Figure 48 where a single acoustic path is divided into multiple path segments based on where it intersects the grid, to populate the L matrix.

$$\mathbf{L} = \begin{bmatrix} \Delta L_{11} & \Delta L_{12} & \cdots & \Delta L_{1N_b} \\ \Delta L_{21} & \Delta L_{22} & \cdots & \Delta L_{2N_b} \\ \vdots & \vdots & \ddots & \vdots \\ \Delta L_{N_t 1} & \Delta L_{N_t 2} & \cdots & \Delta L_{N_t N_b} \end{bmatrix} \tag{64}$$

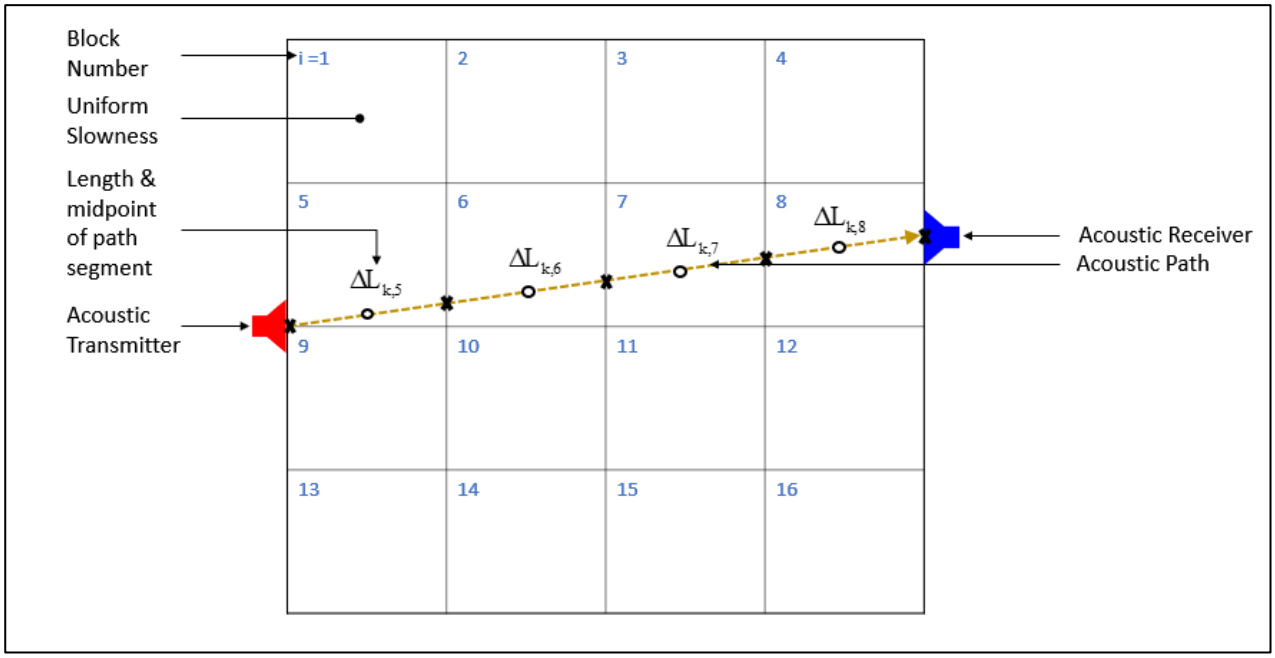

Figure 48 Example of acoustic path in furnace area being split into segment lengths

For previous studies on fixed setups of acoustic pyrometers the L matrix only needed to be populated once and could be manually calculated. However, since this study involves varying the acoustic pyrometer and transmitter/receiver positions and grid, it is imperative that the matrix is programmatically populated every time one of these variables is altered. Thus, this section details the algorithm used to populate the L matrix.

Populate distance matrix algorithm

The overarching function that handles this is called the populate distance matrix function, whose algorithm is outlined in Figure 49. The key role required by this algorithm is that it must be able to identify where each acoustic path crosses the grid, the length of each segment in each block and the block number in which the segment lies.

The function was implemented to start by taking the transmitter and receiver matrices as inputs (all other variables used are treated as global constants). From these matrices the number of

transmitters and receivers is determined and the index variables “i” for the number of transmitters and “j” for the receivers are initialised for a nested for loop.

The outer loop cycles through the transmitters and the inner loop through the receivers. In the inner loop, the start and end co-ordinates for the acoustic path and its wall number are extracted from the transmitter and receiver matrix respectively. If the wall numbers are the same, the path is considered impossible and the next receiver is considered. If they’re not however, it is considered a valid path and the path index is incremented.

The intersection algorithm is then called to determine where the acoustic path intersects with the grid, taking in the start and end co-ordinates and returning a matrix with co-ordinates of intersection. The intersection matrix is then iterated through, taking consecutive points and calculating the distance between them to determine the segment length. If the distance is greater than 0.5 % of the furnace dimension, then the segment is considered, else it is deemed as insignificant. This criterion was arrived at experimentally after noting segment lengths below this size significantly skewed data point determination later on. Once the segment length is calculated, the midpoint between the two co-ordinates (as shown by the circles in Figure 48) is then sent to a block number algorithm which locates the block in which the segment lies. The segment length is then stored in the L matrix (distance matrix) and using the path number as the row index and the block number as the column index.

Once all paths are considered, the distance matrix is fully populated. The populated matrix rows are summed to get the total length of each path. The algorithm finally outputs the distance matrix the length of each path and the start and end coordinates of each path. Two version of this algorithm were implemented, the version using transmitters and receivers as inputs (as shown in Figure 49) and the version for transceivers where the receiver position is used for both loops. Depending on the setting chosen, the relevant function is called.

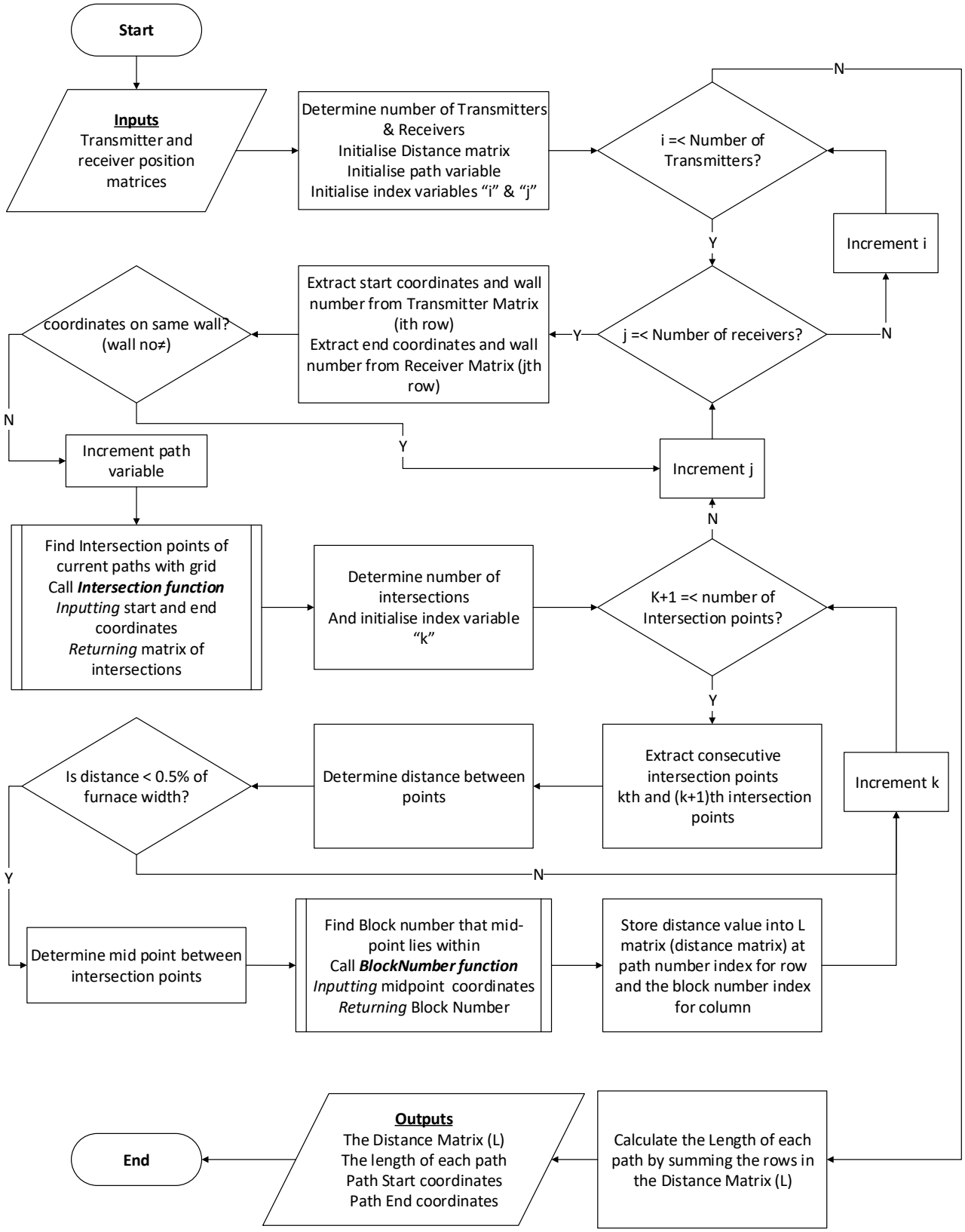

Figure 49 Distance matrix algorithm flowchart for transmitter/receiver case

Due to the convention for inputting transmitter and receiver locations, and the structure of the populate distance function, the resulting path number convention will follow closely to the inputting convention. This will result in the path numbers being labelled from transmitter to receiver, where both the transmitter and receiver loop is labelled anti-clockwise from the bottom. This is shown in Figure 50 where the red icons are numbered transmitters and the blue ones are numbered receivers as per input conventions.

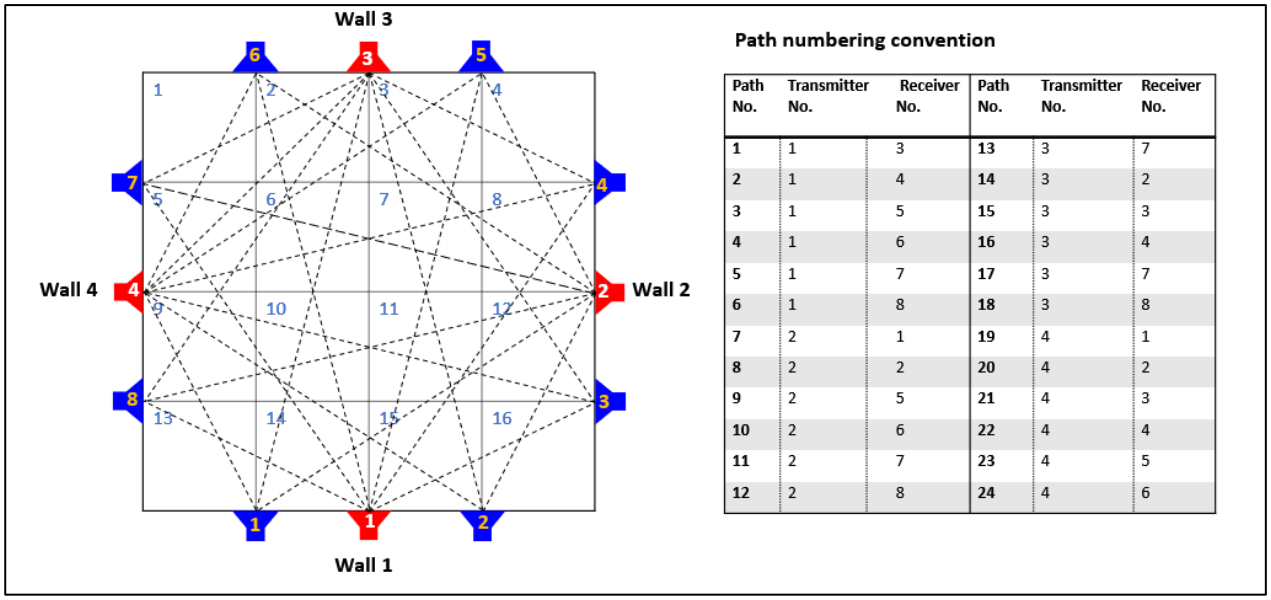

Path No.	Transmitter No.	Receiver No.	Path No.	Transmitter No.	Receiver No.
1	1	3	13	3	7
2	1	4	14	3	2
3	1	5	15	3	3
4	1	6	16	3	4
5	1	7	17	3	7
6	1	8	18	3	8
7	2	1	19	4	1
8	2	2	20	4	2
9	2	5	21	4	3
10	2	6	22	4	4
11	2	7	23	4	5
12	2	8	24	4	6

Figure 50 Acoustic path labelling convention

Determining intersections

Within the distance matrix algorithm, the intersection function is called, to perform the task of determining where each acoustic path intersects with the defined grid. The process followed by this function is outlined in the flowchart shown in Figure 52.

Once the start and end coordinates of the acoustic path are inputted into the function, the first step is to determine whether the path is horizontal, vertical or diagonal (examples of these cases are shown in Figure 51). The paths are first checked for the vertical case by comparing the start and end x coordinates. If these are equal, the y-grid vector is looped through and the constant x coordinate is stored with each y coordinate in the intersection matrix, resulting in the coordinates for each vertical intersection as shown by blue crosses in the vertical path example of Figure 51. The same is done if the line is horizontal, except the start and end y-coordinates are compared and the x-grid is looped through, creating the red crosses as shown for the horizontal path example in Figure 51.

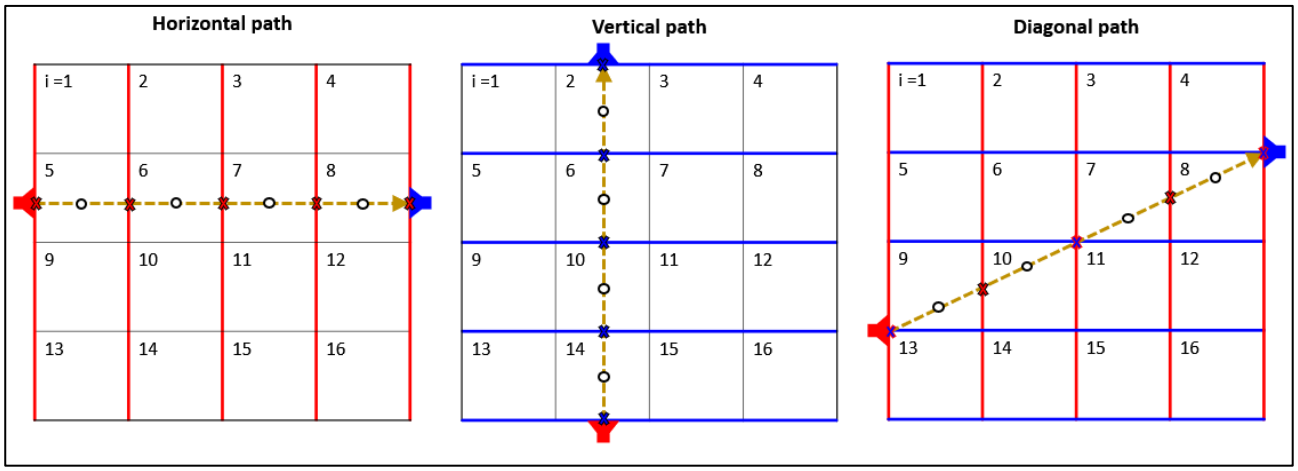

Figure 51 Examples of three path intersection scenarios

Once the intersection matrix is formed for either of these cases, the matrices are sorted in ascending order, with respect to the y coordinate in the vertical case and the x-coordinate in the horizontal case. The coordinates are order so that they are consecutive, as required by the populate distance function when calculating the distance between them.

The last possible case is when the acoustic path is diagonal. In this scenario the first step followed is to determine the cartesian equation of the line by the gradient and y-intercept as shown in equation (65) and (66).

$$m = \frac{y_{end} - y_{start}}{x_{end} - x_{start}} \tag{65}$$

$$c = y_{start} - x_{start} m \tag{66}$$

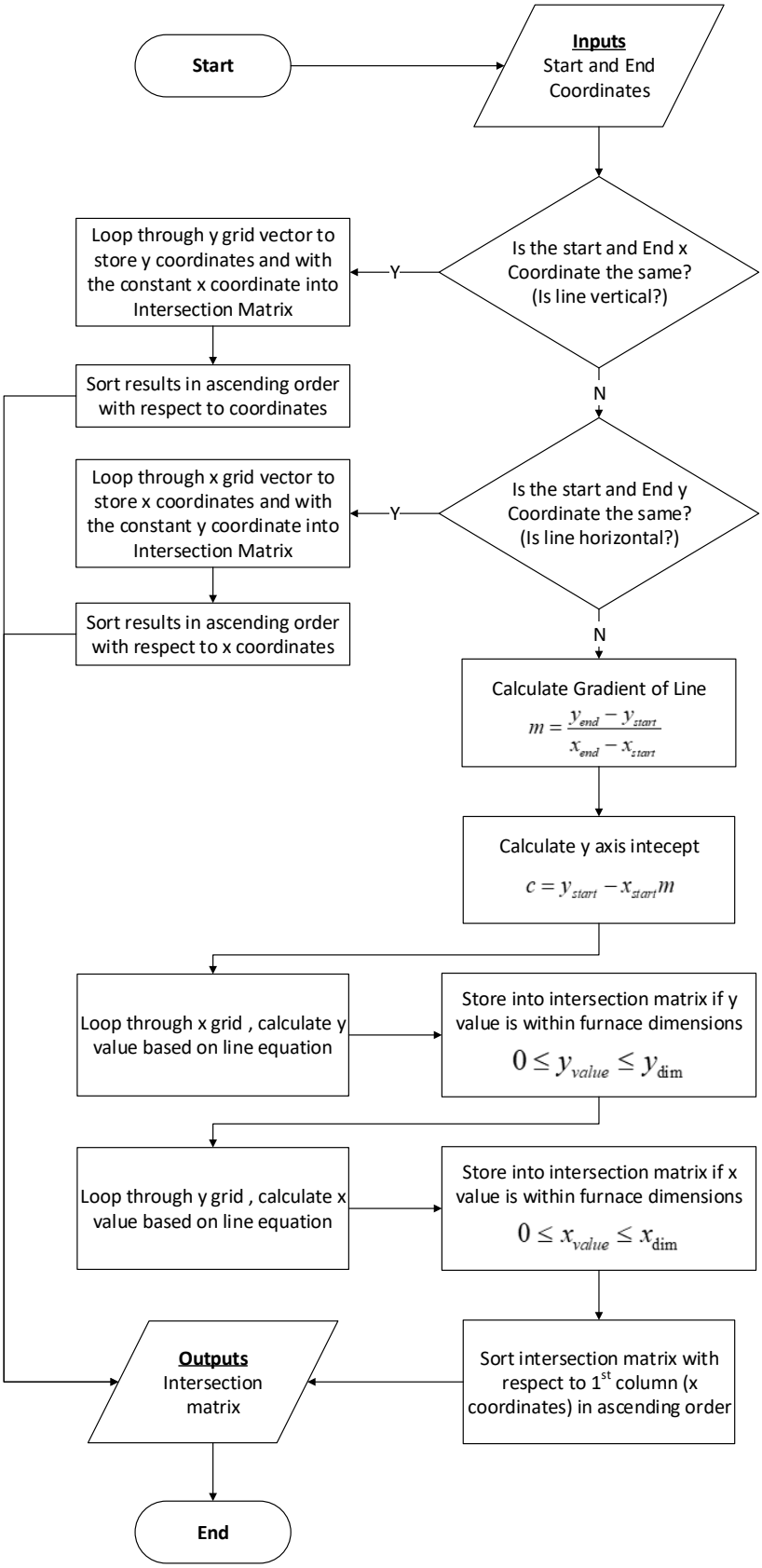
Start
Inputs
Start and End Coordinates
Is the start and End x Coordinate the same? (Is line vertical?)
Y
Loop through y grid vector to store y coordinates and with the constant x coordinate into Intersection Matrix
Sort results in ascending order with respect to coordinates
N
Is the start and End y Coordinate the same? (Is line horizontal?)
Y
Loop through x grid vector to store x coordinates and with the constant y coordinate into Intersection Matrix
Sort results in ascending order with respect to x coordinates
N
Calculate Gradient of Line
$m = \frac{y_{end} - y_{start}}{x_{end} - x_{start}}$
Calculate y axis intecept
$c = y_{start} - x_{start} m$
Loop through x grid , calculate y value based on line equation
Store into intersection matrix if y value is within furnace dimensions
$0 \le y_{value} \le y_{\dim}$
Loop through y grid , calculate x value based on line equation
Store into intersection matrix if x value is within furnace dimensions
$0 \le x_{value} \le x_{\dim}$
Sort intersection matrix with respect to 1st column (x coordinates) in ascending order
Outputs
Intersection matrix
End

Figure 52 Intersection function flowchart

Once the cartesian equations are calculated, the x-grid is once again looped through from left to right, except this time the y-coordinate is calculated by the equation of the line, effectively determining where the line intersects with the vertical lines of the x-grid. The resulting intersections are only stored if they fall within the furnace area. The same process is then followed for the y-grid determining where the path intersects with the horizontal lines of the grid. In Figure 51 the vertical intersections are shown by red crosses and the horizontal ones with blue crosses. However, as shown in this figure, if the intersection lies on a corner, it will be picked up twice, first by the vertical line and then the horizontal line. The solution to this is that the resulting intersection matrix coordinates are sorted with respect to the x-coordinates. The function will then return all the intersection points to the populate distance matrix function. However, when this function calculates distance between points for segment length, the result will be zero and the doubled coordinates will be cancelled.

Determining block number

Once the intersections of the path and grid are determined, the acoustic paths are split into line segments, whose block number must be determined. The algorithm developed for this is outlined and implemented as shown in Figure 54 and an illustrative example is shown in Figure 53.

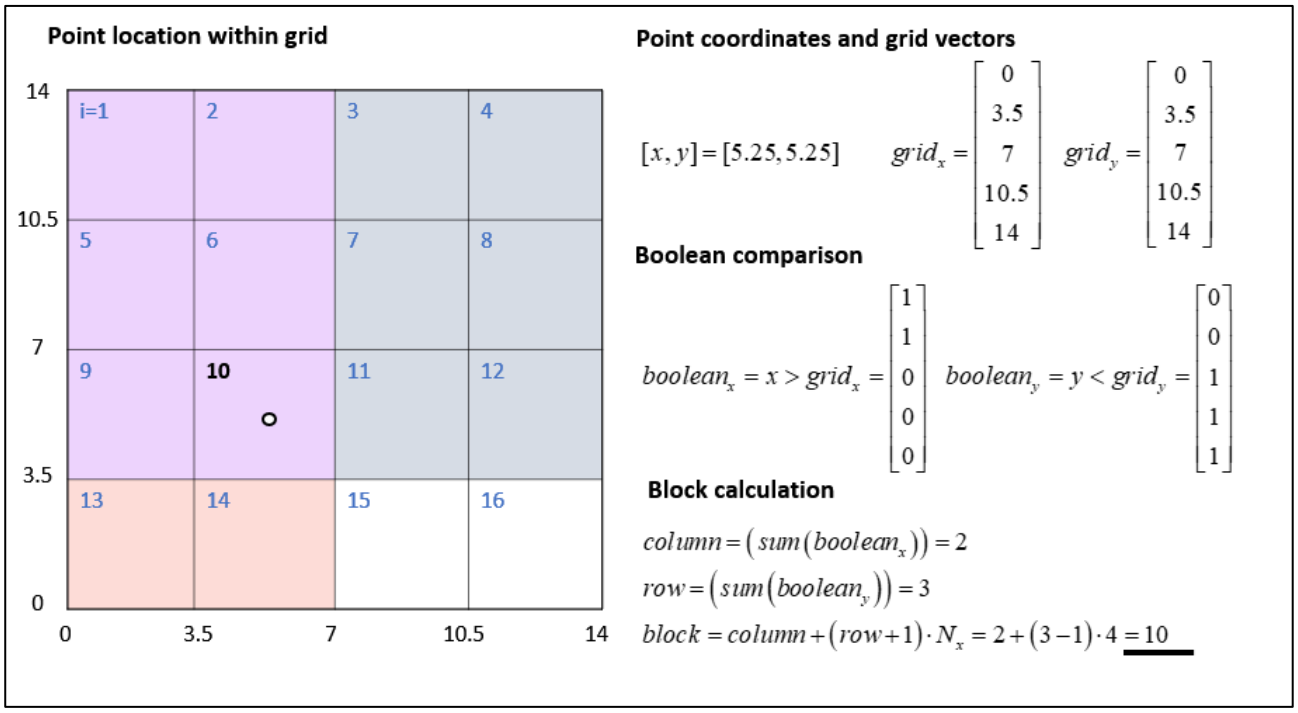

Figure 53 Block number determination example

Once each line segment is determined, the line segment midpoint coordinates will be calculated to input into the block number function. The x coordinate is then compared with the x grid vector to see where it is larger than the values within the vectors. The same is done for the y coordinate where the y values are lower than the y grid. The result of this is two Boolean matrices that can be summed to determine the column and row number respectively. From the row and column number the block can be calculated via equation (67), where N_x is the number of x blocks.

$$block = column + (row + 1) \cdot N_x \tag{67}$$

An example of this is shown in Figure 53, where the midpoint of a segment (the white dot) is in the 10th block, and from the coordinates of the point and the grid vector, the block number is determined.

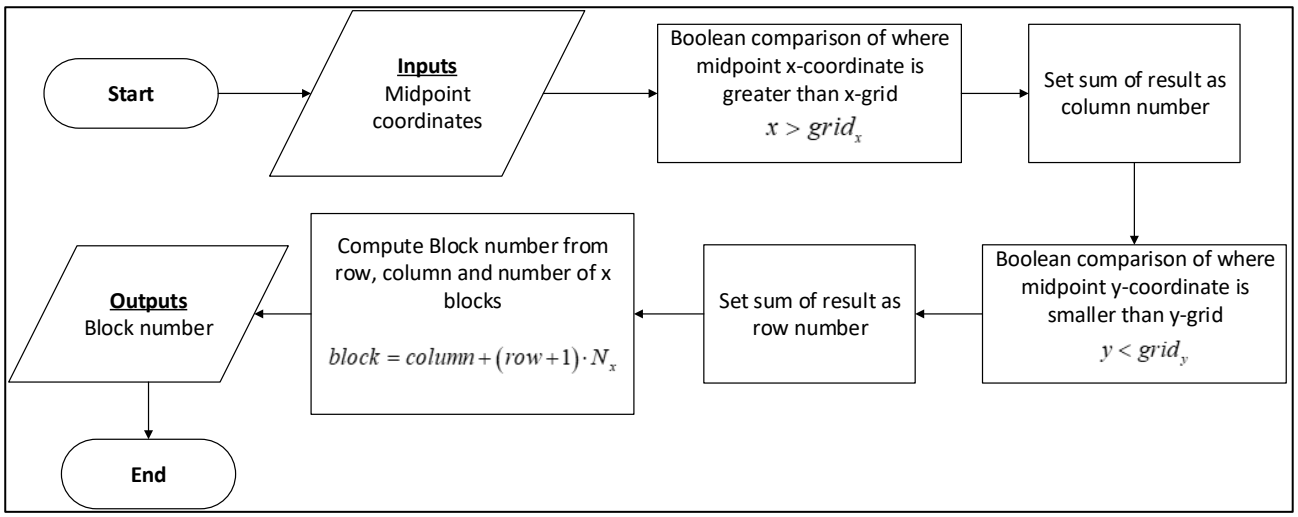

Figure 54 Flowchart of process followed by block number function

The combination of these functions makes it possible to automatically populate the distance matrix for multiple paths using either transmitters and receivers or transceivers. It is however limited to rectangular or square furnace areas and acoustic paths that do not lie directly on grid lines. However, in the latter case the grid lines could just be adjusted to prevent this.

3.3.4 Simulating Time of flight data

After the distance matrix is determined for the given geometry, the time of flight must be simulated for each acoustic path. Since the temperature profile is chosen and defined, for given flue gas

properties, the "slowness" or reciprocal of velocity ($f(x,y)$) can be determined in the furnace plane as shown in equation (69) where the velocity is defined by the flue gas properties and temperature profile as shown in equation (68).

$$v(x,y) = \sqrt{\gamma_{fg} R_{fg} \cdot T_{fg}(x,y)} \tag{68}$$

$$f(x,y) = \frac{1}{v(x,y)} \tag{69}$$

As previously noted in 3.3.3, during the population of the distance matrix the start and end x-y coordinates and length (l) of each acoustic path are determined and outputted in the form of vectors (x_{start} , x_{end} , y_{start} and y_{end}). Since the start and end coordinates are known the time of flight (TOF) for each path can be calculated via a line integral as shown in equation (72), where the x and y coordinates are parametrised as shown in equation (70) and (71).

$$x(s,i) = x_{start_i} + \left(x_{end_i} - x_{start_i}\right) \cdot s \tag{70}$$

$$y(s,i) = y_{start_i} + \left(y_{end_i} - y_{start_i}\right) \cdot s \tag{71}$$

$$t_i = \int_0^1 f\left(x(s,i), y(s,i)\right) \cdot ds \cdot l_i \tag{72}$$

If path error is selected at the input section, the resulting TOF for each path will then be altered to accommodate for both random and constant error. Each path time of flight will be updated as shown in (73), where a random error term and a constant TOF error term are included. The random error term is the product of the TOF, the selected path error (e_{path}) and a random normal distribution term ranging from 0-1, meaning that the selected path error is considered to be stated as the variance in a normal distribution. In addition to this, if selected, a constant TOF error (t_{const}) can be added to the simulated TOF readings.

$$t_i = t_i + t_i \cdot rand_{norm} \cdot e_{path} + t_{const} \tag{73}$$

The resulting time of flights can then be used by the reconstruction process in the absence of physical readings to simulate reconstruction under the given conditions, allowing the simulation and comparison of temperature reconstruction for a variety of setup conditions.

3.3.5 Determining Data points

Once the acoustic path TOF is simulated, a least squares reconstruction approach is taken to determine the temperature data points before interpolation. As mentioned in section 3.2.3, after the furnace area is divided into a grid and the transceiver positions are known, the system of equations shown in (74) can be produced.

$$\mathbf{Lf} = \mathbf{t} \tag{74}$$

$$\mathbf{f} = \begin{bmatrix} \mathbf{f_1} \\ \mathbf{f_2} \\ \vdots \\ \mathbf{f_{N_b}} \end{bmatrix}, \ \mathbf{t} = \begin{bmatrix} \mathbf{t_1} \\ \mathbf{t_2} \\ \vdots \\ \mathbf{t_{N_t}} \end{bmatrix}, \ \mathbf{L} = \begin{bmatrix} \mathbf{\Delta L_{11}} & \mathbf{\Delta L_{12}} & \cdots & \mathbf{\Delta L_{1N_b}} \\ \mathbf{\Delta L_{21}} & \mathbf{\Delta L_{22}} & \cdots & \mathbf{\Delta L_{2N_b}} \\ \vdots & \vdots & \ddots & \vdots \\ \mathbf{\Delta L_{N_t1}} & \mathbf{\Delta L_{N_t2}} & \cdots & \mathbf{\Delta L_{N_tN_b}} \end{bmatrix} \tag{75}$$

Where, t is the TOF vector which is simulated, L is the distance matrix which can be populated and seen as a weighting matrix, leaving $\mathbf{f}$ as the "slowness" matrix to be determined.

Direct matrix inversion would not be suitable to solve for $\mathbf{f}$, since it is likely that the matrix will be overdetermined and non-square, where the number of paths exceed the number of blocks ($N_t > N_b$). As a result, a least squares approach was taken to determine $\mathbf{f}$ using the generalised inverse function in Mathcad.

$$\mathbf{f} = \mathbf{L}^{+}\mathbf{t} \tag{76}$$

This generalised inverse function, also known as the pseudo inverse or Moores-Penrose inverse, uses the pseudo inverse function [43]. When the matrix is square and non-singular, the inverse L^{-1} will be returned, however in most cases the generalised inverse L^{+} will be returned, which will be the least squares solution to the problem, allowing the slowness matrix to be calculated from equation (76).

$$T_i = \frac{1}{\gamma_{fg} R_{fg} f_i^2} \tag{77}$$

Once the slowness of each block is determined the temperature of each block can then be calculated by equation (77), based on the properties of the flue gas and the slowness. The assumption made is that the slowness and therefore temperature is uniform in each block, as shown in Figure 55. The

actual data point taken is then the centre position of this block as denoted by the black dots, and a vector of temperature data points T_{ls} is created.

At this point, if radiation pyrometry readings have been selected, they will be added to T_{ls}, where the temperature value is the temperature of the interpolation function at the location inputted. These data points are then used for interpolation, where multiple interpolation types can be used to complete the reconstruction process.

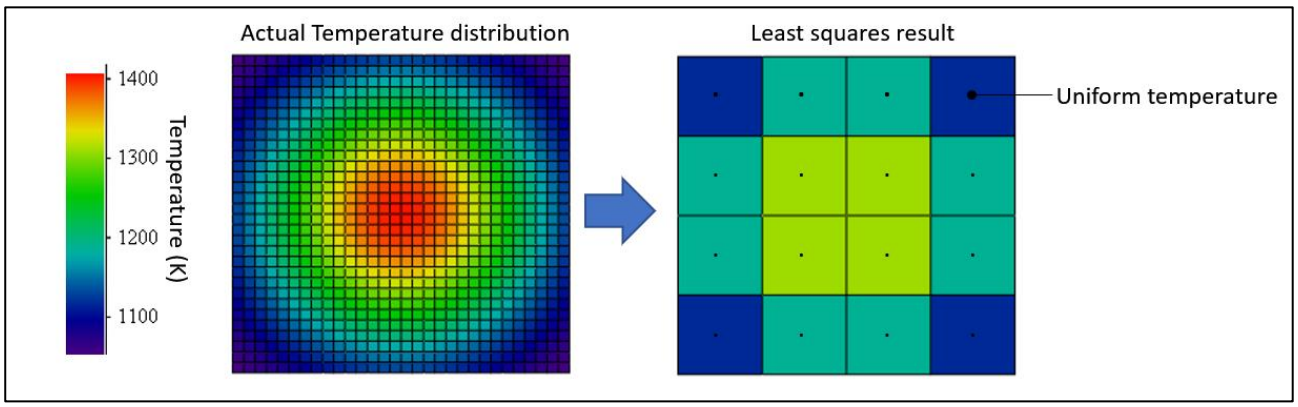

Figure 55 data points created from least squares result

3.3.6 Applying Interpolation algorithms

Once the data points are determined, an interpolation algorithm is used to estimate the temperature profile, before evaluating the error of the reconstruction. As shown in Figure 56, multiple interpolation algorithms are applied to the same data set before the results are compared. They are coded as functions, so they can be individually called to create data sets.

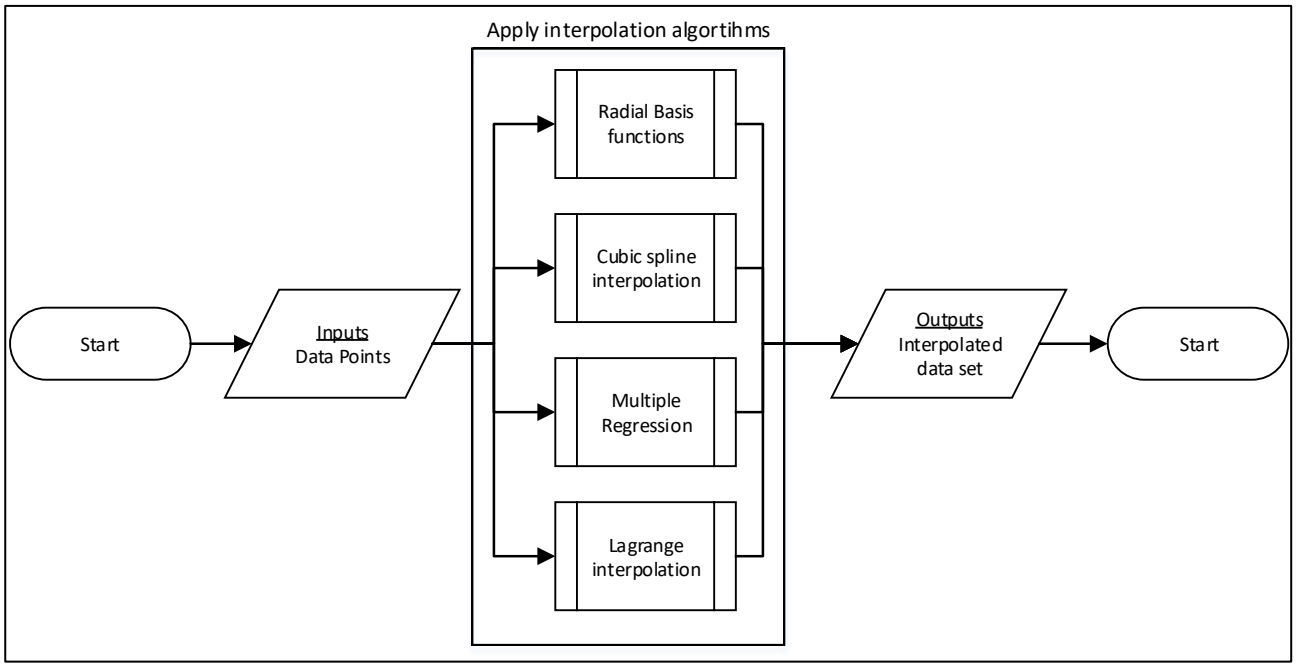

Figure 56 Process for applying interpolation algorithms

The main emphasis of the study was on the RBF interpolation method, however to compare against this method, Cubic spline, multiple regression and Lagrange interpolation were implemented, making use of Mathcad's built-in interpolation tools.

Radial basis functions

The radial basis function interpolation method involves approximating the temperature $T(x,y)$ by the sum of various radial basis functions ϕ_i each weighted by ω_i , as defined by equation (78), which collectively create a continuous surface that passes through all of the data points.

$$T(x,y)=\sum_{i=1}^{N_i}\omega_i\phi_i(x,y) \tag{78}$$

Each radial basis function is radially symmetric about the centre and while multiple radial basis functions exist; through testing it was found that multiquadric version produced the most accurate results and was selected for use in this study. The multiquadratic basis function is defined by equation (79), where ε is a constant shape factor, controlling the steepness of the function.

$$\phi_i(x,y)=\left(1+\left(\varepsilon\left\|(x,y)-(x_i,y_i)\right\|\right)^2\right)^{\frac{1}{2}} \tag{79}$$

Each of these radial basis functions are located at a different centre (x_i, y_i) that coincides with the x-y coordinates of each temperature data point. By forcing the interpolated surface to go through each data point, It would then be the case that equation (80) is true and each temperature data point is the product of the weighting functions and the radial basis functions.

$$T_i = \sum_{j=1}^{N_t} \omega_j \phi_j (x_i, y_i) \tag{80}$$

This would then reduce to equation (81), where the matrices are as shown in (82).

$$T = \Phi \cdot \omega \tag{81}$$

$$T = \begin{bmatrix} T_1 \\ T_2 \\ \vdots \\ T_{N_b} \end{bmatrix}, \ \omega = \begin{bmatrix} \omega_1 \\ \omega_2 \\ \vdots \\ \omega_{N_b} \end{bmatrix}, \ \Phi = \begin{bmatrix} \phi_1(x_1, y_1) & \phi_2(x_1, y_1) & \cdots & \phi_{N_b}(x_1, y_1) \\ \phi_1(x_2, y_2) & \phi_2(x_2, y_2) & \cdots & \phi_{N_b}(x_2, y_2) \\ \vdots & \vdots & \ddots & \vdots \\ \phi_1(x_{N_b}, y_{N_b}) & \phi_2(x_{N_b}, y_{N_b}) & \cdots & \phi_{N_b}(x_{N_b}, y_{N_b}) \end{bmatrix} \tag{82}$$

Since Φ can then be calculated and T is known, then ω can be calculated by matrix inversion and equation (78) could then be used to evaluate the temperature at any point.

At this point, the time of flight simulation, data point determination and radial basis function interpolation method was validated against the set profiles and inputs used in Tootla's study[1]. Under the same conditions, the method produced reconstructions with the same reconstruction accuracy for each temperature profile.

It was found that the accuracy of the interpolation was greatly affected by the shape factor ε defining the interpolant. Previously, fixed shape factors were used, but this resulted in a trade-off of accuracy between possible temperature profile scenarios. As a result Rippa's algorithm[36] was used to predict the optimum shape factor based on each set of data.

The algorithm estimates the best value for ε based on equation (83), which estimates the error of reconstruction for a given shape factor ε.

$$E_k = \frac{\phi_k^{-1} \cdot T_{ls}}{\omega_k^{[k]}} \tag{83}$$

To predict the most accurate ε, a golden section search algorithm was used to find the shape factor that produced the lowest magnitude E_k. An example of this is shown in Figure 57, where the minimised shape factor (blue line) is determined from the minimum magnitude of the error vector (red line).

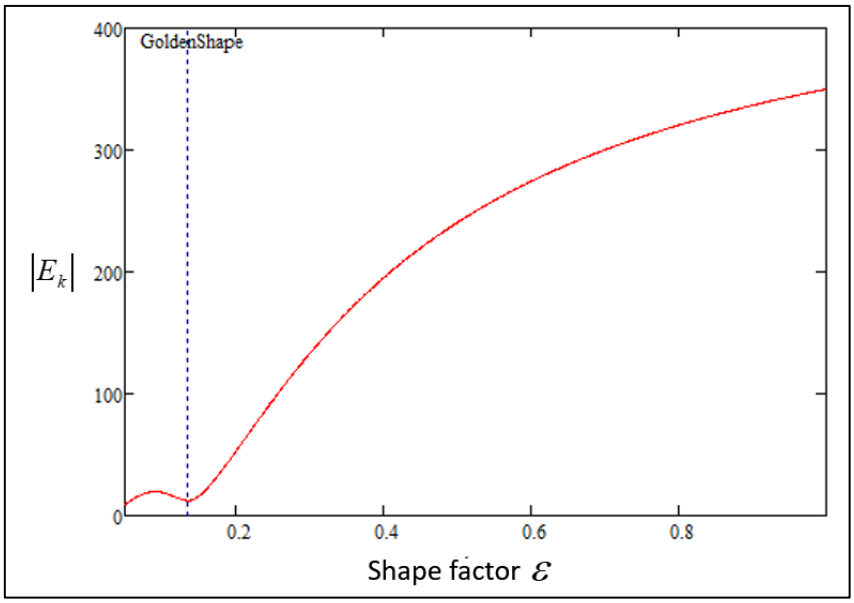

Figure 57 Golden section search to find shape factor that minimises Rippa's algorithm

The result of this is a method of multiquadric radial basis functions, where the shape of the basis function used can effectively be optimised based only on the time of flight readings and the distance matrix. The implication is that the method has increased accuracy for a versatile range of temperature distributions, meaning no a-priori information is needed about the expected temperature profile.

Lagrange interpolation

The Lagrange interpolation algorithm is a prolific and computationally inexpensive interpolation method. Mathcad did not have any built-in functionality for it and thus it was defined manually. The method as defined in equation (84), consists of summing the product of interpolation weights and the value of the temperature data points to determine interpolated temperature values.

$$T(x,y)=\sum_{j=0}^{n_y}\sum_{i=0}^{n_x}L_i(x)L_j(y)T_{i,j} \tag{84}$$

Where the temperature data points are defined in a temperature matrix ($T_{i,j}$) of size N_x by N_y, and $L_{n,i}(x)$ and $L_{n,j}(x)$ are the Lagrange polynomials or weightings as shown in equation (85) and (86).

$$L_i(x) = \prod_{k=0,k\neq i}^{n_x} \frac{x - x_k}{x_i - x_k} \tag{85}$$

$$L_j(y) = \prod_{k=0,k\neq j}^{n_y} \frac{y - y_k}{y_j - y_k} \tag{86}$$

The degree of the polynomial is dependent on the amount of data present, which proves advantageous in the study as the small number of data points (4x4 or less) would prevent the overfitting or high oscillations that could occur with a larger data set. In addition to this, the Lagrange polynomials are defined such that the resulting interpolated surface is constrained to going through the existing data points, which is advantageous when accurate data is obtained, but could be detrimental in high noise or in the presence of outliers since each data point affects the resulting interpolation.

Cubic spline interpolation and multiple regression

In contrast to the previous two interpolation methods, piecewise cubic spline interpolation and multiple regression where considered as methods that do not force the interpolating function to pass through existing data points. Both methods were performed using Mathcad's built-in interpolation libraries.

For cubic spline interpolation two functions are used. The first function is the "spline" function that creates the piecewise polynomials defining the interpolation function such that the first and second derivatives of the surface are continuous across each point and only the adjacent points affect the interpolation. Once the polynomials are determined, the "interpolation" function is used to create the cubic spline function called for interpolation. At the boundaries of the data, the function is required to extrapolate the data, and this was applied using linear, parabolic and cubic endpoints. An example of cubic spline interpolation with cubic and linear endpoints can be seen in Figure 58, where the interpolated surface resulting from the temperature data points (black points) can be compared for each method.

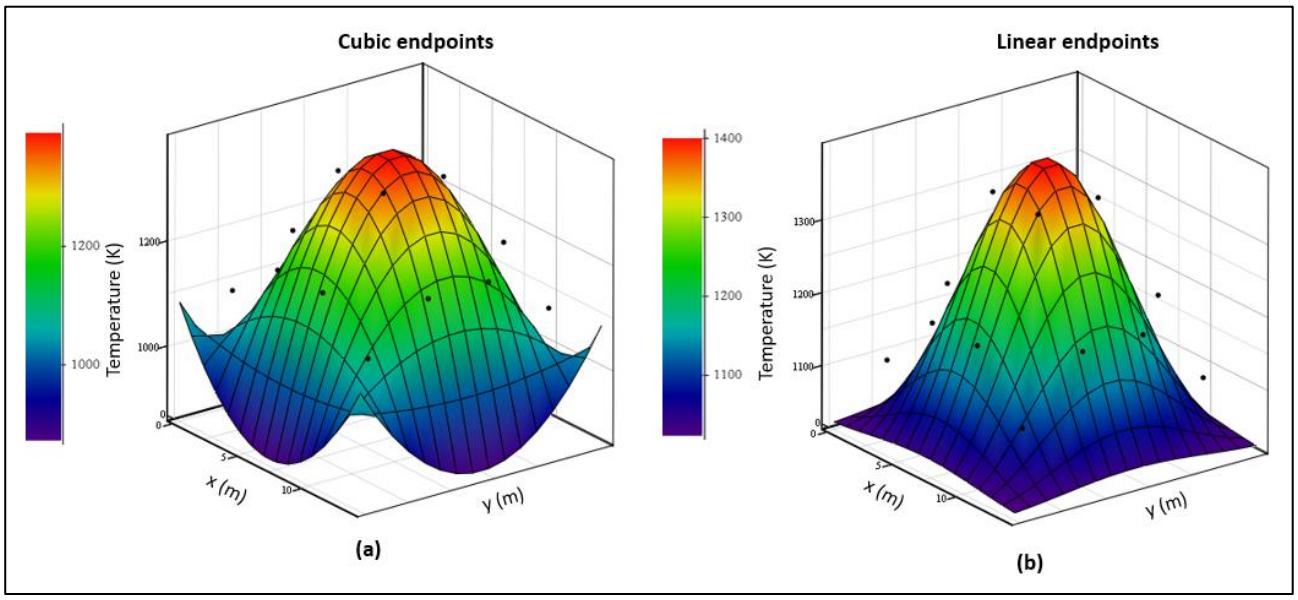

Figure 58 Cubic spline interpolation with linear (b) and cubic endpoints (a)

Similarly, multiple regression was performed using two of Mathcad's built-in functions, "regression" and "interpolation". The regression function takes in the data to be fitted and the degree of the fitting function; and returns the resulting polynomials that minimise the distance between the surface and data in a least-squares sense. The interpolation function then defines the two-variable polynomial function which uses the coefficients produced by the regression function. For this method polynomial functions of the 2nd and 3rd order was considered as well as a localised regression, where only neighbouring data points were considered.

An example of multiple regression with functions having a cubic polynomial fit can be seen in Figure 59, where the interpolated surface resulting from the temperature data points (black points) can be compared for standard and local regression. While local regression allowed for a better fit since only local data points are considered, it also had the disadvantage that it was not able to extrapolate, and thus the full furnace area could not be reconstructed.

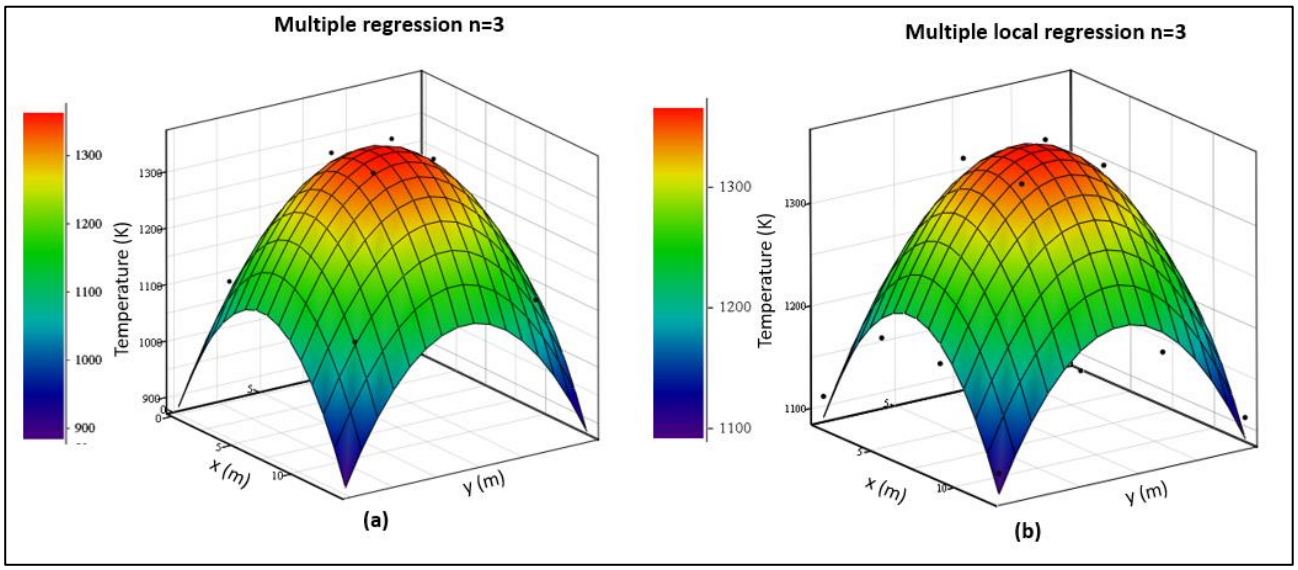

Figure 59 Local (b) and standard (a) multiple regression with 3rd order polynomial fits

Due to the least squares nature of these methods, it is thus expected that regression would be less accurate in ideal conditions since they do not force the interpolation to pass through data points, but would be more accurate when there is variation or noise in readings or outliers.

3.3.7 Evaluating Error

Once each interpolation method is applied, the quality of reconstruction is evaluated by three error metrics as shown by the process outlined in Figure 60. The process is implemented as a function that takes in the name of the interpolating function as a variable and determines the mean, root-mean square(RMS) and energy error of the interpolation.

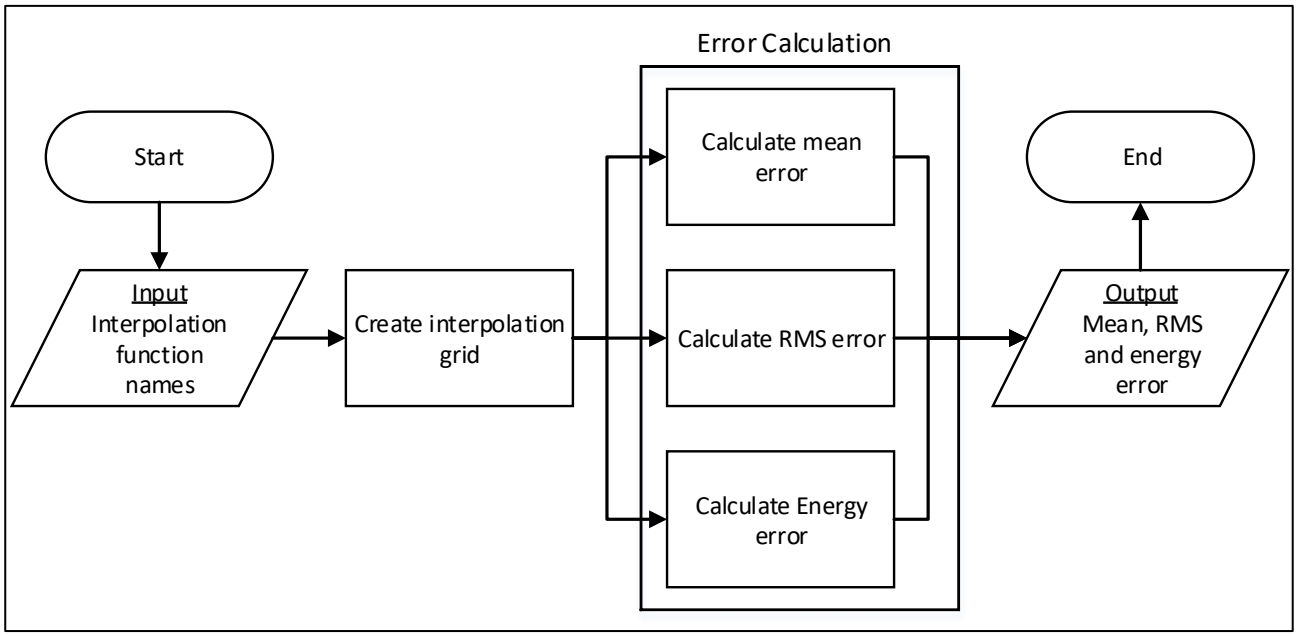

Figure 60 Process followed for evaluating error

Before the error is evaluated however, an interpolation grid is created. In this study the dimension of that grid is determined by the variable N_d (number of interpolation divisions) which was set as 15. The result is a 15x15 interpolation grid (IG) that spans the furnace area where each element is an equally spaced (x, y) coordinate. The mean error is therefore calculate as the average percentage difference between the temperature profile value and the result obtained from the interpolation function as shown in equation (87). This mean error method gives an indication of how well the reconstruction fitted the original profile.

$$E_m = \frac{1}{N_d{}^2} \cdot \sum_{i=1}^{N_d} \sum_{j=1}^{N_d} \frac{\sqrt{\left(T_{fg}\left(IG_{i,j}\right) - T_{\text{int}}\left(IG_{i,j}\right)\right)^2}}{T_{fg}\left(IG_{i,j}\right)} \cdot 100 \tag{87}$$

The next method of error determination is the RMS error calculation (also referred to as RMSE) as shown in equation (89). In this method the error is squared and divided by the mean temperature as calculated by equation (88).

$$T_{mean} = \frac{\sum_{i=1}^{N_d} \sum_{j=1}^{N_d} T_{fg}\left(IG_{i,j}\right)}{N_d{}^2} \tag{88}$$

$$E_m = \sqrt{\frac{\sum_{i=1}^{N_d}\sum_{j=1}^{N_d}\left(T_{fg}\left(IG_{i,j}\right)-T_{\text{int}}\left(IG_{i,j}\right)\right)^2}{{N_d}^2}}\cdot\frac{1}{T_{mean}}\cdot 100 \tag{89}$$

While this method does also give an indication of fit, by squaring the error terms it emphasises regions with large errors and is therefore useful to distinguish reconstructions where large discrepancies exist.

The last error metric considered is the energy error. For a volume of fluid, the energy content in terms of heat can be determined by equation (90) under constant pressure conditions. Since C_p is a constant, the heat content (or enthalpy) can be calculated by integrating the temperature profile over the volume. Thus, to determine energy error, an integration over the temperature profile is considered as a representation of energy.

$$C_p = \left(\frac{\delta Q}{\delta T}\right)_p \tag{90}$$

Two variations of this metric were considered, one that uses the interpolation grid and another that instead uses the dimensions of the furnace area to determine the energy error. The energy error (E_{energy}) version uses the temperature and interpolation function and integrates them over the dimensions of the furnace to get the total energy of the temperature profile and the interpolation function

$$T_{total} = \int_0^{y_{\text{dim}}}\int_0^{x_{\text{dim}}} T_{fg}\left(x,y\right)dxdy \tag{91}$$

$$T_{\text{int }total} = \int_0^{y_{\text{dim}}}\int_0^{x_{\text{dim}}} T_{\text{int}}\left(x,y\right)dxdy \tag{92}$$

Since they cover the same area, the total energy error is then determined as shown in (93).

$$E_{energy} = \frac{T_{total}-T_{\text{int}\,total}}{T_{total}}\cdot 100 \tag{93}$$

In addition to this, an energy sum method (E_{sum}) is used and compared to this method. It is computed by the percentage difference between the sum of the temperature profile data points

and the interpolation function data points. It also gives an indication of energy error; however it is computationally less expensive but also less accurate.

$$E_{sum} = \frac{\sum_{i=1}^{N_d}\sum_{j=1}^{N_d} T_{fg}\left(IG_{i,j}\right) - \sum_{i=1}^{N_d}\sum_{j=1}^{N_d} T_{\text{int}}\left(IG_{i,j}\right)}{\sum_{i=1}^{N_d}\sum_{j=1}^{N_d} T_{fg}\left(IG_{i,j}\right)} \cdot 100 \tag{94}$$

The first two error methods (mean and RMS) give an indication of how accurate the fit of the reconstruction is while the energy error calculation rather gives an indication of the energy or heat flux at the region, a useful metric for predicting heat exchange upstream from the furnace area. These metrics are therefore used to gauge the accuracy of reconstruction in the forthcoming tests.

3.4 Path error tests

Since each reconstruction relies on multiple acoustic path TOF measurements, depending on the reconstruction method used, these small path errors can collectively result in undesirable temperature reconstructions. This is shown in Figure 61 where the addition of random path measurement error produced a much greater reduction in reconstruction accuracy, resulting in the distortion of the original temperature profile.

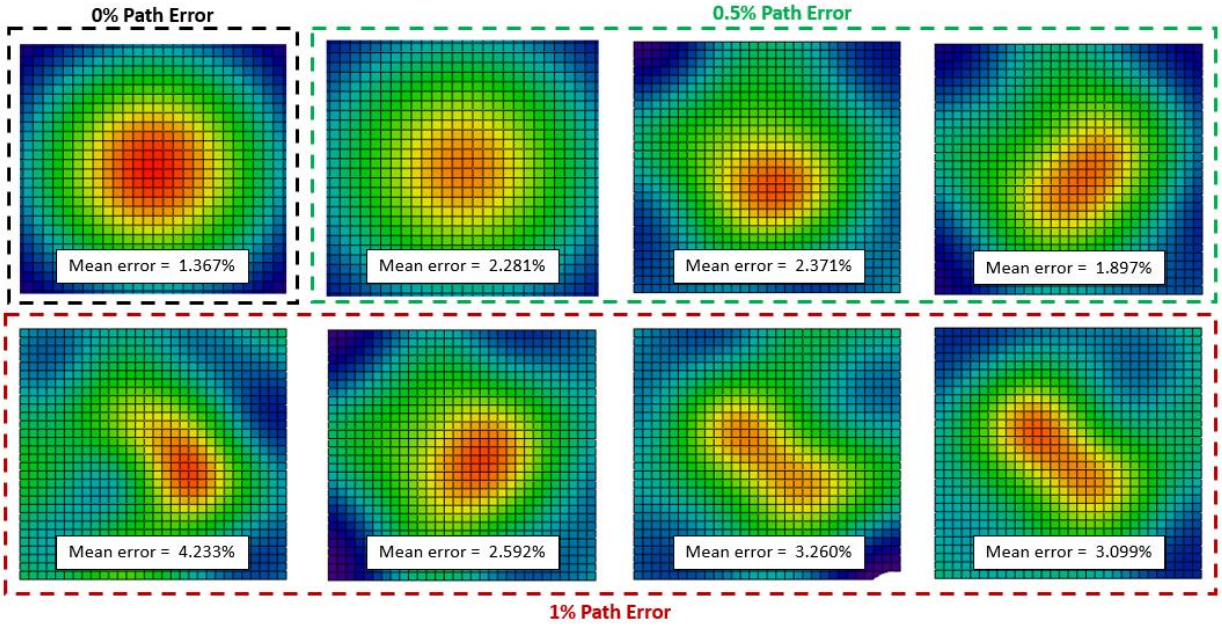

Figure 61 Single peak RBF reconstruction mean error with 0, 0.5 and 1 % random path measurement error

Consequently, this section documents tests done to determine how the inclusion of random path error on TOF measurements affects temperature reconstruction accuracy for different interpolation methods and investigates whether repeating path measurements could compensate for the reduction in error induced by random path error.

3.4.1 Methodology

For path error tests the transmitter positions, receiver positions and grid divisions were considered as constants where a standard symmetric equally spaced setup using 4 transmitters and 8 receivers (24 paths) was used. Similarly, the grid divisions were equally spaced in a 4x4 grid, where the resulting acoustic paths and coordinates are displayed in Figure 62.

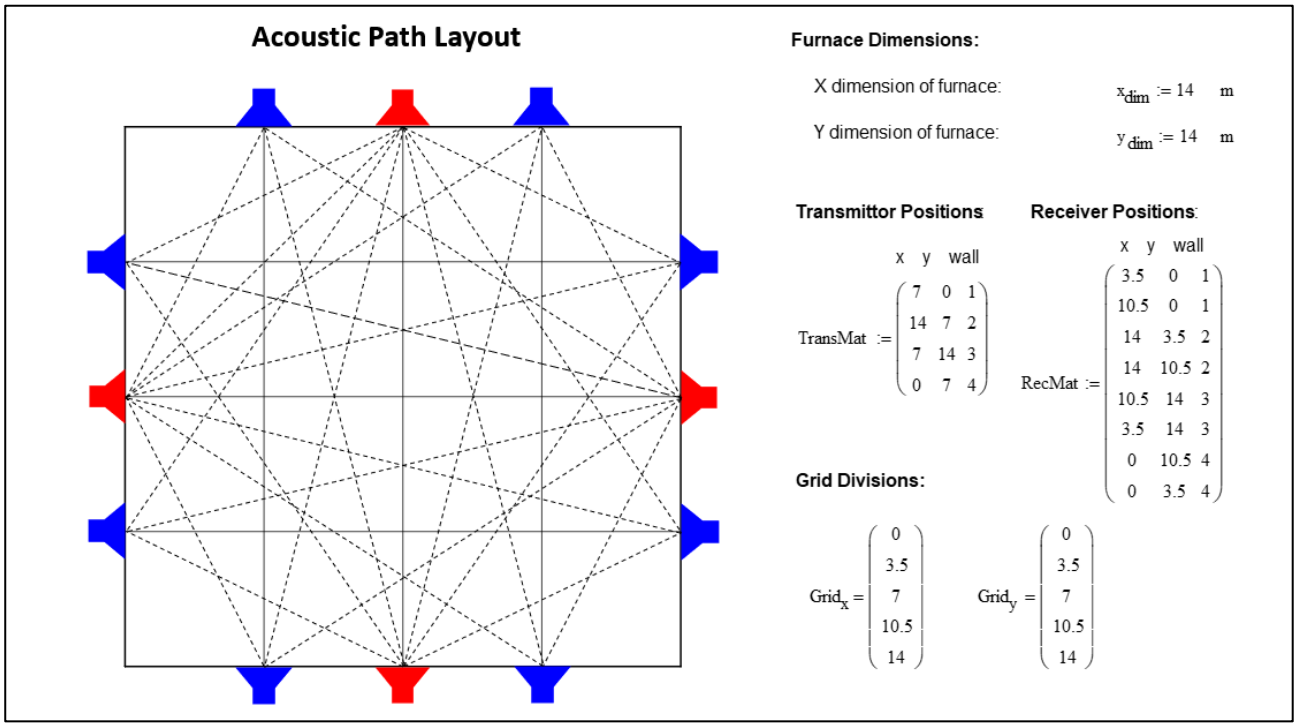

Figure 62 Acoustic Path layout with furnace dimensions, transmitter positions, receiver positions and grid divisions used for testing

To quantify the effect of varying amounts of path error and path measurement repetition on reconstruction accuracy for each set temperature profile, a systematic study as outlined in Figure 63 was followed. The first variable set was the amount of path simulation repetitions, where a range of 1-4 repetitions was considered. This was implemented such that each of the 24 acoustic paths would be simulated 1-4 times and the TOF data set would contain an average of these simulated times with the goal of reducing the variation caused by random path error.

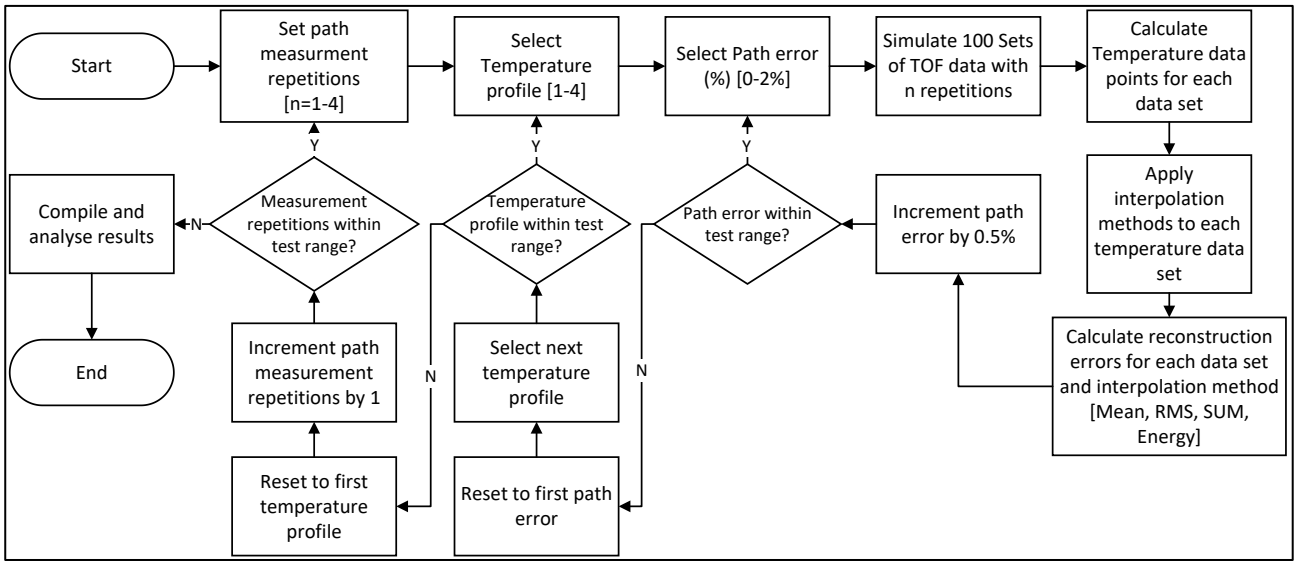

Figure 63 Process followed for collecting path error test data

For the purposes of this test, the 4 set temperature profiles were considered, namely the single peak, steep single peak, asymmetrical peak, and double asymmetrical peak profiles. Since commercial acoustic pyrometers are specified with a path error of 0.5-1 %[29]-[30], an extended range of 0-2 % path error is considered for this test. This error is considered to include all of the physical effects that contribute to single path TOF error.

The test process first specifies the amount of path repetitions, starting at 1 (i.e. no repetition). It then selects the first temperature profile and path error. For this path error and profile it simulates 100 sets of TOF data, where random path error (but zero constant error) is added to each simulated TOF measurement as described in 3.3.4 by equation (73). For each of these sets of TOF, a least-squares method is applied to determine the temperature data point, which is then interpolated by 4 interpolation functions, namely RBF interpolation, cubic spline interpolation, regression and Lagrange interpolation. To limit the amount of data processed, the most promising variations of the cubic spline and regression family was considered, namely cubic spline interpolation with linear endpoints and 2nd order regression. Each of the interpolation functions were then evaluated for their reconstruction error, where data on the mean, RMS, sum and energy error was recorded for each data set.

Once data was generated for a combination of variables, the first one to be varied was the path error, which was incremented by 0.5%. this was repeated until the path error covered the range, and then the temperature profile was varied. When all temperature profiles were considered, the path repetition variable was incremented, and the previous steps were repeated until the end of the path repetition range was reached.

The result of this process was a complete data set, that included temperature reconstruction errors for each interpolation method, temperature profile, path error and path repetition case. The results were then compiled, and summarised tables were produced to analyse the effect of path error on temperature reconstruction on each temperature profile and to ascertain whether repeating readings can significantly reduce this random error.

3.4.2 Results

Effect of time of flight error on reconstruction accuracy

This section presents a summary of the results obtained for temperature reconstruction methods of each set temperature profile when varying levels of random path error is introduced. The mean, RMS, sum and energy reconstruction error are considered for the RBF, Cubic spline, regression and Lagrange interpolation methods.

Table 1: Comparison of temperature reconstruction error (%) for each interpolation method under varying path noise conditions (%) for the single peak temperature profile

	RBF				Cubic Spline (lin endpoints)				Regression (2nd order)				Lagrange			
Error (%)	**Mean**	**RMS**	**Sum**	**Energy**	**Mean**	**RMS**	**Sum**	**Energy**	**Mean**	**RMS**	**Sum**	**Energy**	**Mean**	**RMS**	**Sum**	**Energy**
0	1.37	1.62	1.00	1.06	5.83	5.97	5.72	5.69	2.68	4.30	2.04	1.53	2.04	2.54	1.92	1.49
0.5	2.40	2.94	0.35	0.71	6.45	7.47	5.62	5.59	2.74	4.33	1.94	1.43	4.67	6.87	1.82	1.40
1	3.73	4.65	-0.17	0.39	8.32	10.38	5.50	5.46	3.05	4.58	1.80	1.28	8.21	12.19	1.68	1.25
1.5	5.18	6.56	-0.55	0.12	11.10	14.46	5.47	5.38	3.53	5.05	1.62	1.10	12.34	18.39	1.53	1.07
2	6.31	8.07	-1.44	-0.59	13.90	18.39	4.84	4.86	4.37	5.89	1.23	0.59	16.82	25.23	1.06	0.56

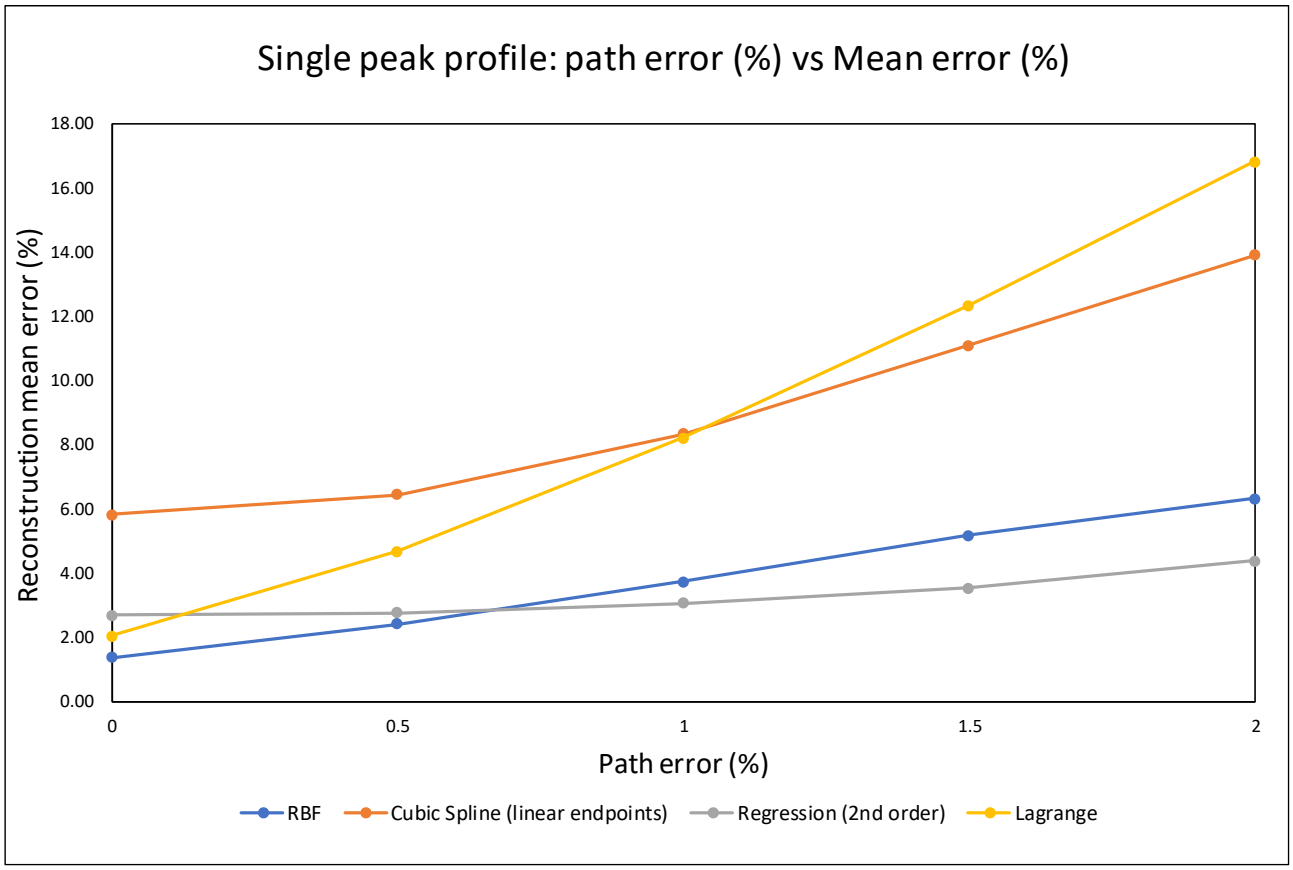

Figure 64 Path error (%) vs mean reconstruction error (%) of each interpolation method for the single peak temperature profile.

Table 2: Comparison of temperature reconstruction error (%) for each interpolation method under varying path noise conditions (%) for the steep single peak temperature profile

	RBF				Cubic Spline (lin endpoints)				Regression (2nd order)				Lagrange			
Error (%)	**Mean**	**RMS**	**Sum**	**Energy**	**Mean**	**RMS**	**Sum**	**Energy**	**Mean**	**RMS**	**Sum**	**Energy**	**Mean**	**RMS**	**Sum**	**Energy**
0	4.49	4.85	3.21	3.37	17.60	17.07	16.41	16.10	8.95	12.33	6.01	4.67	6.79	6.93	5.64	4.43
0.5	4.81	5.26	2.59	3.01	17.56	17.57	16.24	15.96	8.91	12.33	5.88	4.52	8.22	10.05	5.51	4.29
1	5.62	6.47	1.96	2.56	18.46	19.21	16.12	15.82	9.00	12.52	5.70	4.27	12.35	16.03	5.31	4.06
1.5	6.56	7.73	1.54	2.33	19.84	21.30	15.96	15.67	9.10	12.49	5.55	4.16	15.97	21.00	5.17	3.95
2	7.84	9.54	0.85	1.82	21.82	24.27	15.84	15.47	9.39	12.71	5.20	3.77	21.79	28.84	4.85	3.59

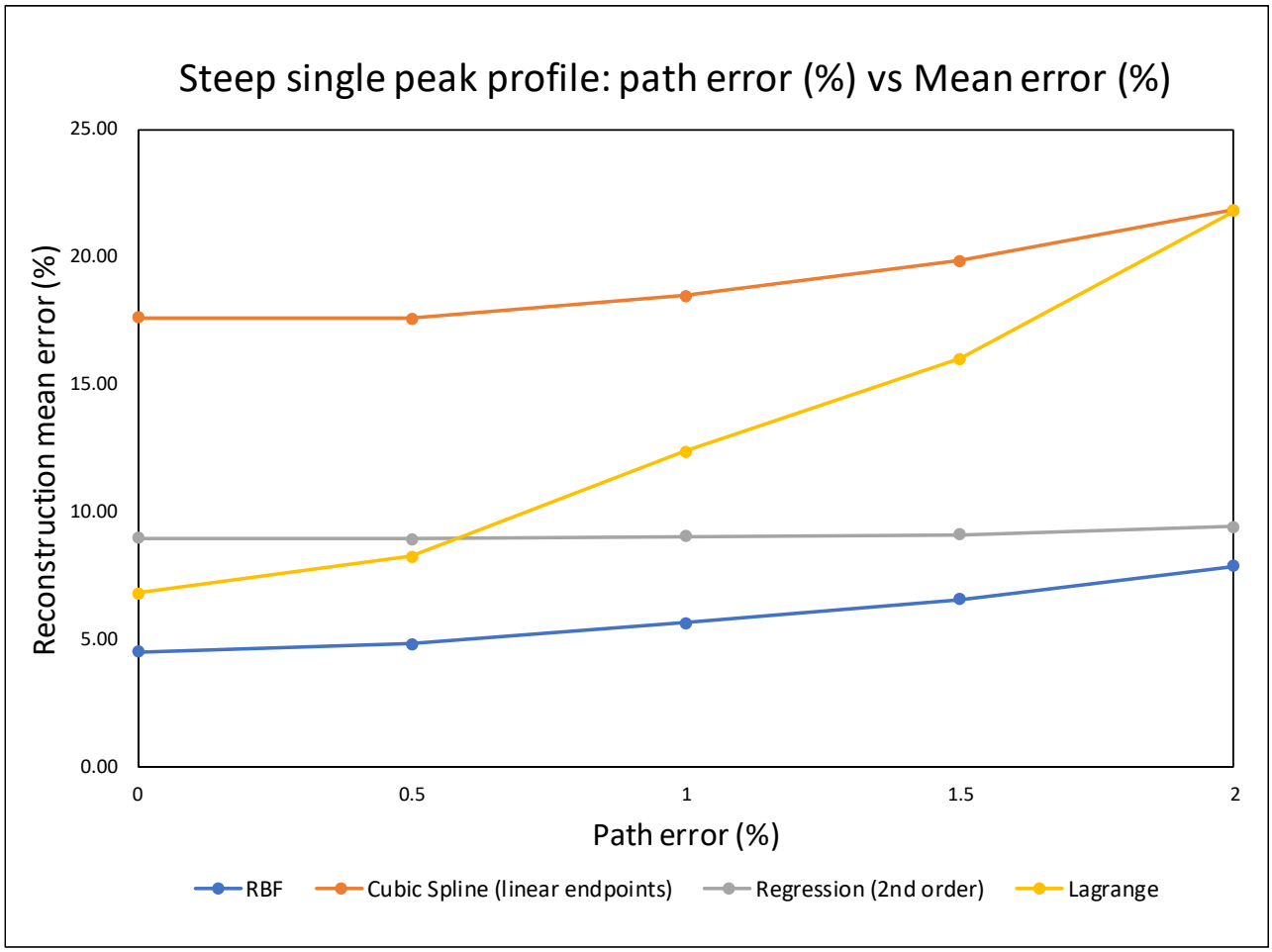

Figure 65 Path error (%) vs mean reconstruction error (%) of each interpolation method for the steep single peak temperature profile.

Table 3 Comparison of temperature reconstruction error(%) for each interpolation method under varying path noise conditions(%) for the asymmetrical peak temperature pro file

	RBF				Cubic Spline (lin endpoints)				Regression (2nd order)				Lagrange			
Error (%)	**Mean**	**RMS**	**Sum**	**Energy**	**Mean**	**RMS**	**Sum**	**Energy**	**Mean**	**RMS**	**Sum**	**Energy**	**Mean**	**RMS**	**Sum**	**Energy**
0	0.56	0.59	0.54	0.55	3.99	4.22	3.77	3.77	1.29	1.95	0.90	0.71	0.90	1.09	0.87	0.70
0.5	2.23	2.98	-0.20	0.18	5.03	6.12	3.72	3.72	1.50	2.12	0.85	0.65	4.00	6.05	0.82	0.65
1	3.84	4.98	-0.86	-0.22	7.46	9.86	3.54	3.54	2.01	2.62	0.66	0.46	7.85	11.85	0.63	0.45
1.5	5.24	6.84	-1.35	-0.51	10.30	14.07	3.44	3.43	2.58	3.33	0.52	0.32	11.68	17.79	0.50	0.31
2	6.56	8.46	-1.91	-0.96	12.80	17.54	3.06	3.05	3.24	4.07	0.16	-0.05	15.43	23.23	0.13	-0.06

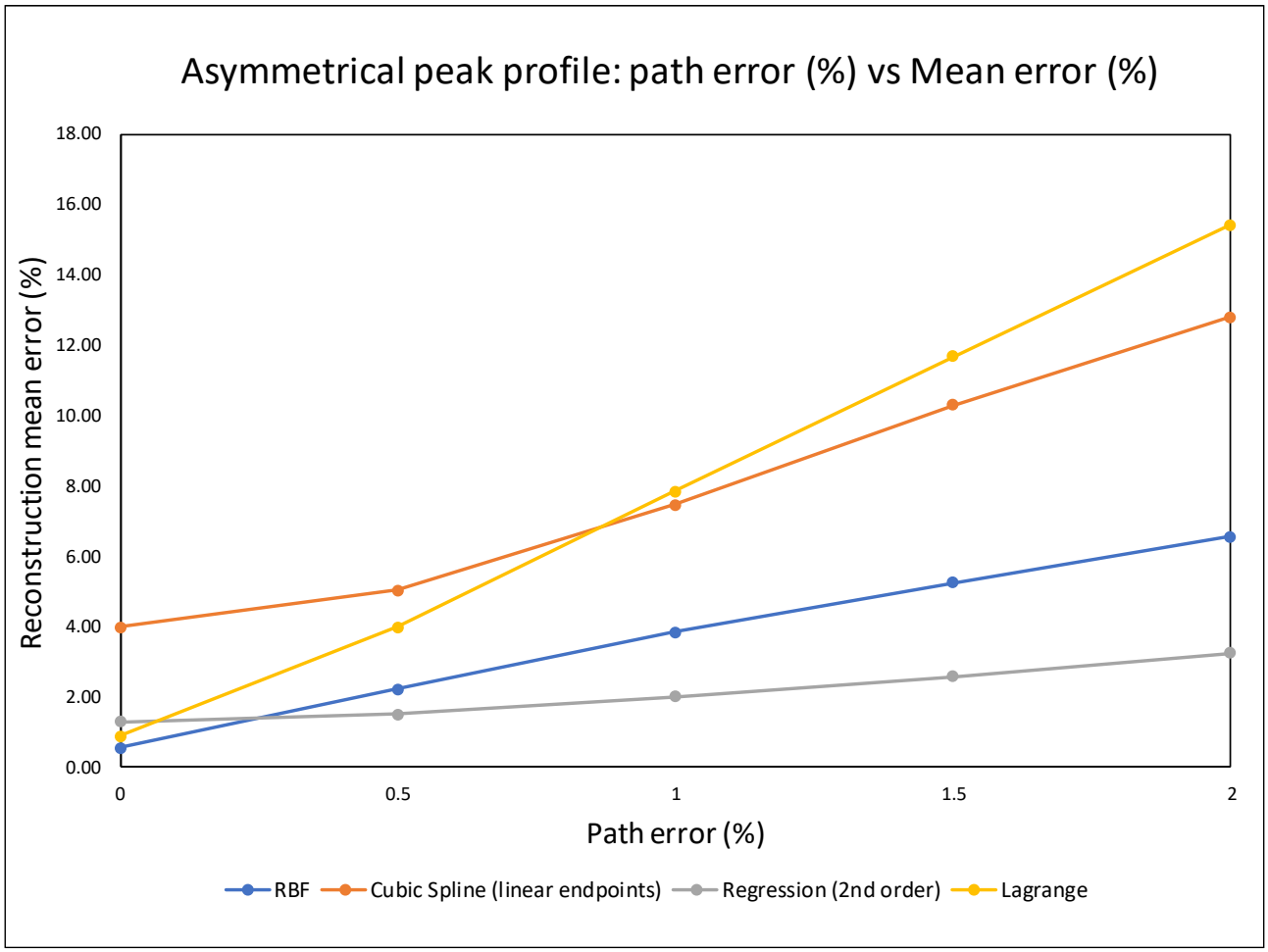

Figure 66 Path error (%) vs mean reconstruction error (%) of each interpolation method for the asymmetrical peak temperature profile.

Table 4: Comparison of temperature reconstruction error (%) for each interpolation method under varying path noise conditions (%) for the double asymmetrical peak temperature profile

	RBF				Cubic Spline (lin endpoints)				Regression (2nd order)				Lagrange			
Error (%)	**Mean**	**RMS**	**Sum**	**Energy**	**Mean**	**RMS**	**Sum**	**Energy**	**Mean**	**RMS**	**Sum**	**Energy**	**Mean**	**RMS**	**Sum**	**Energy**
0	5.1	6.8	0.1	0.4	17.2	20.5	13.2	12.4	14.1	18.1	4.7	2.4	48.9	59.5	4.3	2.3
0.5	5.3	7.1	0.0	0.3	17.4	21.0	13.2	12.4	14.2	18.1	4.6	2.3	49.2	60.0	4.2	2.2
1	5.8	7.9	-0.2	0.1	18.6	22.6	13.1	12.2	14.3	18.2	4.5	2.1	50.7	62.3	4.0	2.0
1.5	6.5	9.1	-0.2	0.0	20.1	25.0	12.9	12.1	14.4	18.3	4.3	2.1	50.0	62.1	3.9	2.0
2	7.4	10.3	-0.6	-0.3	22.5	28.0	12.6	11.8	14.7	18.5	4.0	1.7	51.2	64.1	3.6	1.6

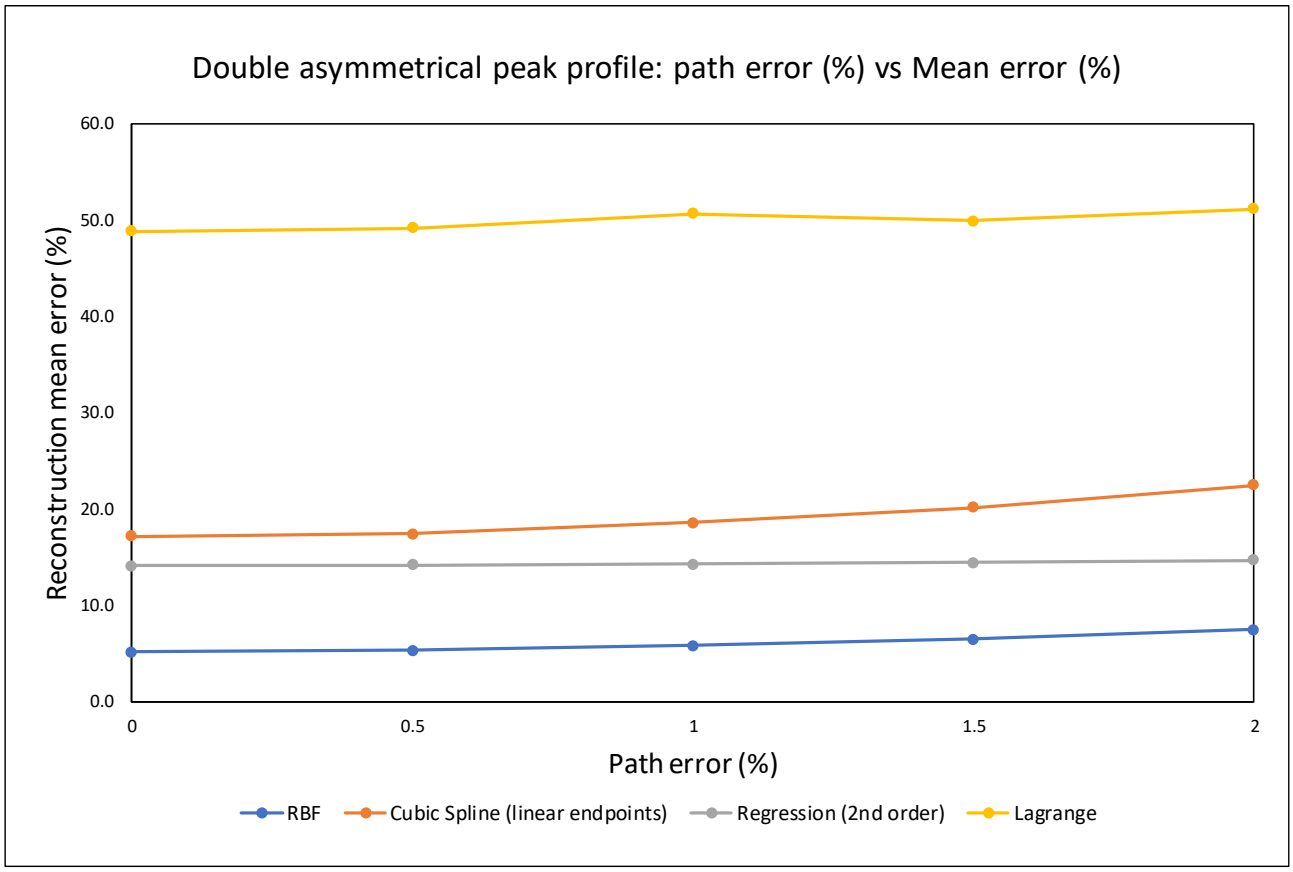

Figure 67 Path error (%) vs mean reconstruction error (%) of each interpolation method for the double asymmetrical peak temperature profile.

Effect of repeated TOF readings on temperature reconstruction error

This section presents the results of repeating TOF readings under varying path noise conditions. The mean error of reconstruction is presented as the main metric with which to judge error reduction for each reconstruction method. These values are summarised below in Table 5 for reconstructing the single peak temperature profile.

Table 5: Path error (%) vs reconstruction error (%) each interpolation method grouped by number of measurement repetitions when reconstructing the single peak temperature profile

	Number of repetitions															
	RBF				Cubic Spline (lin endpoints)				Regression (2nd order)				Lagrange			
Error (%)	**1**	**2**	**3**	**4**	**1**	**2**	**3**	**4**	**1**	**2**	**3**	**4**	**1**	**2**	**3**	**4**
0	1.37	1.37	1.37	1.37	5.83	5.83	5.83	5.83	2.68	2.68	2.68	2.68	2.04	2.04	2.04	2.04
0.5	2.40	1.93	1.77	1.67	6.45	6.07	5.93	5.88	2.74	2.71	2.68	2.67	4.67	3.41	2.97	2.64
1	3.73	2.90	2.55	2.41	8.32	7.11	6.57	6.53	3.05	2.86	2.79	2.73	8.21	5.96	4.90	4.77
1.5	5.18	3.89	3.37	3.01	11.10	8.49	7.75	7.10	3.53	3.14	2.96	2.85	12.34	8.48	7.22	5.99
2	6.31	5.00	4.21	3.78	13.90	10.78	9.15	8.38	4.37	3.39	3.11	3.13	16.82	12.37	9.56	8.18

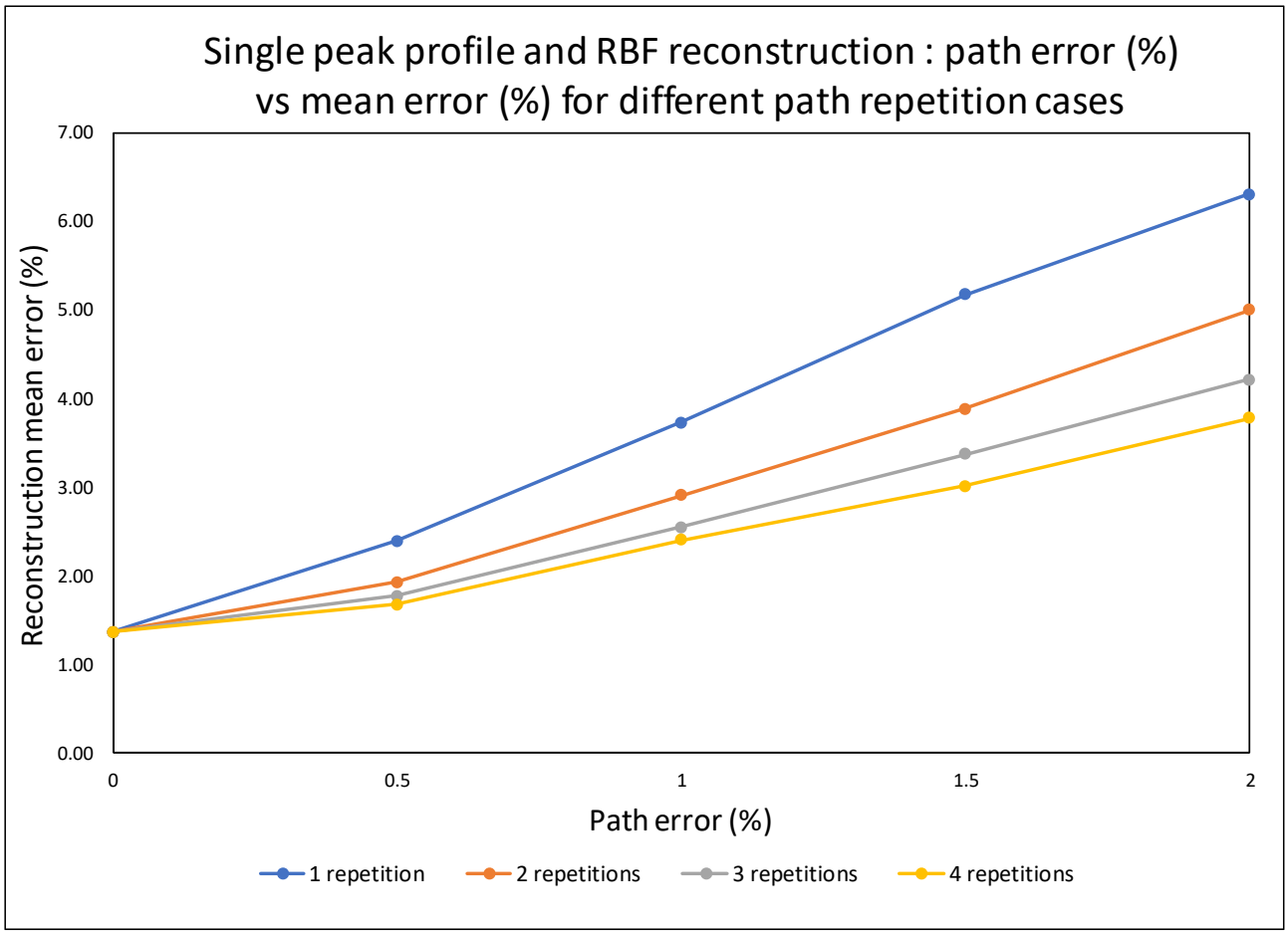

Figure 68 Path error (%) vs RBF reconstruction error (%) grouped by number of measurement repetitions

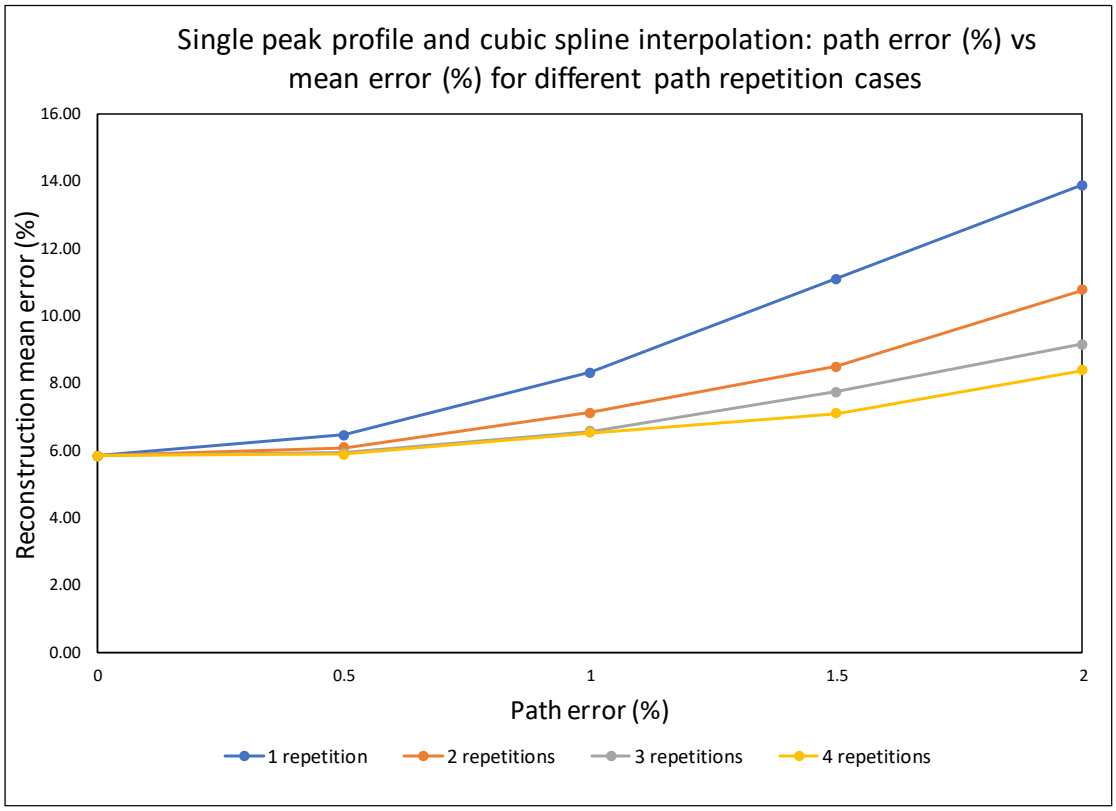

Figure 69 Path error (%) vs cubic spline reconstruction error (%) grouped by number of measurement repetitions

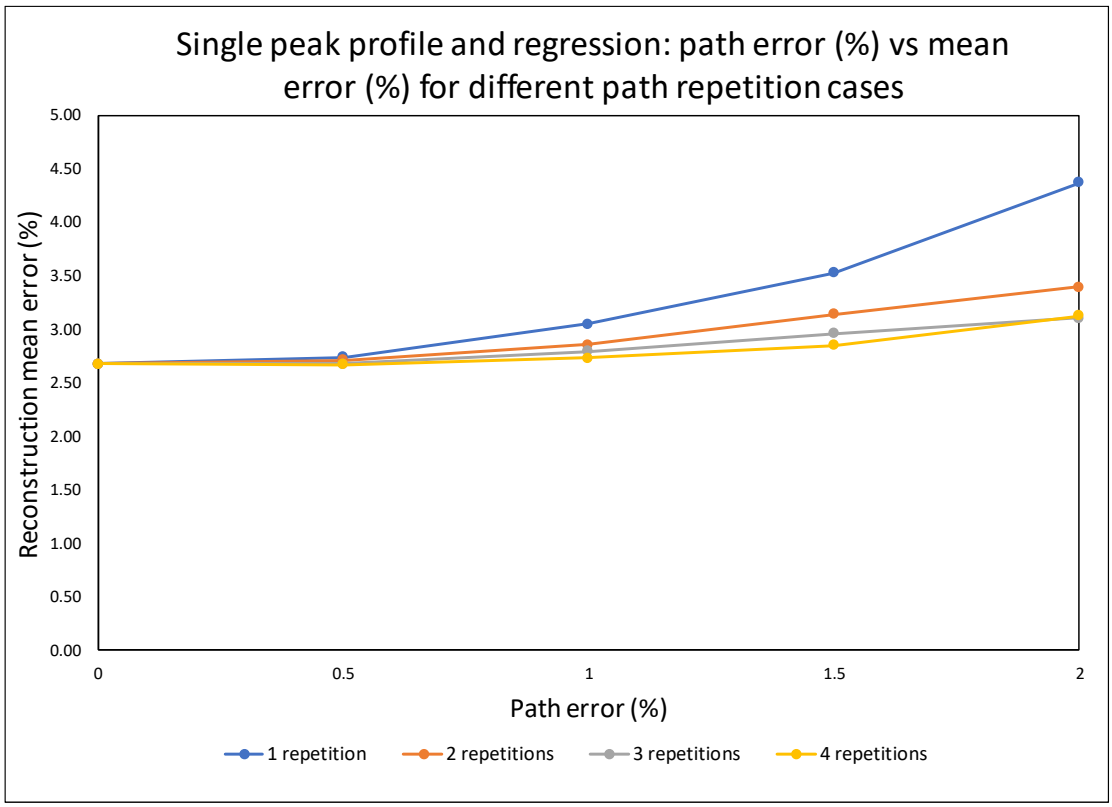

Figure 70 Path error (%) vs regression reconstruction error (%) grouped by number of measurement repetitions

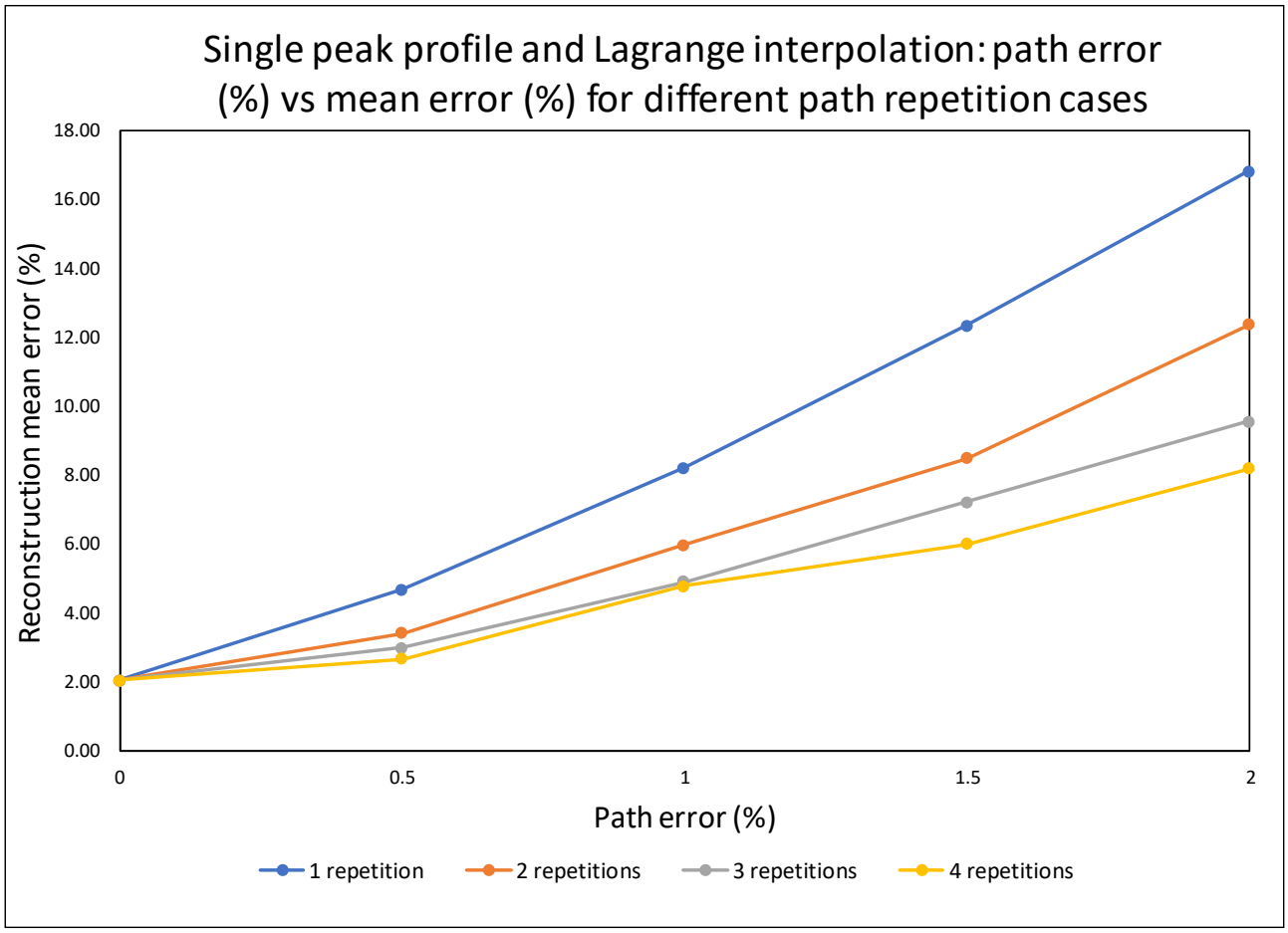

Figure 71 Path error (%) vs Lagrange reconstruction error (%) grouped by number of measurement repetitions

The following tables summarise the effect of path simulation repetition for the steep single peak, asymmetrical peak and double asymmetrical peak temperature profiles.

Table 6: Path error (%) vs reconstruction error (%) each interpolation method grouped by number of measurement repetitions when reconstructing the steep single peak temperature profile

	Number of repetitions															
	RBF				Cubic Spline (lin endpoints)				Regression (2nd order)				Lagrange			
Error (%)	**1**	**2**	**3**	**4**	**1**	**2**	**3**	**4**	**1**	**2**	**3**	**4**	**1**	**2**	**3**	**4**
0	4.49	4.49	4.49	4.49	17.60	17.60	17.60	17.60	8.95	8.95	8.95	8.95	6.79	6.79	6.79	6.79
0.5	4.81	4.72	4.64	4.72	17.56	17.59	17.56	17.60	8.91	8.92	8.92	8.92	8.22	7.45	7.08	7.38
1	5.62	5.20	4.98	5.14	18.46	17.82	17.71	17.92	9.00	8.91	8.91	8.95	12.35	9.68	8.71	9.48
1.5	6.56	5.72	5.47	5.75	19.84	18.63	18.14	18.66	9.10	9.03	8.91	8.99	15.97	13.23	11.23	13.34
2	7.84	6.38	5.95	6.56	21.82	19.52	18.88	19.95	9.39	9.09	9.05	9.11	21.79	15.68	13.99	16.81

Table 7: Path error (%) vs reconstruction error (%) each interpolation method grouped by number of measurement repetitions when reconstructing the asymmetrical peak temperature profile

	Number of repetitions															
	RBF				Cubic Spline (lin endpoints)				Regression (2nd order)				Lagrange			
Error (%)	1	2	3	4	1	2	3	4	1	2	3	4	1	2	3	4
0	0.56	0.56	0.56	0.56	2.87	2.87	2.87	2.87	1.29	1.29	1.29	1.29	0.90	0.90	0.90	0.90
0.5	2.23	1.67	1.53	1.33	5.03	4.44	4.33	4.21	1.50	1.39	1.36	1.34	4.00	2.87	2.48	2.13
1	3.84	2.90	2.56	2.22	7.46	5.70	5.26	5.09	2.01	1.66	1.57	1.51	7.85	5.35	4.60	3.97
1.5	5.24	4.01	3.44	3.15	10.30	8.03	6.79	6.26	2.58	2.13	1.89	1.76	11.68	8.76	7.06	5.98
2	6.56	4.01	4.49	3.95	12.80	8.03	8.55	7.48	3.24	2.13	2.16	2.01	15.43	8.76	9.54	8.05

Table 8: Path error (%) vs reconstruction error (%) each interpolation method grouped by number of measurement repetitions when reconstructing the double asymmetrical peak temperature profile

	Number of repetitions															
	RBF				Cubic Spline (lin endpoints)				Regression (2nd order)				Lagrange			
Error (%)	1	2	3	4	1	2	3	4	1	2	3	4	1	2	3	4
0	5.13	5.13	5.13	5.13	17.17	17.17	17.17	17.17	14.12	14.12	14.12	14.12	48.88	48.88	48.88	48.88
0.5	5.27	5.21	5.17	5.16	17.39	17.33	17.22	17.23	14.17	14.14	14.11	14.11	49.16	49.13	49.04	48.73
1	5.78	5.45	5.35	5.31	18.55	17.79	17.60	17.54	14.29	14.16	14.14	14.19	50.68	48.60	49.51	49.20
1.5	6.49	5.79	5.71	5.50	20.13	18.50	18.54	17.99	14.39	14.23	14.34	14.22	49.97	49.52	50.37	49.58
2	7.45	6.65	6.00	5.84	22.48	21.06	19.07	19.12	14.68	14.70	14.39	14.42	51.18	53.73	50.80	50.82

3.4.3 Discussion

Effect of time of flight error on reconstruction accuracy

As shown by Table 1 - Table 4, path error reduces reconstruction fit across all interpolation methods and temperature profiles. However, this reduction in accuracy is not linear (reconstruction mean and RMS error increases by more than the random path error) and the extent of the reduction varies greatly between interpolation methods.

This is especially shown in Figure 64 and Figure 66, where RBF reconstruction is initially the most accurate method, however when path error increases, regression becomes more accurate than RBF interpolation in terms of mean reconstruction error. For the single peak profile this crossover happens between 0.5-1% path error and for the asymmetrical peak profile it happens before the 0.5% mark. Suggesting that in high noise scenarios regression might be preferable to RBF interpolation.

Furthermore, regression is the least effected by path error on all profiles and often the increase in path error is higher than the increase in reconstruction error. However, this comes at the expense of not being able to accurately reproduce more complex temperature profiles such as the steep single profile and double asymmetrical peak profile, where the mean reconstruction error is ~5 % and ~14 % respectively.

Conversely, RBF interpolation is shown to be the most accurate interpolation method for all temperature profiles with no path error. With the default transceiver layout, it achieves a mean reconstruction error of 1.37 % and 0.56 % for the single peak and asymmetrical peak profile respectively. This error increases with the profiles that have higher temperature changes, resulting in 4.49 % and 5.1 % mean reconstruction error for the steep single peak and double asymmetrical peak profile. However, this trend is consistent for all interpolation methods.

Although RBF interpolation is more susceptible to path noise than regression, it is the only method that sufficiently reconstructs the temperature profiles with more complexity and higher temperature differentials.

In contrast to the RBF interpolation method, cubic spline interpolation was the least accurate interpolation method in noiseless conditions and consistently produced higher mean reconstruction errors. The method did however perform better than the Lagrange interpolation method once path error was added. This can be seen clearly in Figure 64, Figure 65 and Figure 66 where although the Lagrange method started of being the second most accurate method, it was disproportionately affected by path error and promptly overtook the other methods to have the greatest error. The exception to this was the double asymmetrical temperature profile, where the Lagrange method failed altogether to reconstruct both peaks.

Contrary to the reconstruction fit trends, the energy error was not adversely affected by random path noise and reduced in many cases when more path noise was added. In terms of energy error, RBF interpolation produced the best results having and energy error of below 1 % for the single peak, asymmetrical peak and double asymmetrical peak profiles. For the steep single peak profile, the energy error was below 3.37 %. Regression and Lagrange methods both also produced low energy errors following the same trend. However once again cubic spline interpolation was the least accurate in terms of energy error.

Repeated TOF readings

When it came to repeating TOF readings, three out of the for interpolation methods applied exhibited significant improvements to the mean reconstruction error. The exception to this was the regression interpolation method, which as shown in Table 5-Table 8 and by the almost horizontal lines in Figure 70, typically saw an error improvement of less than 1 % for repeating readings. However, this could be attributed to the fact that the regression interpolation method was least affected by path error.

In contrast, cubic spline interpolation and Lagrange interpolation showed the greatest decrease in mean reconstruction by repeating readings. Though these methods were the most adversely affected by path error, as shown in Figure 69 and Figure 71 the residual effect of path error on reconstruction error was still present and greater than the path error.

The method that came closest to reducing the effect of random path error with repetition was the RBF interpolation method. With 4 path repetitions the resulting mean reconstruction error was only slightly higher than the addition of the path error for all temperature profiles. For RBF interpolation (and the other methods tested) the greatest reduction of error is seen between 1-2 repetitions after which the change in reconstruction error is diminished. At this double repetition region with 1% path error, the RBF interpolation method produces a mean reconstruction error of 2.9 %, 5.6 %, 2.9 % and 5.45 % for the single peak, steep single peak, asymmetrical peak and double asymmetrical peak profiles respectively.

Besides being the most practicable of the repetition cases, this improvement strikes a balance between being able to reconstruct complex profiles and being path noise resistant for shallower profiles, since it has a mean reconstruction error very close to regression for these profiles (2.86 %, 8.91 %, 1.66 % and 14.16 % for the single peak, steep single peak, asymmetrical peak and double asymmetrical peak profiles respectively).

In addition to this, the double path repetition case is advantageous when a transceiver acoustic pyrometer is used since acoustic readings can be recorded both ways without having to fire each transceiver again. This provides the benefit of reducing random path error and any velocity effects that may occur due to the velocity of flue gas at the furnace exit without the same resource or time cost.

3.5 Transmitter/receiver location tests

During the model development phase, it was observed that temperature reconstruction accuracy was not only affected by path error, temperature profile or interpolation method, but also largely affected by the placement of the transmitters and receivers, the resulting acoustic paths and the grid chosen for the data points. An example of this is shown in Figure 72 for the reconstruction of the single peak profile. By making minor changes to the transmitter and receiver locations, the mean reconstruction error doubles (in extreme cases reconstruction fails altogether). Additionally, when the grid position changes and brought inwards, the error becomes over 5 times more than the original error (in extreme cases reconstruction fails altogether).

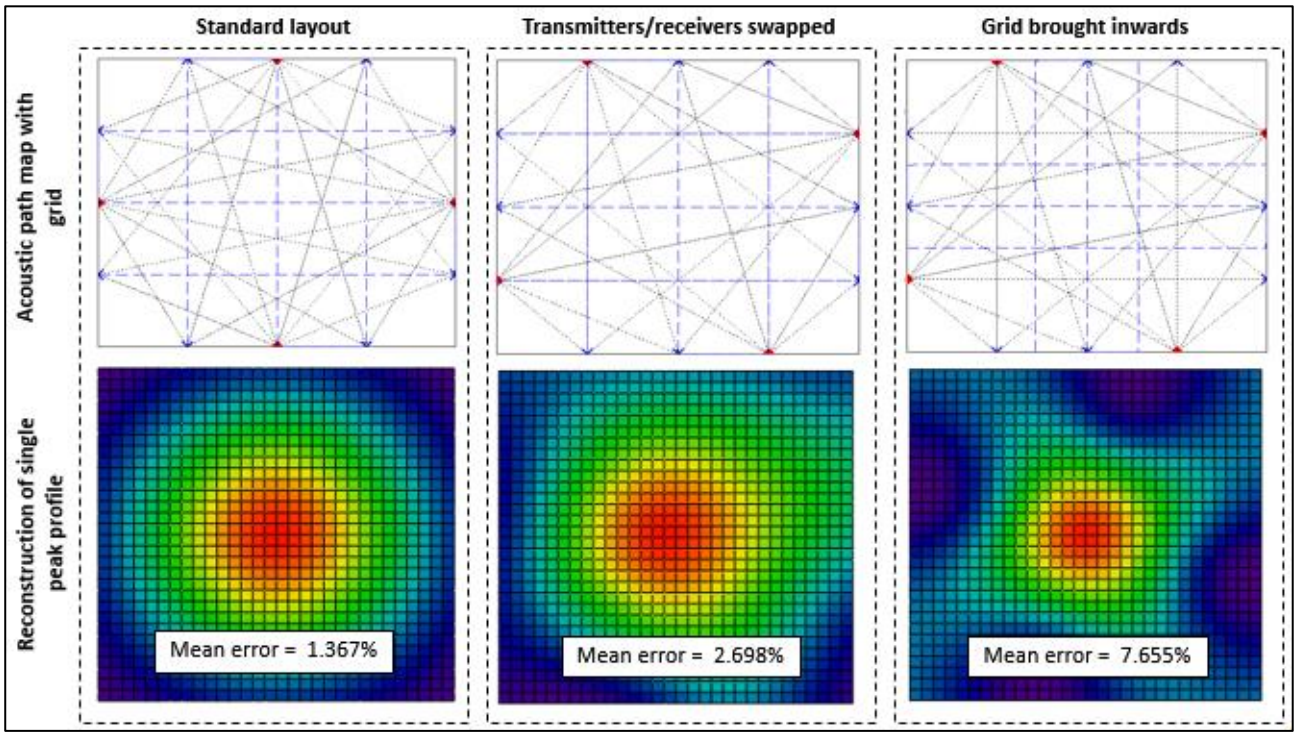

Figure 72 Single peak profile reconstruction with varying transmitter/receiver locations and grid

As a result, the tests in this section aim to determine how transmitter/receiver locations and grid choice affects temperature reconstruction, as to identify trends and draw guidelines to implement reconstruction in a way that reduces these pitfalls.

3.5.1 Methodology

To determine guidelines for implementation of an acoustic pyrometer in terms of temperature profile reconstruction, a systematic study method was used. This involved highlighting variables that

affected reconstruction accuracy and then altering them to determine how to implement these variables to improve reconstruction accuracy. Since the aim of this test was not to find the exact best solution, but rather to identify trends that that produce more accurate results, the methodology takes a more trial and error approach and is less rigid and procedural than the path error test methodology.

Namely the variables of consideration for this test is the positions of the transmitters/receiver or transceivers and setup of the grid. Both types of acoustic pyrometer are considered (transmitter/receiver and transceiver) and all 4 set temperature profiles are considered.

The furnace dimensions are kept the same as the previous test (14x14 m) and the test focusses on the 24-acoustic-path case with a 4x4 grid size, since this is considered the lowest number of paths to adequately reconstruct more complex temperature profiles. The success of the reconstruction is once again measured by the mean, RMS, sum and energy error of reconstruction.

For each acoustic pyrometer type and temperature profile, the process outlined in Figure 73 was followed. This involved first trialling different transmitter and receiver positions, calculated reconstruction error and observing the reconstruction visually and then identifying positive trends from them. More error tests were undertaken for layouts that provided positive results and their variables and error results were captured. Once a range of combinations were tested, the successful transmitter and receiver location combinations were then retested with different grid positions. The same process was then followed, which overall resulted in the gathering of error data for many transmitter, receiver and grid combinations. These results were then analysed and the most accurate results for each temperature profile and acoustic pyrometer was identified to determine the positive guidelines to improve reconstruction accuracy.

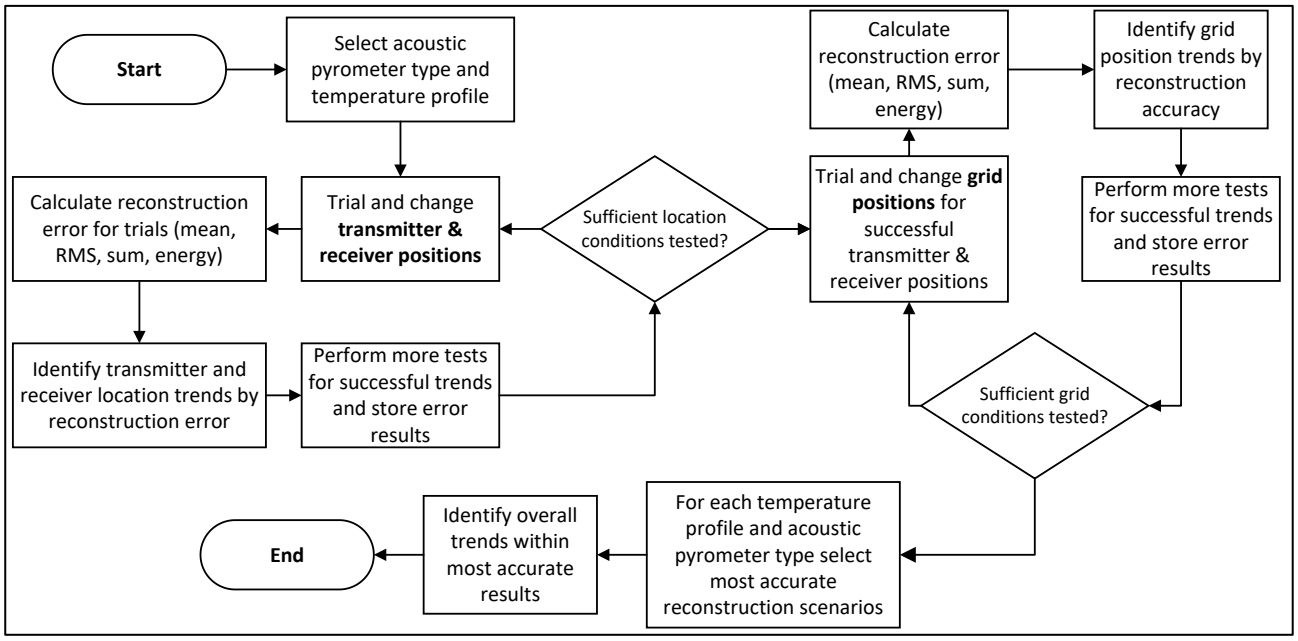

Figure 73 Overall process followed for transmitter/receiver location tests for a given acoustic pyrometer type and temperature profile

Limitations applied while testing

While the previous section described the overall methodology in a high-level sense, this section aims to draw attention to the specific limitations that were set during these tests to produce the more favourable reconstructions shown in the results section. These limitations too have value in identifying rules that negatively affect reconstructions.

One of the first observations made about transmitter and receiver placement, was how symmetry (or the lack thereof) affected temperature reconstruction. During initial trials, non-symmetric layouts were considered, however it quickly became apparent that temperature reconstructions became distorted as a result. Examples of this is shown in Figure 72 and Figure 74, where the latter example shows how by moving certain receivers outwards, the resulting reconstruction peak becomes spread in that direction. The same effect is observed when the grid lines are moved outwards too. As a result, symmetry was applied as a limitation, and receivers or the x and y grid were often changed in unison to preserve symmetry.

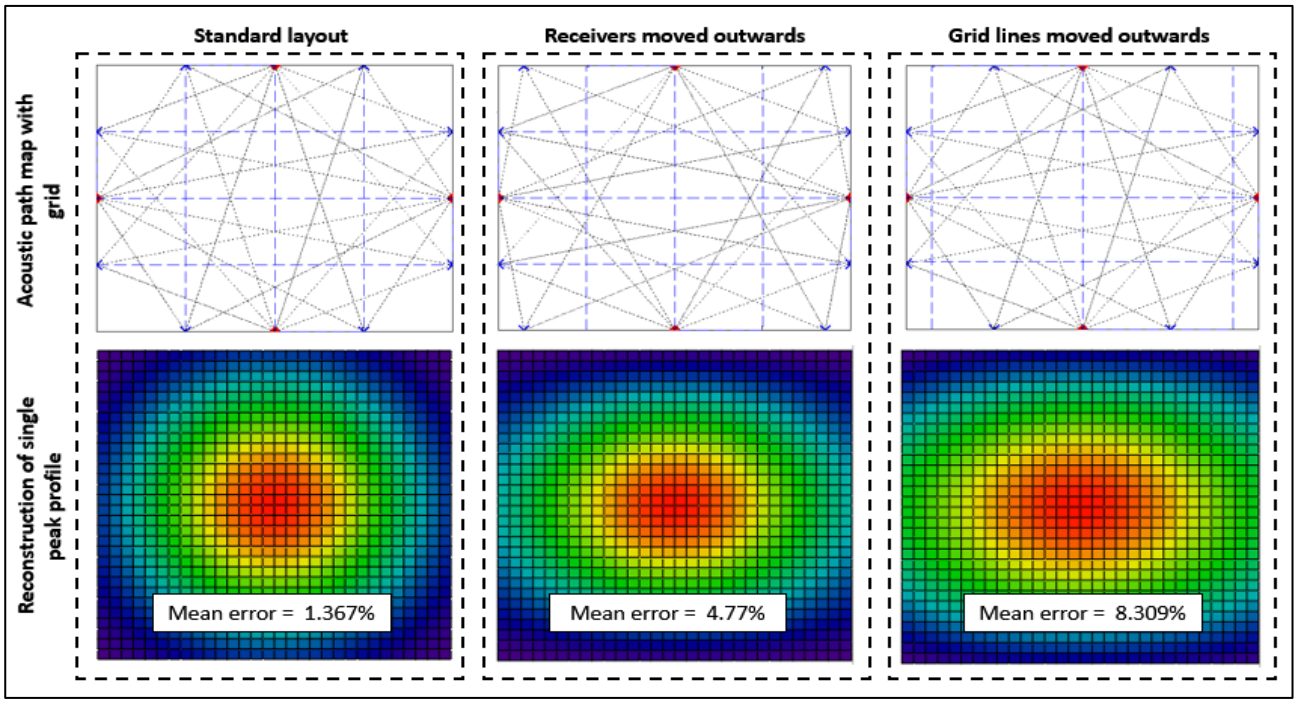

Figure 74 Spreading of single peak profile reconstruction due to receiver placement and grid selection

This effect is not as pronounced for smaller asymmetries and may be desired in some cases, for example in the case in Figure 75, observation ports might limit the receivers to being placed closer to the edges producing a more spread out profile, but by also changing the x grid, this could be corrected. However, for the purposes of this test focus was placed on finding more favourable locations and thus symmetry was preserved.

Tests were also performed with a 4x4 grid instead of a 6x4 or 4x6 grid that was permissible with 24 acoustic paths for this reason. The redundancy is preferable for data point determination and results in more symmetric distributions.

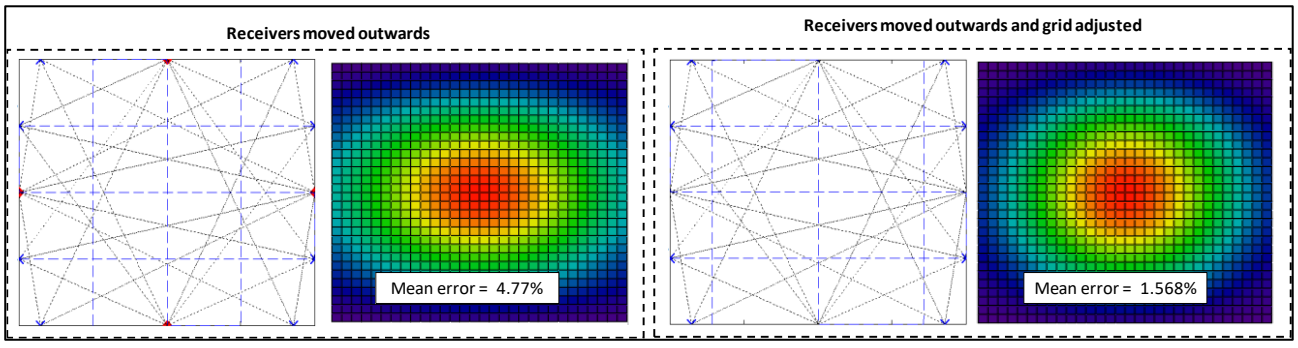

Figure 75 Grid adjustment to reduce spreading of single peak profile

Additionally, the limitations shown in Figure 76 were also applied during testing. Transmitter/receiver positioning that resulted in the first case, where blocks were created with no acoustic paths were not considered as no data point would be able to be determined. Similarly, cases comparable the second example where a very small segment of the path was contained in the block was also not considered as it produced highly inaccurate estimations of the temperature in these blocks. Lastly, when transceiver type acoustic pyrometer testing was done, layouts that resulted in an acoustic path overlapping with a grid line was also not considered, as it produced skewed representations of the temperature in the blocks alongside.

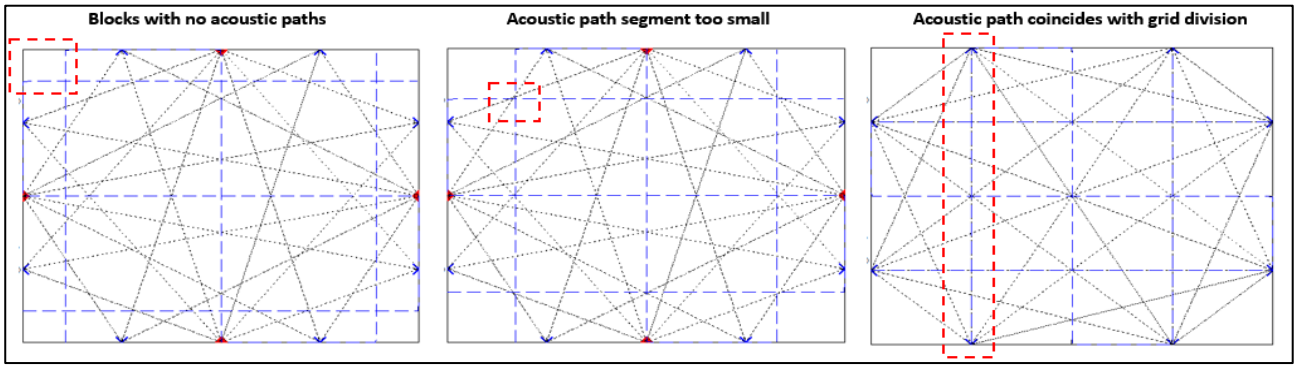

Figure 76 Acoustic path scenarios that significantly reduce reconstruction accuracy

3.5.2 Results

This section presents the summarised results of the transmitter receiver location tests for each interpolation method. More detailed results showing the transmitter receiver location layouts and resulting reconstructions are shown in Appendix B.

Table 9 Summary of Path error tests results for each temperature profile and interpolation method

Temperature profile	Error (%)	RBF			Cubic Spline (lin endpoints)			Regression (2nd order)			Lagrange		
		Mean	RMS	Energy	Mean	RMS	Energy	Mean	RMS	Energy	Mean	RMS	Energy
Single peak profile	0	1.37	1.62	1.06	5.83	5.97	5.69	2.68	4.30	1.53	2.04	2.54	1.49
	0.5	2.40	2.94	0.71	6.45	7.47	5.59	2.74	4.33	1.43	4.67	6.87	1.40
	1	3.73	4.65	0.39	8.32	10.38	5.46	3.05	4.58	1.28	8.21	12.19	1.25
	1.5	5.18	6.56	0.12	11.10	14.46	5.38	3.53	5.05	1.10	12.34	18.39	1.07
	2	6.31	8.07	-0.59	13.90	18.39	4.86	4.37	5.89	0.59	16.82	25.23	0.56
Steep single peak profile	0	4.49	4.85	3.37	17.60	17.07	16.10	8.95	12.33	4.67	6.79	6.93	4.43
	0.5	4.81	5.26	3.01	17.56	17.57	15.96	8.91	12.33	4.52	8.22	10.05	4.29
	1	5.62	6.47	2.56	18.46	19.21	15.82	9.00	12.52	4.27	12.35	16.03	4.06
	1.5	6.56	7.73	2.33	19.84	21.30	15.67	9.10	12.49	4.16	15.97	21.00	3.95
	2	7.84	9.54	1.82	21.82	24.27	15.47	9.39	12.71	3.77	21.79	28.84	3.59
Asymmetrical peak profile	0	0.56	0.59	0.55	3.99	4.22	3.77	1.29	1.95	0.71	0.90	1.09	0.70
	0.5	2.23	2.98	0.18	5.03	6.12	3.72	1.50	2.12	0.65	4.00	6.05	0.65
	1	3.84	4.98	-0.22	7.46	9.86	3.54	2.01	2.62	0.46	7.85	11.85	0.45
	1.5	5.24	6.84	-0.51	10.30	14.07	3.43	2.58	3.33	0.32	11.68	17.79	0.31
	2	6.56	8.46	-0.96	12.80	17.54	3.05	3.24	4.07	-0.05	15.43	23.23	-0.06
Double asymmetrical peak profile	0	5.1	6.8	0.4	17.2	20.5	12.4	14.1	18.1	2.4	48.9	59.5	2.3
	0.5	5.3	7.1	0.3	17.4	21.0	12.4	14.2	18.1	2.3	49.2	60.0	2.2
	1	5.8	7.9	0.1	18.6	22.6	12.2	14.3	18.2	2.1	50.7	62.3	2.0
	1.5	6.5	9.1	0.0	20.1	25.0	12.1	14.4	18.3	2.1	50.0	62.1	2.0
	2	7.4	10.3	-0.3	22.5	28.0	11.8	14.7	18.5	1.7	51.2	64.1	1.6

Figure 77 and

Figure 78 show the x-coordinate position of the most accurate grid line positions relative to the first receiver/transceiver positions for each acoustic path layout considered when testing the single peak temperature profile.

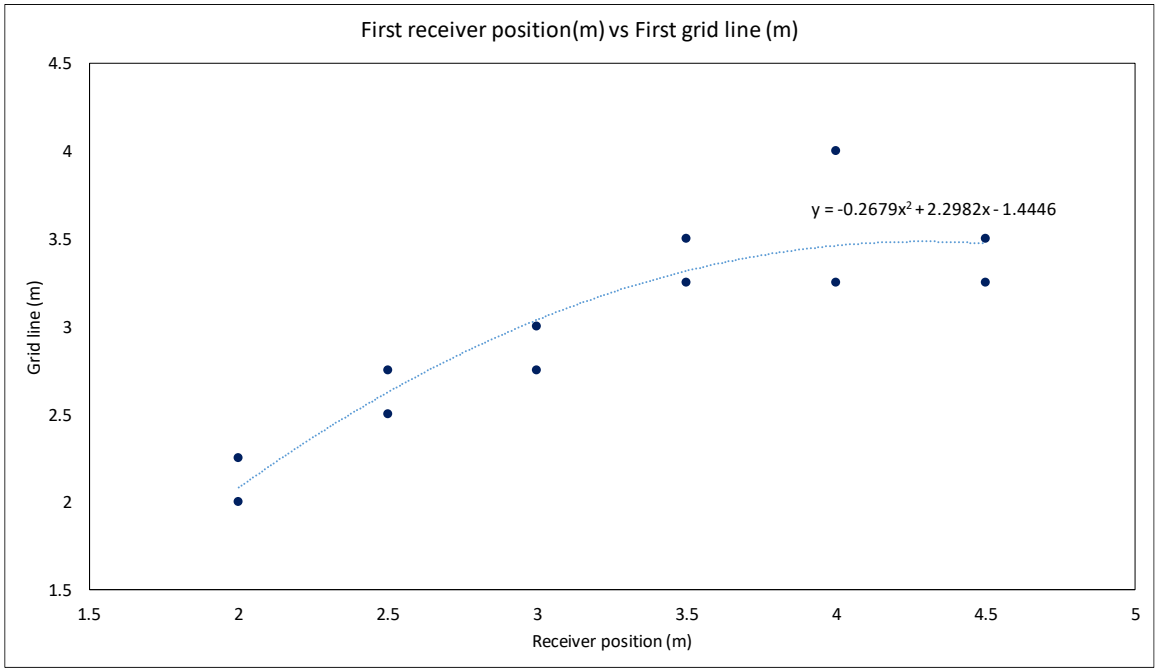

Figure 77 First receiver position(m) vs first grid line position(m) for accurate reconstructions of the single peak profile

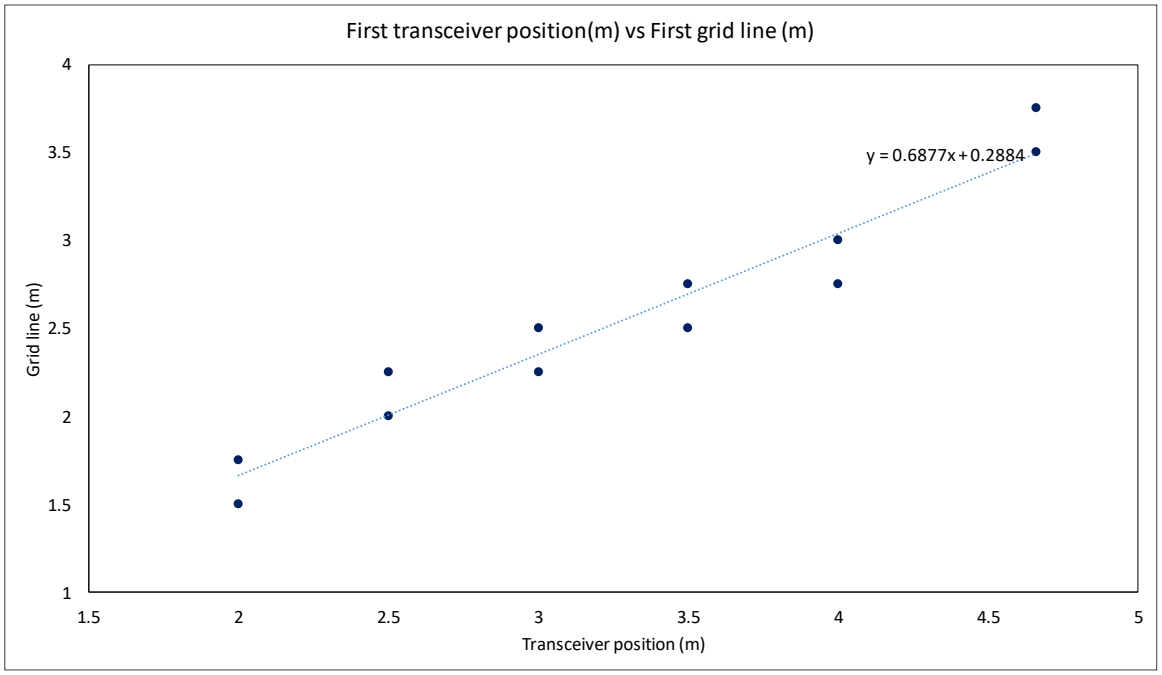

Figure 78 First transceiver position(m) vs first grid line position (m) for accurate reconstructions of the single peak profile

3.5.3 Discussion

Interpolation methods

As observed with the path error tests, across all the tested temperature profiles, RBF interpolation consistently produced the most accurate reconstructions for both types of acoustic pyrometer, which can be seen both by visual correlation and the error results. The only exceptions occurred for reconstructing the asymmetrical peak temperature profile when the grid moved extremely close to the ends of the furnace area, which is expected since RBF interpolation struggles when data points are too spread.

Similarly, as shown in Appendix A, Lagrange interpolation also had good visual correlation for the first three temperature profiles with slightly less accurate results than RBF interpolation. However, it suffered near the borders of the furnace where temperature was often underestimated.

This problem was even more pronounced for cubic spline interpolation, as seen in **Error! Reference source not found.** and **Error! Reference source not found.** where overfitting occurred and there were great oscillations near the border, sometimes exceeding the set colour scale. As a result, cubic spline interpolation produced the least accurate reconstructions by all error measurements.

In contrast to this, reconstructions produced by regression were more likely to be underfit and thus extrapolated better, avoiding the large error spike near the borders. This was adequate for shallower single peak reconstructions where it was able to locate the peak, however it was not able to distinguish two peaks as shown in **Error! Reference source not found.** and **Error! Reference source not found.** resulting in poor reconstruction accuracy.

Transmitter/receiver/transceiver positioning trends

In terms of positioning the transmitter and receiver, it was found that the most accurate results were obtained when the acoustic paths managed to spread over the whole furnace area and the receivers or transceivers where placed slightly closer to the walls. In addition to this, reconstructions were more accurate when the gridlines were slightly closer to the wall than the receiver/transceiver. This trend is shown for the single peak profile in

Figure 77 and

Figure 78 where for each receiver/transceiver arrangement the two most accurate grid positions were selected and plotted. The result shows a tendency for the most accurate reconstructions to reside where the grid is selected to be closer to the wall. This is expected for the transceiver case as the condition where the grid line intersects with the path is suboptimal.

As discussed previously the greatest error incurred by the interpolation methods were in the extrapolation region as depicted in Figure 79 by the red shaded region. By placing receivers and transceiver slightly outwards and reducing the grid side near the walls, the data points are also moved closer to the wall. This results in the extrapolation region being minimised and thus the accuracy of the reconstruction is improved.

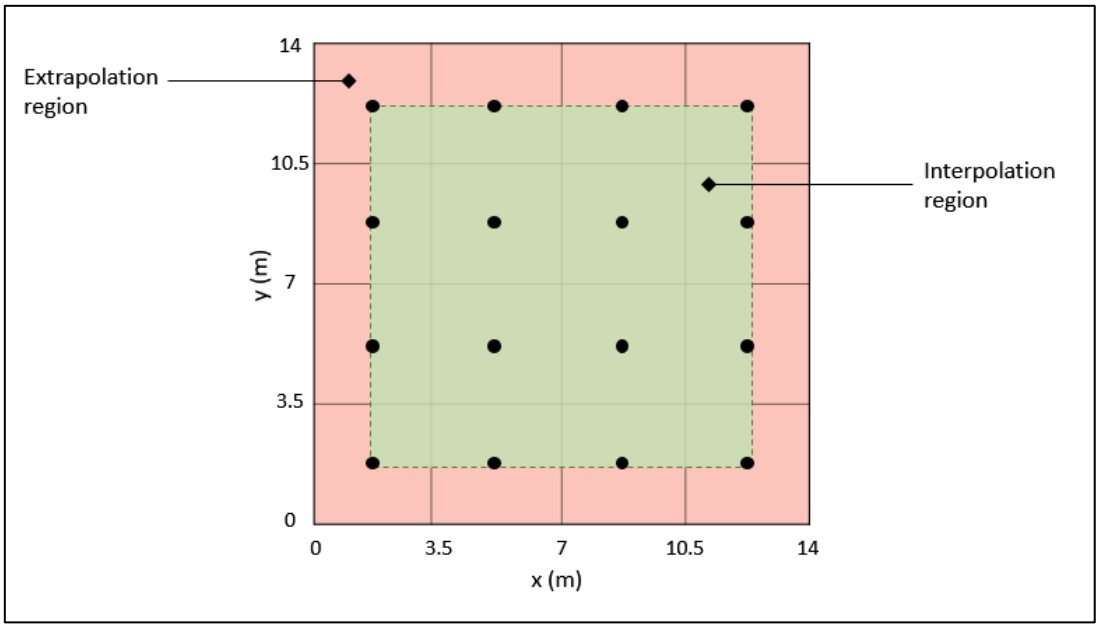

Figure 79 Extrapolation vs interpolation region for a given set of data points

This region also happens to be the exhibit the greatest amount of temperature change, and thus improving accuracy in the region is wholly beneficial to the reconstruction accuracy.

Transmitter/receiver vs transceiver

Based on the results obtained by this test, the acoustic pyrometer type with separate transmitters and receivers has a slightly better reconstruction accuracy when compared to the transceiver type acoustic pyrometer.

Table 10 Comparison of best mean reconstruction error (%) for each acoustic pyrometer type using RBF interpolation

Mean reconstruction error (%)
Acoustic pyrometer type

Temperature profile	Transmitter/receiver	Transceiver
Single peak	1.064	1.323
Steep single peak	3.29	3.523
Asymmetrical peak	0.573	1.516
Double asymmetrical peak	4.67	4.748

As shown above in Table 10, the greatest variation in accuracy is for the asymmetrical peak profile, where the transceiver type tended to merge the peak with the boundary wall. However, in general the discrepancy is not significant (<0.3%) especially since this test was not exhaustive of all possible combinations.

Reconstruction error comparison with previous work

Table 11 compares the best mean error results obtained for each temperature profile for this study with the results obtained by previous work done by Tootla[1]. Across all temperature profiles the reconstruction accuracy was improved by at least 1%, with the largest improvement being on the double asymmetrical peak and asymmetrical peak profile.

Table 11 Comparison of mean reconstruction error (%) for RBF interpolation between this study and previous work done by Tootla[1]

	Mean reconstruction error (%)	
Temperature profile	This study	Tootla (2016)
Single peak	1.064	2.32
Steep single peak	3.29	4.8
Asymmetrical peak	0.573	2.39
Double asymmetrical peak	4.67	7.08

These improvements are likely due to the addition of a variable shape factor for RBF interpolation, and improved transmitter, receiver and grid placement.

3.6 Supplementing acoustic pyrometry with radiation pyrometry

As briefly mentioned in 3.3.2, the Mathcad model was developed having the option of using radiation pyrometer readings with acoustic pyrometer readings to improve reconstruction accuracy. Acoustic pyrometry can map acoustic paths passing though the centre of the furnace, however unless many devices are used it is poor at determining temperature close to the wall of the furnace. Radiation pyrometry however does not reach the centre of the furnace but can determine temperature closer to the furnace wall.

Thus, the radiation pyrometer was implemented as an option to determine point temperature measurements near the wall. It was applied by adding the temperature measurements as data

points to the acoustic pyrometer temperature data points determined by least squares, after which the combined data set is interpolated. For the standard 4 set temperature profiles this addition was found to make results less affected by random path error but did not improve reconstruction accuracy when path error was low. However, for the flat top temperature distribution with a sharp temperature change there was potential for this method.

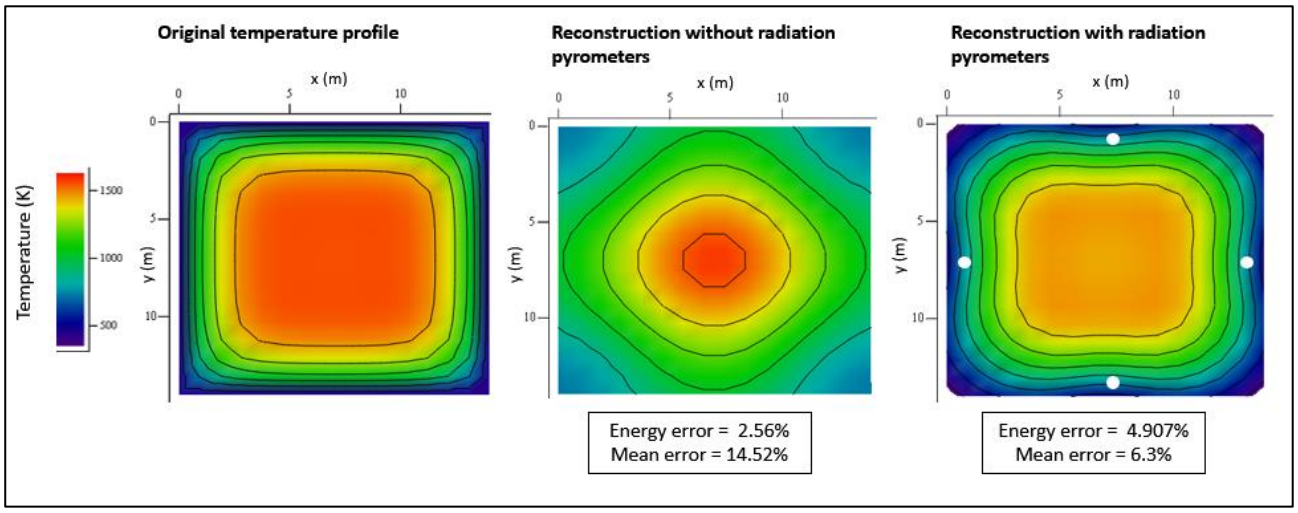

Figure 80 RBF Temperature reconstruction before and after adding radiation pyrometer readings

Sielschott et al.[38] identified that this temperature profile could only be reconstructed with regularisation methods and knowledge of the shape beforehand. However, in the condition where the profile is not known, radiation pyrometers could be used to determine the shape. This is shown in Figure 80, where 4 radiation pyrometers were added near the furnace walls to an equally spaced 24 path acoustic pyrometer setup.

Before the radiation pyrometer addition, the temperature profile shown in the middle was reconstructed with a much sharper peak, not visually resembling that of the original profile as shown on the left. While the energy error was at an acceptable 2.56%, the mean error of reconstruction was extremely high at 14.52%. However, once radiation pyrometers were added, as shown by the white dots on the right-side reconstruction, the resulting reconstruction showed a much greater resemblance to the original profile. While the mean error from the resulting reconstruction is still high at 6.3%, it is less than half of the former result.

While there may be some physical limitations to supplementing acoustic pyrometer readings with radiation pyrometry, such as a lack of furnace opening or observation ports, this does conceptually show that the use of the two methods together could be beneficial. In this case the radiation pyrometer readings were simply added to the data points already determined by the acoustic

pyrometer method, however improved integration of the two methods, such as working radiation pyrometer readings into the data point determination phase could further improve reconstruction accuracy.

3.7 Few acoustic paths

This section presents some possible acoustic pyrometer layouts that could be used for temperature reconstruction with few acoustic paths (less than 24), a situation that could arise due to financial constraints and observation port limitations. Previous tests were completed with a 4x4 grid; however, this section will present reconstruction using transmitter/receiver locations on a 2x2 grid.

Since it is required that $N_b \geq N_t$, for a 2x2 grid at least 4 acoustic paths are required. However, in practice this results in the scenario seen in Figure 81 where since there is only 2 data points in each direction, no shape of profile can be observed and for a symmetrical profile a flat result will be obtained. This profile may have a fairly accurate energy error of 0.151 %, but it gives us no indication of the temperature profile shape, for this case it was reconstructing the single peak profile.

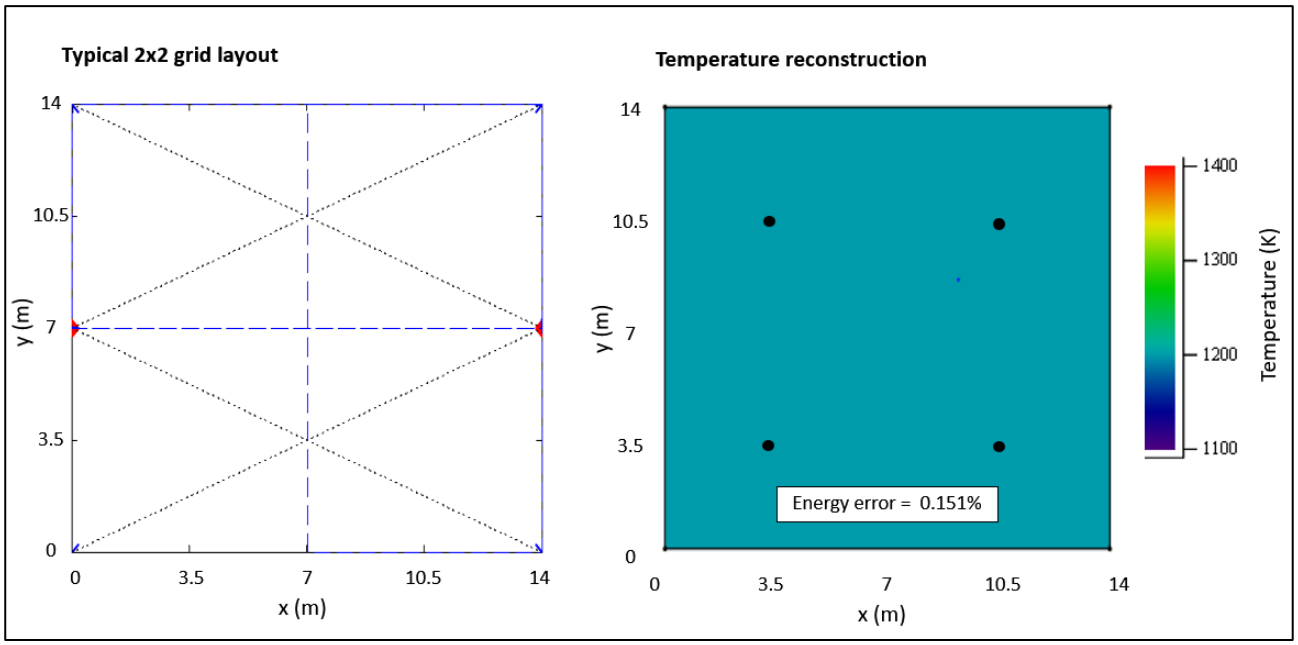

Figure 81 Reconstruction of single peak profile on 2x2 grid and 4 acoustic paths

With this number of acoustic paths, some assumptions need to be made about the temperature profile shape to get a reconstruction. As a result, an approach inspired by the bi-linear

approximation method as documented in 3.2.2 was taken. The code for this method can be found in Appendix A.

Each acoustic path is converted into an average path temperature, where the profile of that path is assumed and converted into 3 data points. The middle of the path (middle data point) is assumed to be higher than the start and end, by scaling it higher based on the standard deviation of temperatures for all paths and scaling the end points lower. The assumption here is that a higher deviation in temperature translates to a steeper temperature profile. These assumptions increase the amount of data to points such that the shape of the resulting profile can be estimated. These data points are then used for interpolation, in this example RBF interpolation is presented.

The data points resulting from this process can be seen in Figure 82, where a data point is added for the midpoint of each path and at the start and end of them. This setup results in 14 data points for 2 transmitters and 4 receivers (duplicate data points on the same position are averaged) and was used to test its reconstruction against the 4 set temperature profiles. The mean and energy reconstruction error were calculated as well as the least squares energy error determined before the bi-linear method is applied.

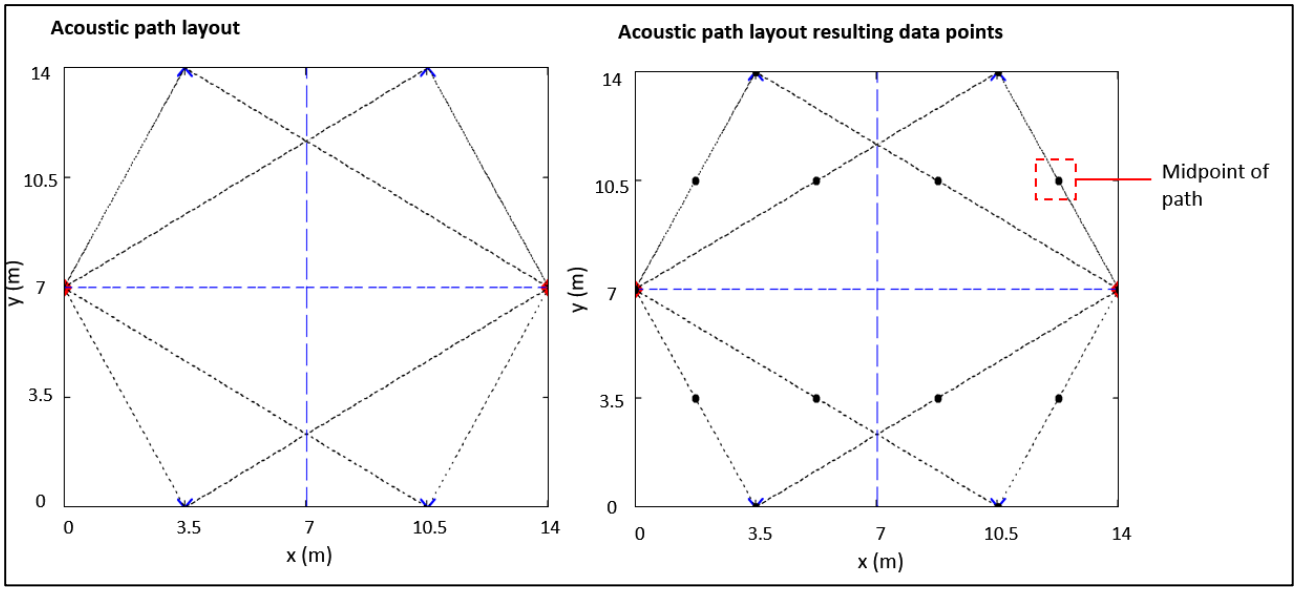

Figure 82 Acoustic path layout (left), Acoustic path layout with resulting data points (right)

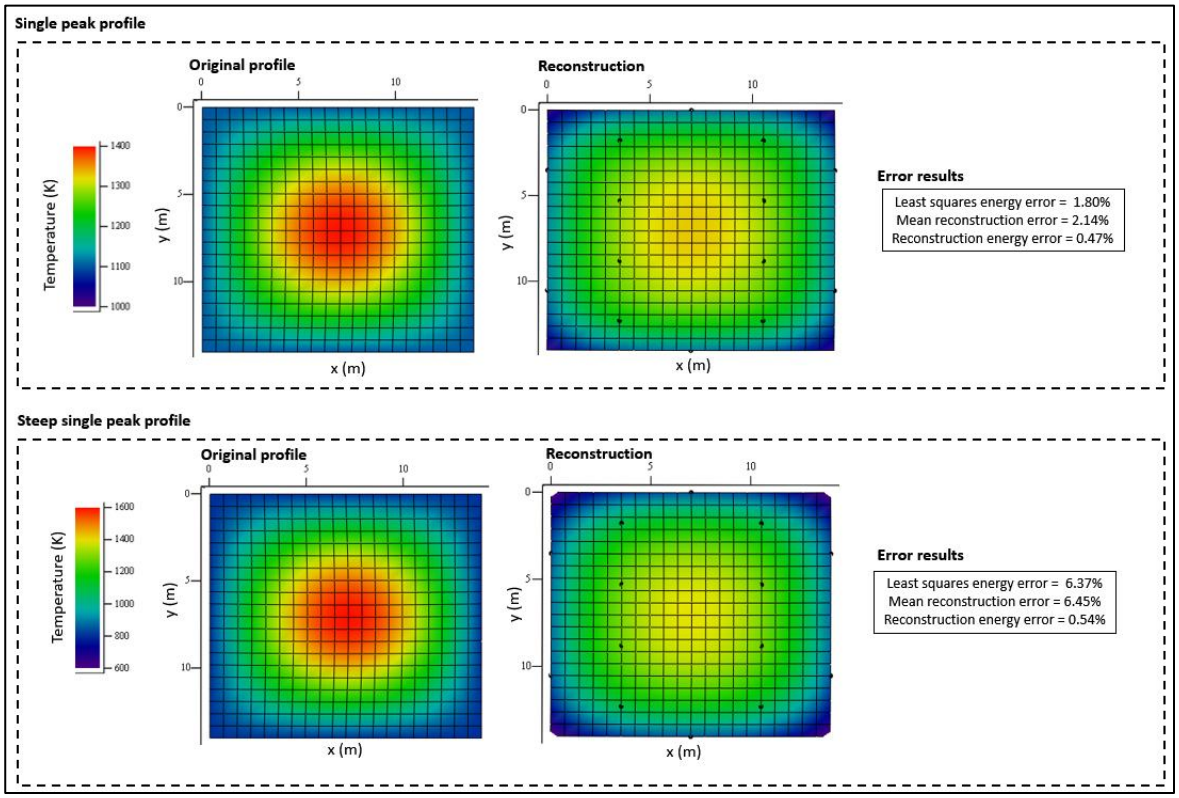

Figure 83 Reconstruction results for single peak and steep single peak profile using RBF interpolation

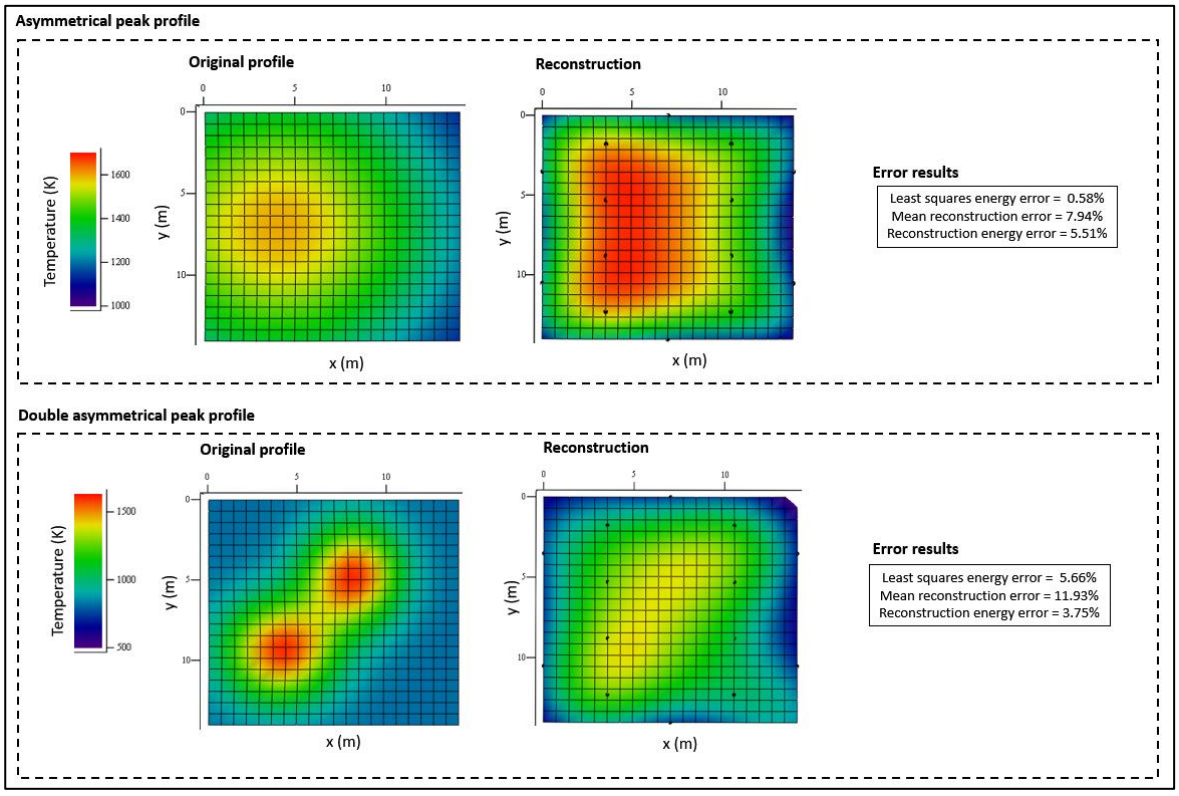

Figure 84 Reconstruction results for asymmetrical peak and double asymmetrical peak profile using RBF interpolation

As shown by Figure 83 and Figure 84, reconstructing a temperature profile with few paths is possible, but not very accurate. Visually we can tell the that there is 1 peak for the single peak profiles and roughly locate them, however the actual temperature of these peaks is inaccurate, and inaccuracy that increases with profile complexity as shown by the inability to reconstruct the double peak profile. Nevertheless, the least squares and reconstruction energy errors tend to be lower than the mean errors, indicating that even though the fit is poor, we can still obtain an estimate for the energy at the furnace region.

3.8 Summary of chapter

A literature review of temperature reconstruction methods applicable to acoustic pyrometry was conducted, identifying and comparing potential reconstruction methods for simulation. From these methods, a least squares approach with RBF interpolation was identified as the most promising method for temperature reconstruction. Thus, a Mathcad model was then developed based around this method.

The model was developed such that the reconstruction of defined temperature profiles could be simulated based on a variation of input conditions. Amongst these conditions is the ability to change acoustic transmitter and receiver locations, the dimensions of the rectangular furnace to be simulated, properties of the gas and accuracy of the acoustic measurement. Four main temperature profiles were considered, namely the single peak, steep single peak, asymmetrical peak and double peak profiles.

Temperature data points were calculated using a Moores-Penrose method to find the least squares solution using the calculated geometric matrices, simulated time of flights and gas properties. After the temperature data point determination, multiple interpolation methods were applied. Most notably an improved RBF interpolation method was used applying Rippa's algorithm for shape factor prediction. As a basis of comparison, cubic spline interpolation, multiple regression and Lagrange interpolation were also applied. The accuracy of these reconstructions was then appraised based on mean, RMS and energy error calculations.

Testing was then conducted to determine the effect of random path error on temperature reconstruction, over a range of 0-2 % path error in increments of 0.5 %. The methodology was devised such that each set temperature profile was systematically tested for each increment of path

noise and acoustic pyrometer type using 100 iterations of TOF simulation for each test. These tests were then repeated up to 4 times.

2nd order regression was identified as the most noise resistant reconstruction method, in many cases surpassing RBF interpolation when 0.5-1 % of path noise was added. However, for 24 acoustic paths this method was not adequately able to reconstruct more complex temperature profiles or profiles that had a greater temperature gradient. In this regard RBF was the most accurate reconstruction method. Conversely, cubic spline and Lagrange methods were greatly affected by random path error and were unsuitable in this regard.

A method for reconstruction in high noise scenarios (interpreted as higher path error) was suggested. It was found that repeating TOF readings produced a significant improvement in reconstruction accuracy for all methods (excluding regression) and proved to be a practical way to mitigate random path error. The optimum amount of repetitions was 2, where RBF interpolation produced the most accurate results having a reconstruction error of 2.9 %, 5.6 %, 2.9 % and 5.45 % for the single peak, steep single peak, asymmetrical peak and double asymmetrical peak profiles respectively with 1% random path noise.

Moreover, it was shown that transmitter/receiver or transceiver locations and grid position had a significant effect on the resulting reconstruction accuracy. Consequently, tests were performed with a trial and error method to identify transmitter/receiver, transceiver and grid position trends that produced the more accurate reconstructions for each temperature profile using 24 acoustic paths.

Namely symmetric acoustic path layouts and grid were found to be preferable where acoustic paths where adequately spread over the whole furnace area. Non-symmetric layouts resulted in the final reconstruction being distorted or spread. In addition to this, layouts that had receivers or transceivers closer to the walls and their grid placement to also be closer to these walls were preferable and resulted in more accurate reconstructions. This occurred since an emphasis was placed on obtaining more accurate data points at a region that exhibited the most significant temperature change and resulting in a smaller region of extrapolation, where errors tended to be higher.

The separate transmitter/receiver type acoustic pyrometer was shown to produce marginally more accurate reconstructions than the transceiver type acoustic pyrometer. However, transceiver type acoustic pyrometers have the advantage of reducing path error by eliminating contributions of planar flue gas velocity.

Acoustic path requirements were determined based on intended use. It was concluded that 24 acoustic paths are adequate for temperature reconstruction fit, being able to identify temperature peaks, their position and determine the overall energy at this region. The minimum number of acoustic paths for simple reconstruction (1 peak, minimal placement) is 4, which also gives an adequate indication of energy at this region but does not provide an accurate reconstruction fit. For one acoustic path an estimation of path error can be determined, however this provides no indication of the profile at this region.

The addition of radiation pyrometer readings to acoustic pyrometer readings was shown to be a promising solution to reconstructing temperature profiles that have a very steep temperature change near the edges and a relatively flat midsection. A vast improvement was shown when included with the RBF interpolation methods.

4. Time of flight determination

This chapter will focus on methods used to determine the time of flight (TOF) for acoustic pyrometry. It will discuss literature on noise and attenuation in the boiler; review TOF signal processing methods, present the experimental testing of this study and a discussion of the results.

4.1 Furnace noise and attenuation

The accuracy of acoustic wave time of flight (TOF) readings are largely dependent on the ability to precisely locate the source (transmitter) signal within the received signal and thus determine the TOF of the acoustic wave. However most industrial scale boilers are subject to strong noise and due to temperature gradients in the particle laden flue gas, acoustic signals are significantly attenuated (where attenuation is the weakening of the signal over distance). The presence of this noise severely affects the reliability of TOF readings and therefore must be considered to employ the correct signal processing techniques and overcome noise when determining the TOF.

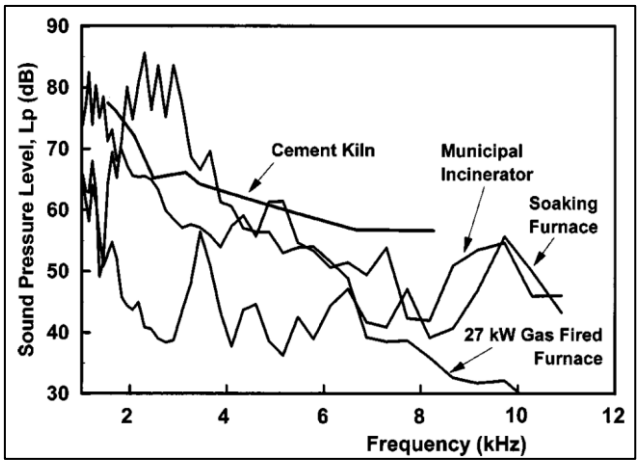

Figure 85 Typical Frequency (kHz) vs Sound Pressure Level (dB) of noise for industrial applications[44]

Numerous studies have measured and categorised the noise in boiler furnaces, one such study done by Tian et al.[45] found the background noise in the furnace of a domestic power plant to be centred at a low frequency of 200-1000 Hz with a total sound pressure of 110-120 dB which increased with boiler load and fuel consumption. This noise was shown to have a symmetrical and Gaussian-like distribution which was attributed to furnace combustion noise, jet burner noise and other mechanical noise. This mechanical noise is created by rotating equipment such as mills or fans and resonant frequencies inside boiler pipework.

While experimental results showed more severe attenuation at higher frequencies, an acoustic range from 500-3000 Hz was shown to be optimum for extraction and processing of the acoustic signal to reduce attenuation[45]. This range is not strictly agreed upon and dependent on the noise and attenuation characteristics of the furnace. However, many sources report a similar operating range, avoiding higher frequency components. A spectrum range of 100-3000 Hz is suggested in [46] and [47], 500 – 3500 Hz is shown in [48] and in [37] the power of the received signals were found to be predominantly located in the 500-3000 Hz range.

However, if Figure 85 is considered, showing the typical frequency components of noise for industrial applications as presented by Ewan and Ireland[44], it is noticeable that for most applications the highest noise levels are below 4000 Hz which overlaps with the acoustic pyrometry range. In addition to this, it was noted that the use of the oil gun and soot blower significantly increased the noise level, where Ceserani et al.[48] measured a 10-20 dB increase in background noise during sootblower operation at a frequency range of 500-4000 Hz.

It is for these reasons that ultrasonic thermometry (>20 000 Hz) is generally not suitable for the furnace environment. When signals in the ultrasonic range are used they have not been able to produce sound at the required intensity to compensate for the severe attenuation and reflection in hot combustion gases. This is especially evident when there is an acoustic impedance mismatch between mediums (for example from air to a combustion gas)[49].

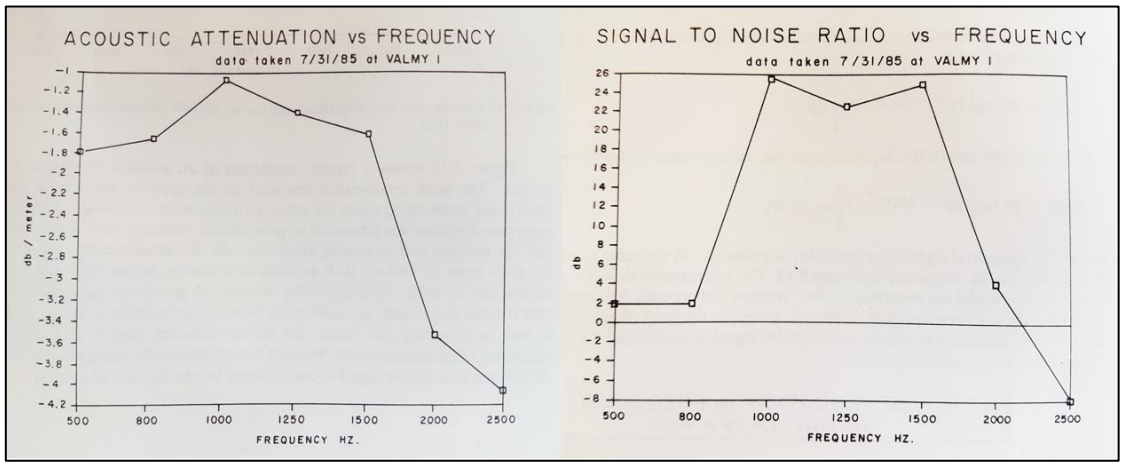

Figure 86 Acoustic attenuation (dB/m) vs frequency (Hz)[left] and Signal-to-Noise Ratio (dB) vs frequency (Hz)[right] inside a 250 MW pulverised coal-fired boiler[19]

Kleppe et al.[19] attempted to determine a suitable range for acoustic pyrometer by taking readings on a 250 megawatt (MW) pulverised coal-fired utility boiler. Their data is shown graphically in Figure

86 where the graph on the left shows acoustic attenuation vs frequency and the right shows the signal to noise ratio vs frequency.

Attenuation is expressed here as the Decibel loss per metre, with the greatest drop occurring after 1500 Hz. Data above 2500 Hz is not shown but it is stated that attenuation increases further thereafter. Nevertheless, displaying attenuation in this manner is misleading because it suggests that the attenuation has a linear relationship with distance. Thus, the relationship was also displayed in terms of the SNR ratio as shown on the right-hand side of Figure 86. This suggests that the optimum acoustic frequency range to avoid attenuation is between 500 – 2000 Hz for the tested utility boiler. While this does give an indication of the attenuation levels at varying frequencies, it should be ne noted that attenuation in boilers with varying widths could vary greatly due to high temperature gradients and velocity scattering of the acoustic wave[19]. Thus, it is suggested that measurements should be taken on the furnace of interest to characterise the noise content and attenuation present in the boiler of interest.

4.2 Signal processing methods

This section discusses and reviews the different signal processing methods that have been applied to determine the time of flight of an acoustic wave and thus the average temperature along the path. Since the boiler furnace can be an environment permeated with noise, signal processing is essential to determine reliable and accurate readings. According to equation (6) the temperature estimate is dependent on the square of the TOF reading, and thus minimising potential time of flight errors is crucial for determining an accurate temperature reading.

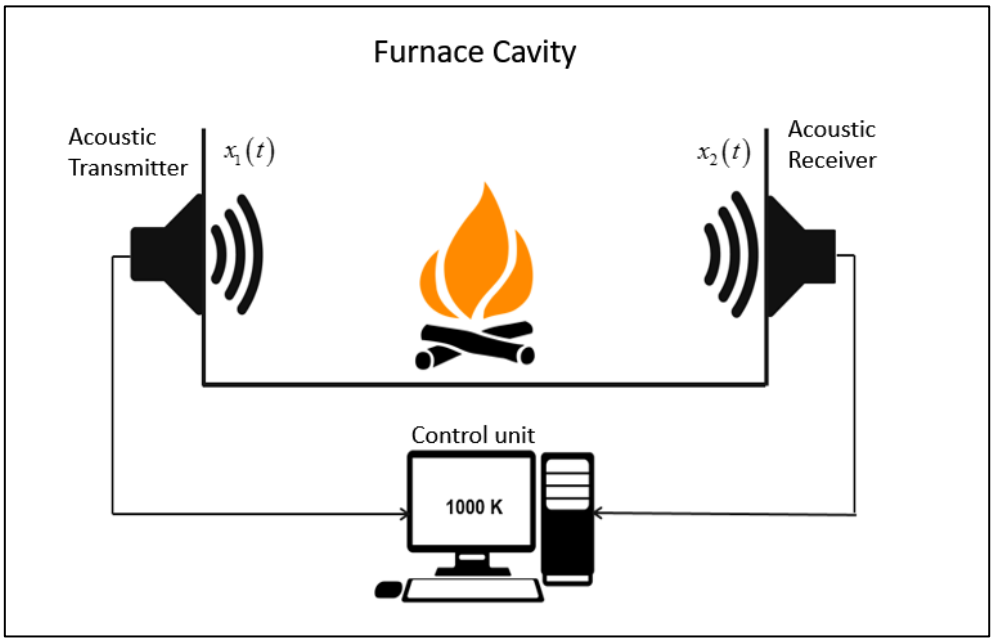

Figure 87 Generic acoustic Pyrometer set-up

The generic set-up for acoustic pyrometry is as shown in Figure 87, where the acoustic generator/transmitter is located on one side of the furnace cavity and transmits a signal $x_1(t)$ which is then received and recorded on the opposite side as $x_2(t)$. The received signals by these spatially separated receivers are generally modelled having a component of the source signal $s(t)$ and boiler noises $n_1(t)$ and $n_2(t)$, where the signal on the receiver side is an attenuated and delayed version on the transmitter side signal.

$$x_1(t) = s(t) + n_1(t) \tag{95}$$

$$x_2(t) = \alpha s(t+d) + n_2(t) \tag{96}$$

The attenuation factor is represented by α and the aim is then to remove the components of noise and determine the time of flight (or delay) represented by d.

4.2.1 Threshold/edge detection

The first and most intuitive approach for determining the time of flight is threshold or edge detection. In low noise conditions, the application is simple and consists of setting an amplitude threshold level and then determining the threshold time at which the amplitude of the received signal exceeds this threshold level on either side of the furnace. The process applied to one of these signals is shown in Figure 88 which is a high intensity signal recorded right after its generation. The threshold level is set just above the amplitude level of ambient noise and the intersection between the threshold and signal is clear. If this method is applied to both signals, the time of flight can simply be determined by the difference between these two threshold times.

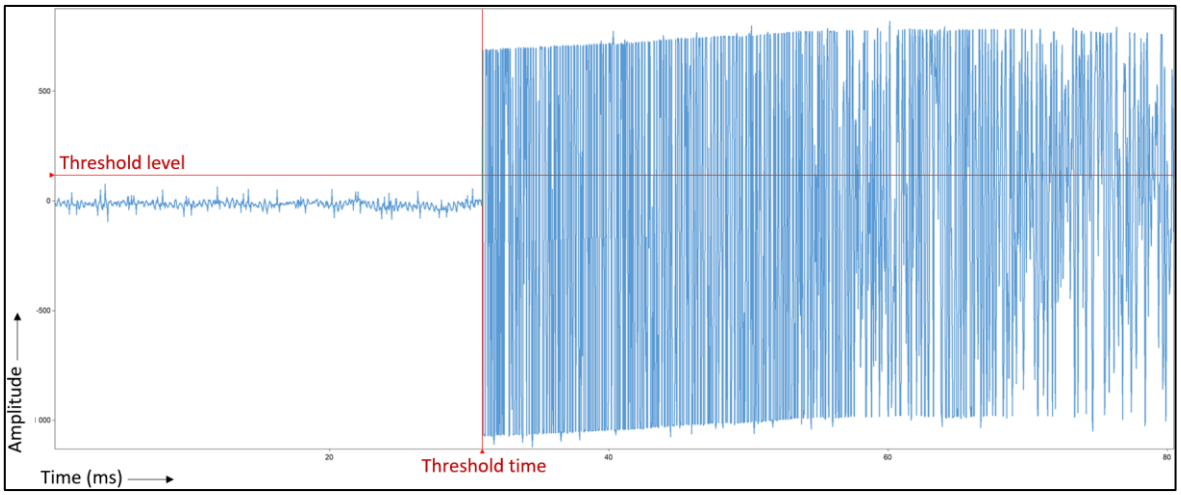

Figure 88 Sound wave with high SNR and sharp rising time exceeding a threshold level[1]

When this method was initially implemented by Green the threshold detection was done manually, using an oscilloscope and visual inspection[31]. However, more modern methods can do this automatically and tend to be more useful for continuous and automated monitoring.

The greatest limitation of this method is that it requires a high signal to noise ratio to distinguish the signal within the noise. Consequently, it is more suitable for use with high intensity sound sources that provide a shockwave front that has a distinct and sharp rising time[19]. However in many boilers the noise level is too high with sound pressure levels (SPL) of 110-120 dB, which approaches the SPL of some modern acoustic pyrometers before attenuation[45], [47].

As a result, once the signal is attenuated and received on the opposite end of the boiler it is often indistinguishable from the boiler noise. An example of this is shown Figure 89, where the received signal is the attenuated signal shown in Figure 88 when received on the opposite end of the boiler. Here there is no clear threshold level that could be set to locate the desired signal within the noise. Thus, to use the threshold method to determine time of flight the received signal must be filtered to extract the desired signal from the noise.

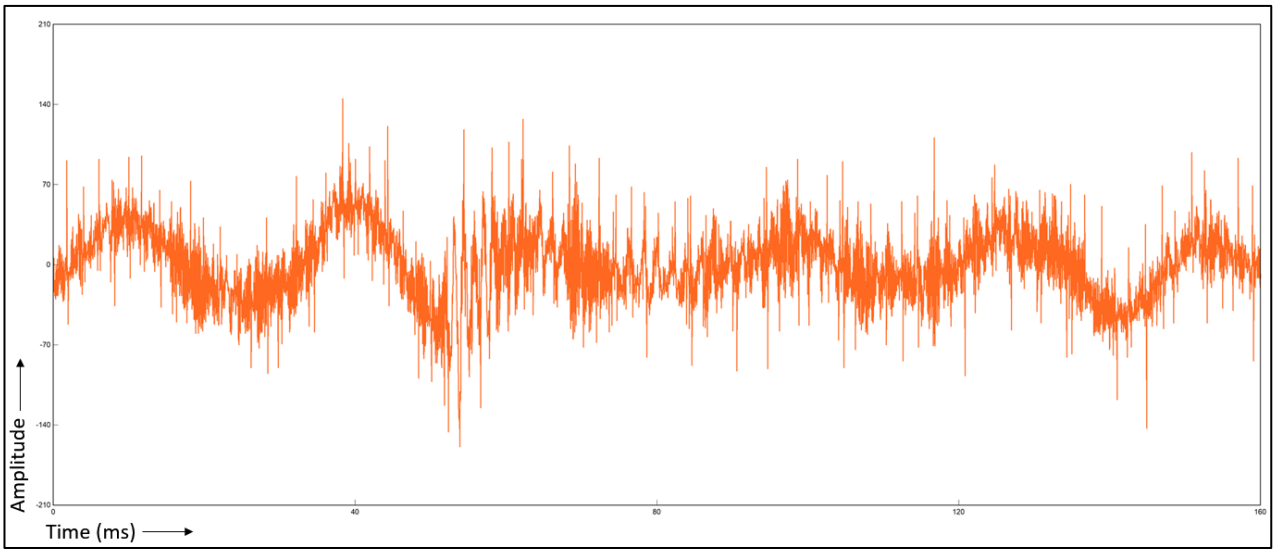

Figure 89 Received signal immersed in noise[1]

A threshold method using filtering was explored by Tootla when he sought to use a commercial acoustic pyrometer that creates a loud (170 dB) wide band shock wave signal to measure furnace exit temperature. Since the filtering method used by the acoustic pyrometer was proprietary and not well documented, he developed and demonstrated an ad-hoc technique based on a threshold method and found that the method produced results comparable to those produced by the proprietary software[1].

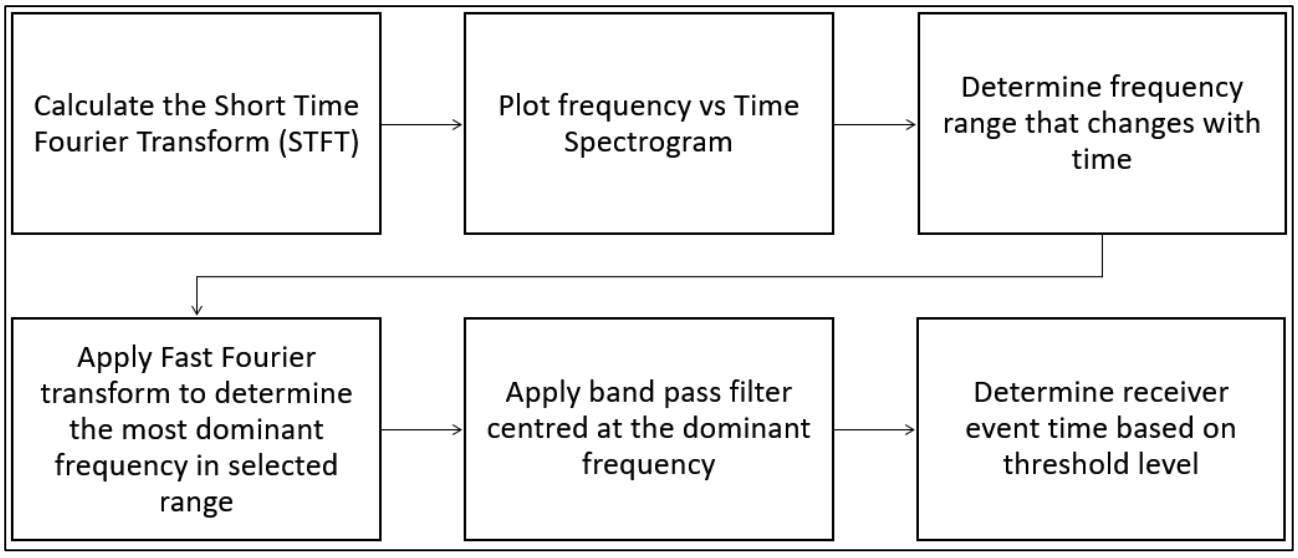

Figure 90 Ad-hoc threshold based algorithm[1]

The ad-hoc algorithm developed is summarised above in Figure 90. Since the signal recorded on the receiver end was not distinguishable in the time domain, the first steps of the algorithm involve

converting the signal to the frequency domain (an example of the received signal is shown in Figure 89). However, just doing this for the signal is not sufficient since it is likely that frequency components associated with the noise will be more powerful than that of the signal. As a result, a Short-Time Fourier transform(STFT) is used to convert the signal into the frequency domain and then plot the changes in frequency over time on a spectrogram.

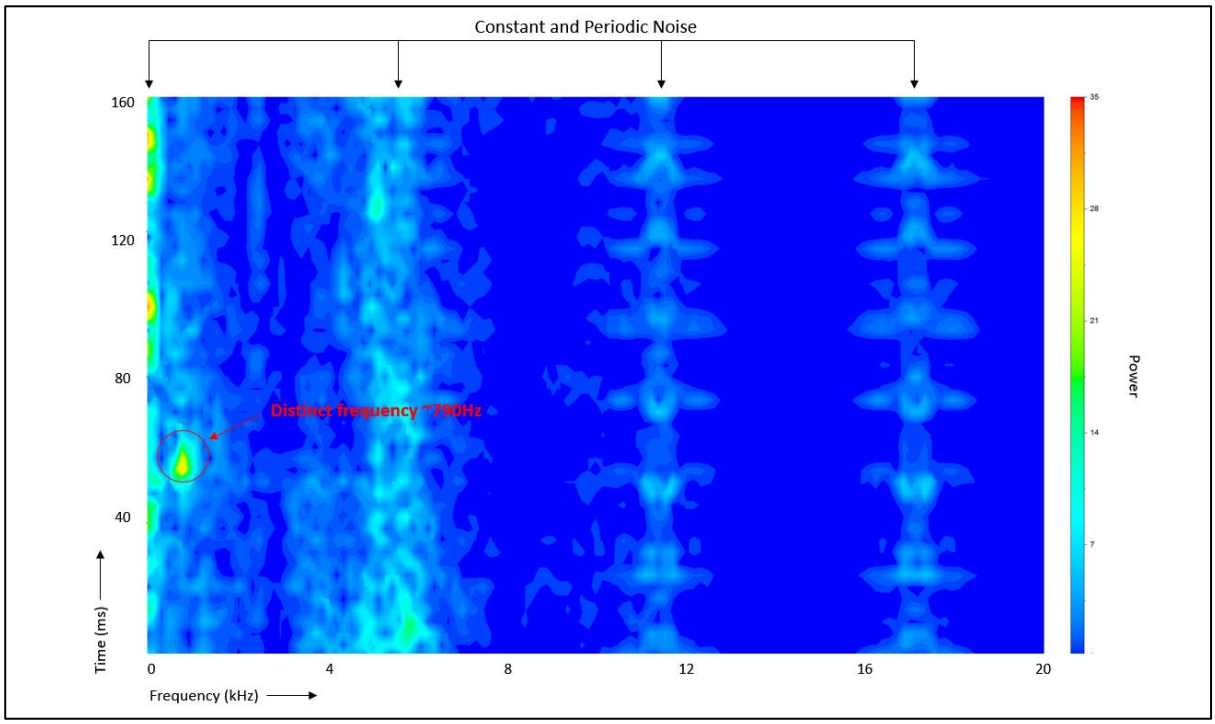

Figure 91 Spectrogram of received signal

By doing a time and frequency analysis, it is possible to distinguish between frequency components that are always present and those that change with time. The vertical lines in Figure 91 represent frequency components that always have power and are therefore associated with being periodic noise, however at around 50 ms and around 790 Hz there is a distinct peak in power that only occurs once and is presumed to belong to the desired signal. Once this frequency range is determined a fast Fourier transform can be applied to the signal and the most dominant frequency in the desired range is determined. A band pass filter is then designed around this frequency to filter out the noise followed by rectifying the signal.

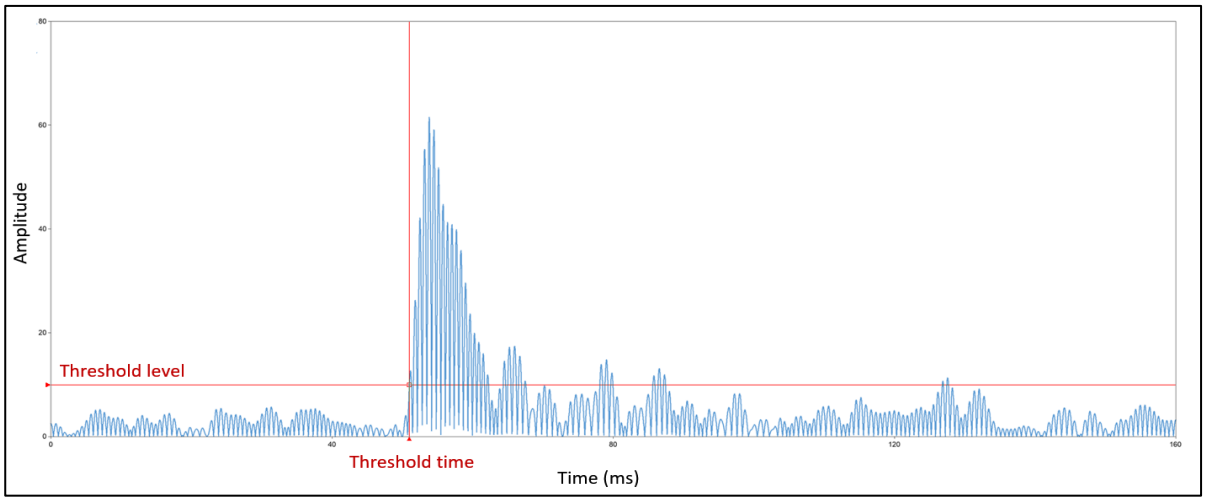

Figure 92 Filtered and rectified signal

The result of this is shown in Figure 92, where the desired signal is extracted, and the receiver event time can be clearly determined using a threshold method. The difference between the event times on the generator and receiver sides can then be used to determine the time of flight, demonstrating that with adequate filtering the threshold method could be used in high noise scenarios as present in the boiler.

Nevertheless, it might not be practical to always consider a time frequency analysis of the received signal and change filter characteristics when there are variations in the signal. In an alternative method Cesarano et al.[48] used a band pass filter that was rather defined based on a power frequency analysis on the generator side signal. Where the centre excitation frequency of the signal could be used to automatically update a band pass filter for use on the receiver side. While this method was developed for use with chirp sound signal sources and a cross-correlation method, the same principle could be implemented into a threshold based approach.

4.2.2 Cross-correlation

An alternate and popular technique for determining the time of flight is cross-correlation. The method effectively determines the similarity or dependence of one signal to another by searching for features that are common between them. Having a wide variety of applications, it has been applied to acoustic pyrometry[12], [19] , ultrasonic thermometry [50], speech recognition[51] and even radar systems[52].

For the application of acoustic pyrometry, the goal is to determine the position of the transmitted signal contained in $x_1(t)$ relative to the delayed signal contaminated with noise at $x_2(t)$.

Mathematically the cross-correlation $R_{x_1x_2}(\tau)$ is defined as the expectation E of signals $x_1(t)$ and $x_2(t)$ as shown in equation (97) which can be estimated by equation (98), where τ is the time lag.

$$R_{x_1x_2}(\tau) = E[x_1(t)\,x_2(t-\tau)] \tag{97}$$

$$R_{x_1x_2}(\tau) = \frac{1}{T}\int_{o}^{T} x_1(t)\,x_2(t-\tau)dt \tag{98}$$

This can be considered as a sliding dot product where the time lag value τ is varied and the resulting value associated with the peak in the correlation function will then represent the time delay between the signals. An example of this can be seen in Figure 93, where two delayed signals can be on the left and the cross-correlation with a distinct peak at one second is shown on the right.

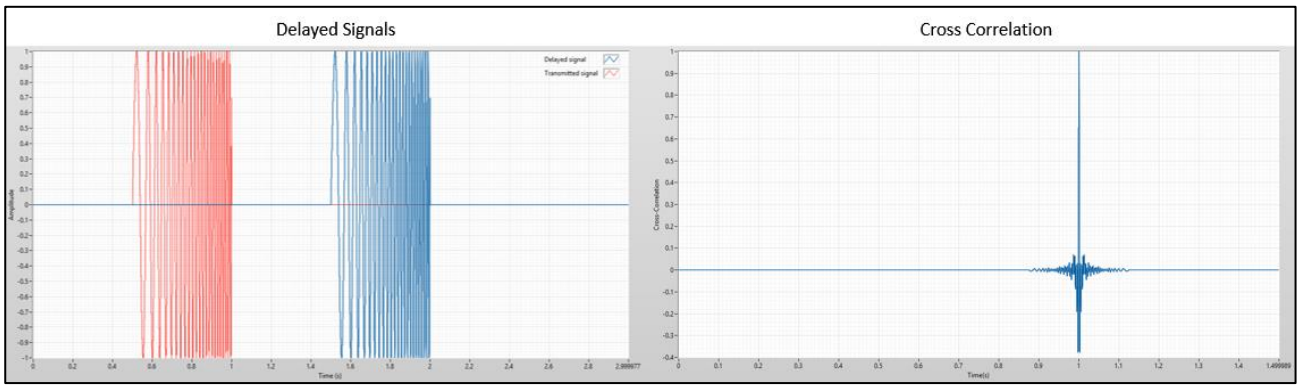

Figure 93 Cross-Correlation of chirp signals with distinct correlation peak

The method is most useful when non-periodic signals are used, such as the time varying chirp used in the example above. When periodic signals are used, the correlation peak is widened and tends to oscillate around the maximum values making it difficult to determine a precise time lag.

The basic cross-correlation method works in an ideal scenario, however it does have its limitations when applied to the real world scenario, for example, in a noise free enclosure this method suffers from reverberations and in a high noise scenario, peak detection becomes difficult[22]. As a result, the generalised cross-correlation method was introduced to improve on some of these weaknesses.

4.2.3 Generalised cross-correlation

The most widely used framework for time delay estimation is the generalised cross-correlation (GCC) or generalised correlation method[53], originally proposed by Knapp and Carter[54]. The GCC algorithm improves the basic cross-correlation algorithm by introducing a general framework that unifies various correlation based algorithms[55]. It achieves this by introducing pre-filters or whitening before cross-correlation with the purpose of accentuating frequencies that belong to the signal and suppressing frequencies that are produced by noise. These filtered signals are then passed through a correlator and the time of flight will be denoted by the time value associated with the peak of the result.

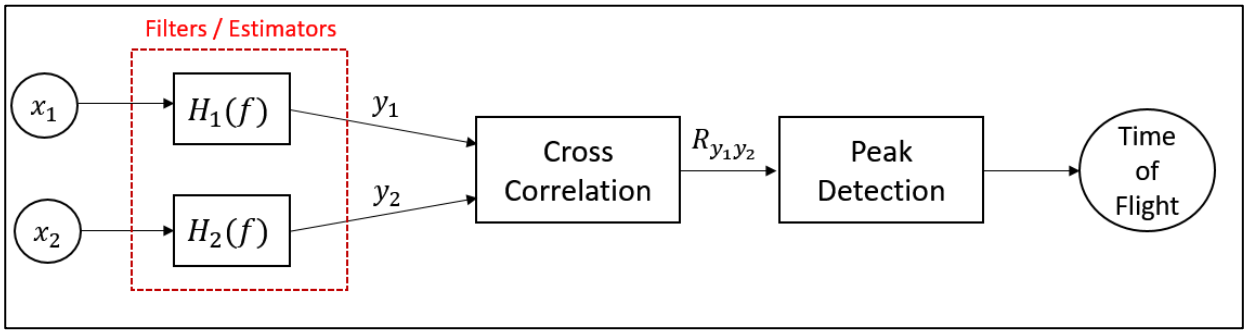

Figure 94 Filters in GCC framework for time of flight measurement

The location of these filters are shown generally in Figure 94, where $x_1(t)$ and $x_2(t)$ represent spatially separated acoustic signals, where $H_1(f)$ and $H_2(f)$ are the filters. Mathematically, the method is defined in the frequency domain using the cross power spectral density. This is possible by means of the Fourier transform as shown in equation (99), since it is known that the integration of the cross power spectral density is equivalent to cross-correlation $R_{x_1x_2}(\tau)$ in the time domain.

$$R_{x_1x_2}(\tau) = \int_{-\infty}^{\infty} G_{x_1x_2}(f) e^{j2\pi ft} df \tag{99}$$

When the inputs are filtered the output cross power spectrum is represented by equation (100)

$$G_{y_1y_2}(f) = H_1(f) H_2^*(f) G_{x_1x_2}(f) \tag{100}$$

The product of $H_1(f)$ and the complex conjugate of $H_2(f)$ can then be replaced by a more convenient frequency weighting of ψ_g.

$$\psi_g(f) = H_1(f) H_2^*(f) \tag{101}$$

Thus, the generalised correlation can be defined by equation (102), where the time value associated with the peak of the result will represent the time of flight.

$$R_{y_1y_2}^{(g)}(\tau) = \int_{-\infty}^{\infty} \psi_g(f) G_{x_1x_2}(f) e^{j2\pi ft} df \tag{102}$$

This framework allows for several processors or generalisations of cross-correlation that each have distinct weighting functions. While many, weightings can fall into this framework, the ones most applicable to time delay estimation and acoustic pyrometry will be discussed.

Phase transform (PHAT)

The most widely used weighting for time delay estimation is the phase transform(PHAT) weighting. It has gained popularity due to the fact that its effective at suppressing reverberant signals, which proves to be an issue in most applications[53], [56]. In addition to this, it is relatively easy to implement and performs more consistently than many other GCC weightings when the characteristics of the sound source change over time, making it applicable to a wide variety of applications[55]. The weighting, as shown in equation (103), is executed by dividing by the magnitude of the cross spectrum. It does suffer from the flaw that errors are accentuated in frequency regions where the signal power is the lowest, since the denominator will approach zero in these regions[57], making it sub-optimal under ideal conditions. However, overall the PHAT method is considered to be robust in nosier and thus more realistic environments[58].

$$\psi_{PHAT}(f) = \frac{1}{\left|G_{x_1x_2}(f)\right|} \tag{103}$$

In the context of acoustic pyrometry, the GCC method has been successfully applied by Zhang et al.[37] for furnace exit temperature measurement on a 600 MW coal-fired boiler. Specifically, the phase transform (PHAT) weighting was used to determine the distance of the acoustic paths while the boiler was in a cold state and the maximum likelihood (ML) weighting for continuous time of flight acquisition in the hot state.

Roth

Another weighting function falling into this family is the Roth weighting, which is also referred to as the impulse response method. Unlike the PHAT method, instead of dividing by the cross spectrum it considers the autocorrelation of the input signal, as shown in equation (104). By normalising by

$G_{x_1x_1}$ and taking the shape of the input spectrum into account, the deterministic error in the measurement is eliminated, provided that $x_1(t)$ and $x_2(t)$ are recorded at the same time[59].

$$\psi_{ROTH}(f) = \frac{1}{G_{x_1x_1}(f)} \tag{104}$$

In comparison to other GCC weightings, the Roth weighting suppresses wide noise bands and frequency ranges where noise is loud[60], but will broaden the peak of the correlation function. Furthermore, it has the advantage over conventional cross-correlation that when used to measure time delay in scenarios that have multiple acoustic paths and only one correct time delay, cross-correlation is at risk of returning the incorrect time delay while the Roth weighting is more likely to produce the correct result[59]. This feature is especially relevant to acoustic pyrometry where multiple paths are advantageous and due to the reflection and refraction of sound waves this scenario could easily occur.

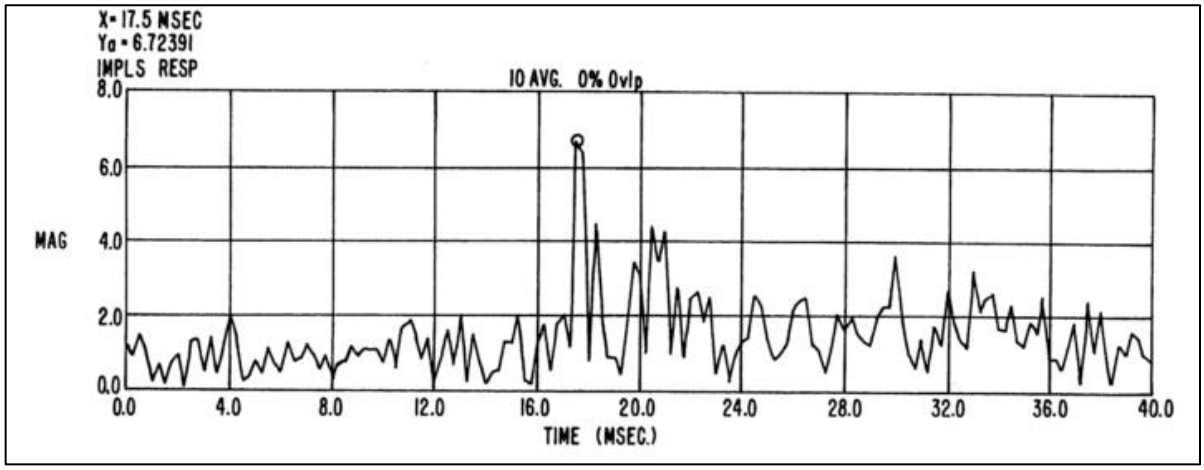

Figure 95 Roth GCC/Impulse response obtained from a 265 MW utility boiler[61], [62]

The Roth method (referred to as the "impulse response" method) has also been detailed as the time of flight acquisition technique in two patents, namely for a "self-purging pneumatic acoustic generator" and a "method and apparatus for measuring acoustic wave velocity using impulse response". Both patents were filed by Kleppe and Scientific Engineering Instruments(SEI), the company that produces the Boilerwatch® MMP II-SSX acoustic pyrometer. The pneumatic generator produces random continuous sound within a large band (100-3000 Hz) and for this type of signal generation the impulse response method is cited as advantageous since it pre-whitens the inputs and improves the definition of individual paths, which is necessary for multipath readings. An

example of the results when applying this method on a 265 MW utility boiler is shown in Figure 95, where the time of flight is represented by the peak of the impulse response[61][62].

Smoothed coherence transform (SCOT)

The smoothed coherence transform (SCOT) is essentially the inverse Fourier transform of the complex coherence function. It is particularly effective at measuring time delay between weak broad band correlated noises[63], [64].

The coherence function is defined as the cross spectrum divided by the square root of the auto spectrum of each channel, as shown in equation (105). Therefore, if you consider equation (106) as the weighting function for use in the GCC equation (102), the result will be the inverse Fourier transform of the coherence function.

$$\gamma(f) = \frac{G_{x_1x_2}(f)}{\sqrt{G_{x_1x_1}(f)G_{x_2x_2}(f)}} \tag{105}$$

$$\psi_{SCOT}(f) = \frac{1}{\sqrt{G_{x_1x_1}(f)G_{x_2x_2}(f)}} \tag{106}$$

It can be considered as an extension of the Roth processor where instead of just including the autocorrelation of the input it considers the impact of both channels and thus broadens the peak of the cross-correlation function. If the noises on both channels are correlated it approaches the Roth function[65], this can be seen mathematically from equation (106).

The SCOT method has been applied to acoustic pyrometry for time delay estimation as documented by Kleppe in[66], and has been further implemented to measure time of flight, and thus temperature, for the outlet gas of turbines[67].

Maximum Likelihood (ML) or Hannon-Thompson (HT)

Another popular processor is the maximum likelihood(ML) or Hannan-Thompson(HT) processor. From a statistical point of view it is the most optimum weighting under the conditions of ideal propagation[56]. The weighting as shown in equation (107) is a function of the cross power spectrum and the magnitude squared coherence defined in equation (108).

$$\psi_{ML}(f) = \frac{|\gamma_{12}(f)|^2}{|G_{x_1x_2}(f)|\left[1-|\gamma_{12}(f)|^2\right]} \tag{107}$$

The magnitude squared coherence will lie between a value of 0 and 1, which will give a normalised indication of the causal relationship between the input and output signals. From this we can interpret to what extent the frequency components present in the output are related to the input[59]. The ML processor will thus give greater weighting to frequency bands where there is unity coherence between the input and output and suppress frequency bands with near zero coherence.

$$|\gamma_{x_1x_2}(f)|^2 = \frac{|G_{x_1x_2}(f)|^2}{G_{x_1x_1}(f)G_{x_2x_2}(f)} \tag{108}$$

Since the weighting is dependent on the magnitude squared coherence, power spectrums must be known a priori or well estimated, otherwise performance is suboptimal[55]. Coherence estimation can be a problem for non-stationary signals.However when spectrums can be well estimated and signals are stationary this weighting is efficient and has strong noise suppression[58].

In the context of acoustic pyrometry, the signal and noise spectra should be well estimated, provided that the noise is relatively periodic. Zhang et al.[37] successfully applied the method for furnace exit temperature measurement on a 600 MW coal-fired boiler with high noise content (115-119 dB). Time delay estimation was achieved with multiple acoustic paths(24 in total) using a linear chirp sound source[37].

4.3 Experimental design

This section describes the approach taken to the design and construction of the experimental setup used for time of flight determination, the development of the control and signal processing model and the methodologies applied to time of flight determination.

4.3.1 Hardware determination

The development of the experimental set-up is in accordance with achieving the third objective of this study, which is to demonstrate TOF determination with its associated signal processing. This objective falls under the broader goal of identifying significant factors that affect TOF determination, in order to inform the application of an acoustic pyrometer system to boiler furnaces. Since noise is

the greatest limitation to determining the TOF, this goal is achieved by comparing the performance of several signal processing methods under various noise conditions.

The design priority of this system is consequently to create a set-up is that is versatile, such that distinct types of signal, noise and signal processing methods can be applied and compared. The emphasis is therefore not on temperature measurement itself but rather on time of flight determination and as a result, the set-up will not attempt to replicate the temperature and fluid conditions of the boiler. The advantage of this approach is that it allows us to test multiple signal processing methods in a low cost, and controlled environment void of the restraints that would normally be associated with testing on the plant.

A generic experimental setup for TOF determination would at minimum require the selection of basic components as shown in Figure 96.

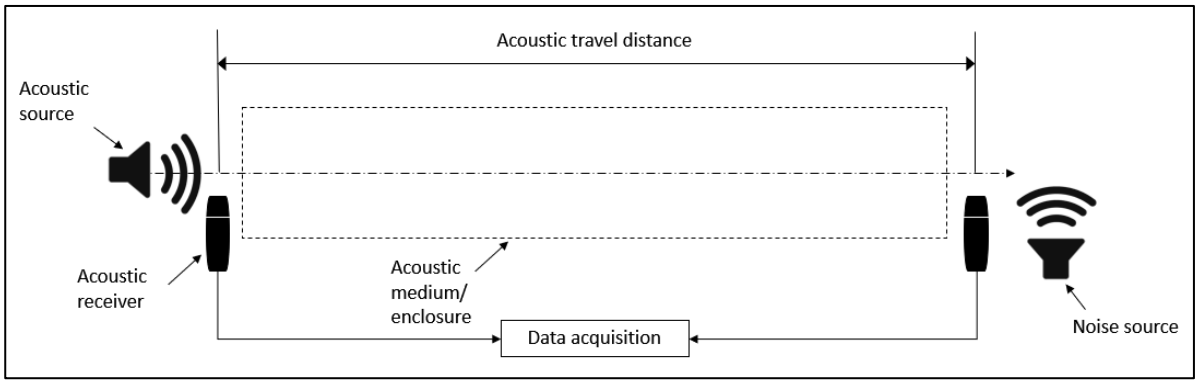

Figure 96 Generic components required for TOF determination

An acoustic source would be required to produce the signal and acoustic receivers would be required to record the acoustic signal produced. These receivers would need to be placed on either side of an acoustic medium or enclosure within which the TOF will be determined and an appropriate data acquisition device will be necessary to record these signals for processing. In addition to this another acoustic source will be required to produce the interference noise hindering the TOF determination.

Acoustic source selection

The first step taken in the design approach was to review the signal processing methods components and software applied to TOF determination. During the literature review, both threshold detection (edge detection) and cross-correlation methods were identified as viable signal processing methods for TOF determination.

While, generally speaking, the recording requirements of these methods are the same, there are differing requirements for the sound source. Threshold detection generally requires either a signal that is much louder than the noise having a sharp rise or a signal at a distinct frequency, while cross-correlation necessitates a distinct time-varying signal.

In conventional acoustic pyrometry, pneumatic sound sources tailored to the signal processing requirements of the device are used. However, these devices are since these tests are not carried out under boiler conditions the high amplitude levels produced by and complexity associated with pneumatic transducers are not required. As a result, an electroacoustic transducer (loudspeaker) was selected as the acoustic source, since it has the versatility to reproduce both types of signals, allowed for the control of the signal amplitude and was relatively cost effective. In addition to this, the same type of transducer could be used to create the interference noise signal.

Generally, when loudspeakers are used as acoustic sources to create a full frequency response, a combination of low, medium and high range transducers are used. However, in the case of acoustic pyrometry the practical operating range is roughly 500-3500 Hz and as a result, mid-range 8-inch drivers were selected as the acoustic and noise sources. These drivers, as shown on the left of Figure 97, have an operating frequency range of 55-8000 Hz and a peak sound intensity of 93 dB (which is more than required for the testing scenarios).

Figure 97 (left) Mounted acoustic source (right) line amplifiers for signal and noise speakers

To provide power to the speakers, some form of amplification is required. It was found that it was more cost effective to use a single 30 W line amplifier for each acoustic source than a single stereo amplifier. This setup allowed for the independent control of the sound intensity of each source as

shown on the right-hand side of Figure 97, where the Aux gain on each amplifier is used to control the signal and noise amplitude.

Acoustic receiver

Existing laboratory apparatus was used for the acoustic receivers and data acquisition since their specifications were suitable for time of flight acquisition. As shown on the left-side of Figure 98, a side address condenser microphone was selected for use as the acoustic receivers. These microphones have high sensitivity, a flat frequency response over the acoustic range of 20-20 kHz and cater for a maximum sound pressure level(SPL) of 144 dB (exceeding the SPL produced by the acoustic transmitters).

Figure 98 (left) acoustic receiver for recording (right) mixer for data acquisition

For the purposes of data acquisition, many studies used dedicated data acquisition cards[37], [41], [49], [68], [69] or digital oscilloscopes[42], while using LabVIEW as the software to interface with these devices. However, for this study it was decided to use a 4-channel stereo mixer as shown on the right side of Figure 98. This decision was made since the mixer was already available (existing laboratory apparatus) and was compatible with the available condenser microphones, which eliminated the need to specify preamplifiers for them. In addition to this, the mixer has a built in digital-to-analog convertor (DAC) with a sampling frequency of 44100 Hz (allowing the coverage of the whole acoustic range) and conveniently interfaces via USB 1.1. The mixer however outputs recorded signals in a stereo format, and to separate the signals simultaneously recorded from both microphones, the highlighted pan dials were used. Each microphone recording is panned to a

distinct channel (transmitter or receiver side) to then be separated later by software for signal processing.

Acoustic enclosure

With respect to the containment and transmission of the acoustic signal, PVC piping was identified as cost effective and convenient acoustic enclosure. Class 4 PVC was used and found to be structurally sufficient with more workability than cheaper alternatives. With this type of enclosure, a suitable pipe diameter and length of the pipe must be determined to provide an observable time of flight difference (and thus temperature) between acoustic receivers and house the necessary equipment.

The selection of the diameter was primarily made to house the speaker (acoustic source) and microphones (acoustic receivers). The signal speaker mount required a diameter of 20 cm and the microphones had a height of a 15 cm. A diameter of 355 mm was selected as the closest standard diameter that allowed for the speaker to be mounted, such that there is still clearance between the speaker centre and the top of the microphone. This diameter was also advantageous since (if necessary) it would allow for the option to line the piping with an attenuative material to reduce reverberation.

The selection of the diameter was also constrained by standard pipe lengths, however since PVC was machinable the length could be worked to the requirements. In general, a longer piping length would be more advantageous for time of flight determination.

$$c = \sqrt{\gamma R_s T} \tag{109}$$

$$c = \frac{d}{t} \tag{110}$$

At a fixed temperature the speed of sound will stay constant as per equation (109), and since we know the speed of sound is the travel distance divided by the time of flight as shown in equation (110), we can infer that there will be a direct relationship between time of flight and distance, implying that for longer distance the time of flight would increase in proportion, making the measurement of this time of flight more accurate.

At the standard pipe length of 6 m, with air at a room temperature of 20°C, the expected time of flight is 17.485 ms. With the mixer sampling at 44100 Hz, the expected resolution at this distance is 0.13 % of the travel time, which is sufficient to demonstrate time of flight determination.

With knowledge that the ambient temperature resided at around 20°C, it was then investigated what the resolution of the temperature deviation would be from this set point. Since we know temperature to be dependent on the square of distance and time of flight as shown in equation (111), it was expected that the increased resolution of shorter piping would result in a greater temperature change.

$$T = \frac{d^2}{t^2 \gamma R_s} \tag{111}$$

The temperature resolution against vs. distance is compared in Figure 99. This was done by determining the expected TOF at each distance and determining what the change in temperature would be based on the time of flight sampling resolution.

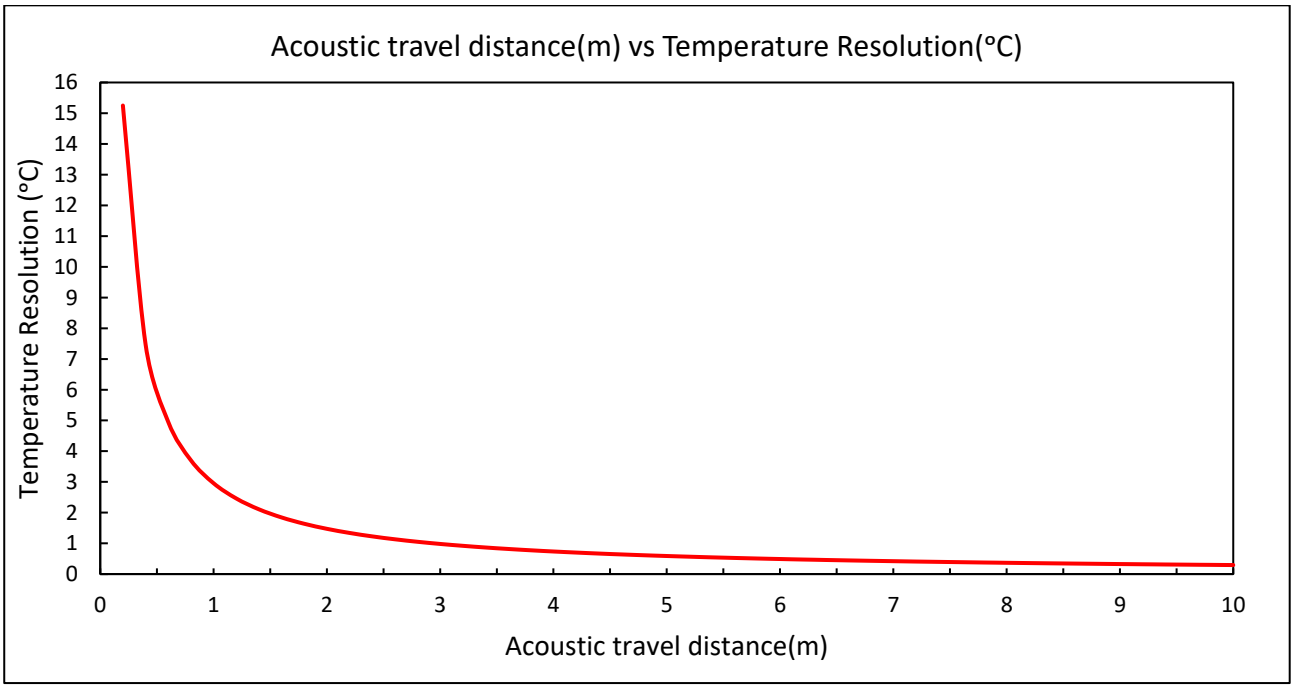

Figure 99 Acoustic travel distance(m) vs Temperature Resolution(K)

A resolution of 1°C was found at a piping size of roughly 3 m, and for the standard size of 6m, a resolution of 0.49°C was calculated, implying that this length was suitable for both time of flight and temperature determination under the environmental conditions.

Final design

Once all the components were selected and sized, the final experimental setup was designed and constructed as shown in Figure 100. The signal source (speaker 1) is mounted to the left-hand side

of the enclosure via circular wooden disk, and the first microphone is mounted within the pipe just in front of it. The acoustic signal then travels along the dotted line through the pipe and is received by the first microphone at the transmitter-end until it eventually is recorded by the second microphone at the open end. The second speaker acts a noise source and is mounted roughly halfway between the microphones to produce the interference noise.

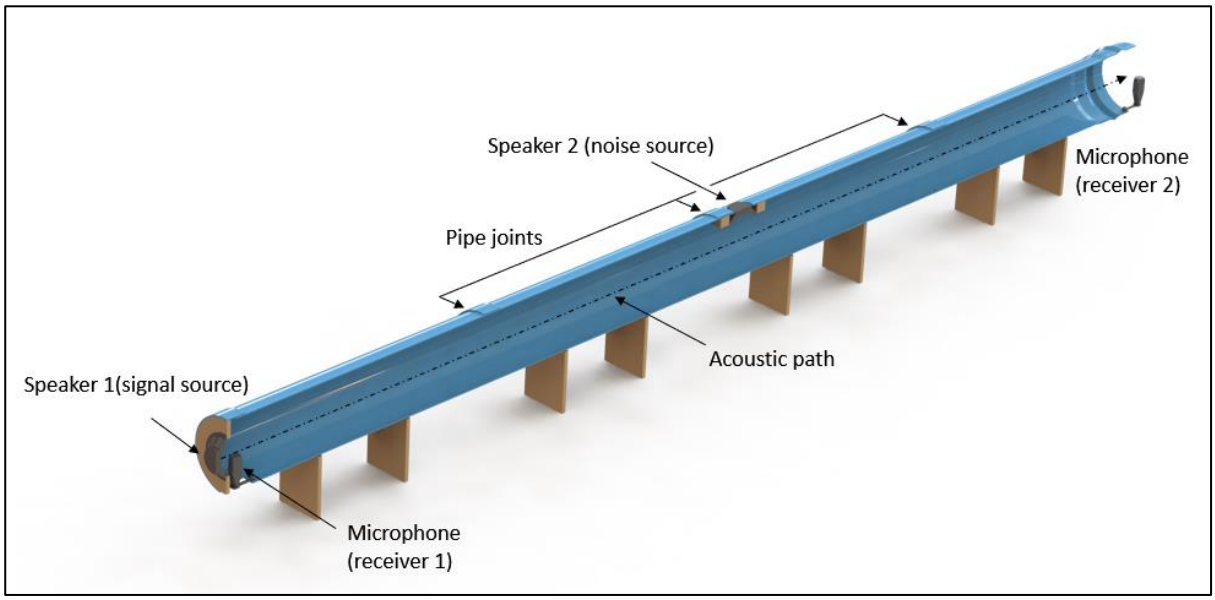

Figure 100 Cross-sectional view of experimental setup

To allow for easier handling of the setup, the full pipe length was divided into four parts of roughly equal length, which were joined by pipe joints, made from stretched offcuts of the same pipe. The final constructed version is shown below in Figure 101, note the setup is viewed from the opposite side as shown in Figure 100. One of these joints was also used to mount the signal speaker. Despite the material removal for the pipe joints, the approximate length of the pipe remained at the desired 6 m. To make sure that the segmented pipes are still stable, four wooden pipe stands were manufactured, having a rubber lining at the contact point between the stand and pipe. In addition to the noise speaker at the centre of the pipe, a hole was made for the insertion a of thermocouple, so temperature measurements could be taken.

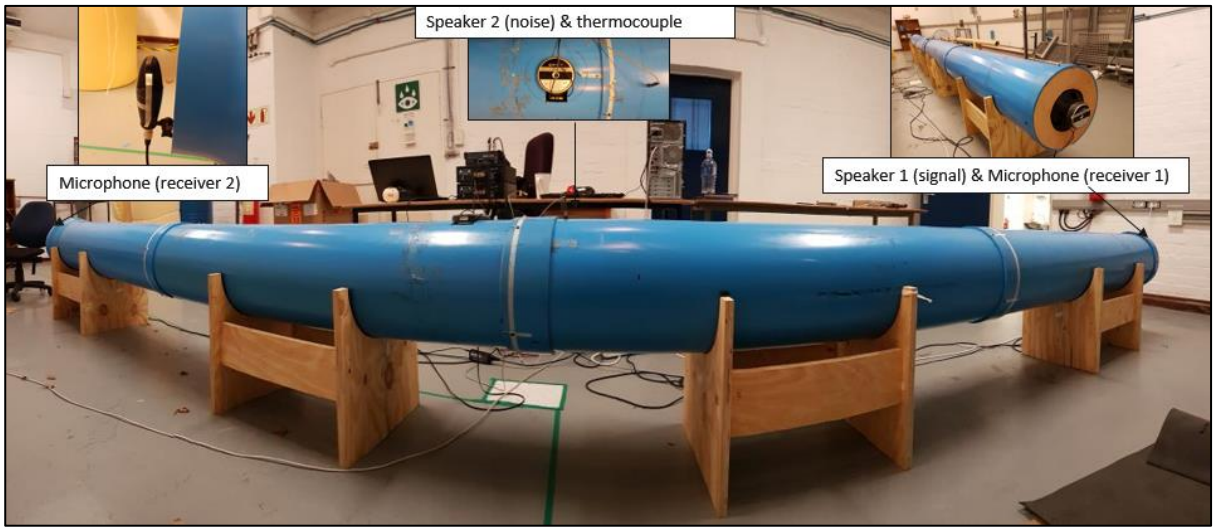

Figure 101 Final constructed experimental setup

In summary, the overall design facilitates for TOF measurements by having versatile acoustic sources (speakers) with amplification, accurate recording devices (microphones) with high frequency data acquisition; and an enclosure that contains and separates the recording devices by a considerable distance to provide the accuracy necessary for TOF determination and temperature measurement.

4.3.2 Control system

Once the hardware of experimental set-up was determined, a control system was necessary to manage the specified hardware. With the goal of practically determining the time of flight, the control system would have to provide means to interface with the audio mixer used for data acquisition, the amplifiers used for generating the signal and noise and prepare the signal for processing.

Interface with hardware

From the literature review the most prolific software used for data acquisition and control in TOF determination studies was found to be LabVIEW[37, 41, 42, 49, 68, 69], a systems engineering platform for testing, measurement and control[70]. It makes use of a visual programming language with a graphical user interface and block diagram style of coding, where each function is characterised by block nodes and execution flow is determined by the connection of these nodes. The combination of the user interface and block diagram code is referred to as a Virtual Instrument (VI), where VIs can be placed within one another (acting as a function), then referred to as a SubVI. The comparative advantage of this software and reason for its widespread application is the ease

with which hardware can be interfaced to, especially since it includes support for various National Instruments hardware platforms (the most notable being its data acquisition devices).

While the aforementioned studies used LabVIEW for control of hardware and data acquisition, the most popular method for signal preparation and processing thereafter was to use MATLAB. For this study, the decision was made to reduce complexity and take advantage of LabVIEW's signal processing library as well as its ability to control and interface with hardware. The result is that the hardware control, signal preparation, data acquisition and processing is performed in LabVIEW. As a result, the experimental set-up is interfaced with hardware as shown by the system map below in Figure 102.

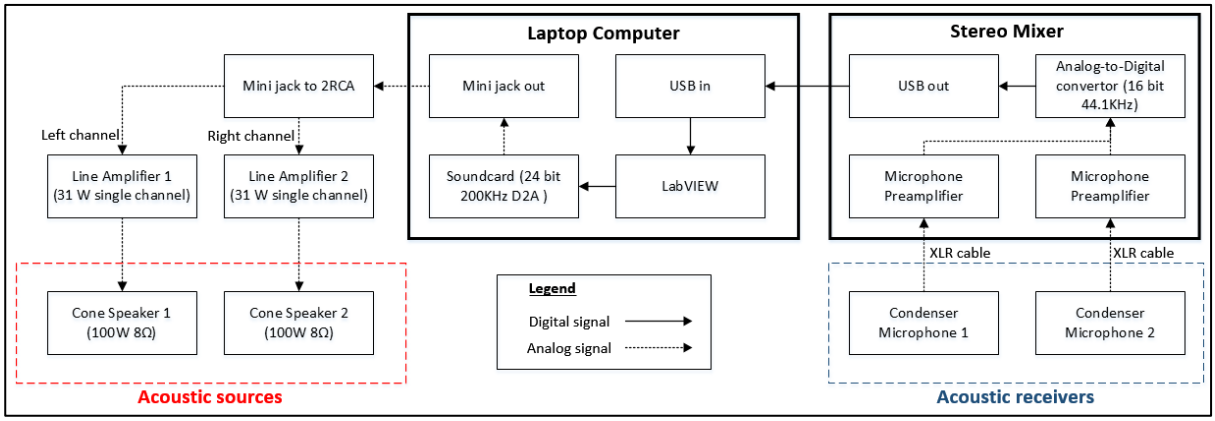

Figure 102 System map of experimental setup

In addition to the components sized previously, a laptop computer is used to control the experimental set-up. LabVIEW is used as the software both for control of the setup but also for the signal processing of the recorded results. The source signal generated in LabVIEW is sent out via the laptop soundcard (used at 44100 Hz) via the mini jack port. A mini jack to RCA convertor is then used to split the stereo signal into the left and right channel which is sent to each line amplifier and then consequently to each respective acoustic source where it propagates through the acoustic enclosure.

Through this propagation, the signal is received by each condenser microphone and sampled by the stereo mixer. The mixer has a preamplifier input with power source for each line, that is then sampled by the built-in analog-to-digital convertor(ADC) at 44100 Hz which then interfaces with the laptop computer via USB. The loop is then completed when the LabVIEW records the incoming signal. The implication of this is that the whole setup can be controlled by a work station consisting of the laptop running LabVIEW alongside the amplifiers and mixer.

LabVIEW Virtual Instrument

Within this experimental setup, the LabVIEW VI acts as the main code and performs multiple functions within the system. It is responsible for generating the signal of interest and noise signal, controlling the hardware that generates and records these signals, storing the recorded signals and applying the signal processing methods to these signals to ultimately determine the time of flight. From a high-level the VI follows the process as outlined in Figure 103.

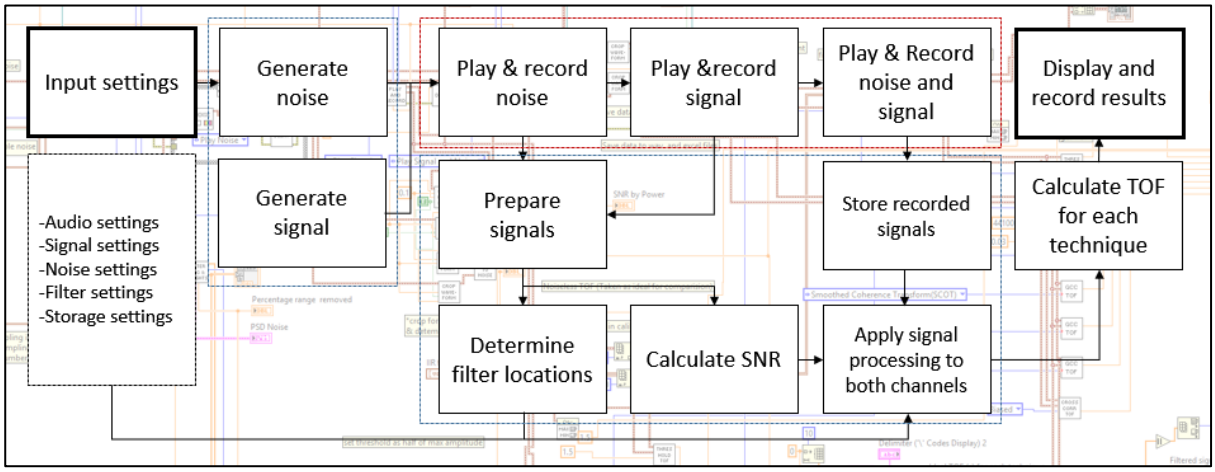

Figure 103 High-level flowchart of LabVIEW VI

The VI starts by accepting the input settings, as displayed in Figure 104, broadly grouped into settings regarding audio, signal, noise, filters, and storage. The audio settings determine the recording duration, the delay between subsequent recordings, and the selection of the identification of the active microphones and speakers. The signal and noise settings determine the amplitude of each waveform, the type of noise and signal and the characteristics of those waveforms (frequency envelope of noise and frequency change of signal). The filter settings include the characteristics of the filters used as well as the maximum allowable noise to be removed. Lastly, the storage settings determine the storage locations of the sound recordings (.WAV), Excel files and number of the test.

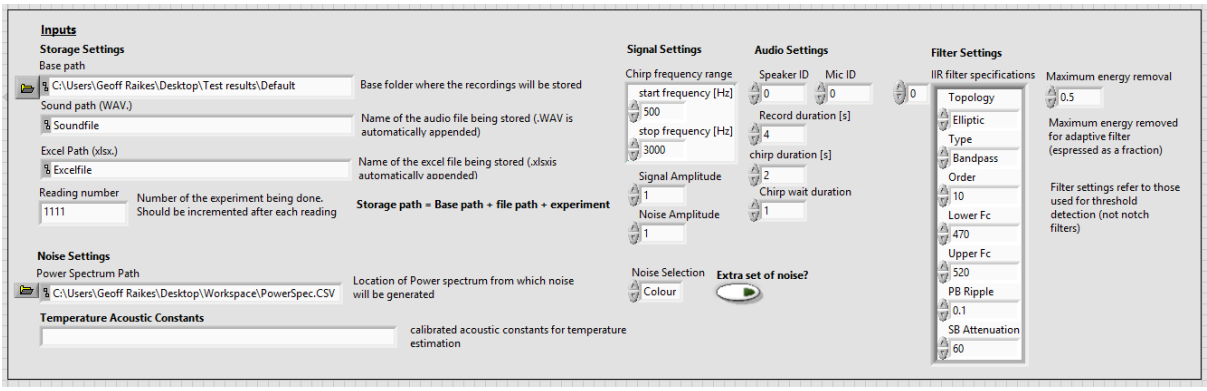

Figure 104 LabVIEW VI inputs

Once the settings are determined, the noise and signal are generated in LabVIEW based on the selected signal and noise type. First the noise waveform is played and recorded simultaneously and after a short delay the signal is played and recorded simultaneously. These two recorded signals are then prepared by cropping the signal from the whole recording (such that just the produced signal remains and no recorded silence). The position and duration of this signal is used to crop the noise waveform at the exact same time. Since both signals are recorded separately, which can then be sued to calculate the signal to noise ratio. In addition to this, the noise signal (before cropping) is used as an input to the variable filter algorithm to determine the location of the notch filters used by that algorithm.

Thereafter, the signal and noise signals are merged into a stereo signal, where the signal plays from the 1st speaker(source) and the noise plays from the 2nd speaker(noise) while both microphones are simultaneously recording. The recorded, combined signal and noise waveform is then used for by multiple signal processing methods from witch the TOF can be determined and displayed.

4.3.3 Signal and noise generation

As mentioned previously, the signal and noise generation occur within the main LabVIEW VI and are based on existing LabVIEW libraries. For the signal waveform, a SubVI was created as shown as the “Create signal” node. This SubVI was built around the Sound and Vibration toolkit using the “Chirp waveform” VI.

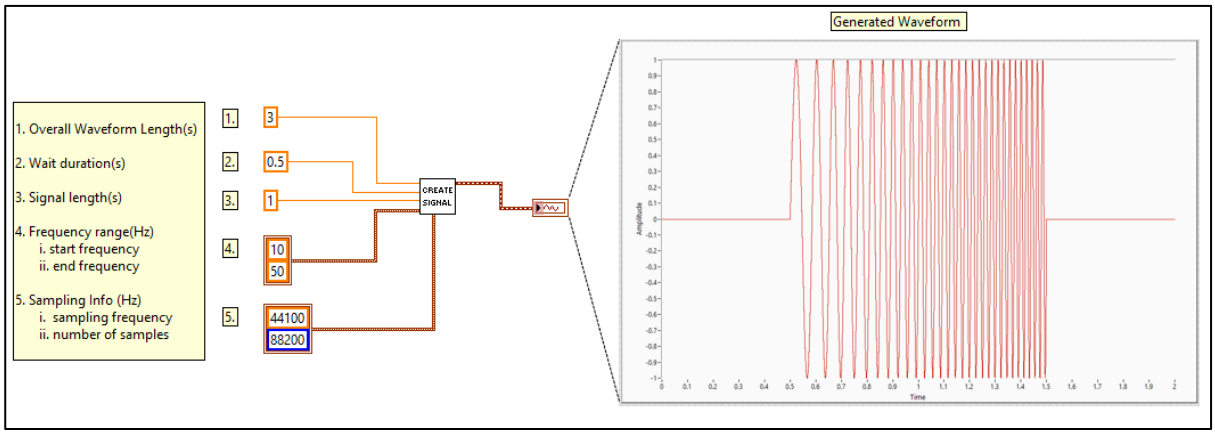

Figure 105 Signal Generation SubVI with example of time varying signal

This SubVI accepts inputs in the form of an overall waveform length, a wait duration, signal length, frequency range and sampling information. The location and length of the signal will be determined from the wait duration and signal length, if the overall waveform length is greater than the sum of these two, the rest of the waveform will have a zero amplitude as shown in the generated waveform in Figure 105. The frequency range input determines the type of signal generated, with the two options being a linear time varying signal (chirp) between the two frequency inputs, or a sinusoidal signal when these two inputs are the same. The final input is the sampling frequency and the number of samples (which in implementation is determined programmatically by the signal length).

In a similar vein, a noise SubVI was developed to generate the noise waveform. The SubVI was created using a "white noise" VI within the signal processing toolkit and a VI adapted from the coloured noise generator. This SubVI as shown in Figure 106, takes three inputs in the form of the path location for the power spectral density (PSD) envelope, a selection for the type of noise and the sampling information.

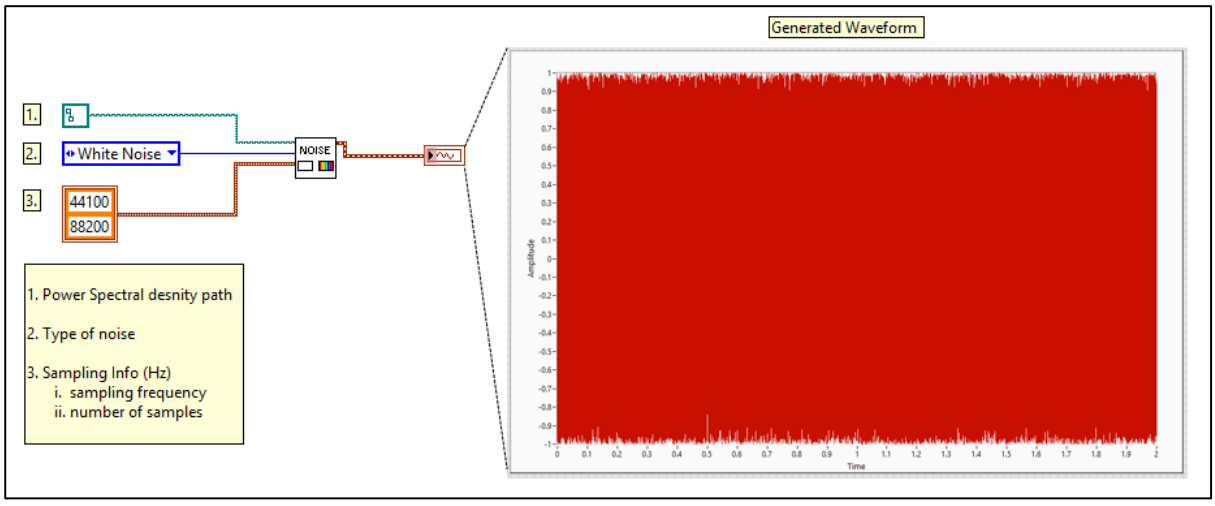

Figure 106 Signal Generation SubVI with example of white noise

The length of the signal is controlled by the sampling information which determines the sampling length and number of samples. When coloured noise is selected an extra input in the form of a PSD envelope is required in the form of a .CSV file. This allows for the generation of not only white noise (broadband noise that occurs across the audible frequency spectrum), but coloured noise that can be shaped to reproduce the specific frequency components found in the boiler (or for any given application).

The requirement for coloured noise was born out of the observation that the frequency components present in boiler noise tend to be repetitive and periodic. This is shown in Figure 107, where a spectrogram was produced from previous boiler acoustic recordings as taken from[1]. It highlights that the noise present in the boiler is not white and tends to have distinct frequency characteristics.

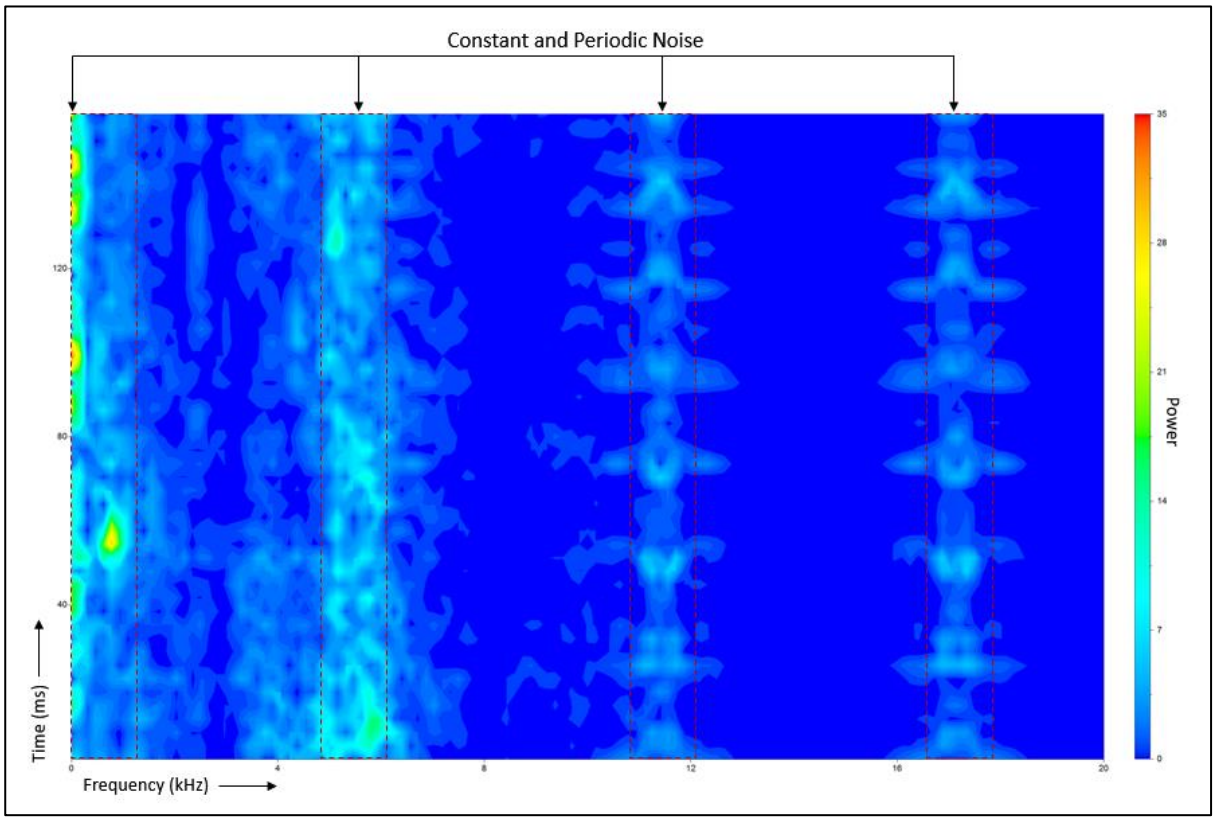

Figure 107 Spectrogram of noise in the boiler

From these readings PSDs where computed, an example of a typical result is shown in below in Figure 108.

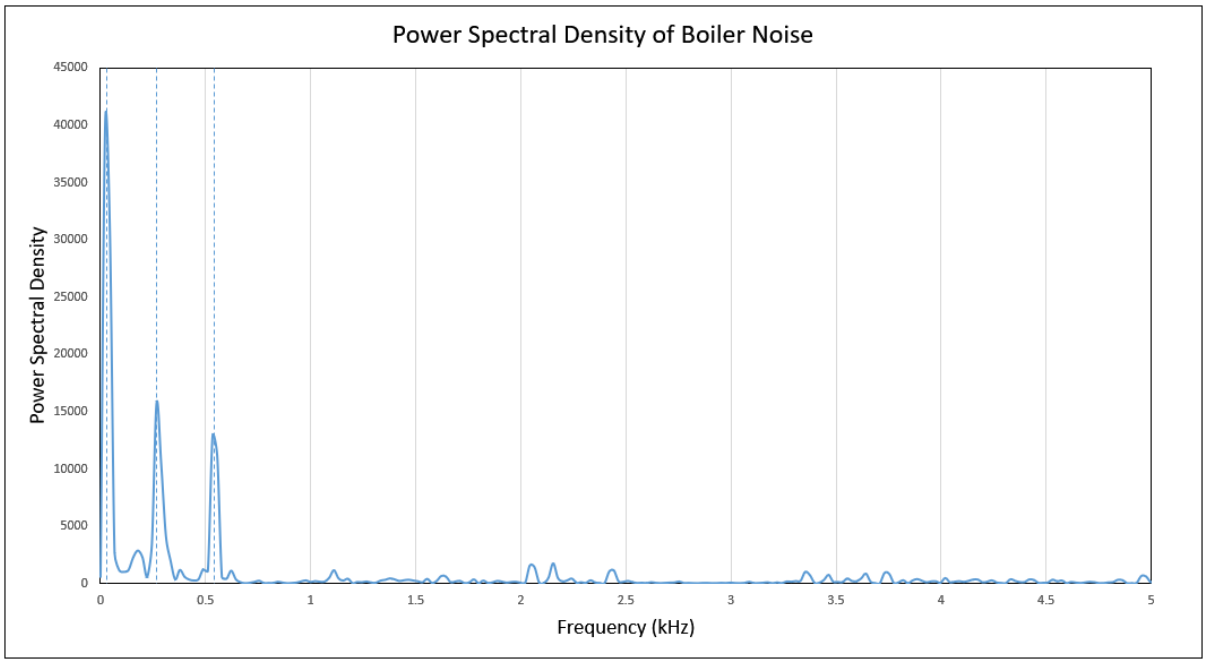

Figure 108 Example of power spectral density of boiler noise

Upon further inspection, it was found that there were predominantly three peaks that reoccur in multiple readings residing at around 44, 260 and 577 Hz. An Additional sound recording was taken outside the observation port of another boiler and produced the PSD shown in Figure 109, where again distinct frequency components were present. In this example the peaks were much sharper and distinct, however this is likely since most of the random combustion noise was contained within the boiler and only the powerful components would be observable from the outside.

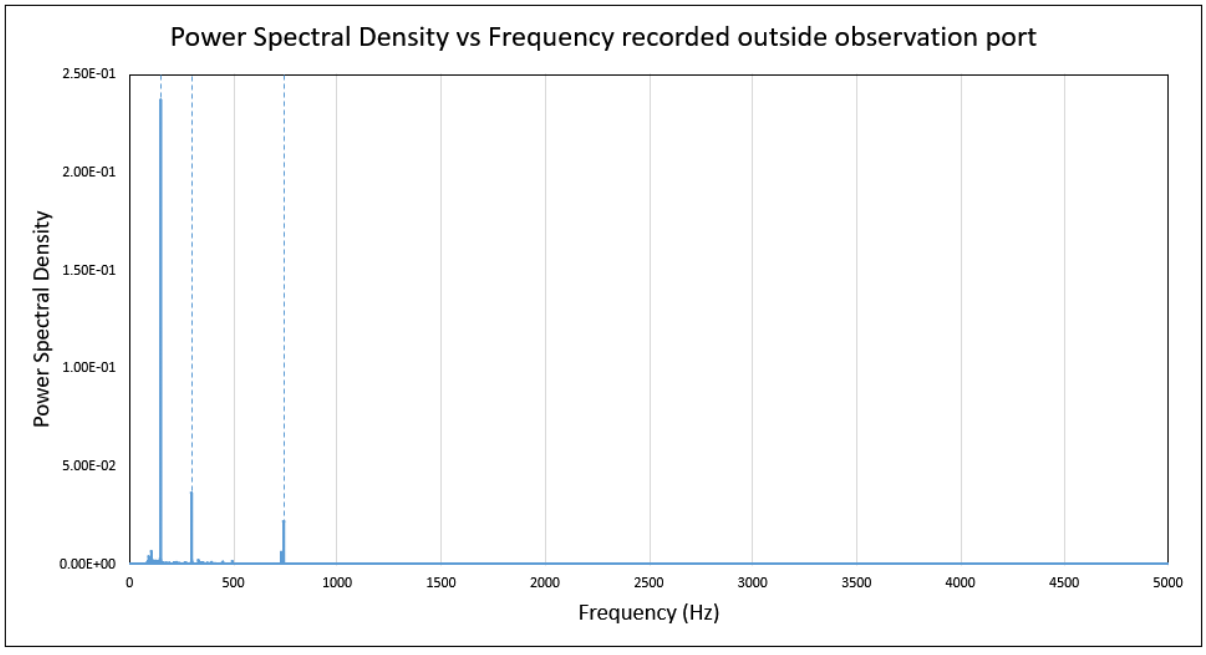

Figure 109 Power Spectral Density of audio recorded at boiler observation port

The PSD in Figure 108 was then used as a set input to the coloured noise generator for later tests as the frequency envelope, producing noise that varies, but resembles the real-world scenario.

4.3.4 Signal playback and recording

Once the signal is generated, it is then required that these signals be played back and recorded to complete the TOF determination cycle. The playback and recording of generated signal and noise waveforms are also controlled within the LabVIEW environment and as previously mentioned, the approach taken is to simultaneously play sound via the speakers and record the generated sound via the microphones. In pursuance of this, another SubVI was developed as shown below in Figure 110.

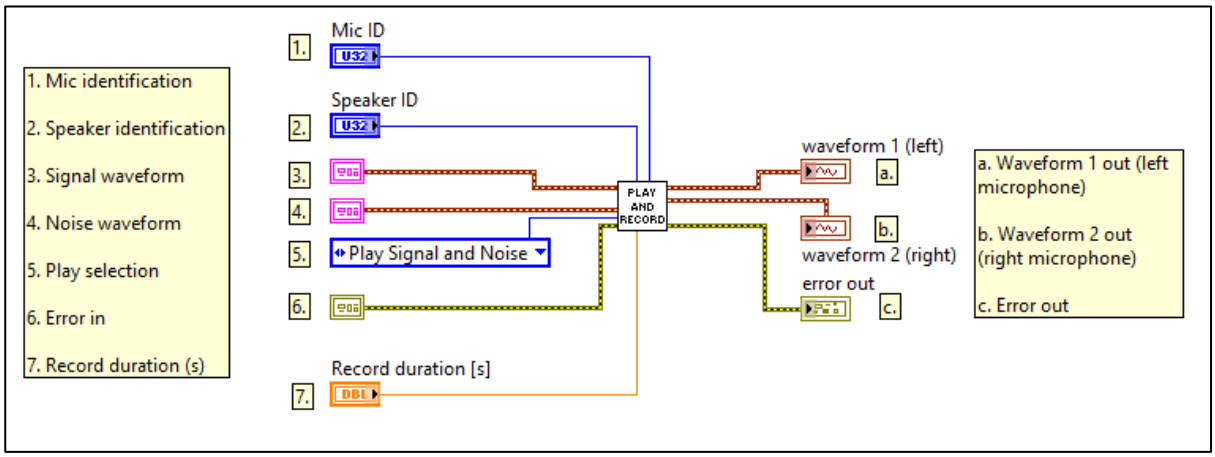

Figure 110 Signal Play and Record SubVI

In order to function play and record as necessary, the SubVI accepts multiple inputs from the main VI. The first inputs are the microphone and speaker identification, used by LabVIEW to identify the correct hardware to interface to. The next inputs are the noise and signal waveforms generated by the Create signal/noise SubVIs and a selection of the playback type. The playback can either be of the signal from the left speaker, noise from the right speaker or both concurrently. The last two inputs are the error input (a list of errors compiled by previous operations) and the duration in seconds to record. After operation the SubVI outputs the signals recorded from both microphones and any error warning generated along the way.

Since the choice was made to simultaneously record and play the signal, the operation of the SubVI is important, allowing some extra functionality but also limitations on application. The actual process followed by the SubVI is summarised below in Figure 111

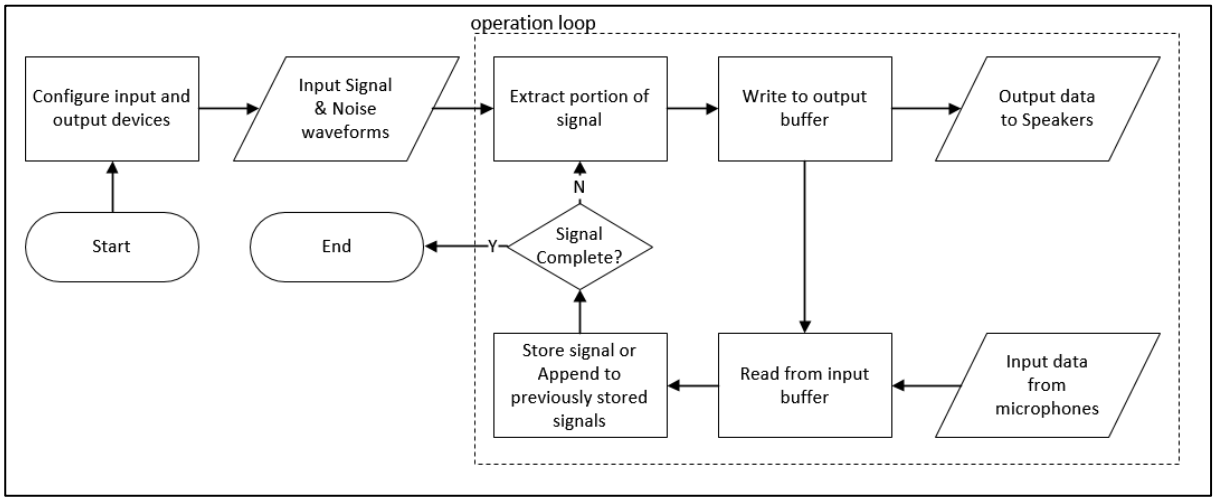

Figure 111 Play and record signal block diagram

The process begins by configuring the input and output devices, in addition to the inputs described previously, playback and recording is set to acquire data of a set sample size continuously while in operation. The inputted signal and noise waveforms enter the operation loop, where a portion equal to the sample size is extracted and written to the output buffer. At this point the output data will be read and played by the speakers, while the code moves onto reading the input buffer to receive the input data (equivalent to the sample size) from the microphones. The read data from the input buffer will then be stored as the start of a signal or appended to an existing signal. If the stored signal length is less than the record length specified, the loop will continue, and the next portion of the signal and noise waveform will be extracted for playback, otherwise the operation loop will end, and the recorded signals will be recorded.

In this setup the sample size selection is important, since short sample sizes will read the buffer to quickly and result in glitches, and larger sample sizes will incur greater delay and not read the buffer in time for playback and recording. The sample size selected was 4410 samples, corresponding to 10% of the sample rate per second. The implication of this implementation is that only one control unit (laptop computer) is required, simplifying the setup, control and reducing cost. However, this means that the signal display and processing cannot be done in real time and only occurs after each process is completed. As a result, signal processing for time of flight determination occurs once the signals have already been recorded.

4.3.5 Time of flight determination methods

While the signal processing methods where reviewed and discussed in section 4.2, this section will discuss the methods that have been implemented into this study. The methods implemented are: Threshold level with bandpass filtering, cross-correlation (including GCC variants) and variable notch filters with cross-correlation.

Threshold method with bandpass filtering

The first method applied was adapted from the threshold method (or edge detection). The process followed is to first apply a bandpass filter to the received signals to isolate frequencies associated with the signal and filter out as much of the noise as possible. Once the signal is filtered the threshold method is applied to determine the time of flight of the signal.

To implement this, two SubVIs were created, as shown in Figure 112, namely the Infinite-impulse response (IRR) filter and Threshold method SubVI. The first SubVI accepts inputs as the signal to be filtered, the filter parameters and error input and is built using the Signal processing toolkit within LabVIEW and the Digital IRR filter VI. An example of the specifications required is shown in Figure 127, where the topology, filter type, cut off frequencies, ripple and sub-band attenuation is specified. The SubVI then outputs the phase and magnitude response of the filter, the filtered signal and any errors produced along the way.

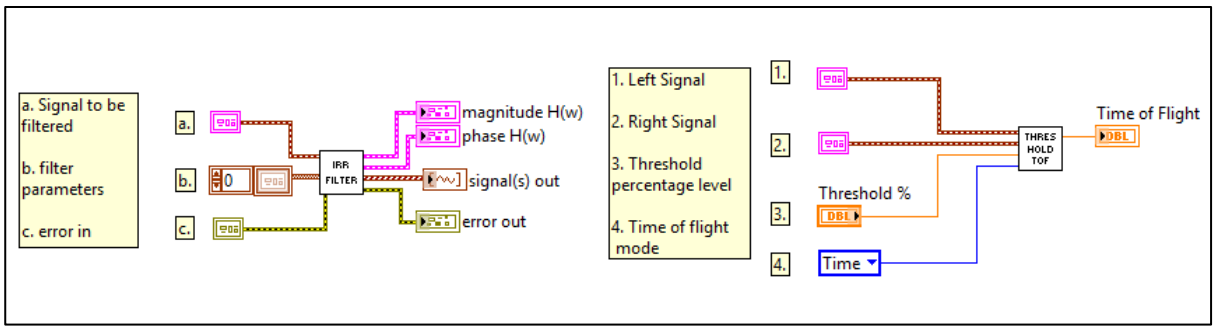

Figure 112 SubVIs created for Threshold detection

The threshold detection SubVI then actually applies the threshold method, by accepting the filtered signals as inputs, the threshold percentage level and the time of flight mode. Threshold detection is performed using a basic trigger level VI, where the trigger(threshold) level is set as a percentage of the maximum signal level and the output is selected as either a time in seconds or samples.

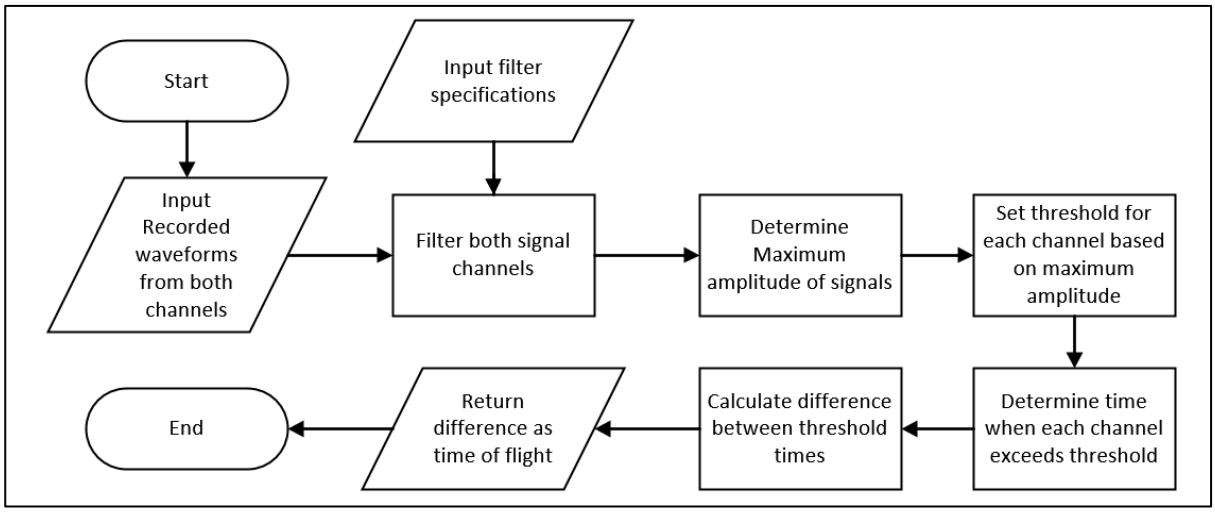

Figure 113 Process followed for threshold method with bandpass filtering

The resulting process followed is thus as shown in Figure 113, where the input waveforms are received and filtered based on the filter specifications. The exact specifications of the filters used will be discussed in the methodology of the test performed.

Both the left and right waveforms are filtered, to remove any TOF discrepancy caused by filter delay. From these filtered signal, a maximum amplitude is determined, and a threshold is set based on the amplitude of each waveform independently. Once each channel exceeds its respective threshold, the time is noted and the TOF is returned based on the difference between these times.

Cross-correlation methods

When it came to cross-correlation methods, two SubVIs were created, one to implement standard cross-correlation and another for generalised cross-correlation (GCC). The first method as shown on the left of Figure 114, was built around the cross-correlation VI in the Time series analysis (TSA) toolkit in LabVIEW. It accepts the transmitter side and receiver side waveforms to be correlated, the weighting, a maximum expected lag and an error in. When implemented the biased weighting was used, that weight peaks closer to the centre as higher, to avoid false edge peaks prominent in longer signals.

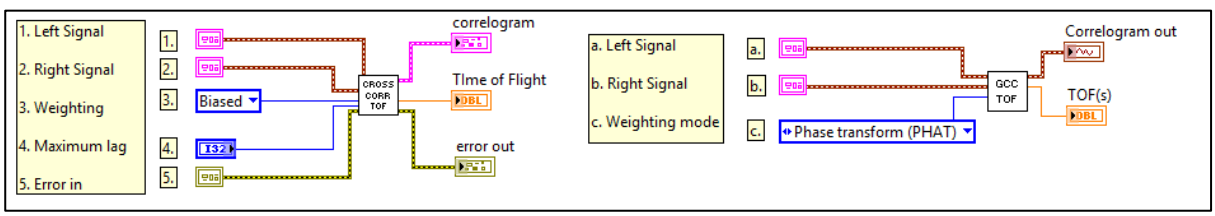

Figure 114 Cross-correlation and GCC SubVIs and inputs

The SubVI produces outputs in the form of a correlogram to visually display the correlation, the error output and the TOF. The straightforward process followed by this method is shown in Figure 115, whereby the recorded waveforms are cross-correlated, the peak of the correlation is determined, and the time associated with that peak is returned.

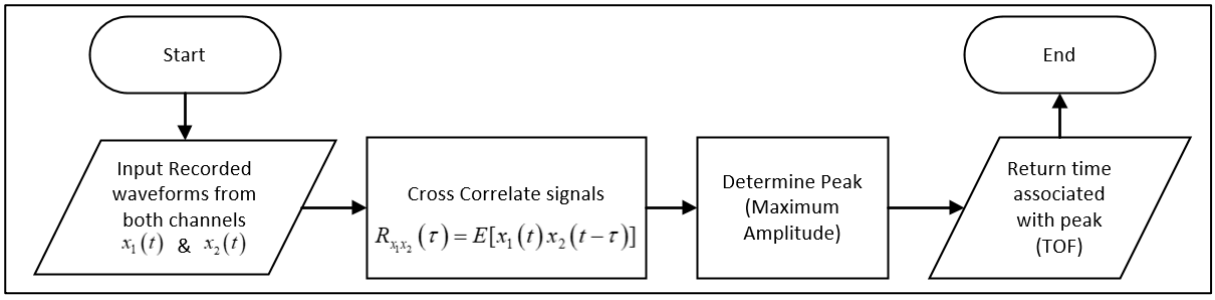

Figure 115 Cross-correlation flowchart

The GCC SubVI has a very similar setup, however instead of using the biased weighting for standard correlation, the weighting choices are the distinct types of GCC weightings, namely the PHAT, SCOT, ROTH and ML weightings. The SubVI can then be repeated multiple times to test each weighting individually to compare their efficacy.

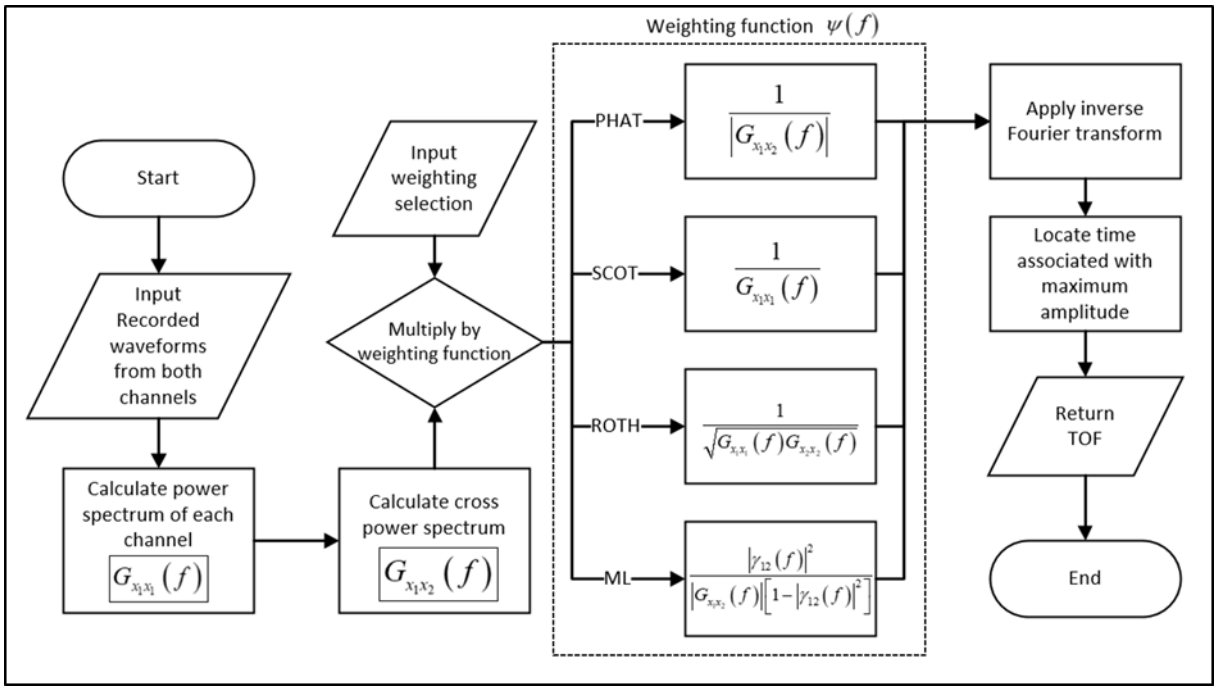

Figure 116 Generalised Cross-correlation process flowchart

The process followed to achieve this, as shown in Figure 116, is somewhat more intricate though. The recorded waveforms taken as an input first undergo FFTs to determine the power spectrums and cross-power spectrums between them. Based on the input weighting selection, the cross-power spectrum is then multiplied by the weighting function selected, as determined by the combination of the previously calculated spectrums. The result of this multiplication then undergoes an inverse Fourier transform (IFT) to produce the correlogram. The maximum value of the correlogram is then determined and the time associated with that maximum is returned as the time of flight.

Variable notch filters

The final method applied is the variable notch filter method. The approach taken with this method is to identify the main components of noise present in the boiler (assuming it is periodic) and then filtering out the significant peaks. The method strives to listen to the noise and update the peak locations before readings and adjust the width of the filters used based on the noise recorded.

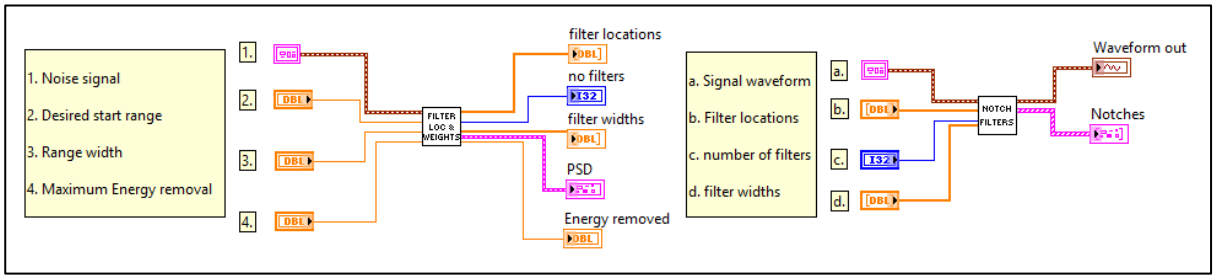

Figure 117 Variable notch filter SubVIs

The method was implemented using the SubVIs shown in Figure 117, where the first SubVI is responsible for determining the notch filter locations and the widths of each filter, while the second one applies those filters. The first SubVI inputs the noise signal recorded before the TOF recording, the desired range for the signal and the maximum allowable energy to remove in the desired signal range. The result of this analysis is the primarily the location of the filters to apply, the number of filters to apply and the widths of those filters.

After this process, the second SubVI accepts the signal waveform, as well as the filter locations, number of filters and filter widths, applying each filter sequentially until the number of filters is reached. The “Digital filter design IIR notch peak design” VI from the special filter design toolkit is used to apply the notch filters within the SubVI.

Consequently, the process followed for the overall method is detailed in the flowchart shown in Figure 118. The process begins by inputting the previously recorded noise waveform, calculating the power spectrum of this waveform and then determining the RMS level of the power spectrum. Any peak in the power spectrum that is above double the RMS level is identified as a significant peak and once the peak detection process is over, they are sorted in descending order based on the power of each peak.

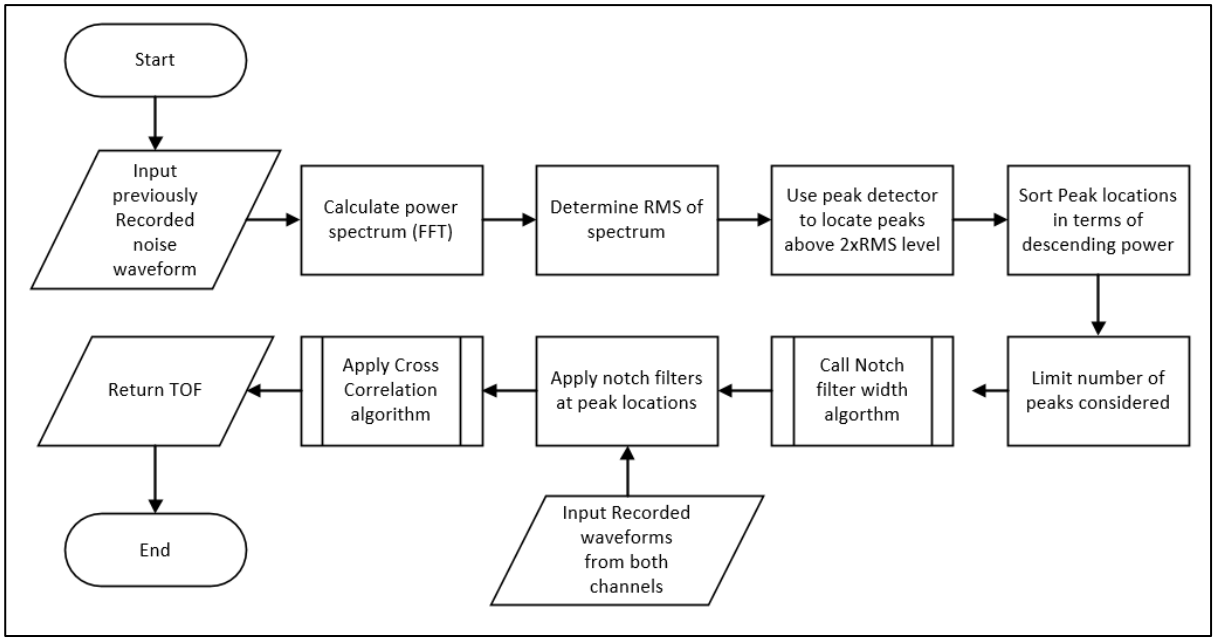

Figure 118 Process followed by Variable notch filter method

The number of peaks considered is then limited if too many (50) peaks are located. From this point the notch filter width algorithm is called, which determines the width of each filter to be applied based on the spread of power at each peak location. Once the widths are determined the notch filters are then applied to the recorded waveforms, before applying the standard cross-correlation method to determine the TOF.

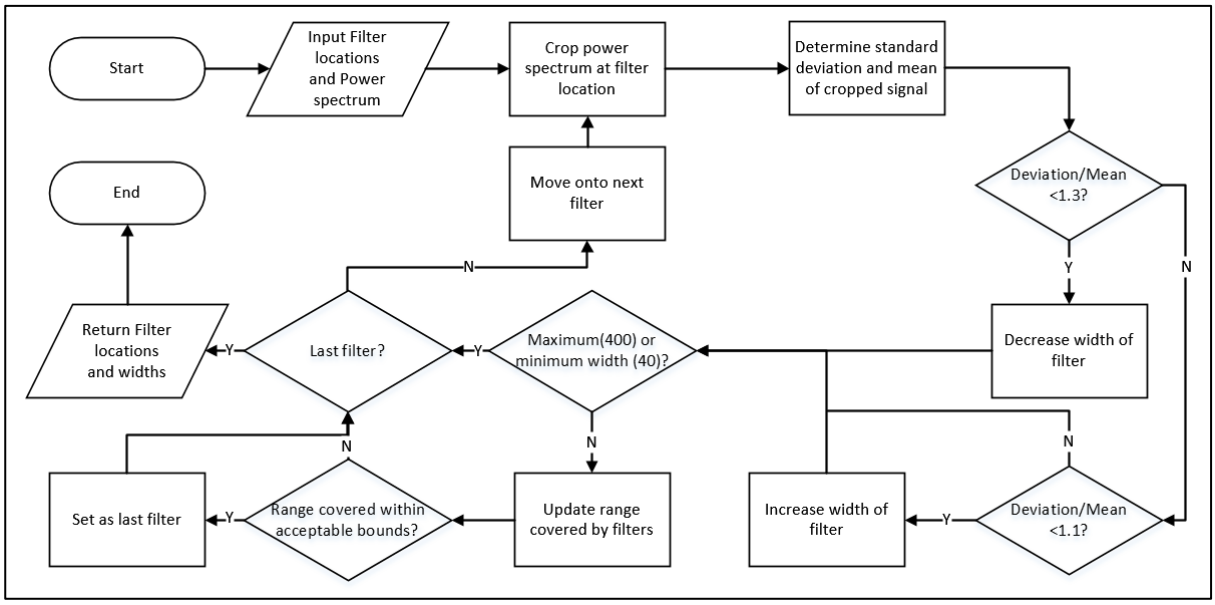

Figure 119 Process followed by notch filter width algorithm

The notch filter width algorithm used by this process is outlined in Figure 119, where the width of each filter applied is determined by the power spectrum surrounding the identified peaks.

It achieves this by starting with the first peak, cropping the region of the power spectrum surrounding it and calculating the standard deviation and mean of the cropped segment. If the quotient of standard deviation and mean is greater than 1.3, this generally signifies a sharp peak that is covered by the filter width, and thus the filter width is decreased. Conversely, if this value is below 1.1, it is considered a wider peak and the filter width is increased. If it lies between these values the filter width remains the same. After this point, the width is compared to the maximum (400 Hz) and minimum filter widths (40 Hz) and limited if necessary. If this occurs a check is done to determine whether it is the last filter to be applied, after which the algorithm will either move onto the next filter peak or complete. If the maximum or minimum filter width is not reached, the cumulative range of the filter and previous filters is checked against the maximum energy removal specified. And if this is reached, the current filter is set as the last filter, otherwise the process repeats itself until the last filter is identified. Once the last filter is identified the algorithm ends and outputs the final filter locations and widths to be applied.

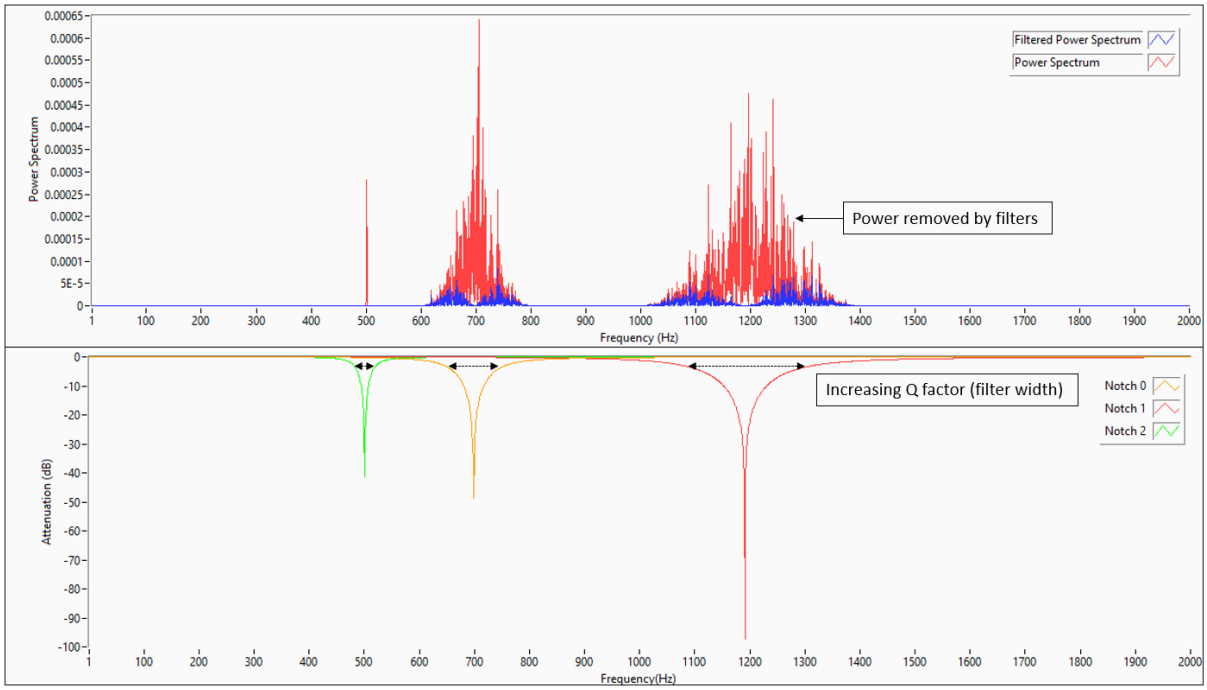

Figure 120 Power Spectrum with noise removed (above) & Notch filter location (below)

An example of this algorithm in practice is shown in Figure 120, where the top figure shows the power spectrum of the noise and the red power represents the resulting noise removed by the notch filters. The source of this power removal is shown in the lower figure which displays the notches identified by the algorithm. The notch filters applied are specified by the centre frequency and a Q factor. The centre frequency is the peak location, and the Q factor is the quotient of the centre frequency and the bandwidth of the filter. It essentially determines the spread of the filter. The result is that when the noise is spread over a greater frequency, the applied filters have greater Q factors to cover this range. Overall the method can be applied over time, constantly adjusting the location and width of the filters based on the noise present in the boiler.

In summary, a range of SubVIs for TOF determination were developed in the LabVIEW environment, so that these methods can be tested and compared in different noise conditions.

4.4 Temperature measurement

This segment documents temperature measurement tests that were performed on the experimental setup. While not a goal or objective of this study, the ability to observe a temperature change via the TOF could be useful as a proof of concept or platform for future research.

4.4.1 Temperature measurement methodology

The objective of these tests was to see if using the existing experimental set-up, temperature change could be measured without considerable change to the design. As a result, a small 2000 W directional electric heater was used as the heat source placed within the entrance of the pipe as shown in Figure 121. The source was capable of increasing temperature by a few degrees, but not more than the allowable design specifications of the hardware used (speakers, microphones etc). The setup already included temperature measurement taps near the centre and acoustic end for thermocouple placement, however to get a more representative temperature of the air inside the pipe, the middle placement was used for the thermocouple (also shown in Figure 121).

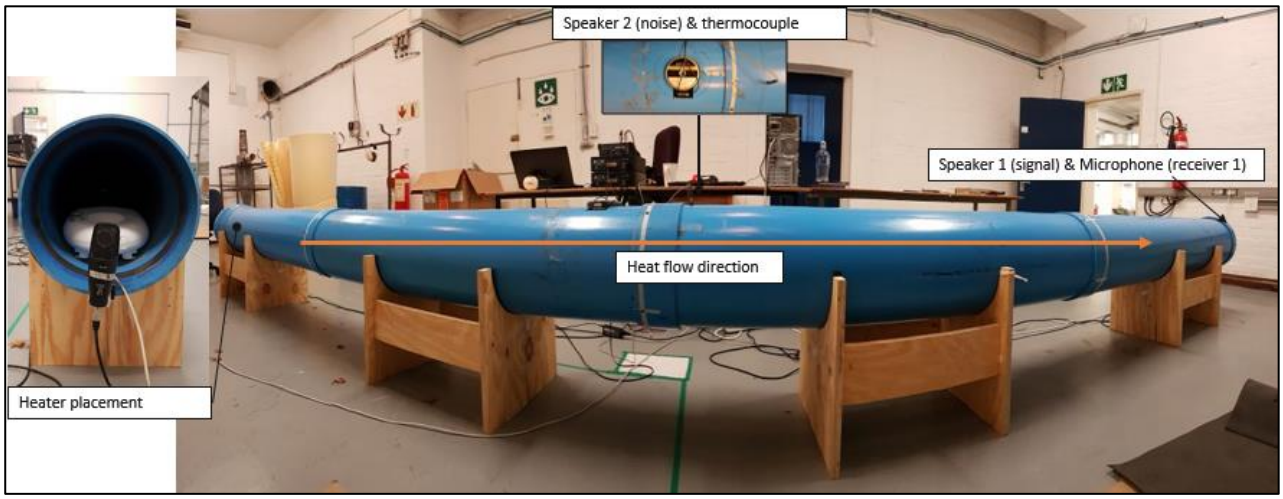

Figure 121 heater and thermocouple placement in experimental setup

Since the goal of these test was solely to measure temperature change, they were conducted without using the second speaker as a noise source. Three TOF determination methods were used for the test. Standard cross-correlation, threshold detection (Without filtering) and a manual method. The manual method consisted of manually using the cursors on the recorded waveforms to identify the start of the signal in each recorded channel. A 500-3000 Hz chirp was used as the signal source, since it would be suitable for both cross correlation and threshold methods without noise.

The actual process followed by these measurements is broadly outlined in Figure 122, where in the beginning, the ambient temperature was recorded using the central thermocouple and 3 readings were taken. Following this the thermocouple was removed and the heater was placed into the pipe as shown in in Figure 121, directing the heat flow downwards into the pipe. The thermocouple was

removed to prevent the measurement of the heat source and rather measure the air within the pipe.

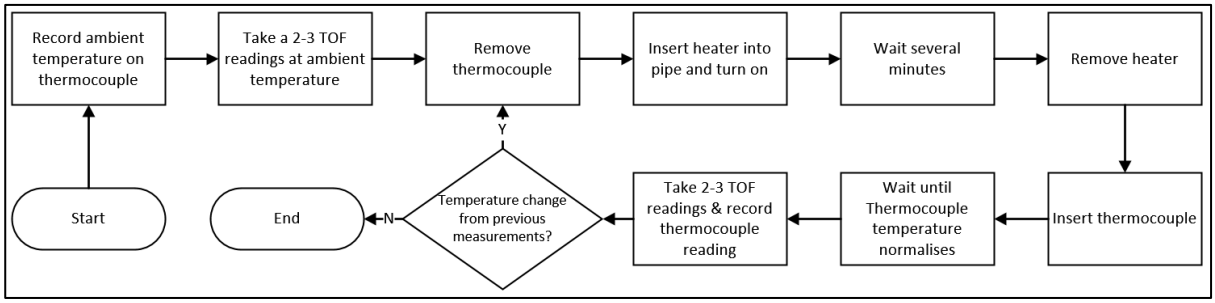

Figure 122 Process followed for temperature tests

After several minutes, the heater was removed, and the thermocouple was inserted again. Once the thermocouple and the air reached thermal equilibrium more TOF readings were taken. This equilibrium point was judged by the rate of change of the temperature reading, as the thermocouple reading started to become stable it was deemed to be in thermal equilibrium. This process was then repeated several times until the heater was not able to add more heat into the environment.

Once TOF readings were obtained, equation (112) was used to calculate the average temperature along the path.

$$T = \frac{d^2}{t^2 \gamma R_s} \tag{112}$$

The path distance was measured as 5.99 m, and the ratio of specific heats (γ) of 1.4 and a specific gas constant (R_s) of 286.9 J/kg°C was used. These average temperatures where then compared to the measured thermocouple for the different methods.

4.4.2 Results

For these tests a measured temperature change of 7 °C was observed via the thermocouple. Over this range the following graphs display the TOF change observed as well as an expected TOF based on estimated properties of air in this temperature region.

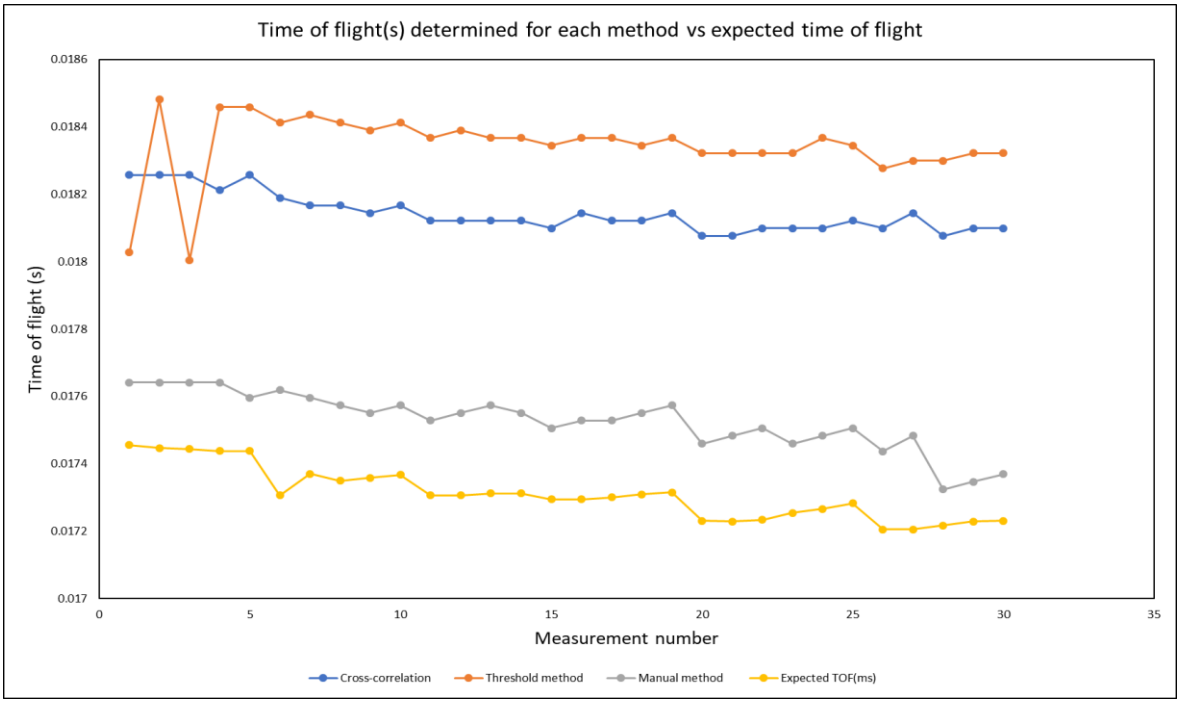

Figure 123 Time of flight(s) determined for each method vs expected time of flight

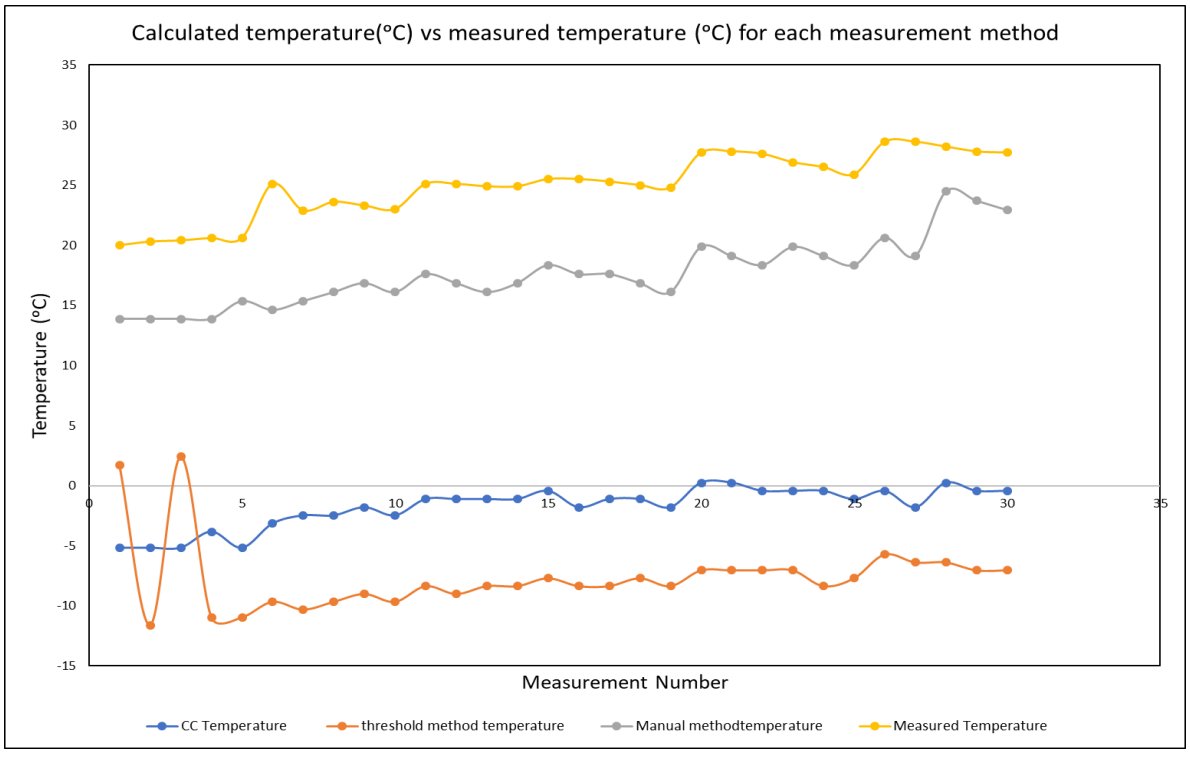

Figure 124 Calculated temperature (°C) vs measured temperature (°C) for each measurement method

By then calibrating these results via the mean difference between each method and the measured method, Figure 125 was produced.

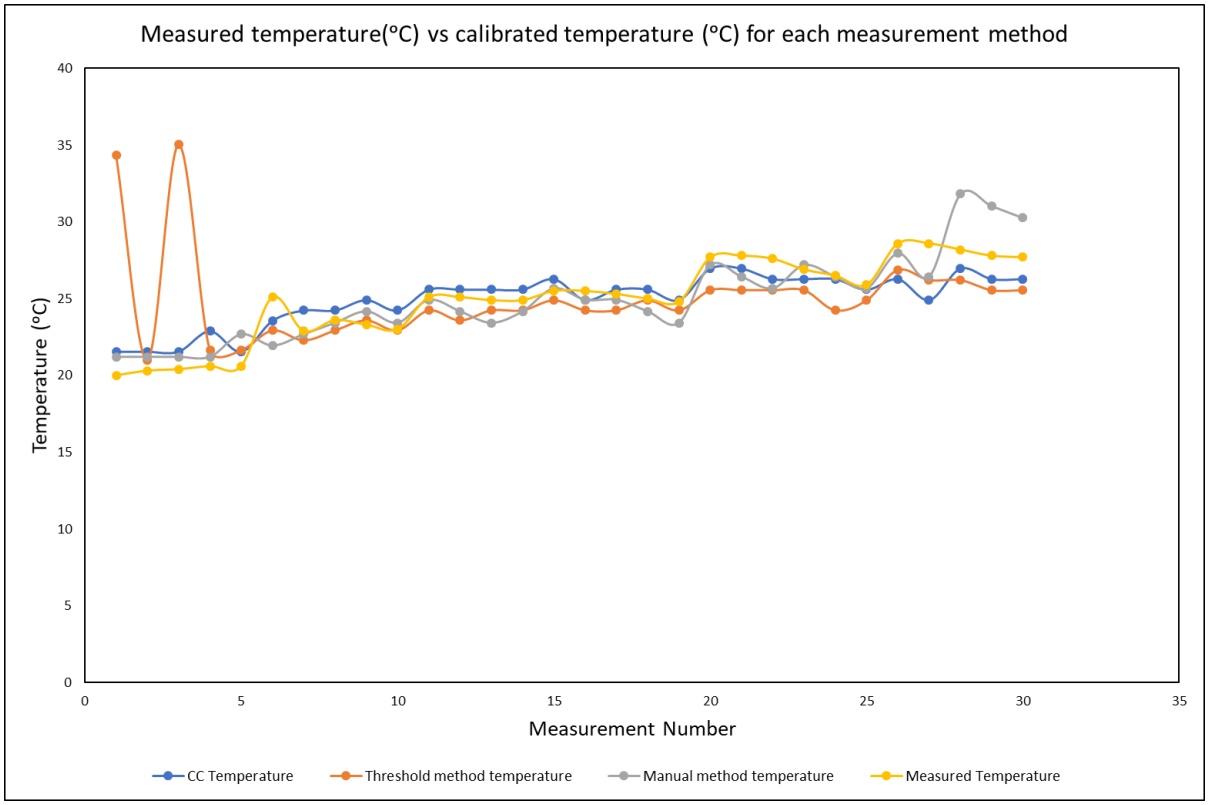

Figure 125 Measured temperature (°C) vs calibrated temperature (°C) for each measurement method

4.4.3 Discussion

Over the temperature range tested, all methods observed a temperature change showing the same trend, which can be observed by the TOF in Figure 123 or the temperature in Figure 124. While the trend was observed, the results are offset from one another, resulting in a relatively large temperature change when the TOF was converted to an average temperature. The cross-correlation and manual method showed relatively low deviation, while the threshold method produced two outliers in the first few readings, after which results became more consistent.

Once these methods were calibrated to the manual method as shown in Figure 125, it could be seen that despite localised deviations, each method was able to track the measured temperature over the range. The resulting temperature trends were typically within 1°C of the measured temperature with many readings approaching the designed 0.5°C accuracy over the length.

4.5 Signal to noise ratio tests

This section details the signal to noise(SNR) tests done, it first discusses the methodology applied to signal to noise tests, the results of these tests and then includes a discussion of those results.

The goal of these tests is to ascertain the efficacy of different signal processing methods in different noise conditions by relating the accuracy of the results to the ratio between the signal and noise amplitude. Methods that still produce more accurate and reliable results at lower SNR are therefore considered to be favourable. The results of this method would then also provide an indication of the type or acoustic pyrometer hardware required (for example acoustic source intensity) relative to the noise present in the boiler.

4.5.1 SNR test methodology

The method applied for signal to noise testing can be broadly summarised by Figure 126. It begins by generating the signal and noise waveforms, which are then played and recorded individually to determine the SNR. After this the waveforms are played together, and the selected signal processing methods are applied to determine the TOF. The resulting TOF from each method and the calculated signal to noise ratios are then recorded, before adjusting the signal and noise amplitudes (effectively changing the SNR) and repeating the process.

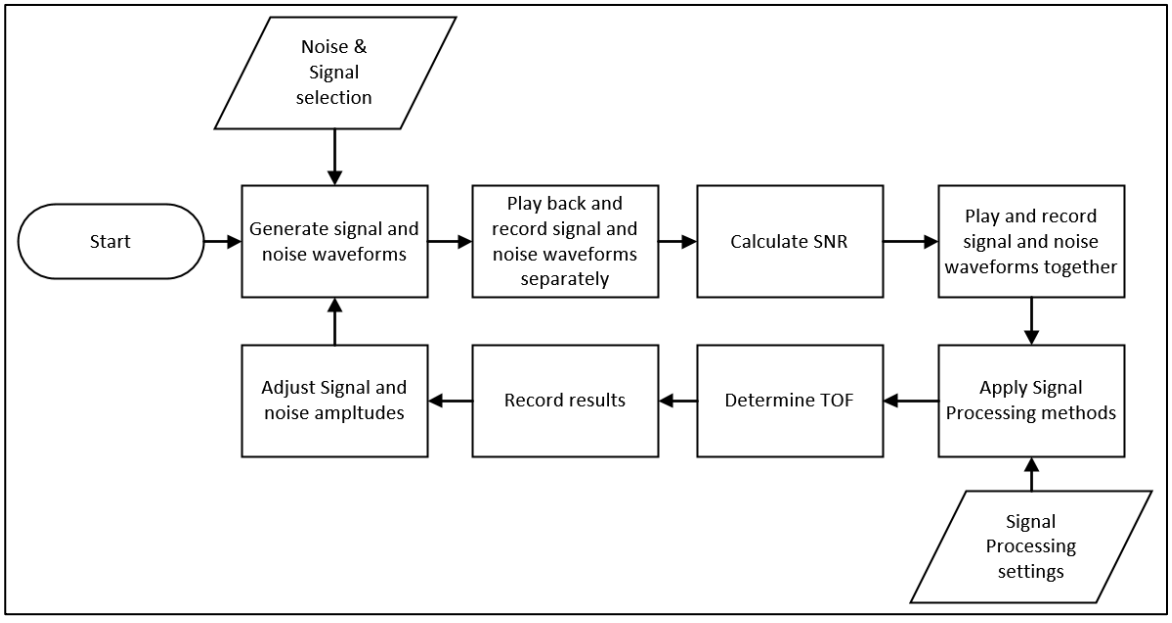

Figure 126 Overview of process for SNR tests

The first variable between test batches is the noise envelope selected. For each batch of tests performed a distinct noise envelope was considered, namely the PSD shown in Figure 108 was used as the noise envelope for coloured noise tests and a white noise generator was used for white noise tests.

Once each individual waveform was played and recorded, the SNR was calculated as per equation (113), as the root mean square(RMS) of the cropped signal divided by the RMS of the cropped noise.

$$SNR = \frac{RMS\left(signal\right)}{RMS\left(noise\right)} \tag{113}$$

This was calculated at both the transmitter end and receiver end of the pipe, however in practice the transmitter side SNR should be considerably higher, and thus the receiver side SNR would be considered.

The signal processing methods implemented were, threshold level with bandpass filtering, cross-correlation, GCC, and variable notch filters with cross-correlation as documented in 4.3.5. Since cross-correlation methods require a time-varying signal, a 2 s chirp signal from 500-3000 Hz was used as the working signal for testing. This allowed for the simultaneous comparison of threshold methods with cross correlation, since we could consider the start of the chirp signal as the frequency of interest for the threshold method.

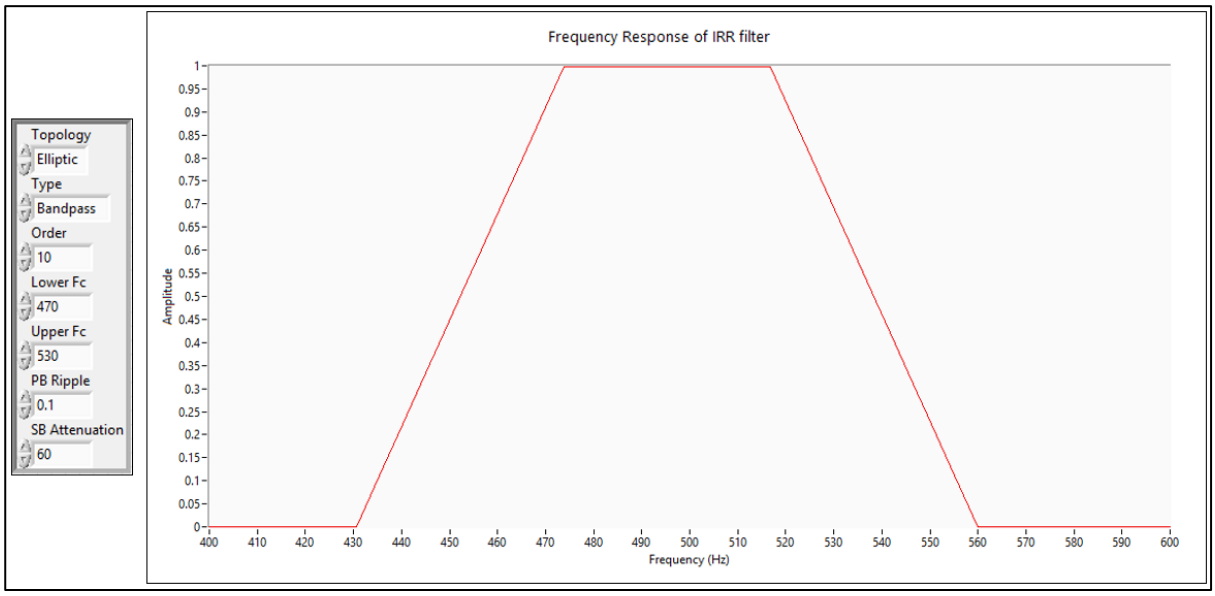

Figure 127 IRR filter specifications and frequency response

The final filter specifications used for this method are shown above in Figure 127 with the resulting frequency response of the filter. An elliptical topology was specified because it provided a sharp transition band and a flat pass band. The lower and higher frequency cut-off bands were set at 470 and 530 Hz respectively, which resulted in an effective passband of 475-515 Hz. This passband was a good compromise between reducing signal attenuation and passing through considerable noise.

Once implemented, the SNRs and TOF results for each individual method along with the temperature recorded by the thermocouple.

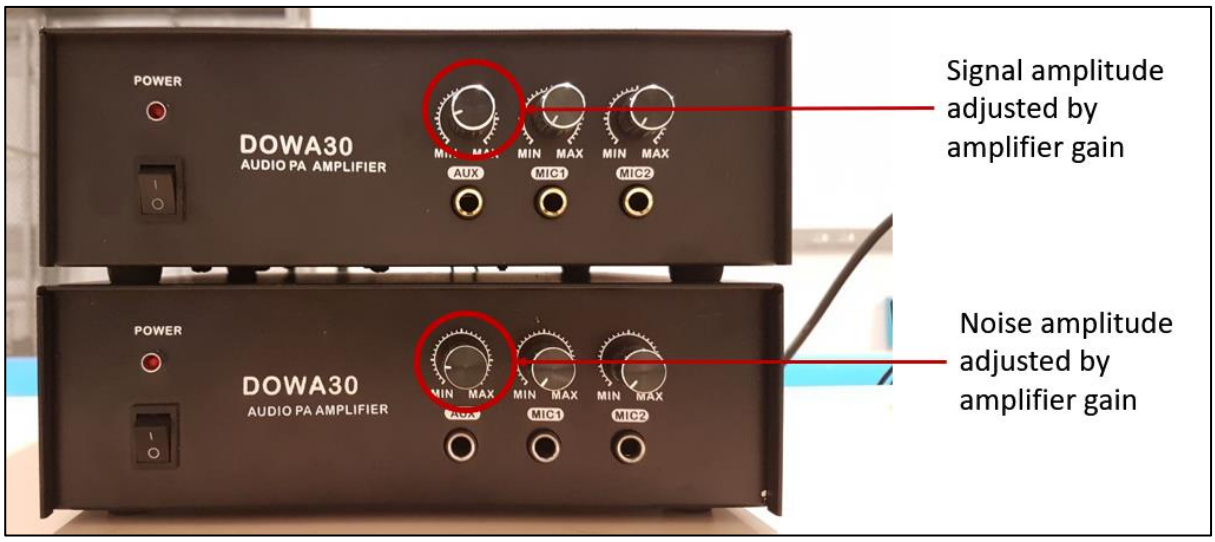

Figure 128 Line amplifier gain dials used to control SNR

Once the results for a singular reading was recorded, the signal to noise ratio was then adjusted to perform the next reading. This was adjusted manually via the respective line amplifier gain dials. This was often achieved by only adjusting the noise dial, however in cases where the sum of the noise and signal exceeded the limits of the recording, both dials were adjusted to stay within the limits and still produce the desired signal to noise ratio.

Once a gain level was set, approximately 5 readings were taken at this level before adjusting it again, since the noise signal will vary between readings cause the SNR to fluctuate slightly. The process taken was to start with higher SNR and gradually work down to lower SNR, taking more readings where greater fluctuation was observed. Approximately 105 readings were taken for the coloured noise test and 80 readings for white noise test.

$$\%Error = \frac{TOF_{ideal} - TOF_{noise}}{TOF_{ideal}} \cdot 100 \tag{114}$$

Once all the results were recorded and compiled the accuracy of each method was determined by comparing the TOF calculated using signal processing in noise to the TOF determined for each method in the absence of noise. That discrepancy was then displayed as a percentage error, where the no noise recorded TOF was considered as the ideal result.

4.5.2 A note on SNR results

Once the acoustic SNR results were compiled, it became apparent that the SNR on the transmitter-side microphone was lower than the receiver-side SNR during tests, contrary to what might be expected. Upon further inspection it was noted that this was likely due to the placement of the transmitter side microphone as shown in Figure 129. The microphones used are side address microphones and thus attenuate signals that are not perpendicular to its sensor and since the transmitter microphone is very close to and slightly below the transmitter speaker, the signal recorded has a lower amplitude than that of the right-side microphone.

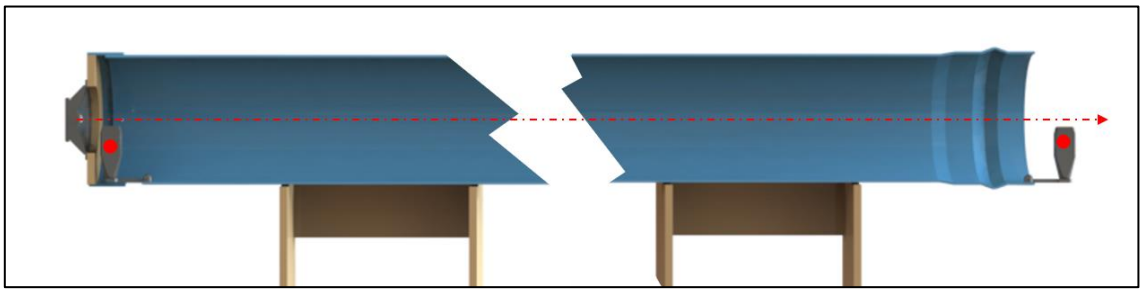

Figure 129 straight line acoustic path relative to the transmitter and receiver side condenser microphones

Due to time constraints, the positioning of the microphones was not corrected, however since SNR data was already collected a relationship between the two SNRs could be plotted as shown in Figure 130. The data shows a strong correlation and thus the transmitter side SNR can be determined from the receiver side SNR. For this study, as per convention the results are stated at the receiver-side SNR. However, in practice the transmitter-side SNR would be observed. Thus, in the discussion and conclusion sections the transmitter-side SNR will be used and referred to as the “corrected SNR” based on in Figure 130.

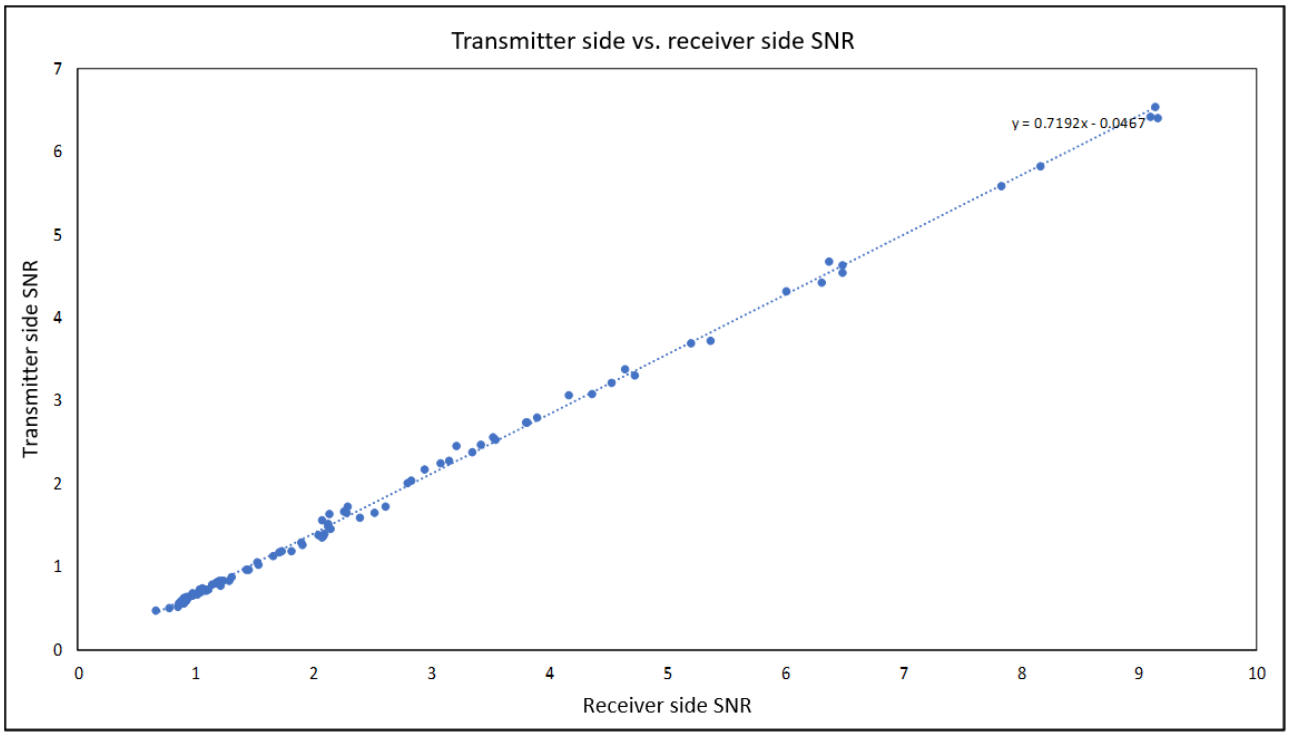

Figure 130 Transmitter side SNR vs Receiver side SNR for tests done

4.5.3 Threshold detection results

This section summarises the results obtained for the SNR tests, the first set of results pertain to the results of coloured noise tests, while the second set refers to results obtained using white noise. While the results of each TOF determination method are based on the same recorded signals, they are displayed and interpreted independently.

Coloured noise results

The first TOF determination method considered is the threshold method using bandpass filtering, producing the TOF readings shown in Figure 131, where the SNR (receiver side) is compared against the TOF recorded.

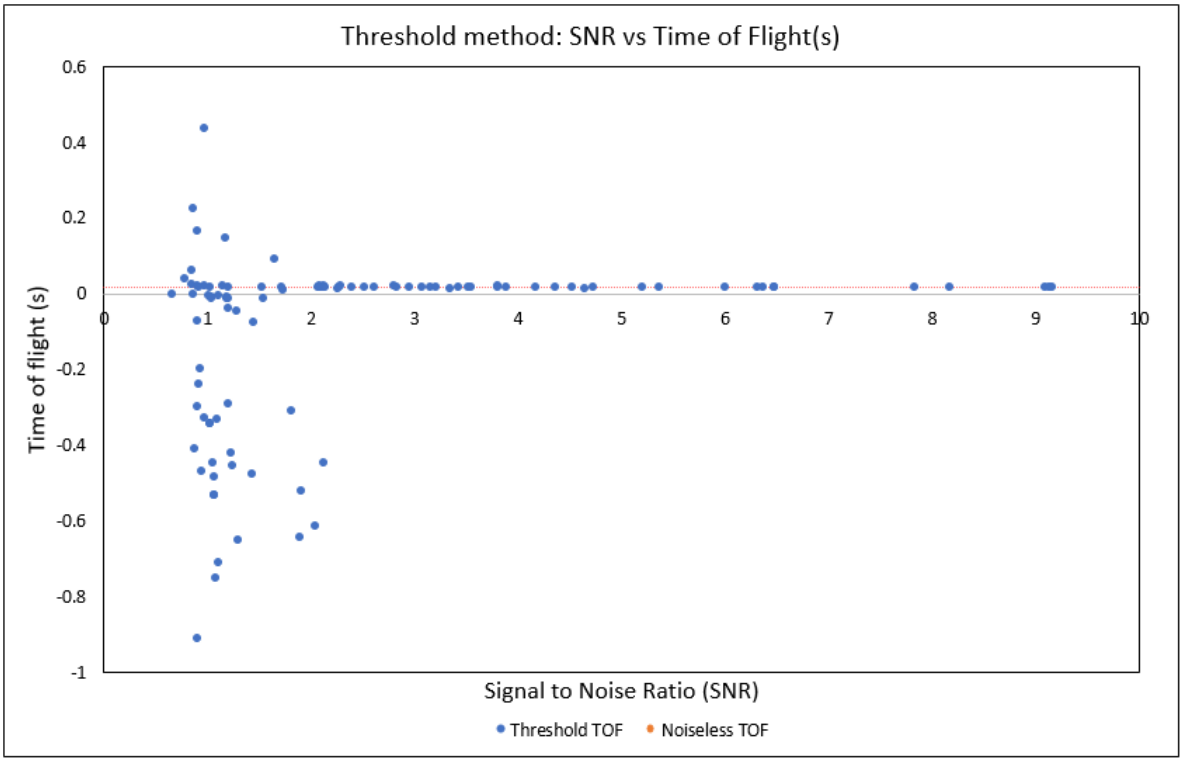

Figure 131 SNR vs TOF(s) for threshold method with bandpass filtering in coloured noise

To improve resolution the same graph is shown with adjusted axes in Figure 132, where on both figures the red line is indicative of the goal TOF recorded in noiseless conditions.

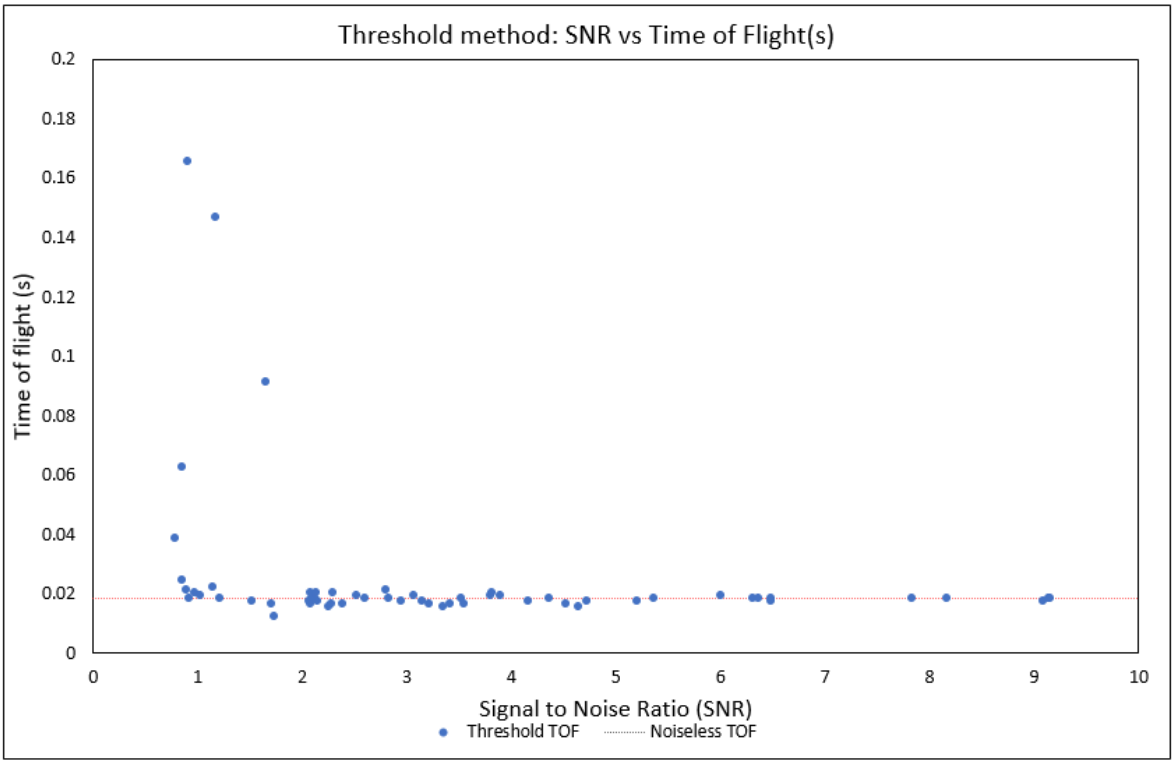

Figure 132 SNR vs TOF(s) for Threshold method with bandpass filtering (zoomed axis)

Furthermore, below in Figure 133 the results are grouped into SNR bands, compared to the average error or deviation from the noiseless TOF.

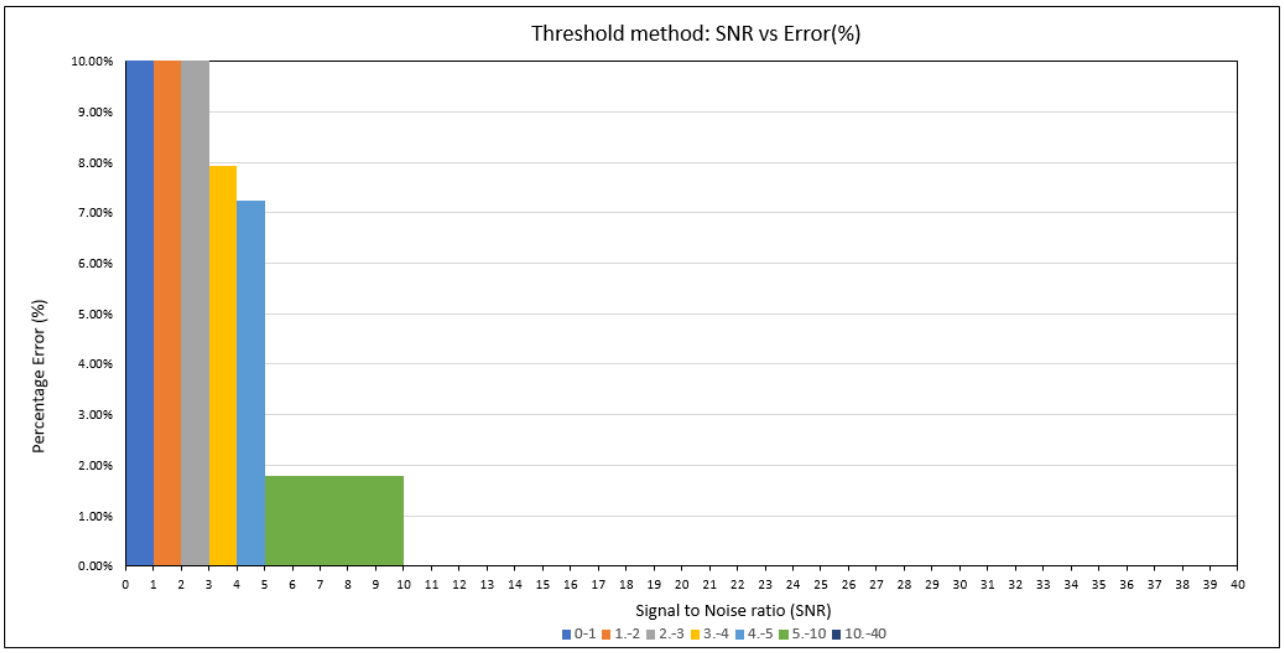

Figure 133 SNR vs TOF Error (%) for threshold method with bandpass filtering in coloured noise

Table 14 shows a comparison between the average error (%) and the standard deviation of the error (%).

Table 12: Comparison of average error (%) with the standard deviation of error (%) by SNR for Threshold detection with bandpass filtering in coloured noise

	Signal to noise ratio (SNR)						
	0-1	1.-2	2.-3	3.-4	4.-5	5.-10	10.-40
Average Error (%)	1133.04	1389.38	337.34	7.92	7.23	1.79	0.00
Standard Deviation of Error (%)	1274.36	1377.93	945.33	3.96	5.20	2.34	0.00

White Noise Results

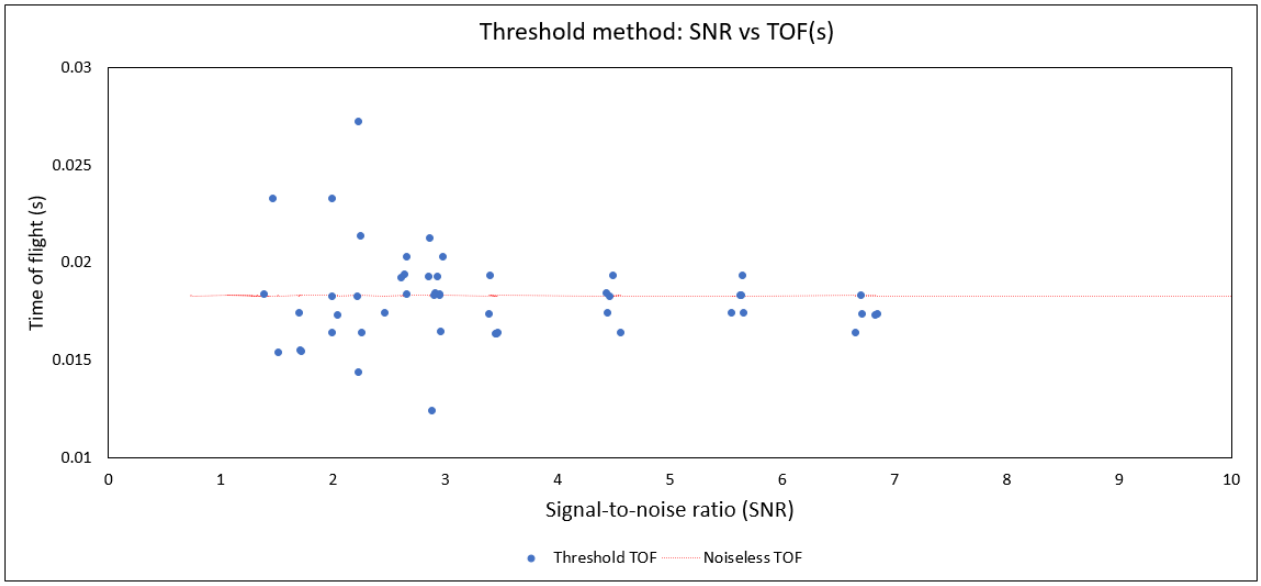

Figure 134 SNR vs TOF(s) for threshold method with bandpass filtering in white noise

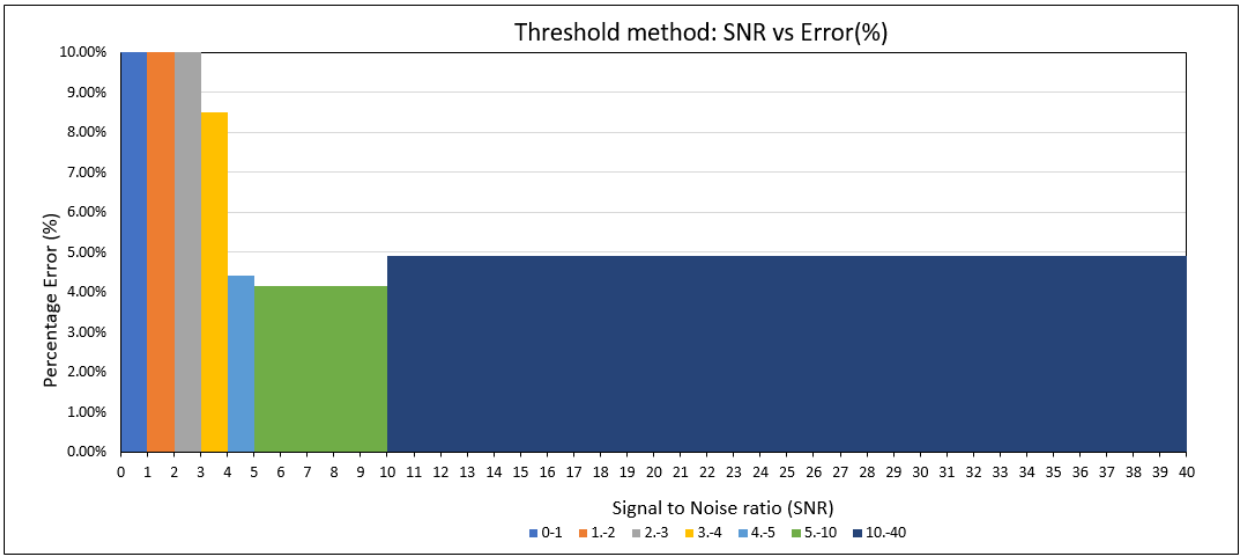

Figure 135 SNR vs TOF Error (%) for threshold method with bandpass filtering in white noise

Table 13: Comparison of average error (%) with the standard deviation of error (%) by SNR for Threshold detection with bandpass filtering in white noise

	Signal to noise ratio (SNR)						
	0-1	1.-2	2.-3	3.-4	4.-5	5.-10	10.-40
Average Error (%)	1288.77%	2550.96%	48.74%	8.51%	4.40%	4.16%	4.90%
Standard Deviation of Error (%)	1912.68%	2989.48%	177.70%	2.62%	3.76%	3.09%	0.06%

4.5.4 Threshold detection discussion

As shown in Figure 131 and Figure 132, the TOF readings for this method in coloured noise are consistent at high signal to noise ratios, but shows a great amount of deviation at lower SNRs. The deviation increases steadily as the SNR is lowered, until the threshold at around 2.5 where readings become completely inaccurate. However, even before this SNR level is reached some outliers are present.

For coloured noise, the threshold detection method produced an average error below 10 % where the SNR was greater than 3, conversely producing exceptionally incorrect results (producing an average error as high as 1377 % in the lower bands) below this SNR¸ as depicted by Figure 133. The band having a SNR of 10-40 matched the expected TOF perfectly and steadily increased to an accuracy of just below 8 % at the 3-4 band. Even within these more accurate results there was a great deviation of results, having a standard deviation of 2.34 % in the 5-10 band, 5.2 % in the 4-5 band and 7.92 % in the 3-4 band. The results within each band were rather erratic with some being very accurate (greater than 1 % accuracy) while others in the same band had large deviations (5-15 %).

In white noise, A similar pattern was observed, where it can be seen from Figure 134 that again around the 2.5 SNR region the accuracy of TOF readings drops drastically. However even before this band there is a large amount of average error, and from a SNR of 3-40 results may be relatively steady, but are not accurate.

The Results were consistent with what would be expected from this method, and as shown in Figure 108, there is a significant peak near the 500 Hz mark which is the start frequency of the signal. As such it is expected that there would be spill over when the noise in this band exceeds the threshold set in comparison to the signal. The result is that the error would drastically increase such as what occurs at the 2-3 SNR band for coloured noise in Figure 133. Furthermore, in white noise the results are less reliable since the broadband nature of the noise results in the condition that there is always interference in the frequency range that is not filtered.

4.5.5 Cross-correlation Results

This section presents the SNR test results in coloured and white noise for the standard cross-correlation method.

Coloured Noise

The cross-correlation results for coloured noise are shown in Figure 136 and Figure 137 as a comparison of the TOF(s) and the SNR. Both figures also show the TOF determined in the noiseless scenario, however the latter figure is zoomed into the more accurate TOF range of -0.018 s to 0.023 s.

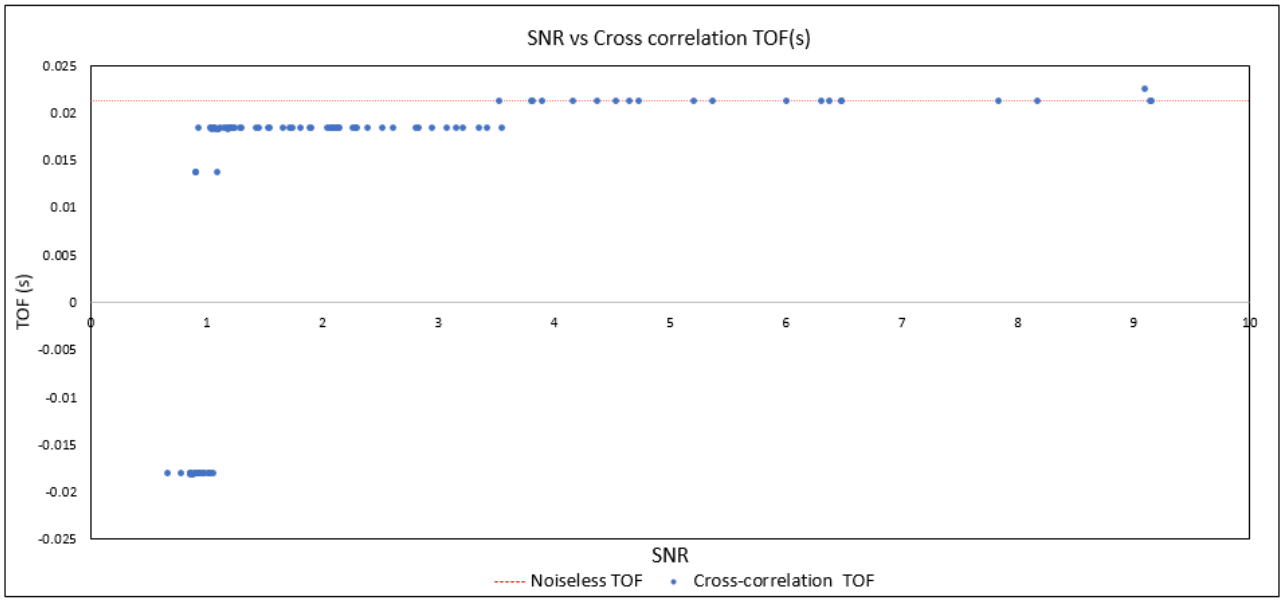

Figure 136 SNR vs Cross-correlation TOF(s) in coloured noise

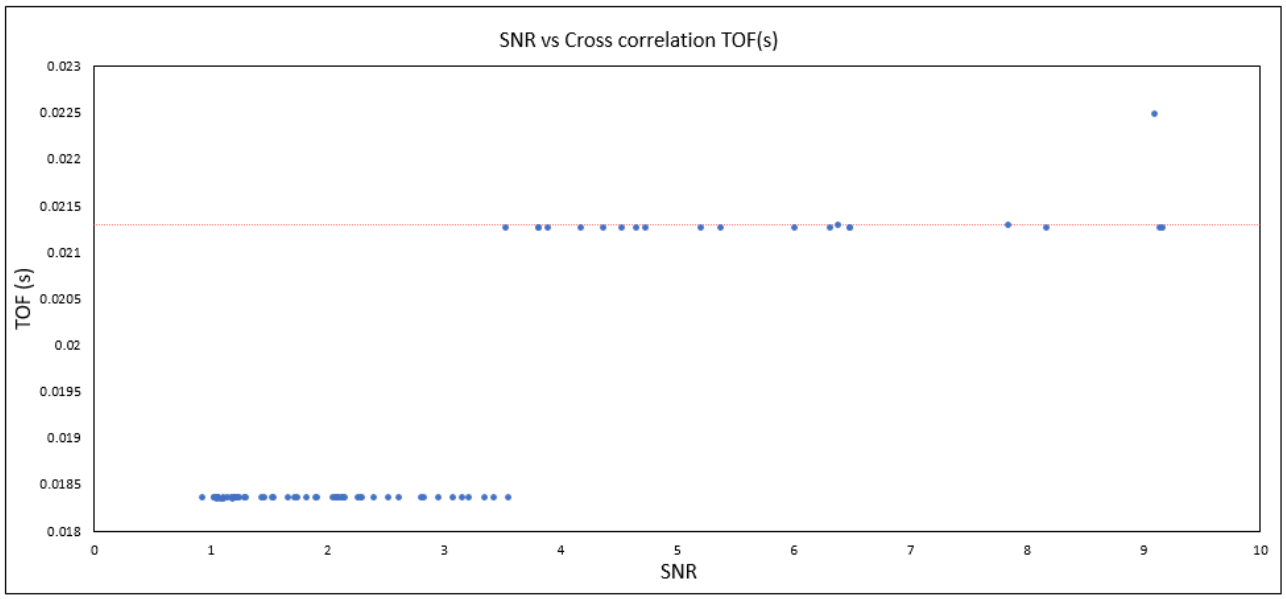

Figure 137 SNR vs cross-correlation TOF(s) in coloured noise (zoomed in)

Figure 138 shows these results are grouped into SNR bands, compared to the average error when compared to the noiseless TOF. A comparison between the average error (%) and the standard deviation of the error (%) is shown in

Table 20.

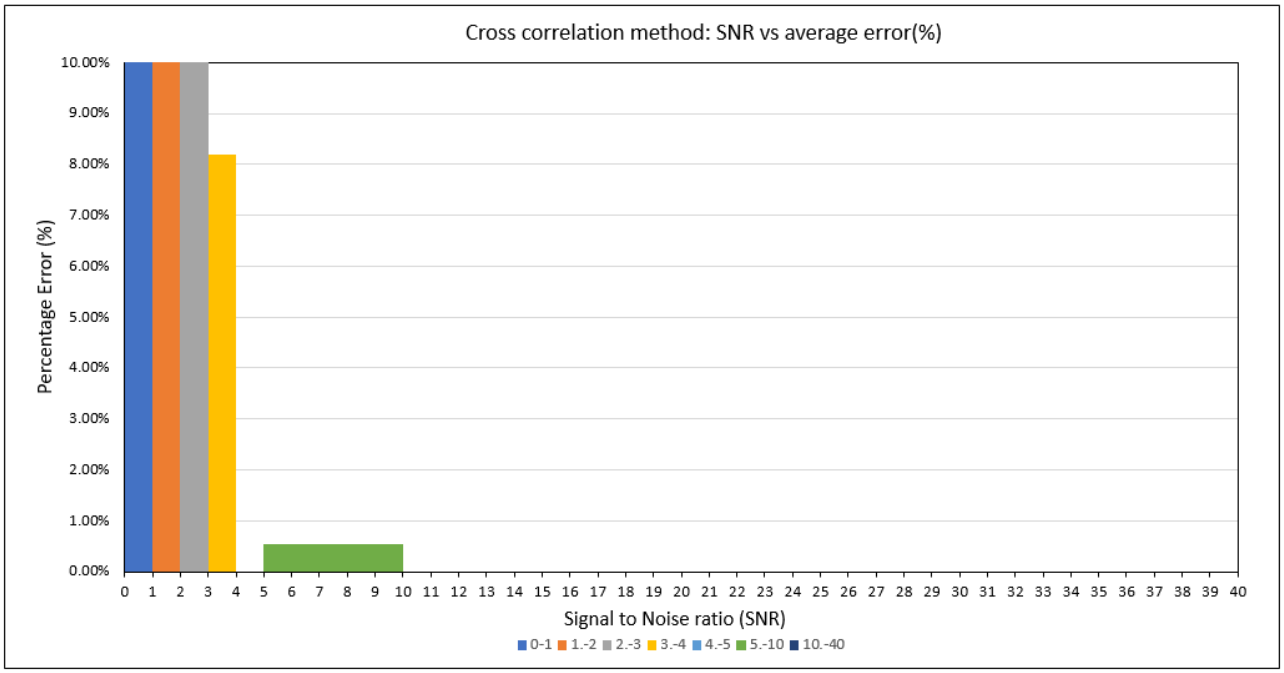

Figure 138 SNR vs average error (%) in coloured noise

Table 14: Comparison of average error (%) with the standard deviation of error (%) by SNR for cross-correlation in coloured noise

	Signal to noise ratio (SNR)						
	0-1	1.-2	2.-3	3.-4	4.-5	5.-10	10.-40
Average error (%)	159.84	33.37	13.65	8.19	0.00	0.53	0.00
Standard deviation of Error (%)	57.13	53.52	0.00	6.69	0.0	1.54	0.00

White noise

For white noise the SNR is compared to the TOF in Figure 139 and the average error in Figure 140. A comparison of the comparison between the average error (%) and the standard deviation of the error (%) is given in Table 21.

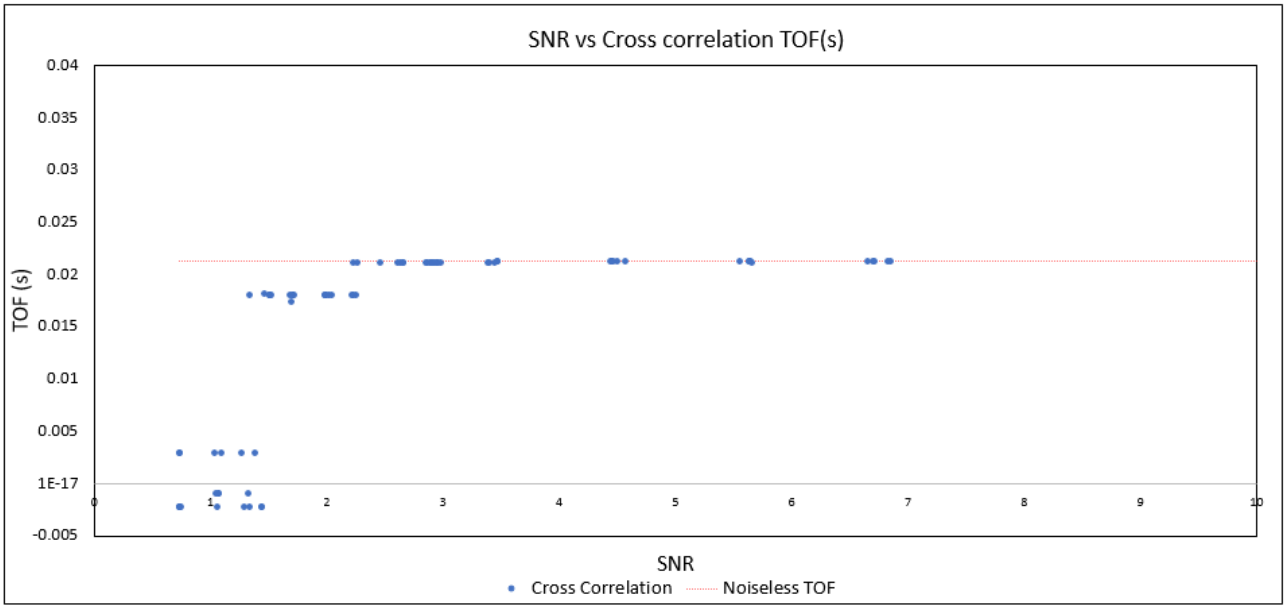

Figure 139 SNR vs Cross-correlation TOF(s) in white noise

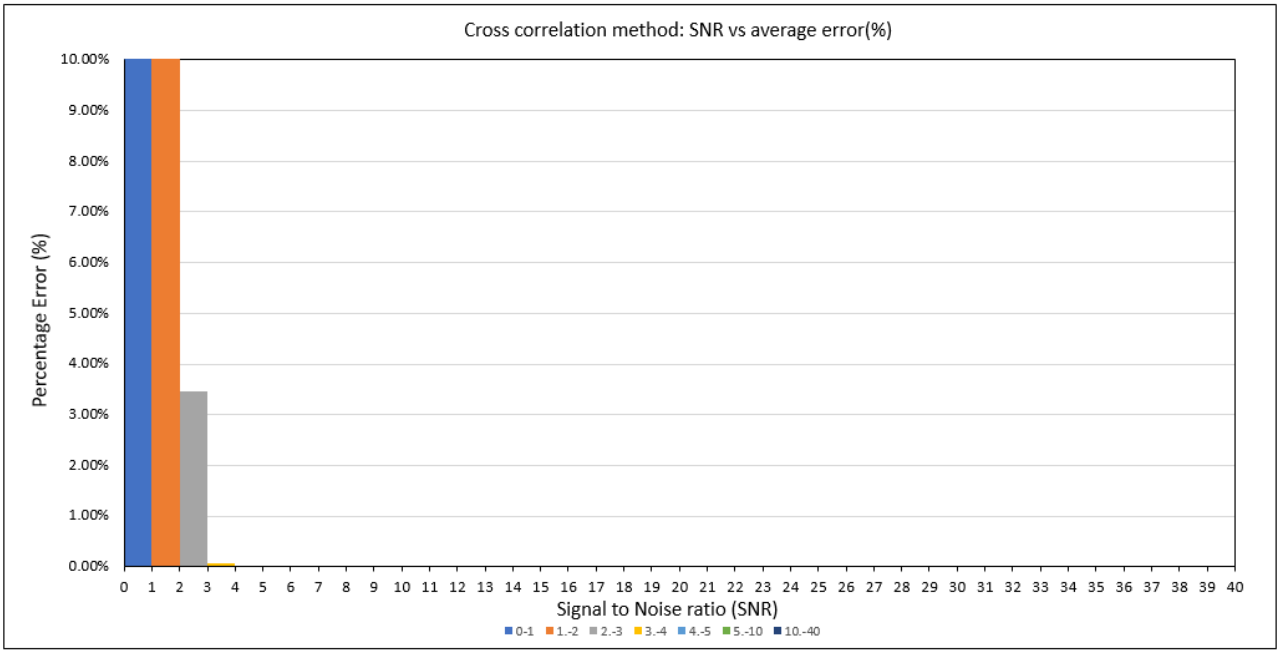

Figure 140 SNR vs average error (%) in white noise

Table 15: Comparison of average error (%) with the standard deviation of error (%) by SNR for cross-correlation in white noise

	Signal to noise ratio (SNR)						
	0-1	1.-2	2.-3	3.-4	4.-5	5.-10	10.-40
Average Error (%)	102.28%	56.35%	3.46%	0.06%	0.00%	0.01%	0.02%

Standard Deviation of Error (%)	11.58%	43.60%	6.18%	0.05%	0.00%	0.03%	0.04%

4.5.6 Cross-correlation discussion

For coloured noise, the first noticeable feature of the results is that cross correlation produces a lot more precise TOF readings than the threshold detection method. This is shown by the close tracking of the noiseless result and clustering of the data in Figure 136 and Figure 137. Furthermore, in

Table 20 in the 2-3 SNR band, the average error is 8.19 % but the standard deviation of that error is 0 %.

Additionally, the method is accurate above a SNR of 4, showing no errors in the 4-5 and 10-40 band. The average error in the 5-10 band is also a low 0.53 %, where most of the results are either entirely accurate or only off by 0.11 % (which equates to one sample difference and can be attributed to the accuracy of the hardware) with one relative outlier of 5.13 % error. Below this SNR however there is a steady drop off in accuracy, first to 8.19 % in the 3-4 range ,13.65 % in the 2-3 range and then much larger errors in the 0-1 and 1-2 range.

In white noise the method shows the same pattern of having precise results before it reaches a SNR threshold and becomes inaccurate. However, its performance is increased in broadband noise, having a greater accuracy at lower SNRs, showing very accurate results from a SNR of 3 with low deviation, as shown in Table 15 and Figure 139.

4.5.7 Variable notch filter results

This section will present the results obtained from coloured and white noise tests using the variable notch filter method with cross correlation.

Coloured noise

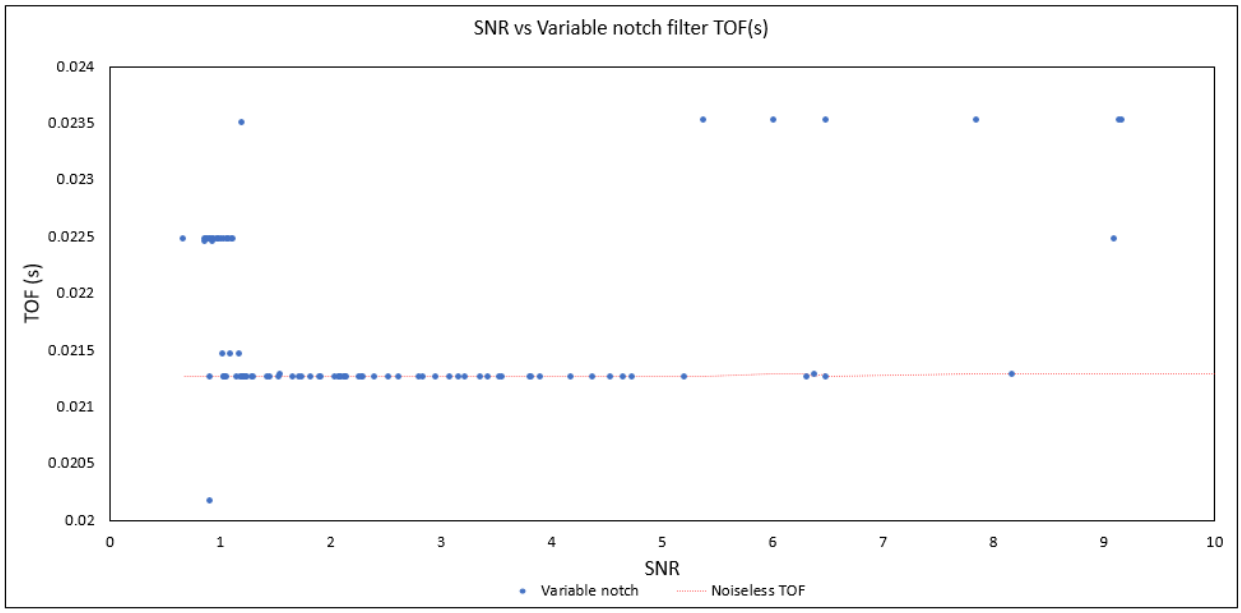

Figure 141 SNR vs TOF(s) for the variable notch method in coloured noise

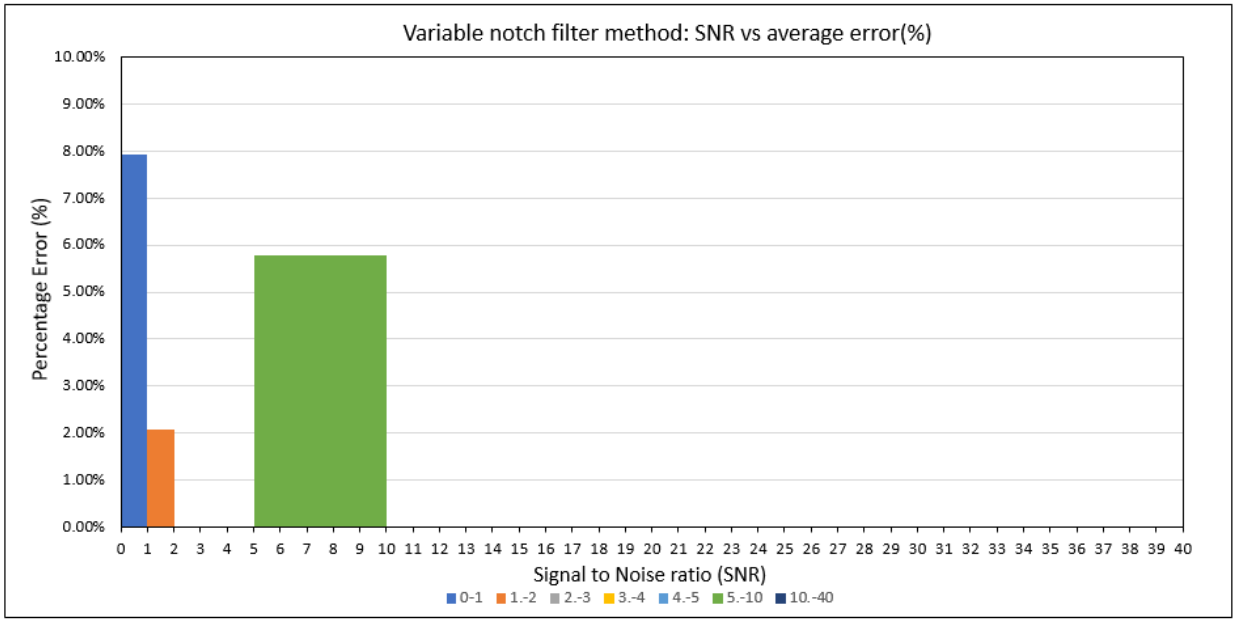

Figure 142 SNR vs average error (%) for variable notch method in coloured noise

Table 16 Comparison of average error (%) with the standard deviation of error (%) by SNR for the variable notch method in coloured noise

	Signal to noise ratio (SNR)						
	0-1	1.-2	2.-3	3.-4	4.-5	5.-10	10.-40
Average Error (%)	7.92%	1.99%	0.00%	0.00%	0.00%	5.79%	0.00%
Standard Deviation of Error (%)	5.20%	5.78%	0.00%	0.00%	0.00%	10.80%	0.00%

White Noise

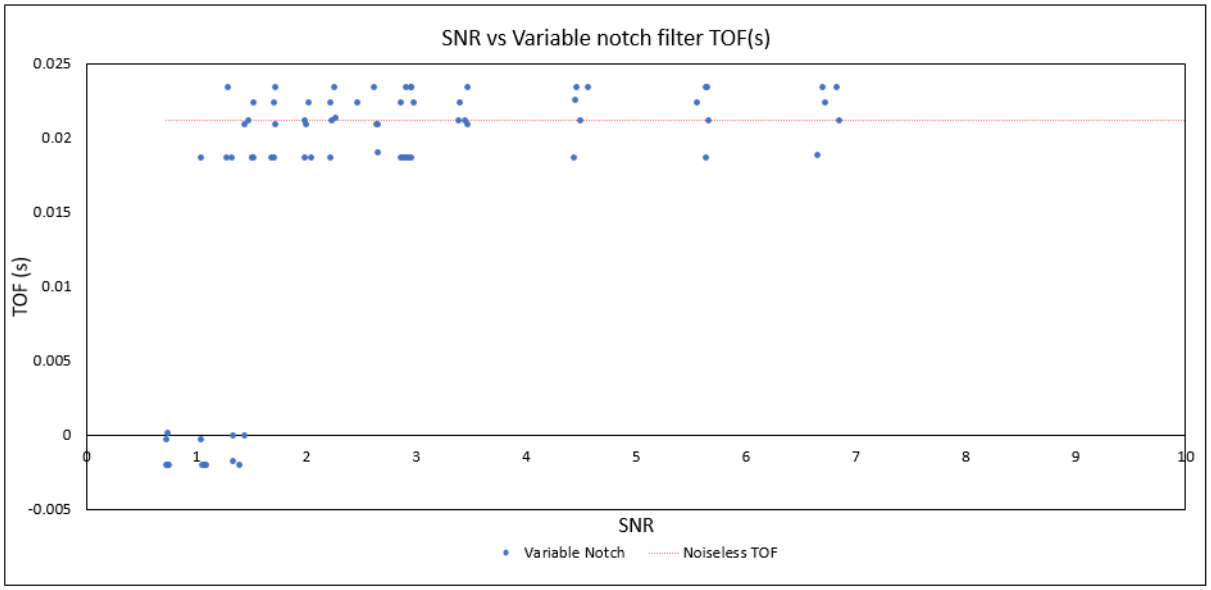

Figure 143 SNR vs TOF(s) for the variable notch method in white noise

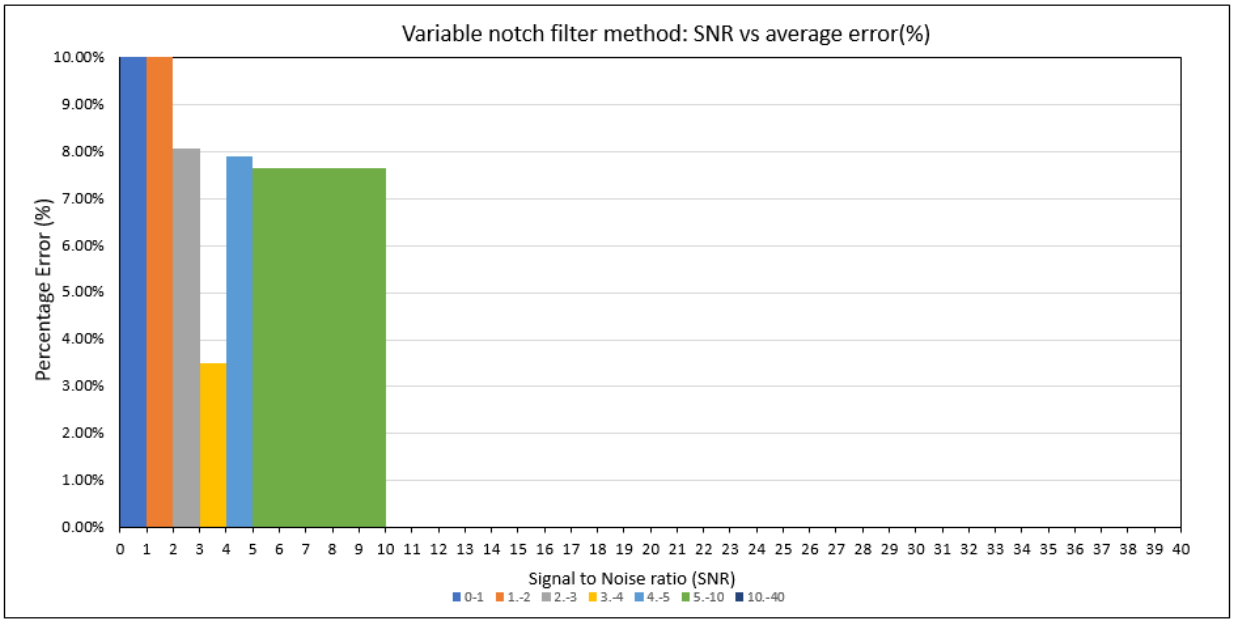

Figure 144 SNR vs average error (%) for variable notch method in white noise

Table 17 Comparison of average error (%) with the standard deviation of error (%) by SNR for the variable notch method in white noise

	Signal to noise ratio (SNR)						
	0-1	1.-2	2.-3	3.-4	4.-5	5.-10	10.-40
Average Error (%)	106.07%	40.67%	8.07%	3.50%	7.91%	7.64%	0.02%

Standard Deviation of Error (%)	4.37%	46.48%	4.16%	4.04%	4.33%	4.31%	0.04%

4.5.8 Variable notch discussion

In coloured noise, the variable notch filter method with cross correlation is noticeably more accurate that standard cross-correlation, achieving an average error of below 1.99 % in the low SNR bin of 1-2, while still having the low deviation of standard cross correlation.

However, there is a region in the 5-10 SNR band where a considerable number of outliers occur, as shown in Figure 141. The result is that the average error rises to 5.79 % while the neighbouring bands have zero error. This is most likely since the algorithm still identifies peaks and applies filters when the noise power is low, potentially applying filters that remove more of the signal than noise, resulting in false readings.

In white noise however, the variable notch method is far less accurate that standard cross-correlation. The only band in which a high accuracy is reached is above a SNR of 10 and, where the average error ranges from 3.5-8.07 % in the 2-10 SNR range. Figure 143, shows that below a SNR of 5 there is great variation in TOF readings, resulting in an unreliable result. While the method does prove successful for the purpose it was designed for (removing repetitive coloured noise) work must still be done to improve its accuracy in broadband noise.

4.5.9 Generalised cross-correlation results

In this section the results for all GCC methods are shown and grouped by the type of noise present in the test. Once all the figures for the individual methods are shown, a table summarising the average errors of each method and the standard deviation from that method is presented.

Coloured Noise

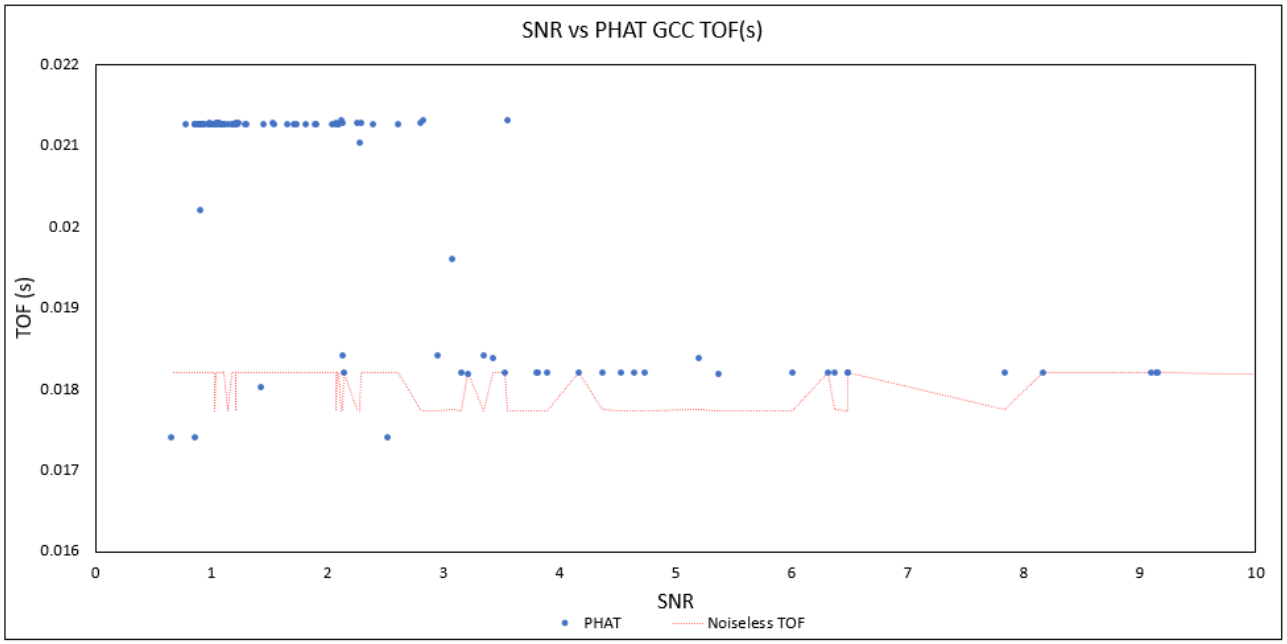

Figure 145 SNR vs TOF(s) for GCC PHAT method in coloured noise

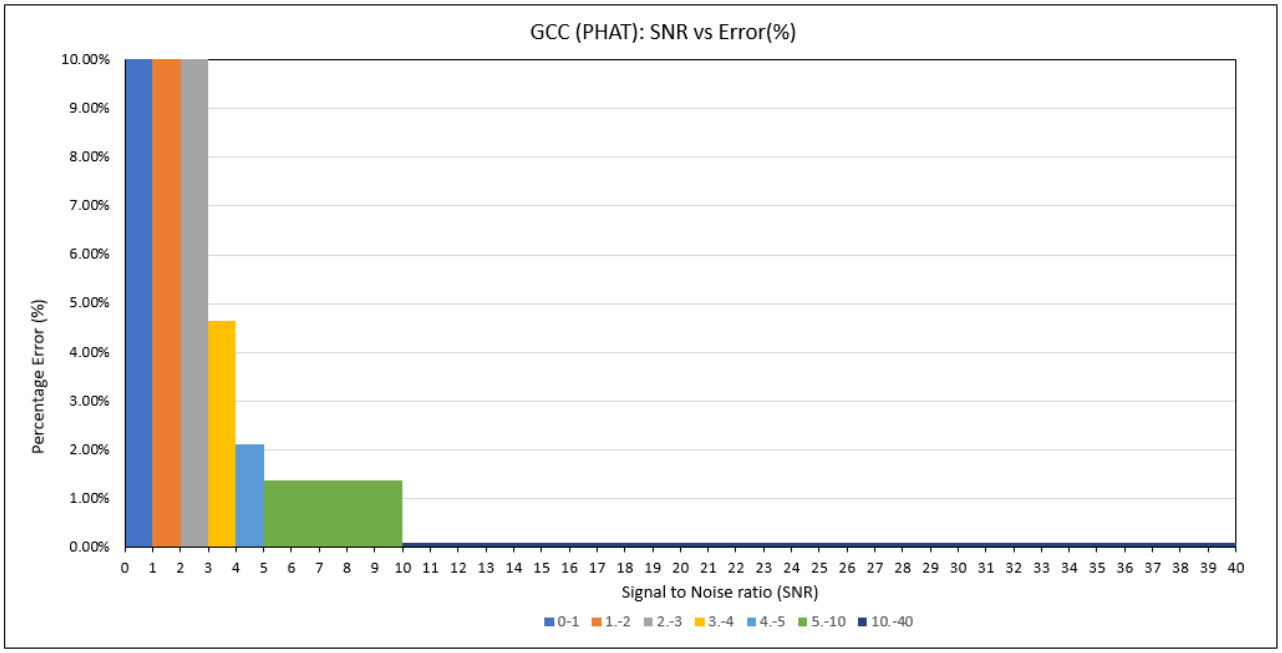

Figure 146 SNR vs average error (%) for GCC PHAT method in coloured noise

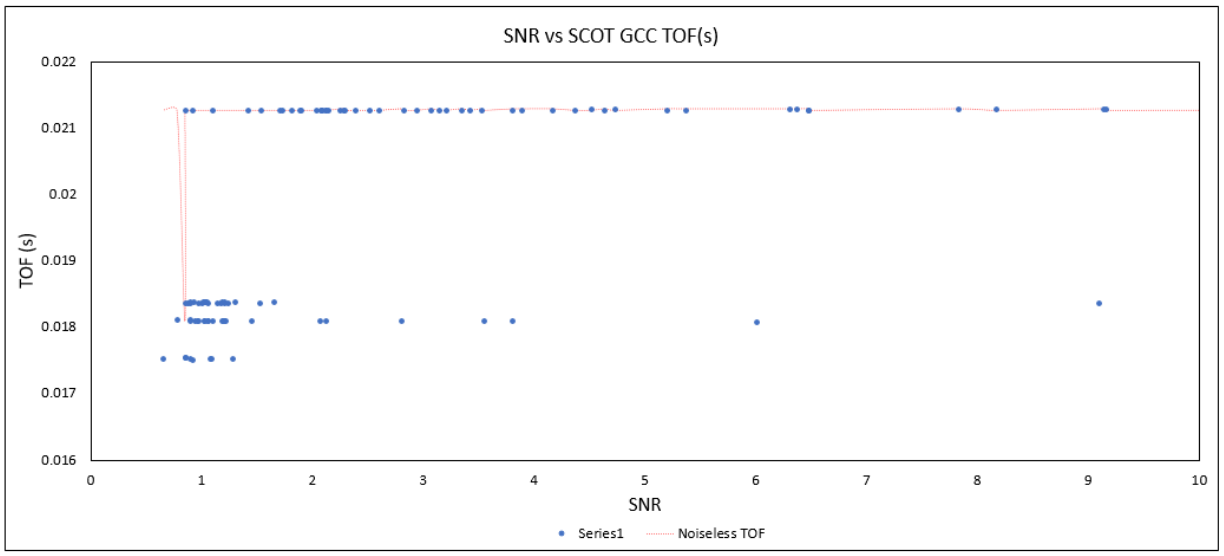

Figure 147 SNR vs TOF(s) for GCC SCOT method in coloured noise

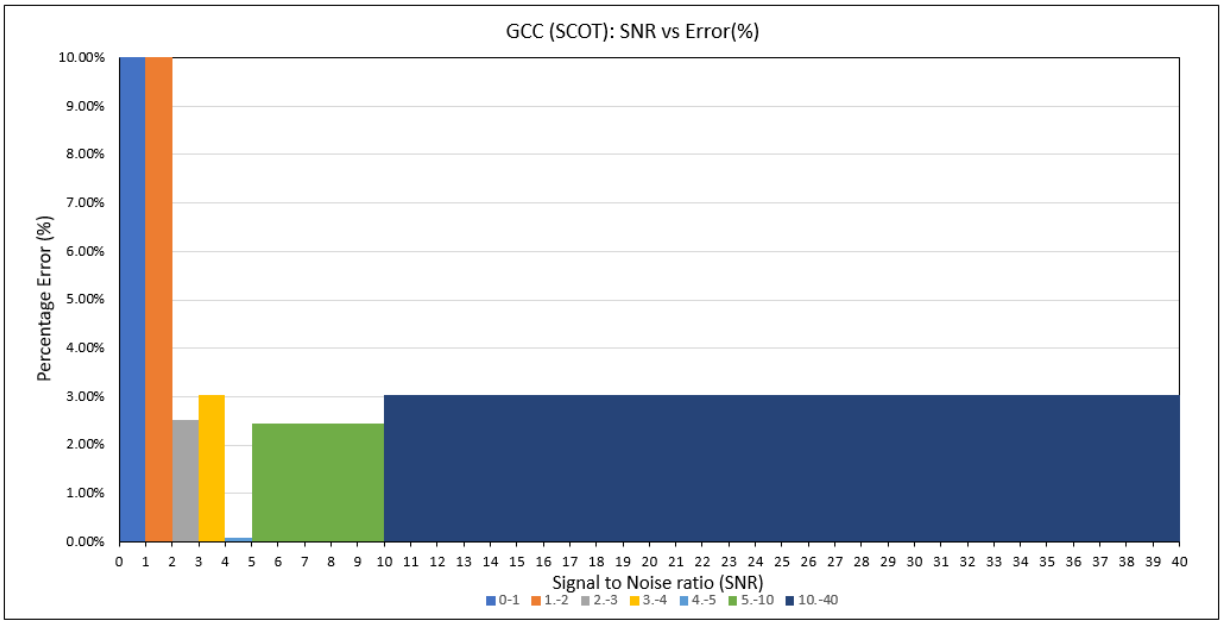

Figure 148 SNR vs average error (%) for GCC SCOT method in coloured noise

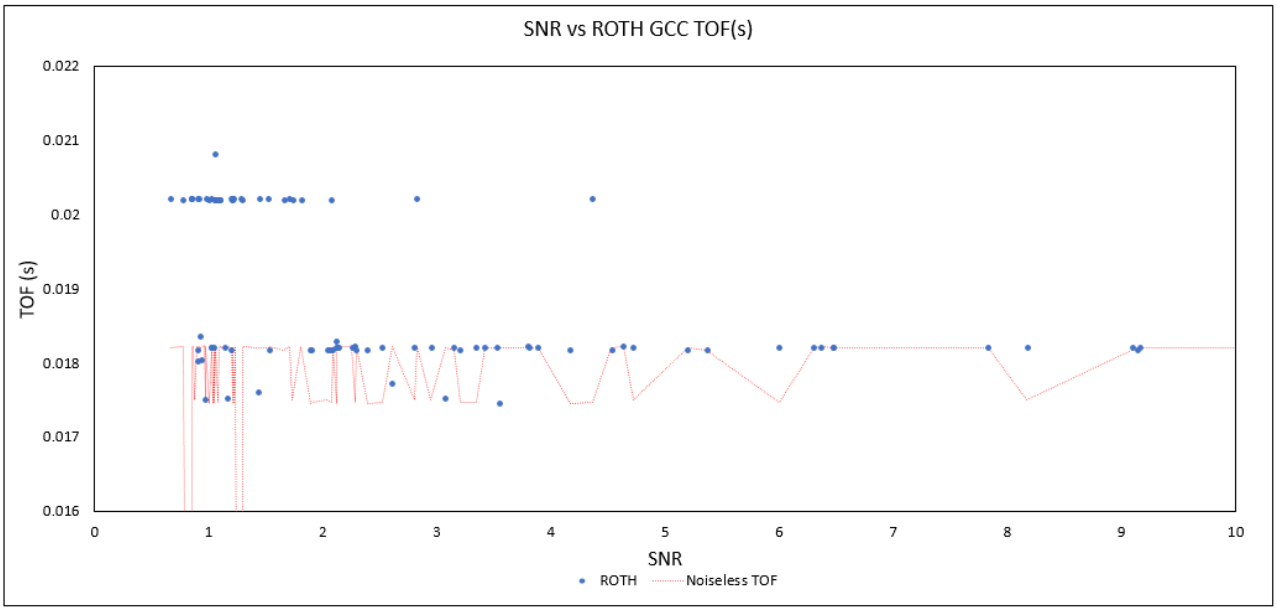

Figure 149 SNR vs TOF(s) for GCC ROTH method in coloured noise

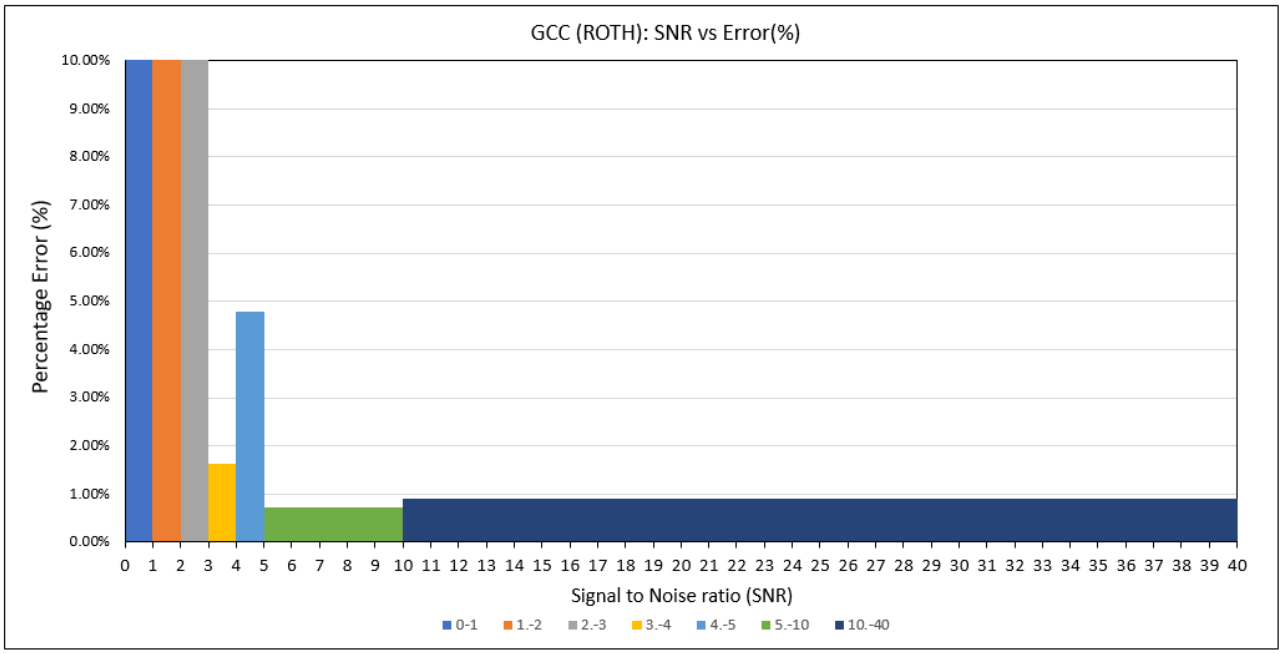

Figure 150 SNR vs average error (%) for GCC ROTH method in coloured noise

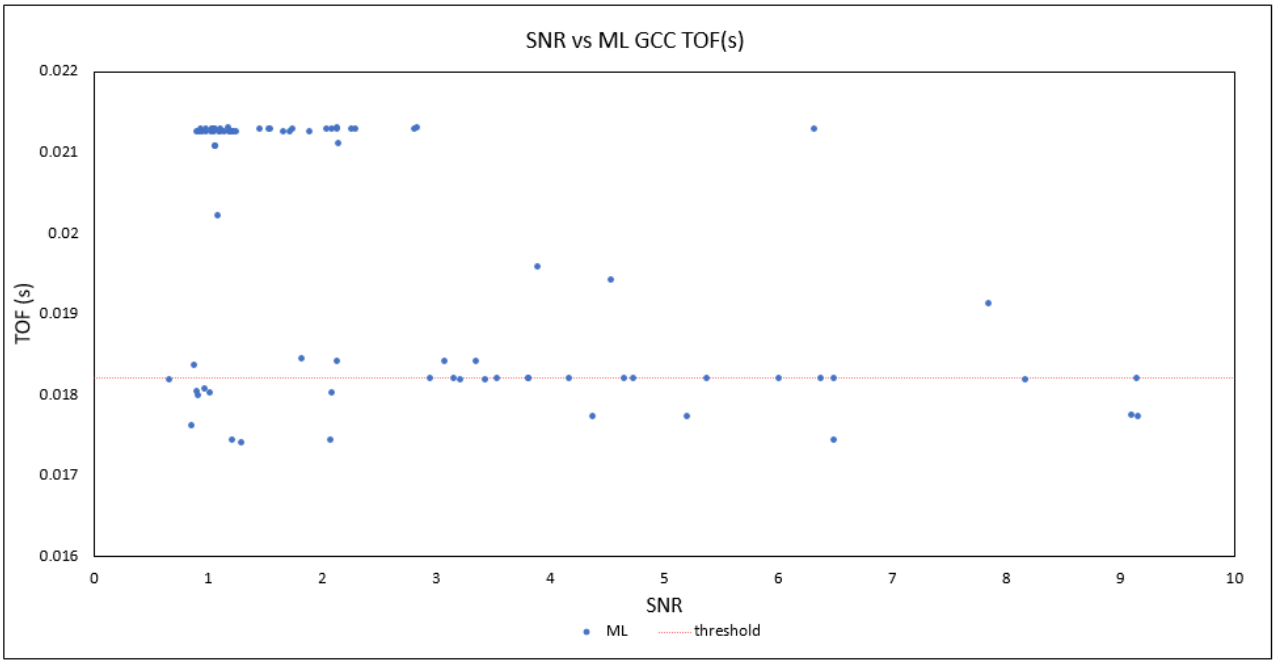

Figure 151 SNR vs TOF(s) for GCC ML method in coloured noise

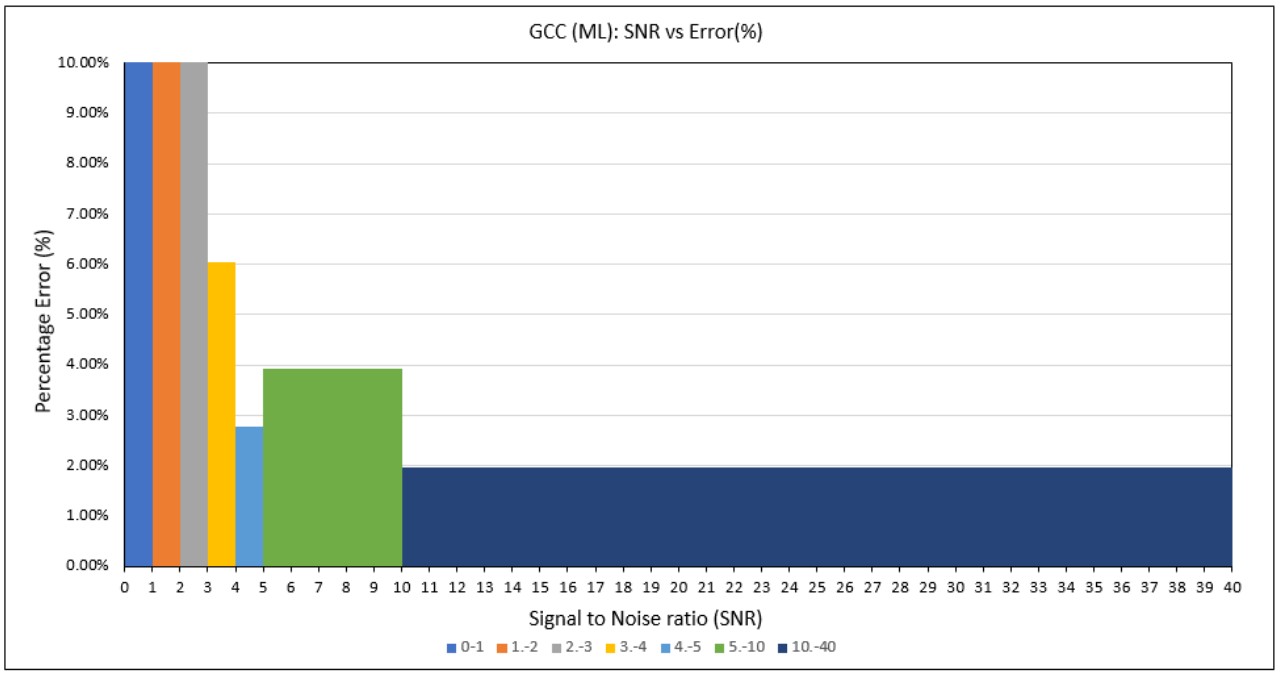

Figure 152 SNR vs average error (%) for GCC ML method in coloured noise

Table 18 Comparison of average error (%) with the standard deviation of error (%) by SNR for each GCC method in coloured noise

		Signal to noise ratio (SNR)						
		0-1	1.-2	2.-3	3.-4	4.-5	5.-10	10.-40
PHAT	Average Error (%)	15.11%	16.65%	14.93%	4.64%	2.12%	1.38%	0.10%
	σ (%)	4.03%	19.47%	21.50%	10.53%	3.18%	2.79%	0.15%
SCOT	Average Error (%)	13.41%	11.27%	2.51%	3.05%	0.09%	2.45%	3.05%
	σ (%)	4.96%	6.12%	5.58%	5.96%	0.04%	5.37%	5.99%
ROTH	Average Error (%)	7380.57%	632.83%	1218.12%	1.63%	4.80%	0.72%	0.90%
	σ (%)	10430.24%	3636.09%	5007.07%	1.94%	5.74%	1.50%	1.62%
ML	Average Error (%)	1070.46%	662.43%	348.79%	6.03%	2.77%	3.92%	1.97%
	σ (%)	4299.27%	3578.96%	1256.20%	9.44%	3.56%	5.58%	0.94%

White Noise

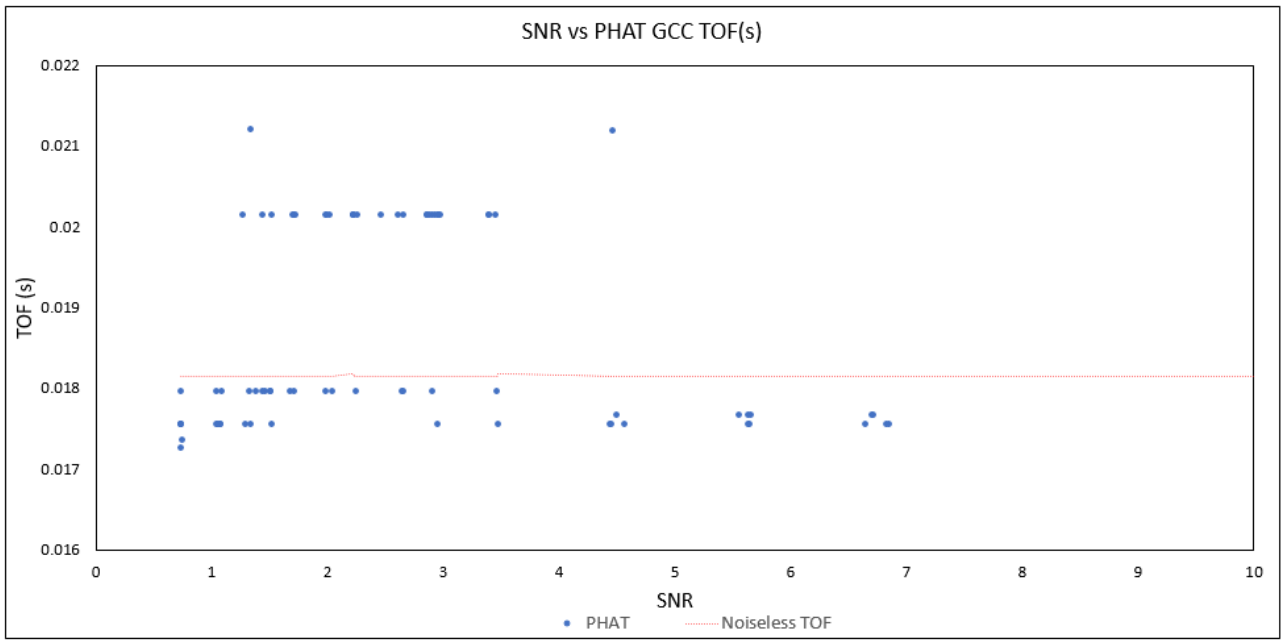

Figure 153 SNR vs TOF(s) for GCC PHAT method in white noise

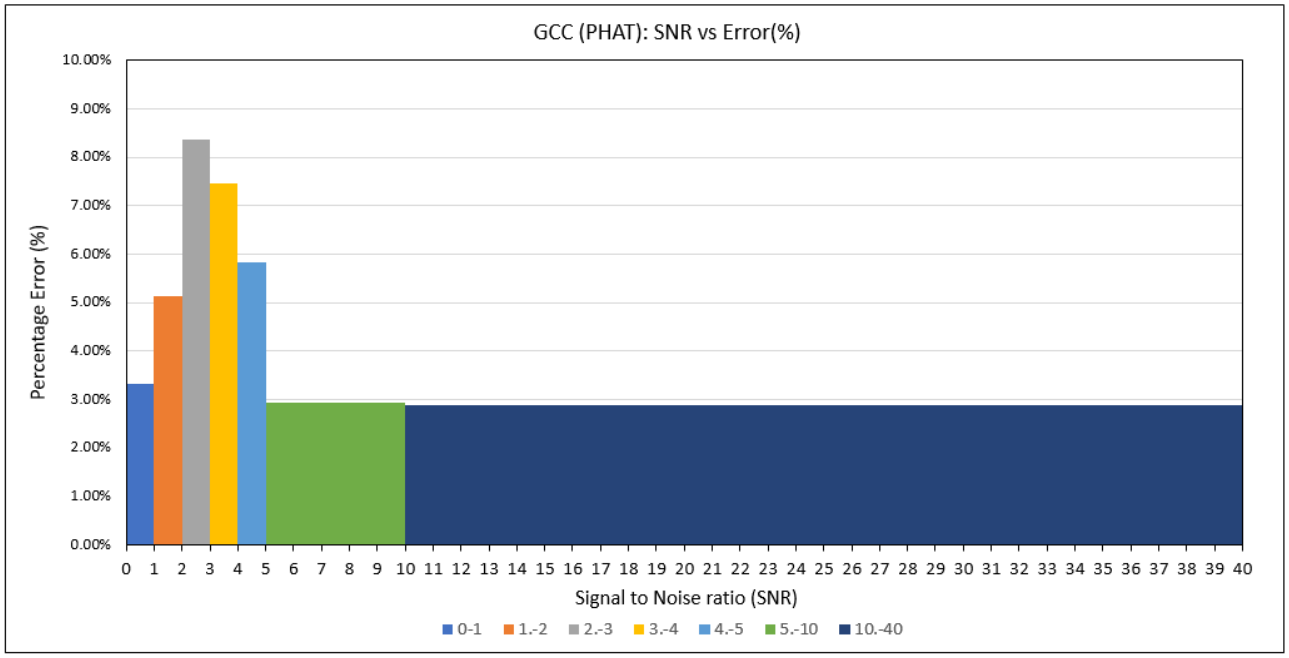

Figure 154 SNR vs average error (%) for variable notch method in white noise

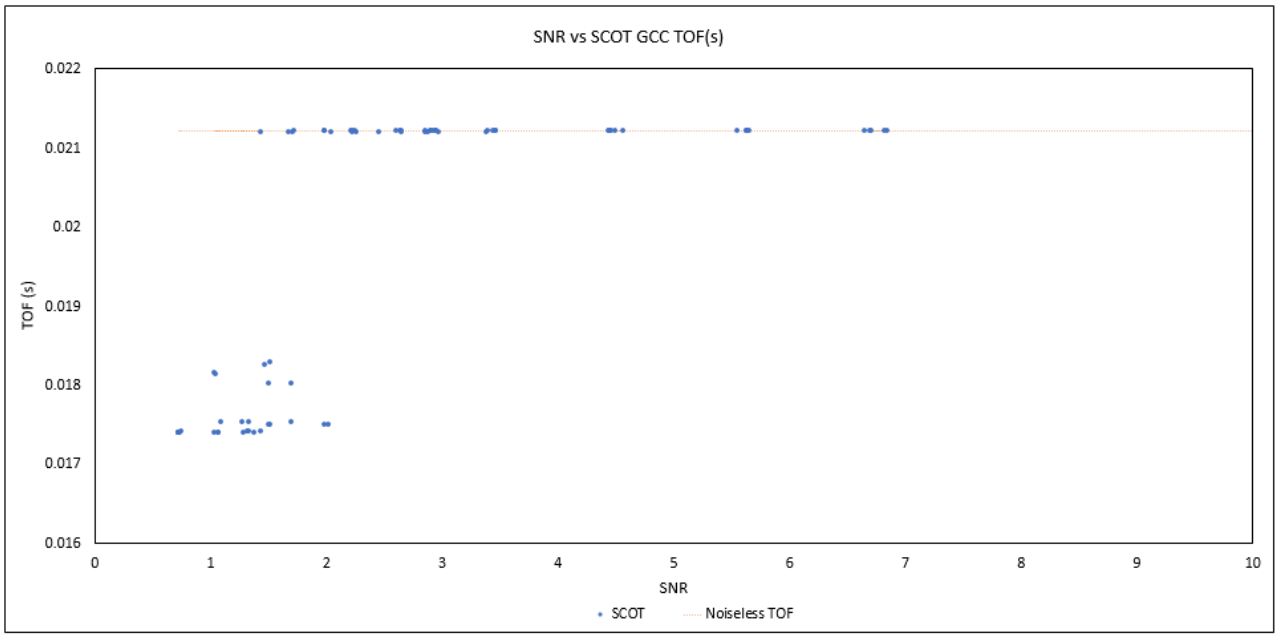

Figure 155 SNR vs TOF(s) for GCC SCOT method in white noise

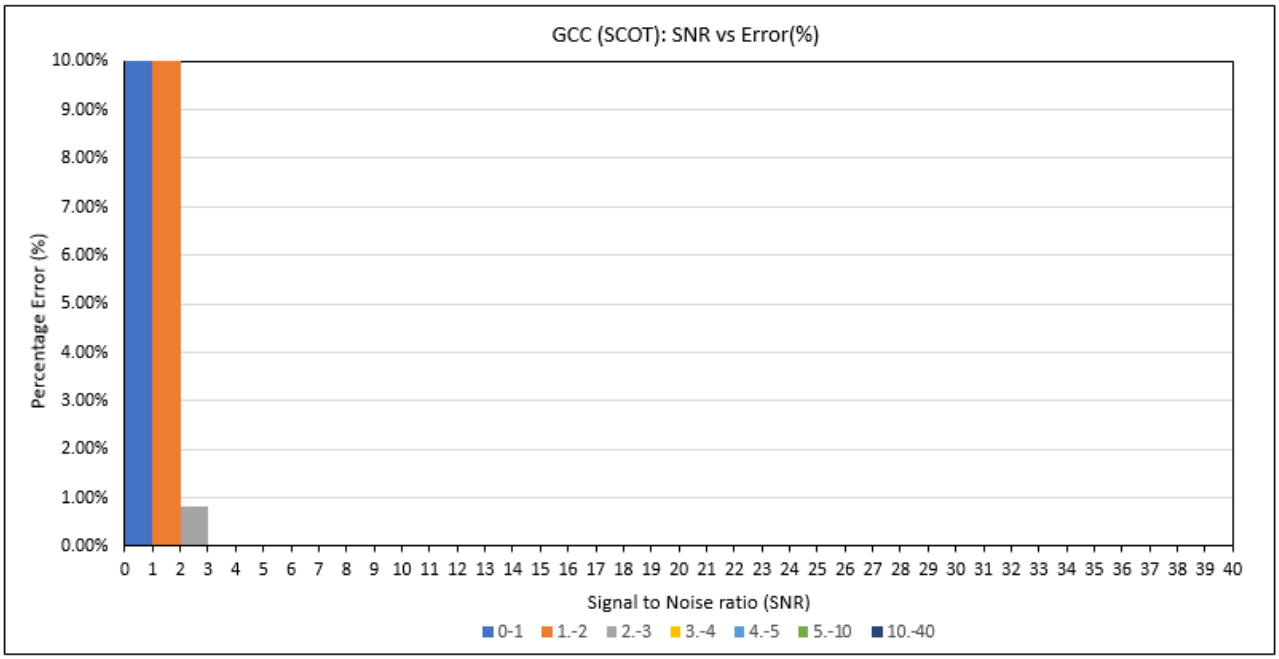

Figure 156 SNR vs average error (%) for GCC SCOT method in white noise

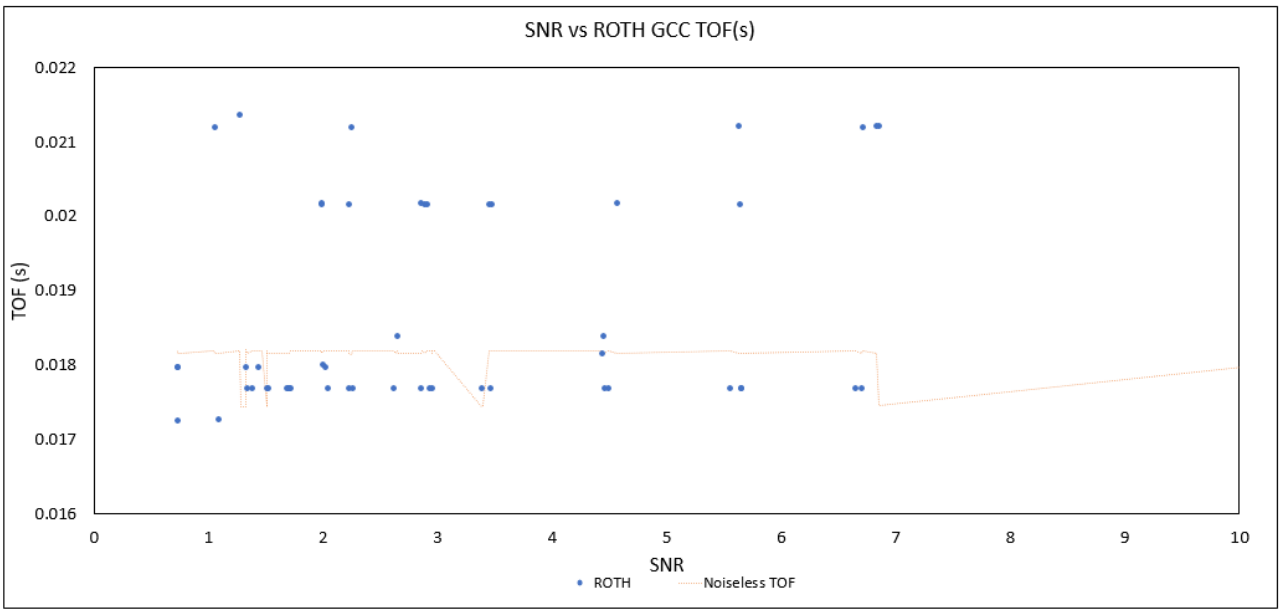

Figure 157 SNR vs TOF(s) for GCC ROTH method in white noise

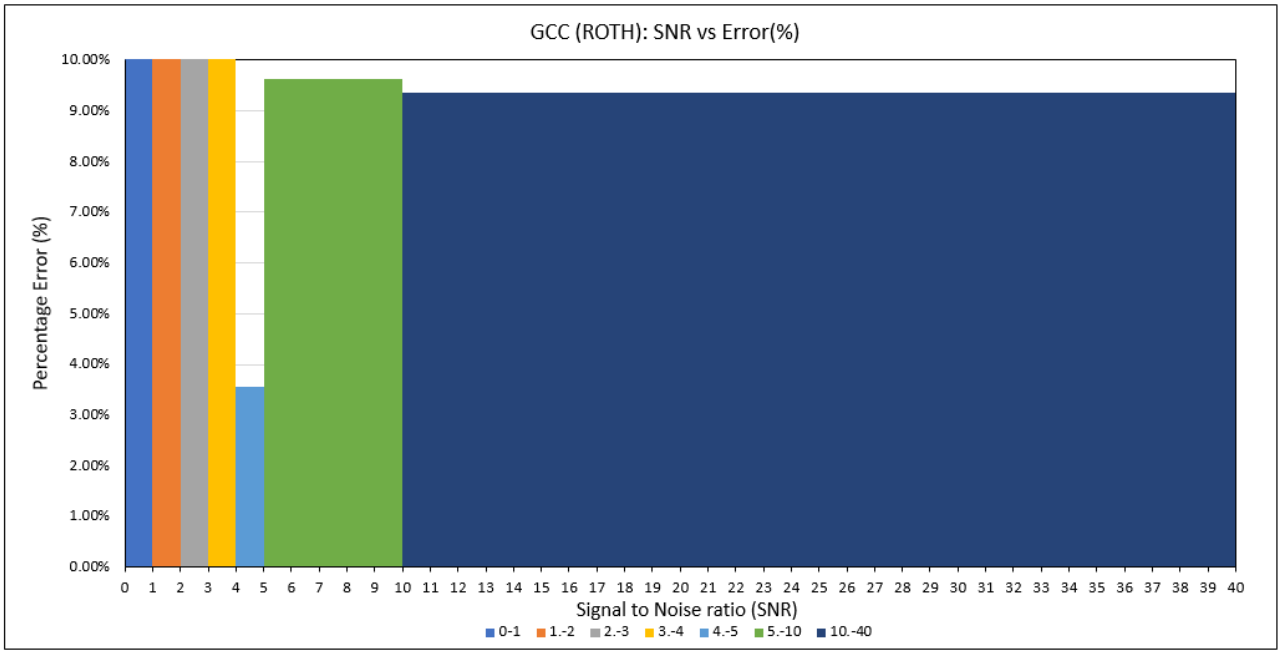

Figure 158 SNR vs average error (%) for GCC ROTH method in white noise

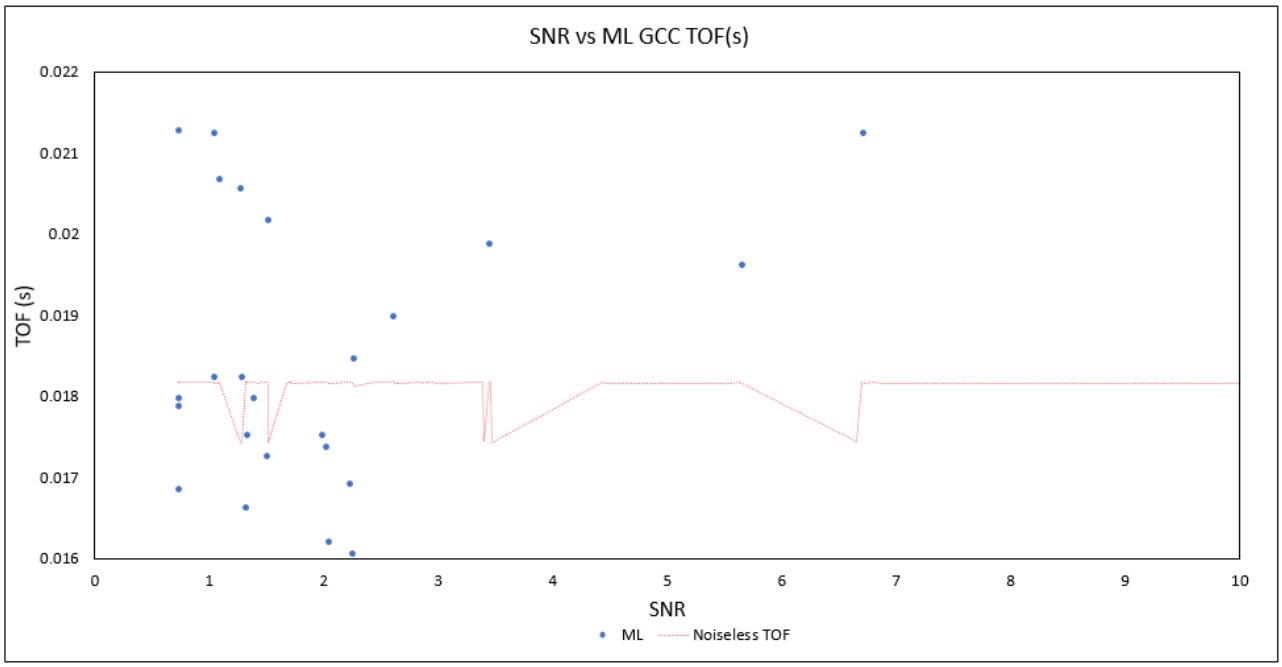

Figure 159 SNR vs TOF(s) for GCC ML method in white noise

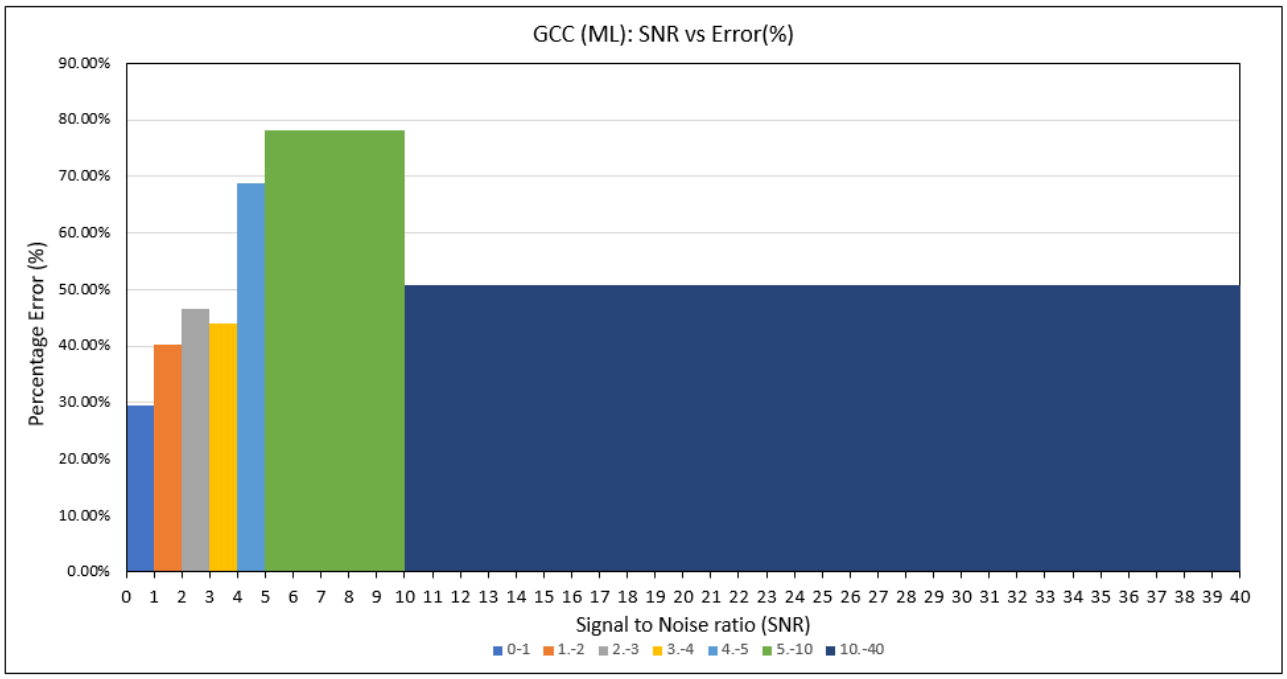

Figure 160 SNR vs average error (%) for GCC ML method in white noise

Table 19 Comparison of average error (%) with the standard deviation of error (%) by SNR for each GCC method in white noise

		Signal to noise ratio (SNR)						
		0-1	1.-2	2.-3	3.-4	4.-5	5.-10	10.-40
PHAT	Average Error(%)	3.33%	5.13%	8.36%	7.46%	5.82%	2.93%	2.87%
	σ (%)	1.22%	4.81%	4.30%	4.38%	5.46%	0.31%	0.36%
SCOT	Average Error(%)	18.04%	13.09%	0.84%	0.02%	0.00%	0.00%	0.00%
	σ (%)	0.04%	7.10%	3.64%	0.04%	0.00%	0.00%	0.00%
ROTH	Average Error(%)	21.75%	19.94%	15.05%	12.08%	3.57%	9.62%	9.36%
	σ (%)	21.14%	20.50%	13.51%	11.90%	3.89%	7.34%	6.24%
ML	Average Error(%)	29.44%	40.28%	46.48%	44.02%	68.76%	78.13%	50.79%
	σ (%)	39.65%	34.22%	46.19%	20.56%	27.78%	53.71%	50.65%

4.5.10 Generalised cross-correlation discussion

In coloured noise, GCC methods overall performed considerably worse than the variable notch method and surprisingly slightly worse than standard cross correlation. In general results tended to be accurate only in the very high SNR range of 10-40. Several weightings, notably PHAT and ROTH also had deviations in the noiseless TOF recorded, as shown by the zig-zagged lines in Figure 145 and *Figure 149*. Consequently, the results from these methods in coloured noise had high deviations, which was especially evident for the ROTH and ML weightings, which were extremely inaccurate a

low SNRs. This is unexpected, since the GCC method should be more accurate than standard cross correlation, especially in high noise scenarios.

While much of the same performance was present for the white tests, the SCOT method showed a huge improvement in accuracy and reliability. The method showed consistently accurate from a SNR of around 2.5, after which the accuracy of the method reduced. This was as expected from literature where the SCOT method was cited as being effective in broad band noise.

The ML and ROTH weightings however did not perform as expected from literature. This could be due to the implementation of the GCC method in LabVIEW. While the standard cross correlation was implemented using VIs from a dedicated toolkit, GCC had to be implemented from the basic LabVIEW functions. Since only one function existed for the inverse Fourier transform, the associated Fourier transform VI was used to maintain consistency, which did not allow for effective windowing to get a more accurate representation of the frequencies present.

4.5.11 Overall comparison

The overall comparison of the average error (%) in SNR bands for TOF determination between all methods are shown in

Table *20* for coloured noise and Table 21 for white noise.

Table 20 Comparison of average error (%) in SNR bands for TOF determination methods in coloured noise

TOF determination method	SNR bands						
	0-1	1.-2	2.-3	3.-4	4.-5	5.-10	10.-40
Threshold method	1133.04%	1389.38%	337.34%	7.92%	7.23%	1.79%	0.00%
Cross-correlation	159.84%	33.37%	13.65%	8.19%	0.00%	0.53%	0.00%
Variable Notch	7.92%	2.09%	0.00%	0.00%	0.00%	5.77%	0.00%
PHAT	15.11%	16.65%	14.93%	4.64%	2.12%	1.38%	0.10%
SCOT	13.41%	11.27%	2.51%	3.05%	0.09%	2.45%	3.05%
ROTH	7380.57%	632.83%	1218.12%	1.63%	4.80%	0.72%	0.90%
ML	1070.46%	662.43%	348.79%	6.03%	2.77%	3.92%	1.97%

Table 21 Comparison of average error (%) in SNR bands for TOF determination methods in white noise

TOF determination method	SNR bands						
	0-1	1.-2	2.-3	3.-4	4.-5	5.-10	10.-40
Threshold method	1288.77%	2550.96%	48.74%	8.51%	4.40%	4.16%	4.90%
Cross-correlation	102.28%	56.35%	3.46%	0.06%	0.00%	0.01%	0.02%
Variable Notch	106.07%	40.67%	8.07%	3.50%	7.91%	7.64%	0.02%
PHAT	3.33%	5.13%	8.36%	7.46%	5.82%	2.93%	2.87%
SCOT	18.04%	13.09%	0.84%	0.02%	0.00%	0.00%	0.00%

ROTH	21.75%	19.94%	15.05%	12.08%	3.57%	9.62%	9.36%
ML	29.44%	40.28%	46.48%	44.02%	68.76%	78.13%	50.79%

In coloured noise, the variable notch method was shown to be the most accurate TOF determination method, having the lowest error in the low SNR bands where the other methods typically became extremely inaccurate. The highest average error seen for this method was 7.92 % in the 0-1 SNR band (0-0.67 corrected SNR) and a 1.99 % error in the 1-2 band (0.67-1.4-corrected SNR), with very low errors below this. There was however a 5.77 % error in the 5-10 band though this is most likely due to the over application of notch filters in a region where noise is still low.

In white noise however, the variable notch method struggled and the GCC SCOT method became the most accurate TOF determination method. Having an error of below 1 % even from the 2-3 SNR band (1.4-2.1 corrected SNR), performing slightly better than standard cross correlation. These results display that the preferable TOF method is largely dependent on the type of noise present in the boiler as well as the intensity of that noise.

5. Conclusions and recommendations

5.1 Conclusions

This chapter presents a summary of the work completed and conclusions drawn for each chapter of this dissertation to satisfy the objectives and thus overall goal of this study – **gain an in-depth understanding of the operation of the acoustic pyrometer and to determine the implementation guidelines of an acoustic pyrometer system for FEGT measurement.**

5.1.1 General literature survey

The first objective for this project was to provide a **review of current methods for FEGT measurement**. In fulfilment of this the following work was completed and outcomes were concluded.

- An overview of the coal fired power plant was presented, explaining fundamental operation and giving context to the boiler and furnace exit and components that might affect the resulting temperature profile at this region. FEGT temperature measurement was then motivated through the benefits that knowledge of this region had from a research perspective and diagnosis tool for operating actions.

- Contact and non-contact temperature measurements were reviewed for FEGT determination. This review concluded that contact thermocouple methods are only useful for spot measurement and not continuous monitoring due to practical limitations. Radiation pyrometry was then presented as a promising alternate non-contact method, however depth limitations are shown to still inhibit its use. Following on, acoustic pyrometry was reviewed, describing its fundamental operating principle, its applications and commercially available variations.

- It was concluded that acoustic pyrometry is the most applicable continuous measurement method for furnace exit temperature measurement, and numerous factors affecting its measurement accuracy were reviewed.

5.1.2 Temperature profile reconstruction

The second objective for this study was to **model acoustic pyrometry temperature reconstruction with multiple acoustic paths,** which was achieved through the following summary of work done and conclusions drawn.

- A literature review of temperature reconstruction methods applicable to acoustic pyrometry was conducted, identifying and comparing 5 potential reconstruction methods for simulation. From these methods, a least squares approach with RBF interpolation was identified as the most promising method for temperature reconstruction.

- In fulfilment of the second project objective, a Mathcad model was then developed in which the reconstruction of defined temperature profiles could be simulated based on a variation of input conditions. Amongst these conditions is the ability to change acoustic transmitter and receiver locations, the dimensions of the rectangular furnace to be simulated, properties of the gas and accuracy of the acoustic measurement. Four main temperature profiles were considered, namely the single peak, steep single peak, asymmetrical peak and double peak profiles.

- The reconstruction model was developed such that the distance matrices and acoustic path geometry are automatically calculated from input conditions, allowing for further testing of a variety of reconstruction scenarios. For each scenario, acoustic time of flight is simulated based on the integration of straight parametrised acoustic paths through a defined temperature profile.

- Temperature data points were calculated using a Moores-Penrose method to find the least squares solution using the calculated geometric matrices, simulated time of flights and gas properties. After the temperature data point determination, multiple interpolation methods were applied. Most notably an improved RBF interpolation method using Rippa's algorithm for shape factor prediction was applied. As a basis of comparison, cubic spline interpolation, multiple regression and Lagrange interpolation were also applied. The accuracy of these reconstructions was then appraised based on mean, RMS and energy error calculations.

- Testing was then conducted to determine the effect of random path error on temperature reconstruction, over a range of 0-2% path error in increments of 0.5%. The methodology was devised such that each set temperature profile was systematically tested for each increment of path noise and acoustic pyrometer type using 100 iterations of TOF simulation for each

test. These tests were then repeated for varying amounts for acoustic time of flight path repetition.

- It was concluded from the tests that random path error reduces reconstruction fit across all interpolation methods. The reduction in accuracy is not additive and as hypothesised, methods that forced compliance were more affected.

  2nd order regression was identified as the most noise resistant reconstruction method, in many cases surpassing RBF interpolation when 0.5-1% of path noise was added. However, for as small a number as 24 acoustic paths this method was not adequately able to reconstruct more complex temperature profiles or profiles that had a greater temperature gradient. In this regard RBF was still the most accurate reconstruction method. Conversely, cubic spline and Lagrange methods were greatly affected by random path error and unsuitable in this regard.

- A method for reconstruction in high noise scenarios (interpreted as higher path error) was suggested. It was found that repeating TOF reading produced a significant improvement in reconstruction accuracy for all methods (excluding regression) and proved to be a practical way to mitigate random path error. The optimum amount of repetitions was 2, where the greatest improvement in accuracy was seen. Under these conditions RBF interpolation produced the most accurate results having a reconstruction error of 2.9%, 5.6%, 2.9% and 5.45% for the single peak, steep single peak, asymmetrical peak and double asymmetrical peak profiles respectively with 1% random path noise.

- It was shown that that transmitter/receiver or transceiver locations and grid position had a significant effect on the resulting reconstruction accuracy. Consequently, tests were performed with a trial and error method to identify transmitter/receiver, transceiver and grid position trends that produced the more accurate reconstructions for each temperature profile using 24 acoustic paths.

- From these tests guidelines were identified for transceiver placement and grid positions that improved accuracy and scenarios to be avoided.

- Namely symmetric acoustic path layouts and grid were found to be preferable where acoustic paths where adequately spread over the whole furnace area. Non-symmetric layouts resulted in the final reconstruction being distorted or spread. In addition to this, layouts that had receivers or transceivers closer to the walls and their grid placement to also

be closer to these walls were preferable and resulted in more accurate reconstructions. This occurred since an emphasis was placed on obtaining more accurate data points at a region that exhibited the most significant temperature change and resulting in a smaller region of extrapolation, where errors tended to be higher.

- In addition to non-symmetric layers being less desirable, scenarios where acoustic path segments are too small in a block, or blocks without acoustic paths, are also to be avoided since they provide a wholly inaccurate estimation of temperature and reduced the reliability of the least-squares temperature data points. In this regard using a 4x4 temperature grid was also preferable over a 6x4 or 4x6 grid with 24 acoustic paths since the symmetry and redundancy improved the temperature data point estimations and resulting reconstruction.

- The separate transmitter/receiver type acoustic pyrometer was shown to produce marginally more accurate reconstructions than the transceiver type acoustic pyrometer. However, transceiver type acoustic pyrometers have the advantage of reducing path error by eliminating contributions of planar flue gas velocity.

- An improved RBF reconstruction method was demonstrated, showing a significant improvement in reconstruction accuracy (>1 %) from previous work for all temperature profiles. A mean reconstruction accuracy of 1.064 %, 3.29 %, 0.573 % and 4.67 % was achieved for the single peak, steep single peak, asymmetrical peak and double asymmetrical peak respectively.

- Acoustic path requirements were determined based on intended use. It was concluded that 24 acoustic paths are adequate for temperature reconstruction fit, being able to identify temperature peaks, their position and determine the overall energy at this region. The minimum number of acoustic paths for simple reconstruction (1 peak, minimal placement) is 4 however this requires a reconstruction method that assumes the shape of the profile. For the least squares approach only, an indication of energy will be produced. For 1 acoustic path an estimation of path error can be determined, however this provides no indication of the profile at this region.

- The addition of radiation pyrometer readings to acoustic pyrometer readings was shown to be a promising solution to reconstructing temperature profiles that have a very steep temperature change near the edges and a relatively flat midsection. A vast improvement was shown when included with the RBF interpolation methods, however errors are still high and should be investigated further.

5.1.3 Time of flight determination

The last goal of the study was to **demonstrate recording an acoustic time of flight reading with its associated signal processing**, which was satisfied by the following work completed and conclusions drawn.

- A review of how acoustic noise and attenuation impedes acoustic TOF determination in the furnace was presented. Within this review the frequency and intensity characteristics of typical noise was presented, as well as typical attenuation bands based on signal frequency. Concluding the operating acoustic frequency to be in the 500-3000 Hz range.

- The fundamental setup for acoustic TOF measurement was presented followed by a literature review of TOF determination methods applicable to acoustic pyrometry, identifying threshold methods with filtering, cross correlation and generalised cross correlation methods as favourable TOF determination methods.

- Based on these conclusions, an experimental setup was designed to fulfil the last project objective and demonstrate TOF measurement. The resulting setup measured TOF over 6 m in a 355 mm diameter PVC pipe enclosure, and generated the acoustic signal and noise with two 8” mid-range loudspeakers. Amplification for these signals was provided though two 30 W line amplifiers and the resulting signal was recorded by two 44100 Hz PG27 condenser microphones connected to a 2-channel USB mixer with a built-in 16-bit DAC. The hardware was controlled using a laptop computer running a LabVIEW VI for acoustic signal generation, acquisition and processing.

- A LabVIEW VI was developed for controlling the experimental setup, for acoustic signal generation, acquisition and processing. The VI can create sine or chirp signals over a specified frequency range and white or coloured noise based on an input power spectrum. Threshold method with bandpass filtering, cross-correlation methods (including 4 GCC variants) and a new variable notch filter method was applied.

- Although not strictly a requirement for this project, the experimental setup demonstrated the ability to observe temperature changes of 7° over time.

- SNR tests were conducted in white and coloured noise comparing each TOF determination method, and in doing so satisfying the last objective by demonstrating TOF determination. Under certain conditions correlation methods can produce TOF results when the SNR is below 1, and in general it was concluded that acoustic sources can have a lower sound intensity than the threshold method (where high SNR levels were required), though cross-correlation methods require a time-varying signal to be applied successfully.

- Threshold detection with bandpass filtering was only effective at high SNR, 3.55 for white noise and 2.831 for coloured noise, implying that low frequency interference between the source signal and noise signal is desired. Indicating that a sound source with significantly louder intensity than the noise present is required.

- Standard cross correlation was effective from a corrected SNR of 2.8 in coloured noise and 1.4 in white noise, where results in accurate bands remain very consistent. In contrast, GCC results showed a large amount of variation in TOF accuracy (even in low noise conditions), however this was due to limitations in directly available inverse Fourier VIs in LabVIEW. Yet, in white noise, it was concluded that the GCC SCOT method was the most applicable TOF determination method being able to reliably record the TOF up to a corrected SNR of 1.4. In coloured noise, before results began to vary having its lowest accurate TOF reading at a corrected SNR of 0.54, however there was variation in readings at this region.

- The variable notch filter method with cross correlation showed potential for TOF determination. This was especially evident in coloured noise where it was reliably accurate up to a corrected SNR of 0.67 having an average TOF error of less than 2 %. Below this region it produced accurate results up to a corrected SNR of 0.55, however there were outliers in this region and the resulting mean error was 7.92 %. Conversely, its white noise performance was worse than standard cross-correlation and applied filtered when not necessary. The implication of this is very promising, suggesting that a variable notch filter approach would be greatly beneficial when determining TOF in a boiler with noise that has distinct repetitive noise frequency components.

5.2 Recommendations for future work

5.2.1 Time of flight determination

It was noted that due to time constraints there were several aspects that could be improved for experimental design and methods applied. For the experimental design future work could be done by modifying the transmitter speaker location such that the microphone lies in the acoustic path to correct the SNR imbalance between the microphones. In addition to this, an acoustic absorbing lining could be placed within the enclosing pipe to attenuate harmonics and resonant regions and even out the frequency response

The LabVIEW model could also be improved for GCC by perhaps using an external program (such as MATLAB as implemented in previous studies) for signal processing. In addition to this the variable notch filter method showed immense potential in coloured noise and should be developed further to better control filter widths and prevent over filtering in white noise and low noise scenarios.

5.2.2 Temperature reconstruction

Through simulation this study has shown the ability of acoustic pyrometry to accurately reconstruct complex temperature profiles and provide reliable estimates of temperature at the furnace exit, thus highlighting the potential of acoustic pyrometry as an online furnace exit temperature monitoring tool.

Consequently, it is recommended that a full multi-path acoustic pyrometer set up be installed to experimentally validate the reconstruction methods applied in this study in a local context. Either a full 24-path system could be installed based on the transmitter/receiver guidelines suggested throughout this text using the improved RBF reconstruction algorithm, or a scaled down version could be installed to simply monitor temperature or the energy at the furnace region.

In terms of TOF determination the noise characteristics of the pilot boiler should be identified to select an appropriate acoustic source, with the possibility of further testing the variable notch filter method identified in this study on a South African boiler.

In addition to this, temperature reconstruction with radiation pyrometry was introduced in a rudimental sense yet presented a scenario where these two methods would be complimentary. Further integration between the two methods should be researched for possible online application.

6. List of References

[1] N. E. Tootla, “Investigation into methods for the calculation and measurement of pulverised coal boiler flue gas furnace exit temperature,” University of Cape Town, 2016.

[2] G. L. Tomei, *Steam - it’s generation and use*, 42nd ed. North Carolina: Babcock & Wilcox, 2015.

[3] E. A. Avallone, T. B. III, and A. Sadegh, “STEAM BOILERS,” *Marks’ Standard Handbook for Mechanical Engineers, Eleventh Edition*. McGraw Hill Professional, Access Engineering, 2007.

[4] J. G. Singer, *Combustion: Fossil Power Systems*, Third Edit. Windsor CT: Combustion Engineering, Inc., 1981.

[5] T. F. . Woodruff, Everet B.;Lammers, Herbert B.; Lammers, *Steam Plant Operation, 10th Edition*, 10th ed. New york: McGraw-Hill Education, 2017.

[6] C. D. Shields, *Boilers: Types, Characteristics, and Functions*. F. W. Dodge, 1961.

[7] T. co. Inc, “Contact Sensor Types.” [Online]. Available: http://www.temperatures.com/csensors.html. [Accessed: 09-Oct-2017].

[8] G. Kychakoff, A. F. Hollingshead, and S. P. Boyd, “Use of acoustic temperature measurements in the cement manufacturing pyroprocess,” *2005 IEEE Cem. Ind. Tech. Conf. Rec.*, vol. 2005, pp. 23–33, 2005.

[9] J. Chedaille and Y. Braud, *Industrial Flames Vol.1*. London (25 Hill Street, London, W1X8LL): Edward Arnold Limited, 1972.

[10] R. Young, K J; Ireland, S N; Melendez-Cervates, M C; Stones, “On the systematic error associated with the measurement of temperature using acoustic pyrometry in combustion products of unknown mixture,” *Meas. Sci. Technol.*, vol. 9, no. 1, pp. 1–5, 1998.

[11] F. Rinaldi and B. Najafi, “Temperature measurement in WTE boilers using suction pyrometers,” *Sensors (Switzerland)*, vol. 13, no. 11, pp. 15633–15655, 2013.

[12] S. P. Nuspl, E. P. Szaminia, J. A. Kleppe, and P. R. Norton, “Acoustic Pyrometer,” 1989.

[13] “IR Thermometers & Pyrometers,” 2016. [Online]. Available: http://www.omega.com/literature/transactions/volume1/thermometers2.html. [Accessed: 11-Apr-2016].

[14] {Collective of authors}, *Pyrometer - Handbook*. Germany: IMPAC Infrared GmbH, 2004.

[15] Z. W. Jiang, Z. X. Luo, and H. C. Zhou, "A simple measurement method of temperature and emissivity of coal-fired flames from visible radiation image and its application in a CFB boiler furnace," *Fuel*, vol. 88, no. 6, pp. 980–987, 2009.

[16] C. Lou and H. C. Zhou, "Deduction of the two-dimensional distribution of temperature in a cross section of a boiler furnace from images of flame radiation," *Combust. Flame*, vol. 143, no. 1–2, pp. 97–105, 2005.

[17] H. C. Zhou *et al.*, "Experimental investigations on visualization of three-dimensional temperature distributions in a large-scale pulverized-coal-fired boiler furnace," *Proc. Combust. Inst.*, vol. 30, no. 1, pp. 1699–1706, 2005.

[18] W. Huajian *et al.*, "Measurements on flame temperature and its 3D distribution in a 660 MWe arch-fired coal combustion furnace by visible image processing and verification by using an infrared pyrometer," *Meas. Sci. Technol.*, vol. 20, no. 11, p. 114006, 2009.

[19] J. A. Kleppe, "Engineering applications of acoustics." Antech House on Demand, pp. 1–47, 1989.

[20] J. Kleppe, J. Maskaly, and G. Beam, "'The Application of Image Processing to Acoustic Pyrometry,'" *Measurement*, no. 702, pp. 8–10, 1996.

[21] H. Sielschott, "Measurement of horizontal flow in a large scale furnace using acoustic vector tomography," *Flow Meas. Instrum.*, vol. 8, no. 3–4, pp. 191–197, 1998.

[22] S. Zhang, G. Shen, L. An, Y. Niu, and G. Jiang, "Monitoring ash fouling in power station boiler furnaces using acoustic pyrometry," *Chem. Eng. Sci.*, vol. 126, pp. 216–223, 2015.

[23] H. Sielschott and W. Derichs, "Tomography with few data : Use of collocation methods in acoustic pyrometry Tomography with few data : Use of collocation methods in acoustic pyrometry," *Scanning*, 1996.

[24] G. Q. Shen, L. S. An, and G. S. Jiang, "Real-time monitoring on boiler combustion based on acoustic measurement," *2006 IEEE Power India Conf.*, vol. 2005, no. 1, pp. 41–44, 2005.

[25] N. Modliński, P. Madejski, T. Janda, K. Szczepanek, and W. Kordylewski, "A validation of computational fluid dynamics temperature distribution prediction in a pulverized coal boiler with acoustic temperature measurement," *Energy*, vol. 92, no. x, pp. 77–86, 2015.

[26] S. Deduck and D. Suplicki, "Advanced Technologies Provide New Insights for Assisting Energy From Waste (EfW) Boiler Combustion Monitoring, Operations and Maintenance," in *North American Waste-To-Energy Conference*, 2008, pp. 1–12.

[27] R. Roubicek, "Gas Temperature Measurement in the Fireside of Process Heaters-using Acoustic Pyrometry," *NPRA Maint. Conf.*, 2003.

[28] Y. Li, H. Zhou, S. Chen, Y. Zhang, X. Wei, and J. Zhao, "Acoustic reconstruction of the velocity

field in a furnace using a characteristic flow model.," *J. Acoust. Soc. Am.*, vol. 131, no. 6, pp. 4399–408, 2012.

[29] Enertechnix, "How PyroMetrix works," 2017. [Online]. Available: https://www.enertechnix.com/wp-content/uploads/2017/06/ETX-New-Acoustic-Pyrometer-Brochure-170201-8.5x11.pdf. [Accessed: 10-Oct-2017].

[30] Sciengr.com, "Boilerwatch MMP-II-SSX," 2018. [Online]. Available: http://sciengr.com/product.html. [Accessed: 01-Oct-2017].

[31] S. F. Green, "An acoustic technique for rapid temperature distribution measurement," *Acoust. Soc. Am. J.*, vol. 77, no. 2, pp. 759–763, 1985.

[32] M. Bramanti, E. A. Salerno, A. Tonazzini, S. Pasini, and A. Gray, "An acoustic pyrometer system for tomographic thermal imaging in power plant boilers," *IEEE Trans. Instrum. Meas.*, vol. 45, no. 1, pp. 159–167, 1996.

[33] G. B. Wallis, *One-Dimensional Two-Phase Flow*. New York: McGrow-Hill, 1969.

[34] X. Shen, Q. Xiong, W. Shi, K. Wang, and G. Lai, "Temperature distribution monitoring using ultrasonic thermometry based on markov radial basis function approximation and singular values decomposition," *Math. Probl. Eng.*, vol. 2014, pp. 18–20, 2014.

[35] X. Shen, Q. Xiong, W. Shi, S. Liang, X. Shi, and K. Wang, "A New Algorithm for Reconstructing Two-Dimensional Temperature Distribution by Ultrasonic Thermometry," vol. 2015, 2015.

[36] S. Rippa, "An algorithm for selecting a good value for the parameter c in radial basis function interpolation," *Adv. Comput. Math.*, vol. 11, pp. 193–210, 1999.

[37] S. Zhang, G. Shen, L. An, and Y. Niu, "Online monitoring of the two-dimensional temperature field in a boiler furnace based on acoustic computed tomography," *Appl. Therm. Eng.*, vol. 75, pp. 958–966, 2015.

[38] H. Sielschott and W. Derichs, "Use of collocation methods under inclusion of a priori information in acoustic pyrometry," pp. 6–8, 1995.

[39] R. Jia, Q. Xiong, and S. Liang, "Acoustic imaging for temperature distribution reconstruction," *AIP Adv.*, vol. 6, no. 12, p. 125018, 2016.

[40] X. Shen, Q. Xiong, X. Shi, K. Wang, S. Liang, and M. Gao, "Ultrasonic temperature distribution reconstruction for circular area based on Markov radial basis approximation and singular value decomposition," *Ultrasonics*, vol. 62, pp. 174–185, 2015.

[41] H. Yan, G. Chen, Y. Zhou, and L. Liu, "Primary study of temperature distribution measurement in stored grain based on acoustic tomography," *Exp. Therm. Fluid Sci.*, vol. 42, pp. 55–63, 2012.

[42] R. Jia, Q. Xiong, G. Xu, K. Wang, and S. Liang, “A method for two-dimensional temperature field distribution reconstruction,” *Appl. Therm. Eng.*, vol. 111, pp. 961–967, 2017.

[43] J. C. Nash, *Compact Methods for Computers. Linear Algebra and Function Minimisation*. 1990.

[44] B. C. R. Ewan and S. N. Ireland, “Error reduction study employing a pseudo-random binary sequence for use in acoustic pyrometry of gases,” *Rev. Sci. Instrum.*, vol. 71, no. 12, p. 4658, 2000.

[45] F. Tian and C. Zhang, “Experimental Study the Measurement of Acoustic Wave Flight Time under Strong Noise in the Boiler,” *2011 Seventh Int. Conf. Comput. Intell. Secur.*, vol. 1493, pp. 1493–1496, 2011.

[46] J. A. Kleppe, “Method and apparatus for measuring acoustic wave velocity using impulse response,” 1994.

[47] “Self-purging pneumatic acoustic generator,” 5,404,833, 11-Apr-1995.

[48] A. Ceserani, Ambrogio;Gregori, Luca; Zanetta, Gian Antonio; Farina, “A sonic approach for the measurement of gas temperature in power generation boilers,” *Acoust. Tech.*, no. 38, pp. 16–23, 2004.

[49] T. a. Hanson, N. Yilmaz, P. Drozda, W. Gill, T. J. Miller, and a. B. Donaldson, “Acoustic Pyrometry using an Off-the-Shelf Range Finding System,” *J. Fire Sci.*, vol. 26, no. 4, pp. 287–308, 2008.

[50] K. Srinivasan, T. Sundararajan, S. Narayanan, and T. J. S. Jothi, “Effects of acoustic source and filtering on time-of-flight measurements,” *Appl. Acoust.*, vol. 70, no. 8, pp. 1061–1072, 2009.

[51] T. M. Sullivan and R. M. Stern, “MULTI-MICROPHONE CORRELATION-BASED PROCESSING FOR ROBUST SPEECH RECOGNITION,” pp. 91–94, 1993.

[52] D. R. Fuhrmann and G. San Antonio, “Transmit Beamforming for MIMO radar systems using signal cross-correlation,” *IEEE Trans. Aerosp. Electron. Syst.*, vol. 44, no. 1, pp. 171–186, 2008.

[53] W. Shu, Lei ; Zhu, Xufeng; Huang, Xiwei; Zhou, ZhangBing ; Zhang, Yu; Xiaolei, “A Review of Research on Acoustic Detection of Heat Exchanger Tube,” *EAI Endorsed Trans. Ind. Networks Intell. Syst.*, vol. 15 (5), no. December, pp. 1–13, 2015.

[54] C. H. Knapp and G. C. Carter, “The Generalized Correlation Method for Estimation of Time Delay,” *IEEE Trans. Acoust.*, vol. 24, no. 4, pp. 320–327, 1976.

[55] J. Chen, J. Benesty, and Y. Huang, “Time delay estimation in room acoustic environments: An overview,” *EURASIP J. Appl. Signal Processing*, vol. 2006, no. i, pp. 1–19, 2006.

[56] J. M. Perez-Lorenzo, R. Viciana-Abad, P. Reche-Lopez, F. Rivas, and J. Escolano, “Evaluation of generalized cross-correlation methods for direction of arrival estimation using two

microphones in real environments," *Appl. Acoust.*, vol. 73, no. 8, pp. 698–712, 2012.

[57] Y. Zhang and W. Abdulla, "A comparative study of time-delay estimation techniques using microphone arrays," *Dep. …*, no. 619, pp. 1–57, 2005.

[58] M. S. Brandstein and H. F. Silverman, "A robust method for speech signal time-delay estimation in reverberant rooms," *1997 IEEE Int. Conf. Acoust. Speech, Signal Process.*, vol. 1, pp. 375–378, 1997.

[59] P. R. Roth, "Effective measurements using digital signal analysis," *IEEE Spetrum*, vol. 4, no. 8, pp. 62–70, 1971.

[60] C. L. Aguilar and L. Alvarez, "A comparative study of time-delay estimation techniques for convolutive speech mixtures."

[61] J. A. Kleppe, "Self-purging pneumatic acoustic Generator," 5,404,833, 1995.

[62] M. Barth and A. Raabe, "Acoustic tomographic imaging of temperature and flow fields in air," *Meas. Sci. Technol.*, vol. 22, no. 3, p. 35102, 2011.

[63] J. Kuhn, "Detection performance of the smooth coherence transform (SCOT)," *1978 IEEE Int. Conf. Acoust. Speech, Signal Process.*, vol. 3, no. 2, pp. 678–683, 1978.

[64] G. C. Carter, A. H. Nuttall, and P. G. Cable, "The Smoothed Coherence Transform," *Proc. IEEE*, vol. 61, no. 10, pp. 1497–1498, 1973.

[65] L. Chen, Y. Liu, F. Kong, and N. He, "Acoustic source localization based on generalized cross-correlation time-delay estimation," *Procedia Eng.*, vol. 15, pp. 4912–4919, 2011.

[66] J. A. Kleppe, "The Application of Digital Signal Processing to Acoustic Pyrometry," in *Proc, 1996 IEEE Digital Signal Processing Workshop*, 1996, pp. 0–2.

[67] "Novel gas trubine exhaust temperature measurement system.pdf." ASME Turbo Expo, San Antonio, pp. 1–8, 2012.

[68] K. Srinivasan, T. Sundararajan, S. Narayanan, T. J. S. Jothi, and C. S. L. V Rohit Sarma, "Acoustic pyrometry in flames," *Meas. J. Int. Meas. Confed.*, vol. 46, no. 1, pp. 315–323, 2013.

[69] S. Liu, S. Liu, and T. Ren, "Ultrasonic tomography based temperature distribution measurement method," *Measurement*, vol. 94, pp. 671–679, 2016.

[70] N. Instruments, "LabVIEW - National Instruments," 2017. [Online]. Available: http://www.ni.com/en-za/shop/labview.html. [Accessed: 15-Nov-2017].

Appendix A. Summary of guidelines

This section summarises some key findings that could be beneficial for plant scale implementation. The basis of these findings can be found in the dissertation body.

Number of acoustic paths required

- **24 or more** acoustic paths are required for temperature reconstruction of complex profiles at the furnace exit (multiple peaks). This would also produce accurate measurements of the energy at the furnace exit. This could be achieved with **4 transmitters** and **8 receivers** or **8 transceivers**.
- **4 or more** acoustic paths would be required for very simple temperature profiles (1 centred peak) or just determining the energy at the furnace exit. This could be achieved with **2 transmitters** and **2 or more receivers** or **4 transceivers**.
- **1** acoustic path would just provide an estimate of the temperature at the furnace exit and provide no profile information. This would be achieved with a **single transmitter** and **receiver** or **transceiver pair**.

Positioning of the acoustic plane

- The temperature reconstruction tests showed that greater temperature gradients and more complex temperature profiles resulted in greater reconstruction error. **The acoustic plane should thus be positioned higher rather than lower in the boiler** to such that the temperature change is lower, and the temperature profile is more developed.
- The acoustic paths should also be positioned on the same plane.

Location of acoustic paths and reconstruction grid

- Acoustic path layouts with **symmetry** should be prioritised if possible. Asymmetrical layouts tend to stretch the temperature profile.
- Acoustic paths should be positioned to be **spread over the furnace** area. Blocks without path coverage tend to produce less accurate data points.
- Focusing on areas where the temperature change is the highest produces more accurate reconstructions, thus receivers or transceivers should be **moved closer to the boiler walls**. However, it should be noted that moving receivers too close to the walls would be impractical to receive a signal with sufficient SNR.
- In addition to this the grid could be chosen to make smaller blocks near the furnace walls.

Temperature reconstruction method

- If the **temperature profile is unknown** or varies **multiquadric radial basis functions with shape factor prediction** is an excellent candidate for temperature reconstruction. The method was the most accurate of the interpolation methods tested (except in very high noise scenarios).
- If the temperature profile is **well known, regularisation methods** should be considered.
- As observed but the path error tests, single path error is not additive and has a greater effect on reconstruction accuracy. In **high noise scenarios**, to reduce random path error, reconstruction methods that do not force interpolants through its data points should be considered. This would be **multiple regression or regularisation methods**. In addition to this **repeating path readings or using transceivers** that measure time of flight in both directions should be considered.

Reducing time of flight error

- To reduce time of flight error, the **gas composition** of the flue gas should be determined to a high degree of accuracy.
- The acoustic **path length distances** should be accurately measured and calibrated.
- High frequency recording should be used to reduce time errors.

Acoustic source

- To prevent signal attenuation, the acoustic source should be selected to produce its signal in the **500-3500 Hz** frequency range.
- For **threshold detection** methods a **high sound intensity** is required and acoustic signals with a sharp rising edge is preferable.
- For **correlation methods** acoustic sources that produce **time varying signals** are required.

Signal processing methods

- Signal processing methods should be selected based on the **noise characteristics** of the boiler and the **signal source** selected.
- Where a high SNR is possible, and the acoustic source has a sharp rising edge, threshold detection with bandpass filtering is acceptable.
- When the **boiler noise is white**, and a time varying acoustic source signal is used, generalised cross correlation with the **SCOT filter** should be used.
- When boiler noise is **repetitive and distinct**, **adaptive filters** with cross correlation should be used.

Appendix B. Transmitter/receiver location test detailed results

This section presents the results from the test as split into the transmitter and receiver type acoustic pyrometer and the transceiver type pyrometer. For each type, the most accurate reconstruction setup (in terms of RBF interpolation) for each temperature profile is presented with the resulting reconstruction and its error results. The transmitter receiver type acoustic pyrometer is presented first, followed by the transceiver type pyrometer.

Transmitter & receiver type acoustic pyrometer

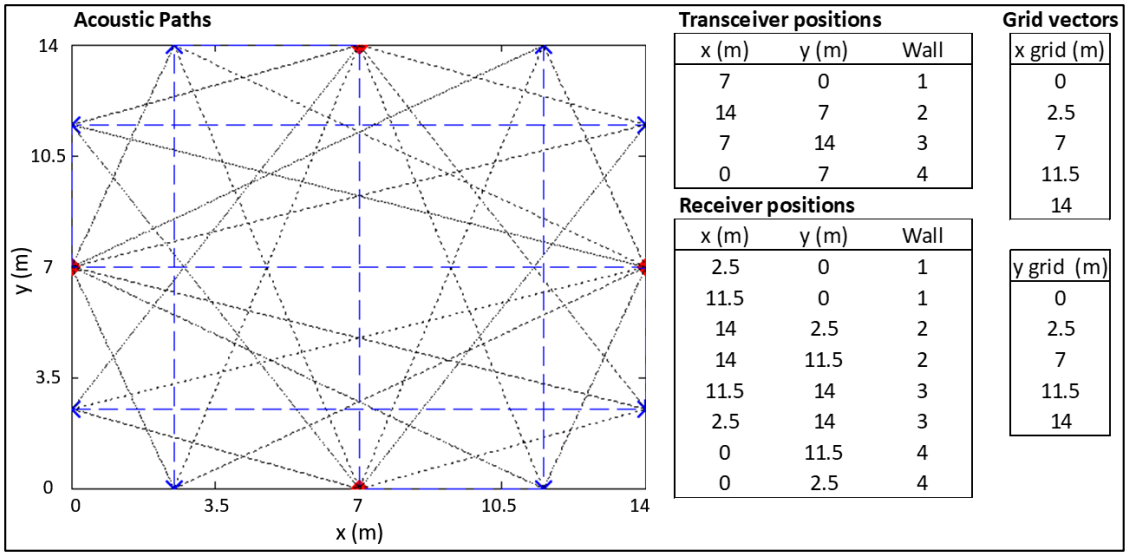

Transceiver positions

x (m)	y (m)	Wall
7	0	1
14	7	2
7	14	3
0	7	4

Receiver positions

x (m)	y (m)	Wall
2.5	0	1
11.5	0	1
14	2.5	2
14	11.5	2
11.5	14	3
2.5	14	3
0	11.5	4
0	2.5	4

Grid vectors

x grid (m)
0
2.5
7
11.5
14

y grid (m)
0
2.5
7
11.5
14

Figure 161 Acoustic path layout (left), transmitter receiver and grid positions (right) for single peak profile reconstruction

Table 22: Reconstruction error (%) of each interpolation method for the single peak temperature profile

	Reconstruction Error			
	Mean (%)	RMS (%)	Sum (%)	Energy (%)
RBF	1.064	1.142	0.999	1.05
Cubic spline	6.989	7.61	6.722	7.606
Regression	2.426	3.26	1.382	1.277
Lagrange	1.438	1.692	1.38	1.179

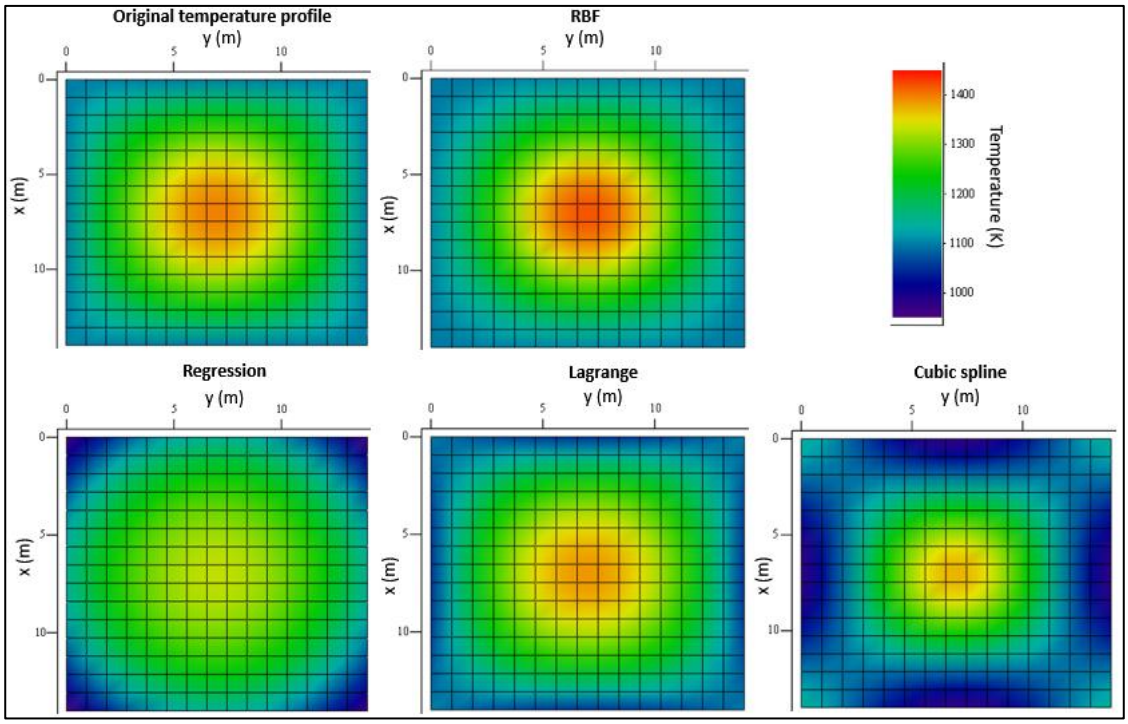

Figure 162 Reconstructed single peak temperature profile for each interpolation method

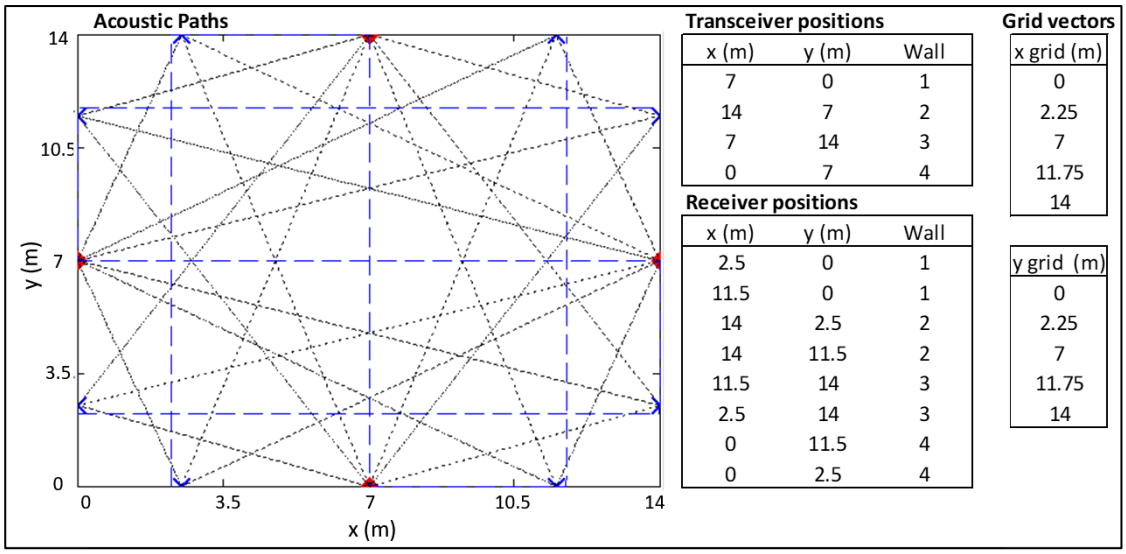

Transceiver positions

x (m)	y (m)	Wall
7	0	1
14	7	2
7	14	3
0	7	4

Receiver positions

x (m)	y (m)	Wall
2.5	0	1
11.5	0	1
14	2.5	2
14	11.5	2
11.5	14	3
2.5	14	3
0	11.5	4
0	2.5	4

Grid vectors

x grid (m)
0
2.25
7
11.75
14

y grid (m)
0
2.25
7
11.75
14

Figure 163 Acoustic path layout (left), transmitter, receiver and grid positions (right) for steep single peak profile reconstruction

Table 23: Reconstruction error (%) of each interpolation method for the steep single peak temperature profile

	Reconstruction Error			
	Mean (%)	RMS (%)	Sum (%)	Energy (%)
RBF	3.29	3.679	2.335	2.857
Cubic spline	22.749	24.1	20.59	21.277

Regression	7.575	9.497	3.725	3.642
Lagrange	4.325	4.672	3.646	2.981

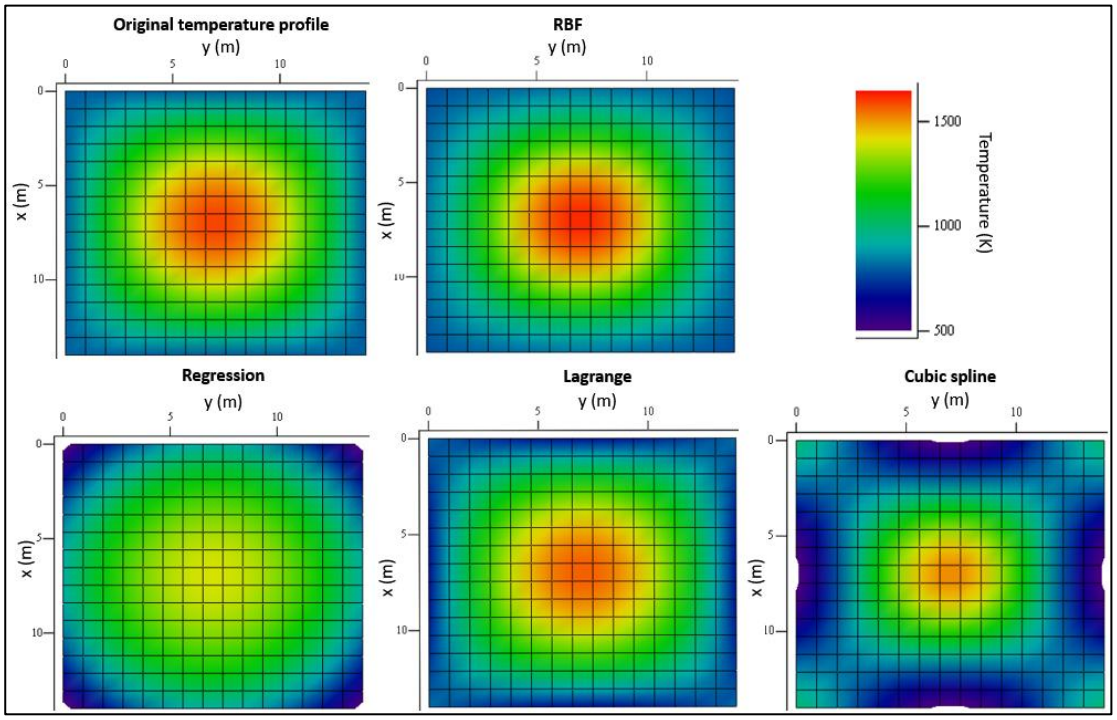

Figure 164 Reconstructed steep single peak temperature profile for each interpolation method

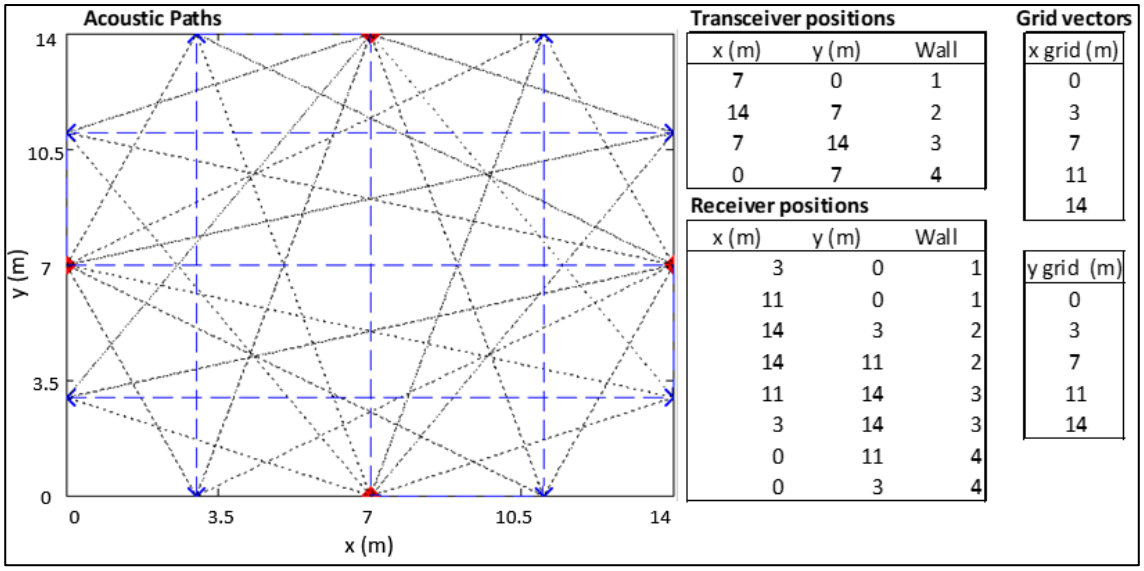

Figure 165 Acoustic path layout (left), transmitter, receiver and grid positions (right) for asymmetrical peak profile reconstruction

Table 24: Reconstruction error (%) of each interpolation method for the asymmetrical peak temperature profile

	Reconstruction Error

	Mean (%)	RMS (%)	Sum (%)	Energy (%)
RBF	0.573	0.611	0.539	0.581
Cubic spline	4.908	5.092	4.735	4.726
Regression	1.243	1.806	0.848	0.697
Lagrange	1.023	1.384	0.86	0.664

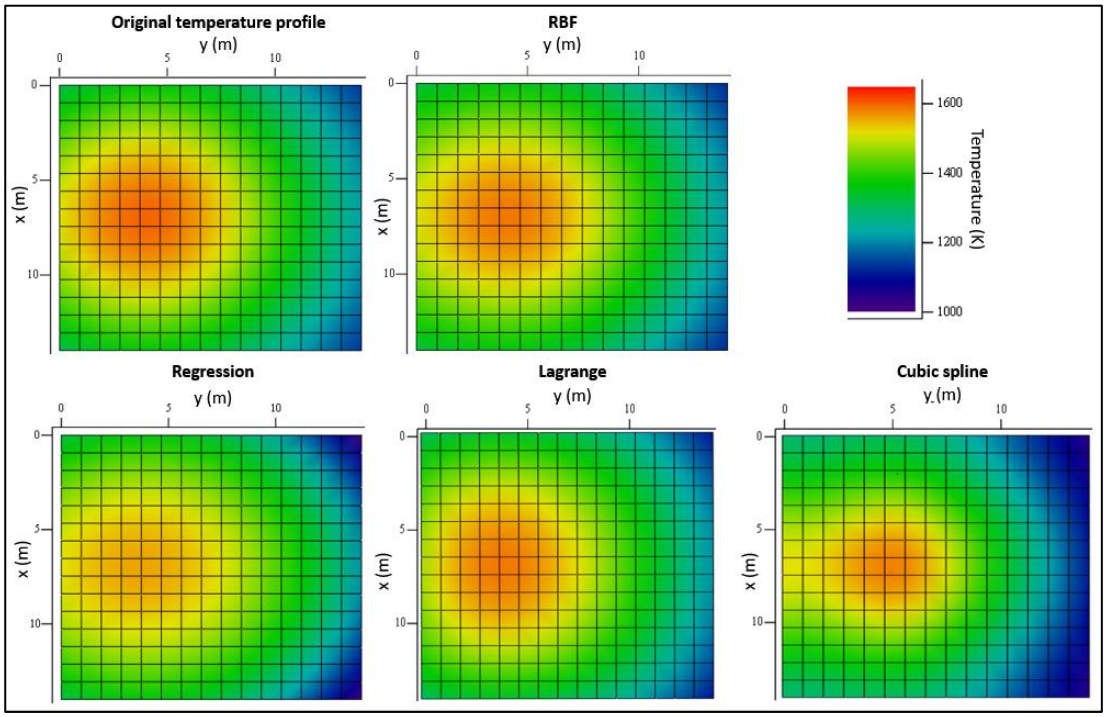

Figure 166 Reconstructed asymmetrical peak temperature profile for each interpolation method

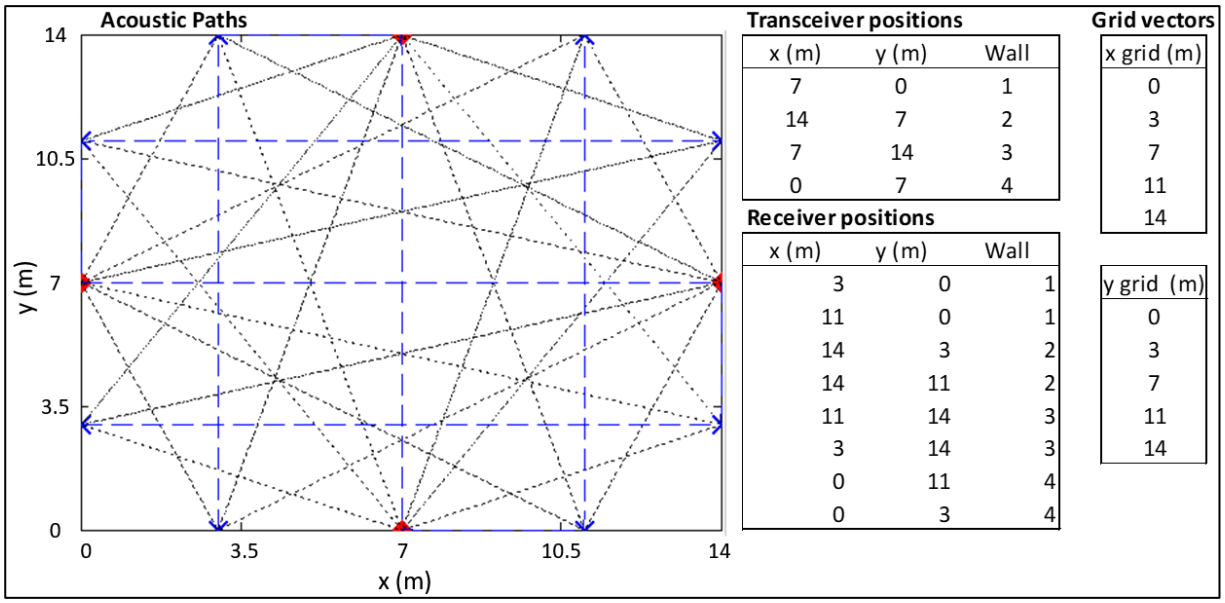

Transceiver positions

x (m)	y (m)	Wall
7	0	1
14	7	2
7	14	3
0	7	4

Receiver positions

x (m)	y (m)	Wall
3	0	1
11	0	1
14	3	2
14	11	2
11	14	3
3	14	3
0	11	4
0	3	4

Grid vectors

x grid (m)
0
3
7
11
14

y grid (m)
0
3
7
11
14

Figure 167 Acoustic path layout (left), transmitter receiver and grid positions (right) for double peak profile reconstruction

Table 25: Reconstruction error (%) of each interpolation method for the double peak temperature profile

	Reconstruction Error			
	Mean (%)	RMS (%)	Sum (%)	Energy (%)
RBF	4.67	7.094	1.173	1.651
Cubic spline	18.778	23.22	14.124	13.999
Regression	12.235	16.034	3.977	2.578
Lagrange	31.489	38.461	3.887	2.49

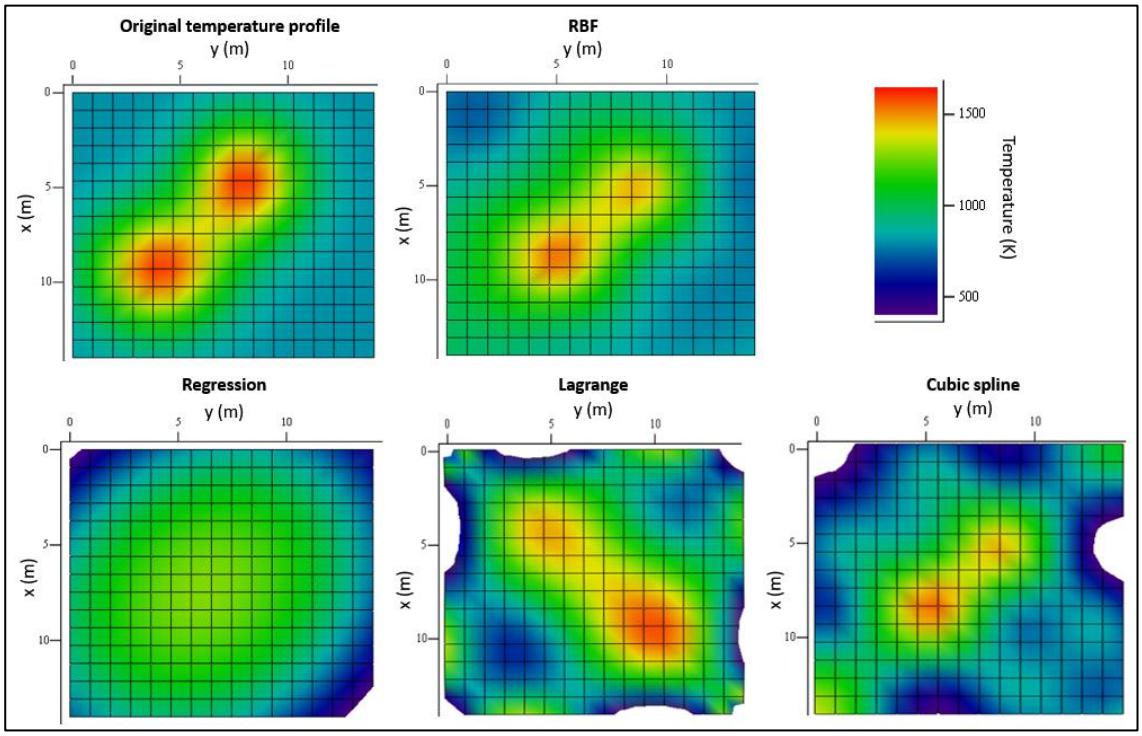

Figure 168 Reconstructed asymmetrical double peak temperature profile for each interpolation method

Transceiver type acoustic pyrometer

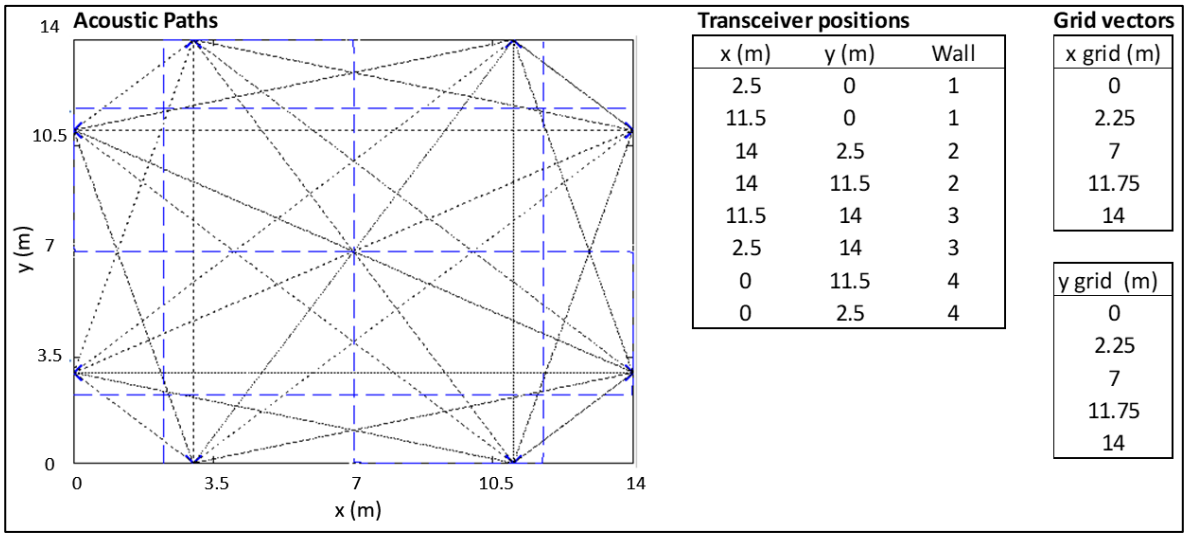

Transceiver positions

x (m)	y (m)	Wall
2.5	0	1
11.5	0	1
14	2.5	2
14	11.5	2
11.5	14	3
2.5	14	3
0	11.5	4
0	2.5	4

Grid vectors

x grid (m)
0
2.25
7
11.75
14

y grid (m)
0
2.25
7
11.75
14

Figure 169 Acoustic path layout (left), transceiver and grid positions (right) for single peak profile reconstruction

Table 26: Reconstruction error (%) of each interpolation method for the single peak temperature profile

	Reconstruction Error			
	Mean (%)	RMS (%)	Sum (%)	Energy (%)
RBF	1.323	1.459	1.321	1.332
Cubic spline	7.967	8.116	7.932	8.814
Regression	2.502	3.333	1.577	1.523
Lagrange	1.581	1.762	1.56	1.4

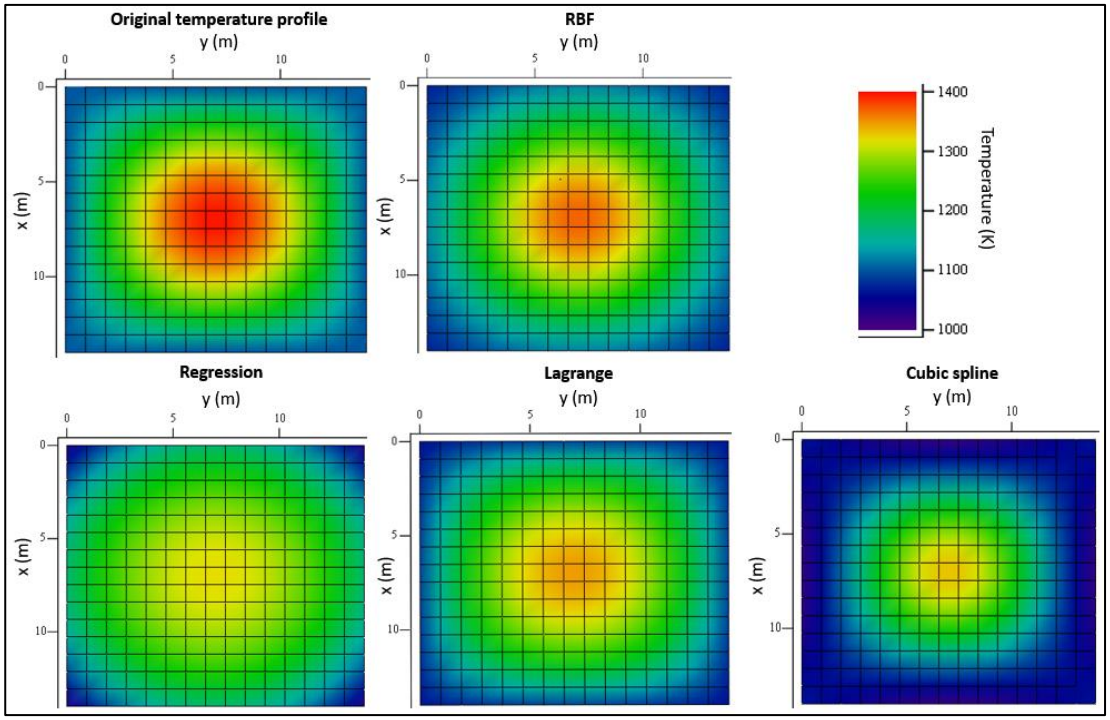

Figure 170 Reconstructed single peak temperature profile for each interpolation method

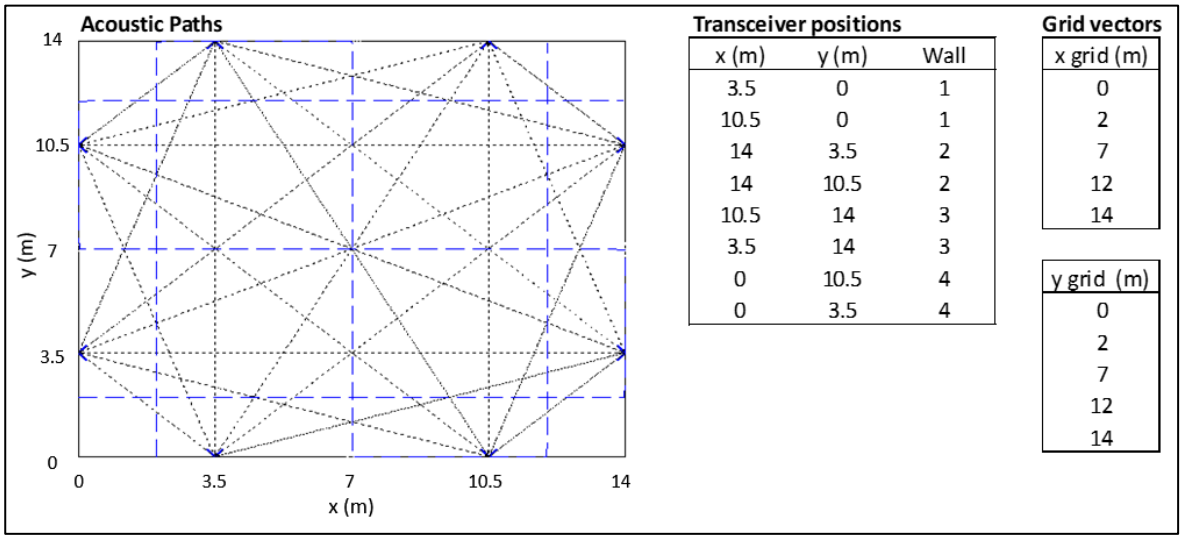

Figure 171 Acoustic path layout (left), transmitter receiver and grid positions (right) for steep single peak profile reconstruction

Table 27 : Reconstruction error (%) of each interpolation method for the steep single peak temperature profile

	Reconstruction Error			
	Mean (%)	RMS (%)	Sum (%)	Energy (%)
RBF	3.523	4.163	2.561	2.877
Cubic spline	26.023	27.363	21.762	22.709
Regression	7.603	9.602	3.911	3.95
Lagrange	4.711	5.575	3.645	2.827

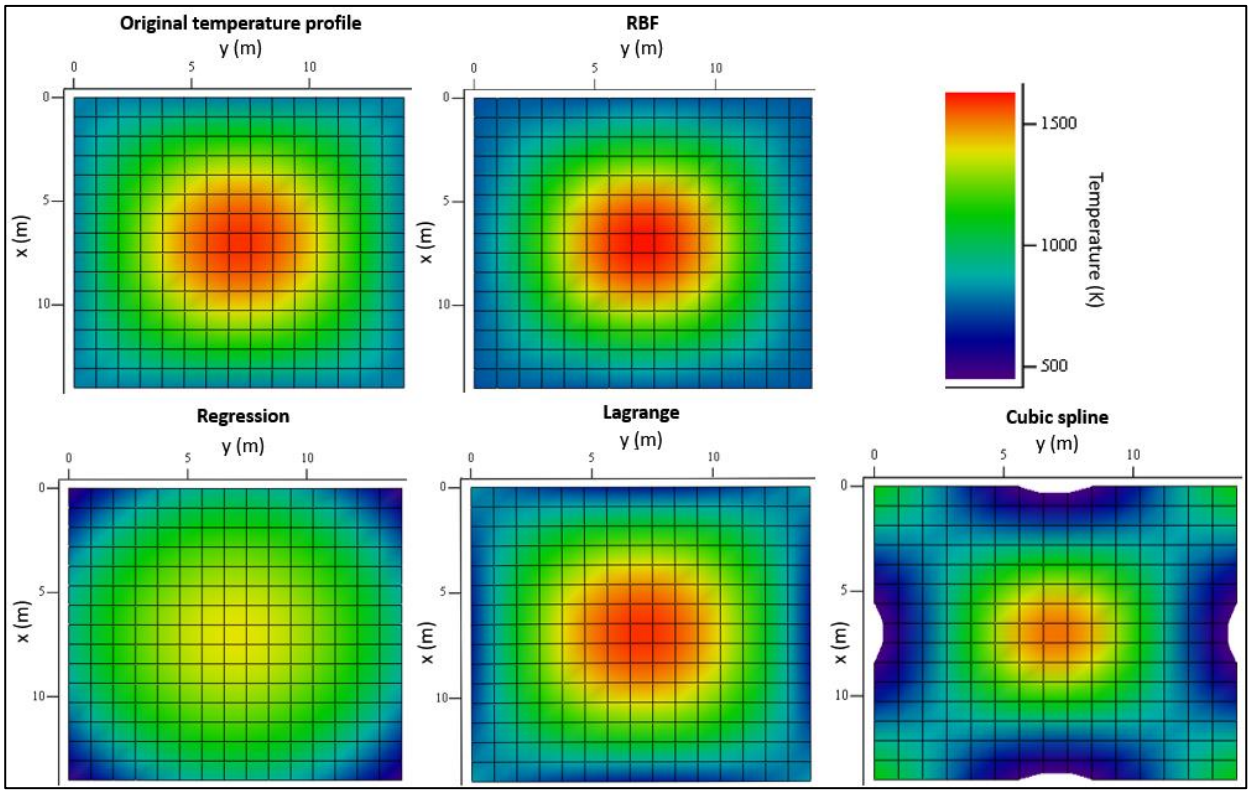

Figure 172 Reconstructed steep single peak temperature profile for each interpolation method

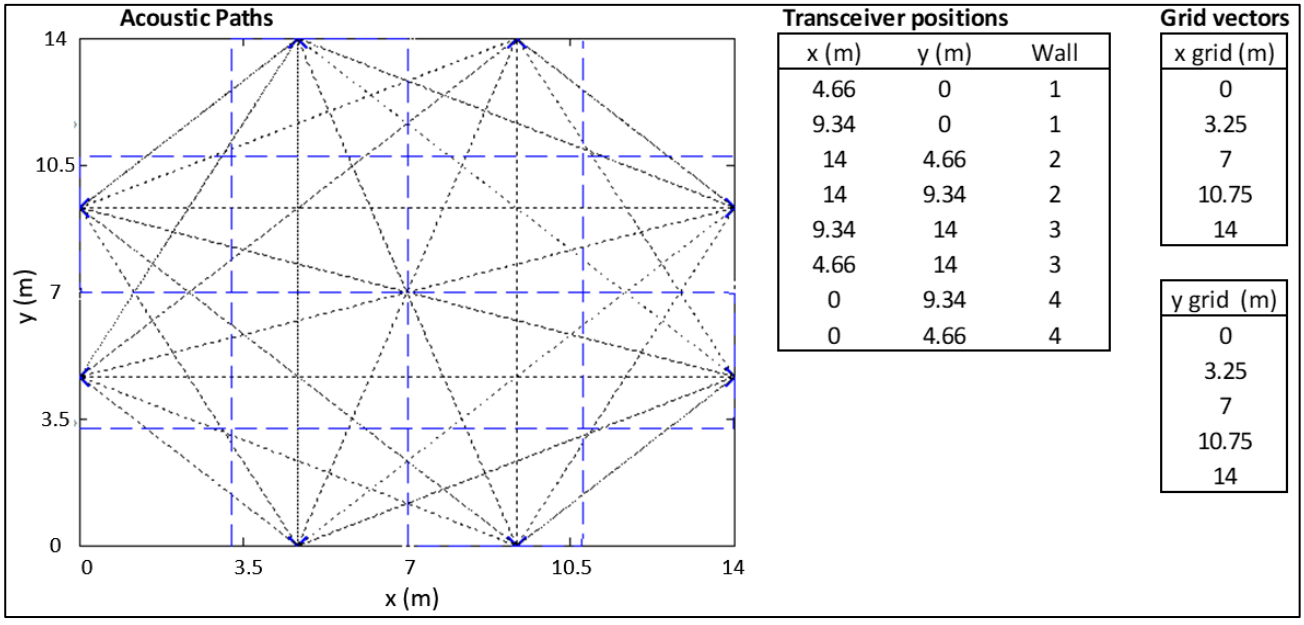

Figure 173 Acoustic path layout (left), transceiver and grid positions (right) for asymmetrical peak profile reconstruction

Table 28: Reconstruction error (%) of each interpolation method for the asymmetrical peak temperature profile

	Reconstruction Error			
	Mean (%)	RMS (%)	Sum (%)	Energy (%)
RBF	1.516	1.944	1.104	0.829
Cubic spline	5.907	6.402	5.545	5.254
Regression	1.779	2.721	1.302	0.913
Lagrange	1.804	2.431	1.298	0.905

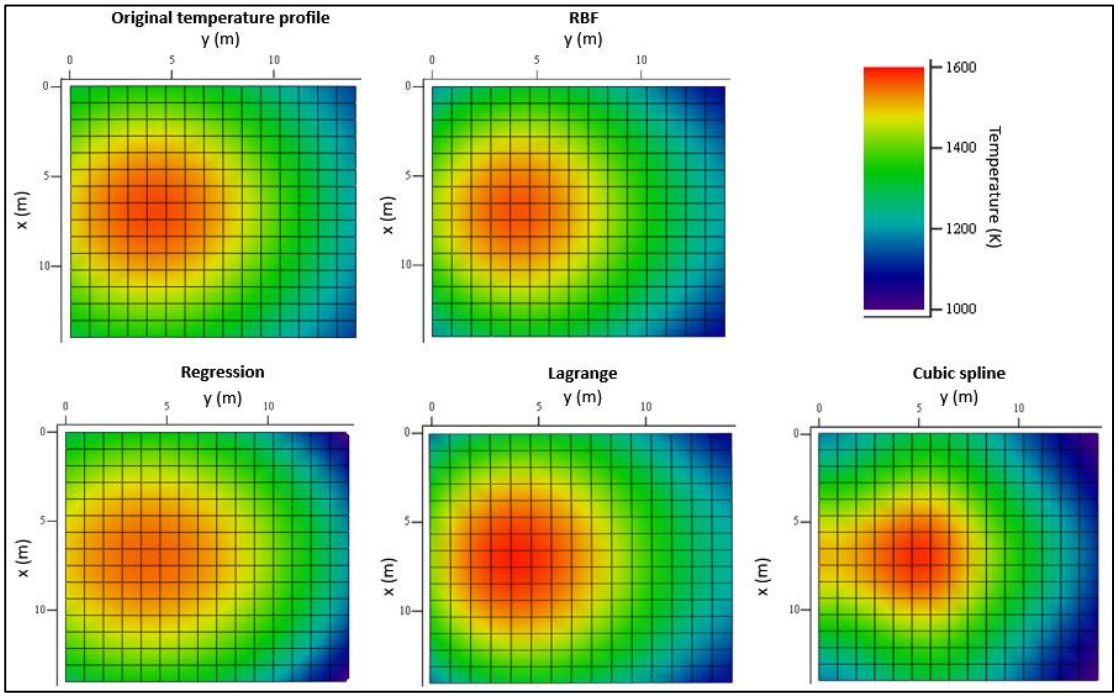

Figure 174 Reconstructed asymmetrical peak temperature profile for each interpolation method

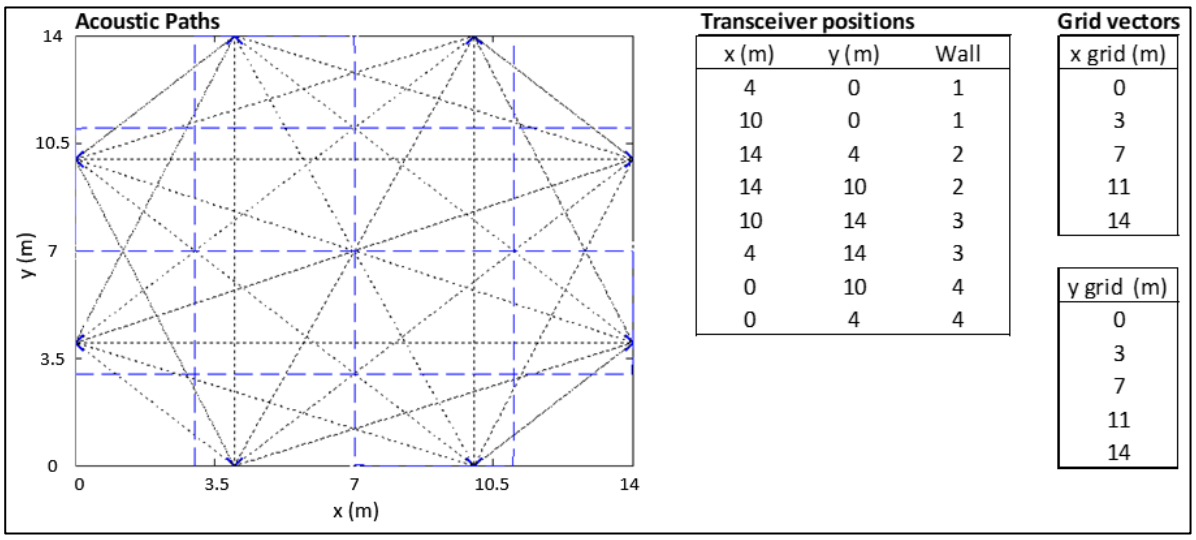

Transceiver positions

x (m)	y (m)	Wall
4	0	1
10	0	1
14	4	2
14	10	2
10	14	3
4	14	3
0	10	4
0	4	4

Grid vectors

x grid (m)
0
3
7
11
14

y grid (m)
0
3
7
11
14

Figure 175 Acoustic path layout (left), transceiver and grid positions (right) for double peak profile reconstruction

Table 29: Reconstruction error (%) of each interpolation method for the double peak temperature profile

	Reconstruction Error			
	Mean (%)	RMS (%)	Sum (%)	Energy (%)
RBF	4.748	7.02	2.574	2.494
Cubic spline	16.479	18.983	15.934	15.325
Regression	12.433	16.325	4.693	3.329
Lagrange	22.224	26.984	4.633	3.207

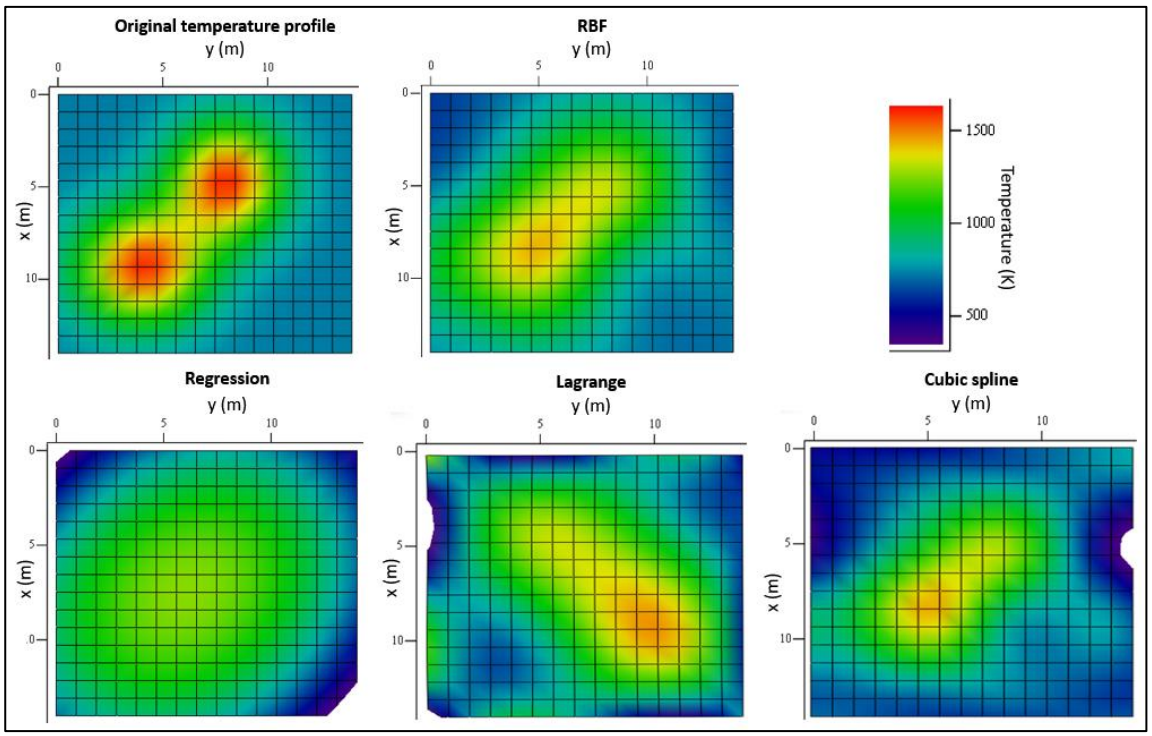

Figure 176 Reconstructed asymmetrical double peak temperature profile for each interpolation method

Appendix C. Temperature reconstruction code

The following code is displayed as seen in Mathcad.

Note: Mathcad computes sequentially, thus order of functions and calculations is deliberate.

Inputs

Current Temperature Function:

Single Peak
Steep Single Peak
Asymmetrical Peak
Double Asymmetrical Peak
Flat Distribution

Peak Location:

Off Centre Peak

DistanceFromCentre := 3 (m)

AngleFromHorizontal := –90 (deg)

TemperatureRise := 200 (K)

Path Noise:

Constant TOF Error

0%
0.5%
1%
1.5%
2%
2.5%
3%
3.5%
4%

Repeat Readings

NoRepetitions := 2

Contents:

Type of Acoustic Pyrometer:

Transmitter/Receiver
Transceiver

* When in transceiver mode, only the reciever position matrix is used

Transmittor Positions:

$$TransMat := \begin{pmatrix} x & y & wall \\ 7 & 0 & 1 \\ 14 & 7 & 2 \\ 7 & 14 & 3 \\ 0 & 7 & 4 \end{pmatrix}$$

Receiver Positions:

$$RecMat := \begin{pmatrix} x & y & wall \\ 3.5 & 0 & 1 \\ 10.5 & 0 & 1 \\ 14 & 3.5 & 2 \\ 14 & 10.5 & 2 \\ 10.5 & 14 & 3 \\ 3.5 & 14 & 3 \\ 0 & 10.5 & 4 \\ 0 & 3.5 & 4 \end{pmatrix}$$

Grid Divisions:

Predict Grid?

only in 4 block mode

(grid divisions include walls of furnace)

$$Grid_x = \begin{pmatrix} 0 \\ 3.5 \\ 7 \\ 10.5 \\ 14 \end{pmatrix} \qquad Grid_y = \begin{pmatrix} 0 \\ 3.5 \\ 7 \\ 10.5 \\ 14 \end{pmatrix}$$

Furnace Dimensions:

X dimension of furnace: $x_{dim} := 14 \quad m$

Y dimension of furnace: $y_{dim} := 14 \quad m$

Number of Acoustic Paths:

Number of blocks in x-plane: $N_x := 4$

Number of blocks in y-plane: $N_y := 4$

Number of blocks: $N_b := N_x \cdot N_y = 16$

Number of interpolation divisions: $N_d := 15$

Flue Gas Properties:

Specific heat ratio: $\gamma_{fg} := 1.28$

Specific gas constant of flue gas: $R_{fg} := 258 \quad \frac{J}{kgK}$

Constant TOF error offset $TOFerror := 0.0001 \quad s$

Add Radiation Pyrometry Readings:

Radiation Pyrometers

$G1 := 3.5$

$G3 := 14 - G1$

$$RadX := \begin{pmatrix} 0.05 \\ 7 \\ 13.95 \\ 7 \end{pmatrix} \qquad RadY := \begin{pmatrix} 7 \\ 0.05 \\ 7 \\ 13.95 \end{pmatrix}$$

$$Grid_x := \begin{pmatrix} 0 \\ G1 \\ 7 \\ G3 \\ 14 \end{pmatrix} \qquad Grid_y := \begin{pmatrix} 0 \\ G1 \\ 7 \\ G3 \\ 14 \end{pmatrix}$$

Functions

General functions

$$\begin{pmatrix} Grid_x \\ Grid_y \end{pmatrix} :=$$

if PredictGrid = 1 — Predicts grid for 4x4 block case if predict grid is selected

  if Transceiver = 1

    $G2 \leftarrow 0.69 \cdot RecMat_{1,1} + 0.29$

    $G4 \leftarrow x_{dim} - G2$

  if Transceiver = 0

    $G2 \leftarrow -0.2321 \cdot \left(RecMat_{1,1}\right)^2 + 1.9661 \cdot RecMat_{1,1} - 0.8518$

    $G2 \leftarrow RecMat_{1,1}$ if $\left[G2 \geq \left(RecMat_{1,1} - 0.15\right)\right] \wedge \left(G2 \leq RecMat_{1,1} + 0.15\right)$

    $G4 \leftarrow x_{dim} - G2$

  $$Grid_x \leftarrow \begin{pmatrix} 0 \\ G2 \\ \frac{x_{dim}}{2} \\ G4 \\ x_{dim} \end{pmatrix}$$

  $$Grid_y \leftarrow \begin{pmatrix} 0 \\ G2 \\ \frac{y_{dim}}{2} \\ G4 \\ y_{dim} \end{pmatrix}$$

  if PredictGrid = 0

    $$Grid_x \leftarrow \begin{pmatrix} 0 \\ G1 \\ \frac{x_{dim}}{2} \\ G3 \\ x_{dim} \end{pmatrix}$$

    $$Grid_y \leftarrow \begin{pmatrix} 0 \\ G1 \\ \frac{y_{dim}}{2} \\ G3 \\ y_{dim} \end{pmatrix}$$

  return $\begin{pmatrix} Grid_x \\ Grid_y \end{pmatrix}$

Number of Acoustic Paths calculated based on inputs

```
N_t := | N_t ← 0
       | NoRec ← length(RecMat^⟨1⟩)
       | NoTrans ← length(TransMat^⟨1⟩)
       | if Transceiver = 1
       |   | IterationStart ← 2
       |   | for i ∈ 1.. NoRec
       |   |   | for j ∈ IterationStart .. NoRec
       |   |   |   N_t ← N_t + 1 if RecMat_{i,3} ≠ RecMat_{j,3}
       |   |   | IterationStart ← IterationStart + 1
       |   |   | IterationStart ← NoRec if IterationStart ≥ NoRec
       | for i ∈ 1.. NoTrans                          if Transceiver = 0
       |   for j ∈ 1.. NoRec
       |     N_t ← N_t + 1 if TransMat_{i,3} ≠ RecMat_{j,3}
       | return N_t
```

$N_t = 24$

```
zeroes(x, y) := | 0
                | return 0
```

Function that just returns 0. used to initiliase zero matrices

```
MatSum(M) := | S ← 0
             | for i ∈ 1.. cols(M)
             |   S ← S + M^⟨i⟩
             | ∑S
```

Sums up all the elements of a matrix

```
RowSum(M) := [ | M ← M^T
               | for i ∈ 1.. length[(M^T)^⟨1⟩]
               |   LVect_i ← ∑(M)^⟨i⟩
               | return LVect ]
```

Sums up all the rows of a matrix

```
Nest(Matrix) := | n_rows ← length(Matrix^⟨1⟩)
                | for i ∈ 1.. n_rows
                |   NestedMatrix_i ← (Matrix^T)^⟨i⟩
                | return NestedMatrix
```

Turns a matrix into a nested vector

$$\text{DistPts}(Pt1, Pt2) := \left| \begin{array}{l} Dist \leftarrow |Pt1 - Pt2| \\ \text{return } Dist \end{array} \right.$$

Calculates the distance between two points

$$\text{GoldenMin}(Funcname, a, b, tol) := \left| \begin{array}{l} goldratio \leftarrow \dfrac{\left(1 + \sqrt{5}\right)}{2} \\ \text{while } \sqrt{(a - b)^2} > tol \\ \quad \left| \begin{array}{l} x1 \leftarrow b - \dfrac{(b - a)}{goldratio} \\ x2 \leftarrow a + \dfrac{(b - a)}{goldratio} \\ f1 \leftarrow Funcname(x1) \\ f2 \leftarrow Funcname(x2) \\ a \leftarrow x1 \text{ if } f1 \geq f2 \\ b \leftarrow x2 \text{ otherwise} \end{array} \right. \\ xmin \leftarrow \dfrac{(a + b)}{2} \\ \text{return } xmin \end{array} \right.$$

Golden Section Search for finding minima:

$$\text{DeNest}(NestedMatrix) := \left(\begin{array}{l} N \leftarrow \text{length}(NestedMatrix) \\ \text{for } i \in 1..N \\ \quad \left| \begin{array}{l} Vect \leftarrow NestedMatrix_i \\ Matrix^{\langle i \rangle} \leftarrow Vect \end{array} \right. \\ Matrix \leftarrow Matrix^T \\ \text{return } Matrix \end{array} \right)$$

Turn Nested Vectors back into a matrix

$$TransPos := Nest(TransMat)$$

$$RecPos := Nest(RecMat)$$

Prepare transmitter and receiver matrices

Distance Matrix functions:

Intersc

Populates distance matrix for transmitter/receiver case

```
PopulateDMat (TransPos , RecPos) :=
    NoTrans ← length (TransPos )                    determine number of
    NoRec ← length (RecPos)                         transmitters and
    DistMat ← matrix(N_t , N_b , zeroes)            receivers
    path ← 0
    for i ∈ 1.. NoTrans
      for j ∈ 1.. NoRec
        pt1 ← TransPos_i                            acoustic path goes from
        pt2 ← RecPos_j                              ot1 - pt2 i.e transmitter
                                                    to receiver
        if pt1_3 ≠ pt2_3                            check if transmitter/receivers
                                                    are on same wall
          path ← path + 1
          Start ← submatrix(pt1 , 1, 2, 1, 1)
          End ← submatrix(pt2 , 1, 2, 1, 1)
          x_start_path ← Start_1
          y_start_path ← Start_2
          x_end_path ← End_1
          y_end_path ← End_2
          IntPts ← Intersection (Start, End)        determine
          NoPts ← length (IntPts)                   intersections
                                                    with grid
          for k ∈ 1.. NoPts − 1
            IntPt1 ← IntPts_k
            IntPt2 ← IntPts_(k+1)
            distpt ← DistPts(IntPt1 , IntPt2)       only consider
            if distpt > 0.005·x_dim                 viable if segments
                                                    is above 0.5% of
                                                    furnace dimension
              AvPt ← (IntPt1 + IntPt2) / 2
              BlockNo ← BlockNumber(AvPt)           determine block No. of path
              DistMat_path , BlockNo ← distpt       segements and insert into
                                                    Distance matrix
    Length ← RowSum(DistMat)
    return (DistMat, Length, x_start, x_end, y_start, y_end)
```

Transceiver version of the Populate distance function

```
PopulateDMatTrans (RecPos) :=
    NoRec ← length (RecPos)
    DistMat ← matrix(N_t, N_b, zeroes)
    IterationStart ← 2
    path ← 0
    for i ∈ 1.. NoRec
        for j ∈ IterationStart .. NoRec
            pt1 ← RecPos_i
            pt2 ← RecPos_j
            if pt1_3 ≠ pt2_3
                path ← path + 1
                Start ← submatrix(pt1, 1, 2, 1, 1)
                End ← submatrix(pt2, 1, 2, 1, 1)
                x_start_path ← Start_1
                y_start_path ← Start_2
                x_end_path ← End_1
                y_end_path ← End_2
                IntPts ← Intersection (Start, End)
                NoPts ← length (IntPts)
                for k ∈ 1.. NoPts − 1
                    IntPt1 ← IntPts_k
                    IntPt2 ← IntPts_(k+1)
                    distpt ← DistPts(IntPt1, IntPt2)
                    if distpt > 0.005·x_dim
                        AvPt ← (IntPt1 + IntPt2)/2
                        BlockNo ← BlockNumber(AvPt)
                        DistMat_(path, BlockNo) ← distpt
        IterationStart ← IterationStart + 1
        IterationStart ← NoRec if IterationStart ≥ NoRec
    Length ← RowSum(DistMat)
    return (DistMat, Length, x_start, x_end, y_start, y_end)
```

Determines a lines intersections with the grid
based on start and end coordinates

```
Intersection(Start, End) :=
    IntPt ← matrix(2, 1, zeroes)
    if Start_1 = End_1                                   is line vertical?
        N ← length(Grid_y)
        for i ∈ 1..N
            IntPt_1 ← Start_1
            IntPt_2 ← Grid_y_i
            IntPts_i ← IntPt
        IntPts ← csort(DeNest(IntPts), 2)
    if Start_2 = End_2                                   is line horizontal?
        N ← length(Grid_x)
        for i ∈ 1..N
            IntPt_1 ← Grid_x_i
            IntPt_2 ← Start_2
            IntPts_i ← IntPt
        IntPts ← csort(DeNest(IntPts), 1)
    if (Start_2 ≠ End_2) ∧ (Start_1 ≠ End_1)             neither horizontal or veritcal
        grad ← (End_2 − Start_2) / (End_1 − Start_1)
        yint ← Start_2 − Start_1·grad
        N ← length(Grid_x)
        k ← 0
        for i ∈ 1..N
            IntPt_2 ← grad·Grid_x_i + yint
            if (IntPt_2 ≥ 0) ∧ (IntPt_2 ≤ y_dim)
                k ← k + 1
                IntPt_1 ← Grid_x_i
                IntPts_k ← IntPt
        N ← length(Grid_y)
        for j ∈ 1..N
            IntPt_1 ← (Grid_y_j − yint) / grad
            if (0 ≤ IntPt_1) ∧ (IntPt_1 ≤ x_dim)
                k ← k + 1
                IntPt_2 ← Grid_y_j
                IntPts_k ← IntPt
        IntPts ← csort(DeNest(IntPts), 1)                sort intersections
                                                         by x coordinate
    IntPts ← Nest(IntPts)
    return IntPts
```

Determines block number that coordinate lies within

$$\begin{aligned}&\text{BlockNumber}(Pt) := \\ &\quad colvect \leftarrow Pt_1 > Grid_x \\ &\quad col \leftarrow \text{MatSum}(colvect) \\ &\quad rowvect \leftarrow Pt_2 < Grid_y \\ &\quad row \leftarrow \text{MatSum}(rowvect) \\ &\quad BlockNo \leftarrow col + (row - 1)\cdot N_x \\ &\quad \text{return } BlockNo\end{aligned}$$

Function that creates grid in format necessary for use with the "interp" function

$$\begin{aligned}&\text{CreateGrid}(Grid_x, Grid_y) := \\ &\quad nx \leftarrow \text{length}(Grid_x) \\ &\quad ny \leftarrow \text{length}(Grid_y) \\ &\quad \text{for } ix \in 1..nx \\ &\quad\quad \text{for } iy \in 1..ny \\ &\quad\quad\quad Grid_{ix,iy} \leftarrow \begin{pmatrix} Grid_{x_{ix}} \\ Grid_{y_{iy}} \end{pmatrix} \\ &\quad \text{return } Grid\end{aligned}$$

$$\begin{aligned}&\text{Interdependancy} := \\ &\quad Bool \leftarrow DistMat > 0 \\ &\quad \text{Interdependancy} \leftarrow \text{MatSum}(Bool) \\ &\quad \text{return Interdependancy}\end{aligned}$$

determine vectors of centre points in grid
i.e data point coordinates

$$\begin{aligned}&\text{Centres}(Grid_x, Grid_y) := \\ &\quad \text{for } i \in 1..N_b \\ &\quad\quad j \leftarrow \text{mod}(i, N_x) \\ &\quad\quad j \leftarrow N_x \text{ if } j = 0 \\ &\quad\quad x_i \leftarrow \frac{Grid_{x_j} + Grid_{x_{j+1}}}{2} \\ &\quad\quad j \leftarrow N_y + 1 - \text{ceil}\left(\frac{i}{N_x}\right) \\ &\quad\quad y_i \leftarrow \frac{Grid_{y_j} + Grid_{y_{j+1}}}{2} \\ &\quad \text{return } \begin{pmatrix} x_i \\ y_i \end{pmatrix}\end{aligned}$$

Temperature profile functions:

determines x-y coordinates of off centre peak

$$Peakx := \frac{x_{dim}}{2} + DistanceFromCentre \cdot \cos\left(AngleFromHorizontal \cdot \frac{\pi}{180}\right) = 7$$

$$Peaky := \frac{y_{dim}}{2} + DistanceFromCentre \cdot \sin\left(AngleFromHorizontal \cdot \frac{\pi}{180}\right) = 4$$

Set temperature profiles

$$T_{fg}(x,y) := \left| \begin{array}{l} T_{fg} \leftarrow \left\lfloor 1000 + TemperatureRise \cdot e^{\frac{-\left[(x-Peakx)^2+(y-Peaky)^2\right]}{25}} \right\rfloor \text{ if } OffCentrePeak = 1 \\ \text{otherwise} \\ \quad \left| \begin{array}{ll} T_{fg} \leftarrow \left(1100 + 300\cdot\sin\left(\frac{\pi}{14}\cdot x\right)\cdot\sin\left(\frac{\pi}{14}\cdot y\right)\right) \text{ if } CF = 1 & \text{single peak} \\ T_{fg} \leftarrow \left(800 + 800\cdot\sin\left(\frac{\pi}{14}\cdot x\right)\cdot\sin\left(\frac{\pi}{14}\cdot y\right)\right) \text{ if } CF = 2 & \text{steep single peak} \\ T_{fg} \leftarrow \left\lfloor 1000 + 600\cdot e^{\frac{-\left[(x-7)^2+(y-4)^2\right]}{100}} \right\rfloor \text{ if } CF = 3 & \text{asymmetrical peak} \\ T_{fg} \leftarrow \left\lfloor \begin{array}{l} 800 + 800\cdot e^{\left[-20\left[\left(\frac{x}{14}-\frac{1}{3}\right)^2+\left(\frac{y}{12}-\frac{2}{3}\right)^2\right]\right]} \ldots \\ \quad + 800\cdot e^{\left[-\left[20\left(\frac{x}{14}-\frac{2}{3}\right)^2+15\left(\frac{y}{12}-\frac{1}{3}\right)^2\right]\right]} \end{array} \right\rfloor \text{ if } CF = 4 & \text{double asymmetrical peak} \\ T_{fg} \leftarrow BezDist(x,y) \text{ if } CF = 5 & \text{flat distribution} \end{array} \right. \\ \text{return } T_{fg} \end{array} \right.$$

$$cntrl := \begin{pmatrix} 650 & 650 & 650 & 650 & 650 & 650 & 650 & 650 & 650 & 650 \\ 650 & 1400 & 1400 & 1400 & 1400 & 1400 & 1400 & 1400 & 1400 & 650 \\ 650 & 1400 & 1300 & 1300 & 1300 & 1300 & 1300 & 1300 & 1400 & 650 \\ 650 & 1400 & 1300 & 1200 & 1200 & 1200 & 1200 & 1300 & 1400 & 650 \\ 650 & 1400 & 1300 & 1200 & 1300 & 1300 & 1200 & 1300 & 1400 & 650 \\ 650 & 1400 & 1300 & 1200 & 1300 & 1300 & 1200 & 1300 & 1400 & 650 \\ 650 & 1400 & 1300 & 1200 & 1200 & 1200 & 1200 & 1300 & 1400 & 650 \\ 650 & 1400 & 1300 & 1300 & 1300 & 1300 & 1300 & 1300 & 1400 & 650 \\ 650 & 1400 & 1400 & 1400 & 1400 & 1400 & 1400 & 1400 & 1400 & 650 \\ 650 & 650 & 650 & 650 & 650 & 650 & 650 & 650 & 650 & 650 \end{pmatrix}$$

cntrl matrix for bezier surface

$$Bern(u,i,n) := \left[\frac{n!}{i!\,(n-i)!}\right]\cdot\left[u^{i}\cdot(1-u)^{n-i}\right]$$

Bernstein polynomial function

$$BezDist(u,v) := \sum_{i=0}^{9}\sum_{j=0}^{9}\left(Bern\left(\frac{u}{x_{dim}},i,9\right)\cdot Bern\left(\frac{v}{y_{dim}},j,9\right)cntrl_{i+1,j+1}\right)$$

Bezier

Radial basis function:

$$RBF\left(x_i, y_i, \varepsilon\right) := \left| \begin{array}{l} \text{for } row \in 1..\left(\text{length}\left(x_i\right)\right) \\ \quad \text{for } col \in 1..\left(\text{length}\left(y_i\right)\right) \\ \quad \Phi fg_{row,col} \leftarrow \left[1+\left[\varepsilon\cdot\left[\sqrt{\left(x_{i_{row}}-x_{i_{col}}\right)^2+\left(y_{i_{row}}-y_{i_{col}}\right)^2}\right]\right]^2\right]^{0.5} \\ \Phi fg \end{array} \right.$$

populate basis function matrix based on shape factor

Simulating time of flight functions:

Velocity Function:

$$Vel(x,y) := \left| \begin{array}{l} Vel \leftarrow \left(R_{fg}\cdot\gamma_{fg}\cdot T_{fg}(x,y)\right)^{0.5} \\ \text{return } Vel \end{array} \right.$$

Slowness Function:

$$a(x,y) := \left| \begin{array}{l} a \leftarrow \frac{1}{Vel(x,y)} \\ \text{return } a \end{array} \right.$$

Paramaterise x function:

$$x(s,i) := \left| \begin{array}{l} x \leftarrow x_{start_i} + \left(x_{end_i} - x_{start_i}\right)\cdot s \\ \text{return } x \end{array} \right.$$

Paramaterise y function:

$$y(s,i) := \left| \begin{array}{l} y \leftarrow y_{start_i} + \left(y_{end_i} - y_{start_i}\right)\cdot s \\ \text{return } y \end{array} \right.$$

Integrand Function:

$$a_{int}(s,i) := \left| \begin{array}{l} a_{int} \leftarrow a(x(s,i),y(s,i)) \cdot Length_i \\ \text{return } a_{int} \end{array} \right.$$

$$normdist := Normal(1000)$$ prepare vector with normal distribution

Time of flight function:

$$TOF(N_t) := \left| \begin{array}{l} \text{for } i \in 1..(N_t) \\ \quad \left| \begin{array}{l} t_i \leftarrow \int_0^1 a_{int}(s,i)\, ds \\ t_i \leftarrow t_i + t_i \cdot normdist_{ceil(rnd(1000))} \cdot PathError \text{ if } ConstantError = 0 \\ t_i \leftarrow t_i + TOFerror \text{ if } ConstantError = 1 \end{array} \right. \\ \text{return } t \end{array} \right.$$

Functions for plotting acoustic paths and grid

creates matrix of data points to create acoustic path plot

$$PlotMatrix := \left| \begin{array}{l} cnt \leftarrow 1 \\ \text{for } i \in 1..\text{length}(TransMat^{\langle 1 \rangle}) \text{ if } Transceiver = 0 \\ \quad \left| \begin{array}{l} \text{for } j \in 1..\text{length}(RecMat^{\langle 1 \rangle}) \\ \quad \text{if } TransMat_{i,3} \neq RecMat_{j,3} \\ \quad \quad \left| \begin{array}{l} PlotMat_{cnt,1} \leftarrow TransMat_{i,1} \\ PlotMat_{cnt,2} \leftarrow TransMat_{i,2} \\ cnt \leftarrow cnt + 1 \\ PlotMat_{cnt,1} \leftarrow RecMat_{j,1} \\ PlotMat_{cnt,2} \leftarrow RecMat_{j,2} \\ cnt \leftarrow cnt + 1 \\ PlotMat_{cnt,1} \leftarrow TransMat_{i,1} \\ PlotMat_{cnt,2} \leftarrow TransMat_{i,2} \end{array} \right. \\ AllMat_i \leftarrow PlotMat \\ cnt \leftarrow 1 \end{array} \right. \\ \text{return } AllMat \end{array} \right.$$

```
PlotTransMatrix := | NoRec ← length(RecMat^⟨1⟩)
                   | StartIteration ← 2
                   | cnt ← 1
                   | for i ∈ 1.. NoRec
                   |     for j ∈ StartIteration .. NoRec
                   |         PlotMat_(cnt,1) ← RecMat_(i,1)
                   |         PlotMat_(cnt,2) ← RecMat_(i,2)
                   |         cnt ← cnt + 1
                   |         PlotMat_(cnt,1) ← RecMat_(j,1)
                   |         PlotMat_(cnt,2) ← RecMat_(j,2)
                   |         cnt ← cnt + 1
                   |         PlotMat_(cnt,1) ← RecMat_(i,1)
                   |         PlotMat_(cnt,2) ← RecMat_(i,2)
                   |         cnt ← cnt + 1
                   |     StartIteration ← StartIteration + 1
                   |     StartIteration ← NoRec if StartIteration > NoRec
                   | return PlotMat
```

```
(Trans1)   |  if Transceiver = 1
(Trans2)   |      Trans1 ← PlotTransMatrix
(Trans3)   |      Trans2 ← (0 0)
(Trans4)   |      Trans3 ← (0 0)
           |      Trans4 ← (0 0)
           |  if Transceiver = 0
           |      TransPaths ← PlotMatrix
           |      Trans1 ← TransPaths_1
           |      Trans2 ← TransPaths_2
           |      Trans3 ← TransPaths_3
           |      Trans4 ← TransPaths_4
           |  return (Trans1)
           |         (Trans2)
           |         (Trans3)
           |         (Trans4)
```

creates matrix of data points to create the grid on the acoustic path plot

```
PlotGridx :=
    cnt ← 1
    PlotGridx[cnt, 1] ← Grid_x[2]
    PlotGridx[cnt, 2] ← 0
    cnt ← cnt + 1
    PlotGridx[cnt, 1] ← Grid_x[2]
    PlotGridx[cnt, 2] ← x_dim
    cnt ← cnt + 1
    for i ∈ 3.. (length(Grid_x) − 1)
        if PlotGridx[cnt−1, 2] = 0
            PlotGridx[cnt, 1] ← Grid_x[i]
            PlotGridx[cnt, 2] ← 0
            cnt ← cnt + 1
            PlotGridx[cnt, 1] ← Grid_x[i]
            PlotGridx[cnt, 2] ← x_dim
            cnt ← cnt + 1
        otherwise
            PlotGridx[cnt, 1] ← Grid_x[i]
            PlotGridx[cnt, 2] ← x_dim
            cnt ← cnt + 1
            PlotGridx[cnt, 1] ← Grid_x[i]
            PlotGridx[cnt, 2] ← 0
            cnt ← cnt + 1
    return PlotGridx
```

```
PlotGridy :=
    cnt ← 1
    PlotGridy[cnt, 2] ← Grid_y[2]
    PlotGridy[cnt, 1] ← 0
    cnt ← cnt + 1
    PlotGridy[cnt, 2] ← Grid_y[2]
    PlotGridy[cnt, 1] ← y_dim
    cnt ← cnt + 1
    for i ∈ 3.. (length(Grid_y) − 1)
        if PlotGridy[cnt−1, 1] = 0
            PlotGridy[cnt, 2] ← Grid_y[i]
            PlotGridy[cnt, 1] ← 0
            cnt ← cnt + 1
            PlotGridy[cnt, 2] ← Grid_y[i]
            PlotGridy[cnt, 1] ← y_dim
            cnt ← cnt + 1
        otherwise
            PlotGridy[cnt, 2] ← Grid_y[i]
            PlotGridy[cnt, 1] ← y_dim
            cnt ← cnt + 1
            PlotGridy[cnt, 2] ← Grid_y[i]
            PlotGridy[cnt, 1] ← 0
            cnt ← cnt + 1
    return PlotGridy
```

Main code

Simulate time of flight

$$t := \left| \begin{array}{l} t \leftarrow \text{matrix}\left(N_t, 1, \text{zeroes}\right) \\ t \leftarrow \text{TOF}\left(N_t\right) \text{ if } \text{RepeatReadings} = 0 \\ \text{if } \text{RepeatReadings} = 1 \\ \quad \left| \begin{array}{l} \text{for } i \in 1..\text{NoRepetitions} \\ \quad t \leftarrow t + \text{TOF}\left(N_t\right) \\ t \leftarrow \dfrac{t}{\text{NoRepetitions}} \end{array} \right. \\ \text{return } t \end{array} \right.$$

Populate Distance Matrix, Length vector, and start and end path coordinate vectors

$$\begin{pmatrix} \text{DistMat} \\ \text{Length} \\ x_{start} \\ x_{end} \\ y_{start} \\ y_{end} \end{pmatrix} := \left| \begin{array}{l} \text{DistData} \leftarrow \text{PopulateDMatTrans}\left(\text{RecPos}\right) \text{ if } \text{Transceiver} = 1 \\ \text{DistData} \leftarrow \text{PopulateDMat}\left(\text{TransPos}, \text{RecPos}\right) \text{ if } \text{Transceiver} = 0 \\ \text{return } \text{DistData} \end{array} \right.$$

$\text{Slow} := \text{geninv}\left(\text{DistMat}\right) \cdot t$ Apply generalised inverse to find slow vector

$T_{ls} := \left(\dfrac{1}{R_{fg} \cdot \gamma_{fg}}\right) \cdot \left(\dfrac{1}{\text{Slow}^2}\right)$ Calculate least squares temperature

$$T_i\left(T_{ls}\right) := \left| \begin{array}{l} \text{for } i \in 1..N_x \\ \quad \text{for } j \in 1..N_y \\ \quad\quad \left| k \leftarrow j + N_x \cdot (i - 1) \right. \\ \quad\quad \left| T_{i_{i,j}} \leftarrow T_{ls_k} \right. \\ T_i \end{array} \right.$$

Convert Temperature vector into matrix for plotting

$T_{plot} := T_i\left(T_{ls}\right)$

$$CentreVectors := Centres\left(Grid_x, Grid_y\right)$$

$$x_i := CentreVectors_1$$

$$y_i := CentreVectors_2$$

determine coordinates for temperature data points

$$Trad := \left| \begin{array}{l} \text{for } i \in 1..\,length\,(RadX) \\ \quad Trad_i \leftarrow T_{fg}\left(RadX_i, RadY_i\right) \\ \text{return } Trad \end{array} \right.$$

calculating raditation pyrometer readings

$$\begin{pmatrix} x_i \\ y_i \\ T_{ls} \end{pmatrix} := \left| \begin{array}{l} \text{if } RadiationPyrometer = 1 \\ \quad \left| \begin{array}{l} T_{ls} \leftarrow stack\left(T_{ls}, Trad\right) \\ x_i \leftarrow stack\left(x_i, RadX\right) \\ y_i \leftarrow stack\left(y_i, RadY\right) \end{array} \right. \\ \text{return } \begin{pmatrix} x_i \\ y_i \\ T_{ls} \end{pmatrix} \end{array} \right.$$

Add radiation pyrometer readings to temperature and coordinate matrices

RBF interpolation

$$PredictShape(\varepsilon) := \left| \begin{array}{l} \Phi_{fg} \leftarrow RBF\left(x_i, y_i, \varepsilon\right) \\ errormat \leftarrow \dfrac{\left(\Phi_{fg}^{-1} \cdot T_{ls}\right)}{\left(diag\left(\Phi_{fg}^{-1}\right)\right)} \\ Predictor \leftarrow \sqrt{errormat \cdot errormat} \\ \text{return } Predictor \end{array} \right.$$

Rippa's algorithm for predicting shape factor

$BracketMin := 0.02 \qquad BracketMax := 1 \qquad tolerance := 0.001$

$DPredictShape(\varepsilon) := DP \leftarrow \frac{d}{d\varepsilon} PredictShape(\varepsilon)$ derivative of predictor function

Golde

Apply golden search function to find shape factor that minimises Rippa's algorithm.
If algorithm minimises at minimum then use derivative to find local minimum

$$\varepsilon := \begin{| shape \leftarrow GoldenMin(PredictShape, BracketMin, BracketMax, tolerance) \\ shape \leftarrow GoldenMin\left(DPredictShape, BracketMin, \frac{BracketMax}{3}, tolerance\right) \text{ if } shape \le BracketMin + 0.001 \\ return\ shape \end{|$$

$\Phi_{fg} := RBF(x_i, y_i, \varepsilon)$ populate basis function matrix

$\omega_{fg} := \Phi_{fg}^{-1} \cdot T_{ls}$ determine weightings via matrix inversion

Define RBF temperature function

$$TRBF(x,y) := \begin{| T_{rbf} \leftarrow 0 \\ \text{for } i \in 1..(length(x_i)) \\ \quad T_{rbf} \leftarrow T_{rbf} + \omega_{fg_i} \cdot \left[1 + \left[\varepsilon \cdot \left[\sqrt{(x - x_i)^2 + (y - y_i)^2}\right]\right]^2\right]^{-0.5} \\ T_{rbf} \end{|$$

Cubic spline interpolation

$ix := 1..N_x$ $iy := 1..N_y$

$X_{ix} := ix$ $Y_{iy} := iy$

$Mxy := augment(sort(X), sort(Y))$

$coef3 := cspline(Mxy, T_{plot})$ $coef1 := lspline(Mxy, T_{plot})$ prepare coefficients for each endpoint type

$coef2 := pspline(Mxy, T_{plot})$

$$CubicSpline(x,y) := \left| \begin{array}{l} pt \leftarrow \begin{bmatrix} \frac{x}{x_{dim}} \cdot (N_x + 1) \\ \frac{y}{y_{dim}} (N_y + 1) \end{bmatrix} \\ Temp \leftarrow interp(coef3, Mxy, T_{plot}, pt) \\ return\ Temp \end{array} \right.$$

cubic spline function

$$ParCubSpline(x,y) := \left| \begin{array}{l} pt \leftarrow \begin{bmatrix} \frac{x}{x_{dim}} \cdot (N_x + 1) \\ \frac{y}{y_{dim}} (N_y + 1) \end{bmatrix} \\ Temp \leftarrow interp(coef2, Mxy, T_{plot}, pt) \\ return\ Temp \end{array} \right.$$

cubic spline function with parabolic endpoints

$$LinCubSpline(x,y) := \left| \begin{array}{l} pt \leftarrow \begin{bmatrix} \frac{x}{x_{dim}} \cdot (N_x + 1) \\ \frac{y}{y_{dim}} (N_y + 1) \end{bmatrix} \\ Temp \leftarrow interp(coef1, Mxy, T_{plot}, pt) \\ return\ Temp \end{array} \right.$$

cubic spline function with linear endpoints

Regression

$Mreg := augment\left(x_i, y_i\right)$

2nd order multiple regression

$$Regression2\,(x,y) := \begin{| n \leftarrow 2 \\ Reg \leftarrow regress\left(Mreg, T_{ls}, n\right) \\ Temp \leftarrow interp\left[Reg, Mreg, T_{ls}, \begin{pmatrix} x \\ y \end{pmatrix}\right] \\ return\ \ Temp}$$

3nd order multiple regression

$$Regression3\,(x,y) := \begin{| n \leftarrow 3 \\ Reg \leftarrow regress\left(Mreg, T_{ls}, n\right) \\ Temp \leftarrow interp\left[Reg, Mreg, T_{ls}, \begin{pmatrix} x \\ y \end{pmatrix}\right] \\ return\ \ Temp}$$

localised multiple regression

$$RegressionL\,(x,y) := \begin{| n \leftarrow 3 \\ Reg \leftarrow loess\left(Mreg, T_{ls}, n\right) \\ Temp \leftarrow interp\left[Reg, Mreg, T_{ls}, \begin{pmatrix} x \\ y \end{pmatrix}\right] \\ return\ \ Temp}$$

Lagrange interpolation

Bernstein polynomials

$$Lgx(x,i) := \begin{| P \leftarrow 1 \\ for\ \ j \in 1..N_x \\ \quad P \leftarrow P \cdot \frac{x - x_{i_j}}{x_{i_i} - x_{i_j}} \ \ if\ \ x_{i_i} \neq x_{i_j} \\ return\ \ P}$$

$$Lgy(y,i) := \begin{| P \leftarrow 1 \\ for\ \ j \in 1..N_y \\ \quad P \leftarrow P \cdot \frac{y - y_{i_{j \cdot N_x}}}{y_{i_i} - y_{i_{j \cdot N_x}}} \ \ if\ \ y_{i_i} \neq y_{i_{j \cdot N_y}} \\ return\ \ P}$$

Legrange interpolation function

$$\text{Lagrange}(x,y) := \sum_{j=1}^{N_y} \sum_{i=1}^{N_x} \left(\text{Lgx}(x,i) \cdot \text{Lgy}\left(y, j \cdot N_x\right) \cdot T_{\text{plot}_{i,j}} \right)$$

Evaluating Error

$npx := N_d$ $\quad$ $npy := N_d$

$ix := 0 .. npx - 1$ $\quad$ $iy := 0 .. npy - 1$

$$intx_{ix+1} := ix \cdot \frac{x_{dim}}{npx - 1} \quad inty_{iy+1} := iy \cdot \frac{y_{dim}}{npy - 1}$$

$InterpGrid := CreateGrid(intx, inty)$

Calculate mean, RMS and Energy error

$$
\begin{aligned}
&\text{CalcError}(\text{InterpGrid}, f) := \\
&\quad ni \leftarrow \text{length}\left(\text{InterpGrid}^{\langle 1\rangle}\right) \\
&\quad nj \leftarrow \text{length}\left[\left(\text{InterpGrid}^{T}\right)^{\langle 1\rangle}\right] \\
&\quad \text{for } i \in 1..ni \\
&\qquad \text{for } j \in 1..nj \\
&\qquad\quad pt \leftarrow \text{InterpGrid}_{i,j} \\
&\qquad\quad \text{Err}_{i,j} \leftarrow \frac{\sqrt{\left(T_{fg}\left(pt_1, pt_2\right) - f\left(pt_1, pt_2\right)\right)^2}}{T_{fg}\left(pt_1, pt_2\right)} \cdot 100 \\
&\qquad\quad \text{ErrSquare}_{i,j} \leftarrow \left(T_{fg}\left(pt_1, pt_2\right) - f\left(pt_1, pt_2\right)\right)^2 \\
&\qquad\quad \text{Temp}_{i,j} \leftarrow T_{fg}\left(pt_1, pt_2\right) \\
&\qquad\quad F_{i,j} \leftarrow f\left(pt_1, pt_2\right) \\
&\quad \text{MeanErr} \leftarrow \text{mean}(\text{Err}) \\
&\quad \text{SumT} \leftarrow \text{MatSum}(\text{Temp}) \\
&\quad \text{SumF} \leftarrow \text{MatSum}(F) \\
&\quad \text{SumErr} \leftarrow \frac{\text{SumT} - \text{SumF}}{\text{SumT}} \cdot 100 \\
&\quad \text{IntgT} \leftarrow \int_0^{y\text{dim}} \int_0^{x\text{dim}} T_{fg}(x, y)\, dx\, dy \\
&\quad \text{IntgF} \leftarrow \int_0^{y\text{dim}} \int_0^{x\text{dim}} f(x, y)\, dx\, dy \\
&\quad \text{EnergyErr} \leftarrow \frac{\text{IntgT} - \text{IntgF}}{\text{IntgF}} \cdot 100 \\
&\quad \text{ErrRMS} \leftarrow \sqrt{\frac{\text{MatSum}(\text{ErrSquare})}{ni \cdot nj}} \cdot \frac{100}{\text{mean}(\text{Temp})} \\
&\quad \text{return } (\text{MeanErr}\ \ \text{ErrRMS}\ \ \text{SumErr}\ \ \text{EnergyErr})
\end{aligned}
$$

$$
\begin{aligned}
&\text{CalcErr}(\text{InterpGrid}, f) := \\
&\quad ni \leftarrow \text{length}\left(\text{InterpGrid}^{\langle 1 \rangle}\right) \\
&\quad nj \leftarrow \text{length}\left[\left(\text{InterpGrid}^{T}\right)^{\langle 1 \rangle}\right] \\
&\quad \text{for } i \in 1..ni \\
&\qquad \text{for } j \in 1..nj \\
&\qquad\quad pt \leftarrow \text{InterpGrid}_{i,j} \\
&\qquad\quad \text{Shiftedpt} \leftarrow \begin{pmatrix} -pt_2 \\ pt_1 \end{pmatrix} + \begin{pmatrix} x_{dim} \\ 0 \end{pmatrix} \\
&\qquad\quad \text{Err}_{i,j} \leftarrow \frac{\sqrt{\left(T_{fg}\left(pt_1, pt_2\right) - f\left(\text{Shiftedpt}_1, \text{Shiftedpt}_2\right)\right)^2}}{T_{fg}\left(pt_1, pt_2\right)} \cdot 100 \\
&\qquad\quad \text{ErrSquare}_{i,j} \leftarrow \left(T_{fg}\left(pt_1, pt_2\right) - f\left(\text{Shiftedpt}_1, \text{Shiftedpt}_2\right)\right)^2 \\
&\qquad\quad \text{Temp}_{i,j} \leftarrow T_{fg}\left(pt_1, pt_2\right) \\
&\qquad\quad F_{i,j} \leftarrow f\left(\text{Shiftedpt}_1, \text{Shiftedpt}_2\right) \\
&\quad \text{MeanErr} \leftarrow \text{mean}(\text{Err}) \\
&\quad \text{SumT} \leftarrow \text{MatSum}(\text{Temp}) \\
&\quad \text{SumF} \leftarrow \text{MatSum}(F) \\
&\quad \text{SumErr} \leftarrow \frac{\text{SumT} - \text{SumF}}{\text{SumT}} \cdot 100 \\
&\quad \text{IntgT} \leftarrow \int_0^{y_{dim}} \int_0^{x_{dim}} T_{fg}(x, y)\, dx\, dy \\
&\quad \text{IntgF} \leftarrow \int_0^{y_{dim}} \int_0^{x_{dim}} f(x, y)\, dx\, dy \\
&\quad \text{EnergyErr} \leftarrow \frac{\text{IntgT} - \text{IntgF}}{\text{IntgT}} \cdot 100 \\
&\quad \text{ErrRMS} \leftarrow \sqrt{\frac{\text{MatSum}(\text{ErrSquare})}{ni \cdot nj}} \cdot \frac{100}{\text{mean}(\text{Temp})} \\
&\quad (\text{MeanErr}\ \ \text{ErrRMS}\ \ \text{SumErr}\ \ \text{EnergyErr})
\end{aligned}
$$

calculates the error between the least squares data points and the actual average temperature of each block

$$\begin{aligned}
&\text{DataPtErr} := \\
&\quad ni \leftarrow \text{length}\left(\text{Grid}_x\right) - 1 \\
&\quad nj \leftarrow \text{length}\left(\text{Grid}_y\right) - 1 \\
&\quad \text{for } i \in 1..ni \\
&\qquad \text{for } j \in 1..nj \\
&\qquad\quad \text{IntgT}_{i,j} \leftarrow \frac{\int_{\text{Grid}_{y_i}}^{\text{Grid}_{y_{i+1}}} \int_{\text{Grid}_{x_j}}^{\text{Grid}_{x_{j+1}}} T_{fg}(x,y)\,dx\,dy}{\left(\text{Grid}_{x_{j+1}} - \text{Grid}_{x_j}\right)\cdot\left(\text{Grid}_{y_{i+1}} - \text{Grid}_{y_i}\right)} \\
&\qquad\quad \text{ErrMat}_{i,j} \leftarrow \frac{\text{IntgT}_{i,j} - \text{Tplot}_{ni+1-i,j}}{\text{IntgT}_{i,j}} \cdot 100 \\
&\quad \text{for } i \in 1..ni \\
&\qquad \text{for } j \in 1..nj \\
&\qquad\quad \text{AbsErr}_{i,j} \leftarrow \sqrt{\left(\text{ErrMat}_{i,j}\right)^2} \\
&\quad \text{MeanErr} \leftarrow \text{mean}(\text{AbsErr}) \\
&\quad \text{return} \begin{pmatrix} \text{ErrMat} \\ \text{IntgT} \\ \text{MeanErr} \end{pmatrix}
\end{aligned}$$

integrate temperature over each block and divide by the area of theat block to determine the average temperature

Error results

Errors of each interpolation function

ErrorRBF := CalcError(InterpGrid , TRBF) = (5.13 6.838 0.113 0.378)

ErrorCubic := CalcErr(InterpGrid , CubicSpline) = (198.797 373.344 19.147 17.063)

ErrorParabolic := CalcErr(InterpGrid , ParCubSpline) = (75.282 114.748 19.147 17.063)

ErrorLin := CalcErr(InterpGrid , LinCubSpline) = (17.165 20.484 13.195 12.419)

ErrorReg3 := CalcError(InterpGrid , Regression3) = (13.814 17.938 4.699 2.413)

ErrorReg2 := CalcError(InterpGrid , Regression2) = (14.116 18.059 4.699 2.413)

ErrorLag := CalcErr(InterpGrid , Lagrange) = (48.879 59.511 4.268 2.317)

Acoustic Path Plot

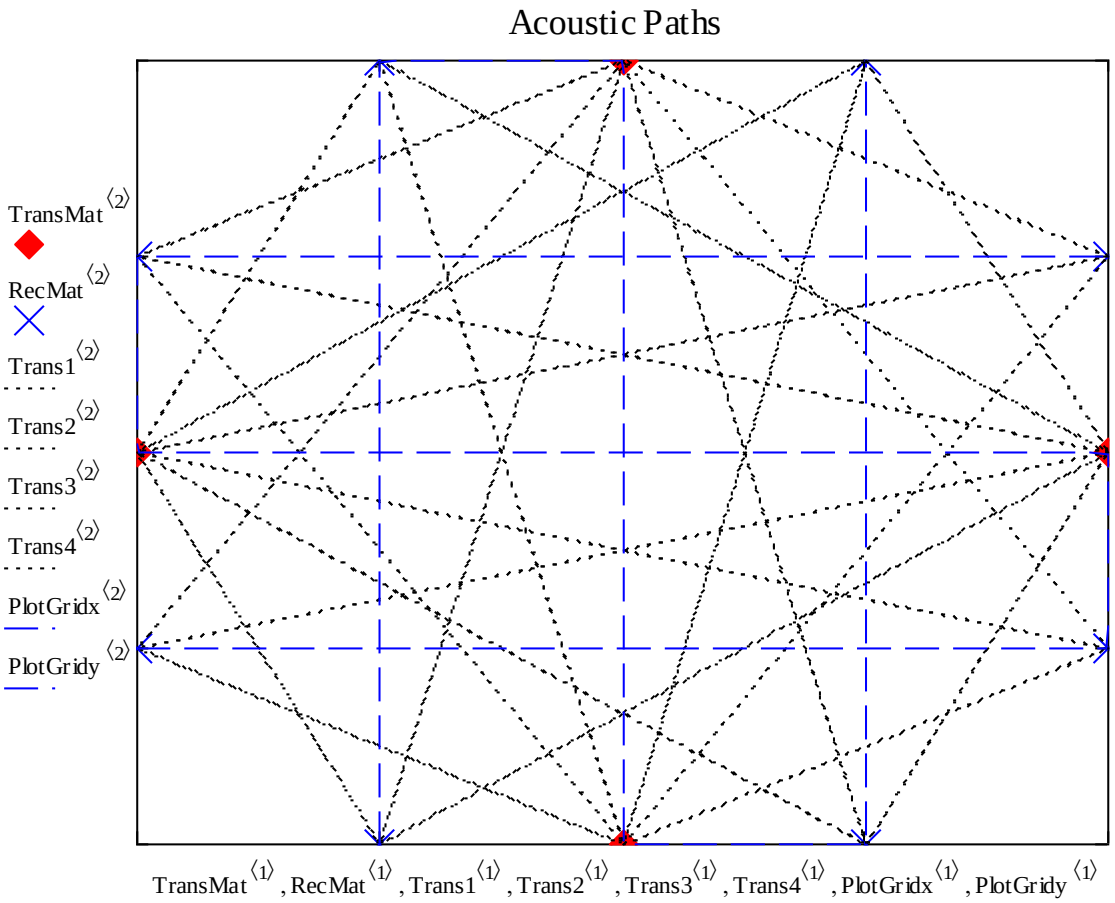

Error testing code

This section of code pertains specifically to studying the effects of path error on reconstruction. Various functions are redefined to be applied for multiple iterations at a time to account for the induced random path error.

$NoIterations := 100$ number of error data points

$PopulateTOFmatrix :=$

for $i \in 1..NoIterations$

$t \leftarrow matrix(N_t, 1, zeroes)$

$t_i \leftarrow TOF(N_t)$ if $RepeatReadings = 0$

if $RepeatReadings = 1$

for $j \in 1..NoRepetitions$

$t \leftarrow t + TOF(N_t)$

$t_i \leftarrow \frac{t}{NoRepetitions}$

$Slow_i \leftarrow geninv(DistMat) \cdot t_i$

$T_{ls_i} \leftarrow \left(\frac{1}{R_{fg} \cdot \gamma_{fg}}\right) \cdot \left[\frac{1}{(Slow_i)^2}\right]$

$T_{plot_i} \leftarrow T_i(T_{ls_i})$

return $\begin{pmatrix} T_{ls} \\ T_{plot} \\ Slow \end{pmatrix}$

Algorithm for determining TOF data for path error tests
It populates least squares temperature and Slowness matrix for NoIterations.

$TOFdata := PopulateTOFmatrix$

$T_{ls} := TOFdata_1$

$T_{plot} := TOFdata_2$

$Slow := TOFdata_3$

extract least squares temperature and slowness matrices from nested matrix this data set is then used for interpolation

RBFerrorData :=

for $i \in 1..\ NoIterations$

  $PredictShapeErr(\varepsilon) \leftarrow$

    $\Phi_{fg} \leftarrow RBF\left(x_i, y_i, \varepsilon\right)$

    $errormat \leftarrow \dfrac{\left(\Phi_{fg}^{-1} \cdot T_{ls_i}\right)}{\left(diag\left(\Phi_{fg}^{-1}\right)\right)}$

    $Predictor \leftarrow \sqrt{errormat \cdot errormat}$

    return Predictor

redefine predict shape function to change least square temperature matrix used between iterations

  $\varepsilon_i \leftarrow GoldenMin\ (PredictShapeErr, BracketMin, BracketMax, tolerance)$

  $\Phi_{fg_i} \leftarrow RBF\left(x_i, y_i, \varepsilon_i\right)$ populate basis function matrix

  $\omega_{fg_i} \leftarrow \left(\Phi_{fg_i}\right)^{-1} \cdot T_{ls_i}$ determine weightings via matrix inversion

for $i \in 1..\ NoIterations$

  $TRBFerr(x, y) \leftarrow$

    $T_{rbf} \leftarrow 0$

    for $j \in 1..\left(length\left(x_i\right)\right)$

      $T_{rbf} \leftarrow T_{rbf} + \left(\omega_{fg_i}\right)_j \cdot \left[1 + \left[\varepsilon_i \cdot \left[\sqrt{\left(x - x_{i_j}\right)^2 + \left(y - y_{i_j}\right)^2}\right]\right]^2\right]^{0.5}$

    T_{rbf}

redefine RBF interpolation function to access shape factor and weighting based in current iteration (i.e. uses updated weighting and shape factor matrices)

  $ErrorRBF \leftarrow CalcError(InterpGrid, TRBFerr)$ if $i = 1$

  $ErrorRBF \leftarrow stack(ErrorRBF, CalcError(InterpGrid, TRBFerr))$ if $i > 1$

return ErrorRBF

ErrorRBF := RBFerrorData Extract RBF error data

InterpolationErrorData :=

for $i \in 1..\text{NoIterations}$

$\text{coef1}_i \leftarrow \text{lspline}\left(\text{Mxy}, \text{T}_{\text{plot}_i}\right)$ prepare coefficients for each endpoint type

$\text{coef2}_i \leftarrow \text{pspline}\left(\text{Mxy}, \text{T}_{\text{plot}_i}\right)$

$\text{coef3}_i \leftarrow \text{cspline}\left(\text{Mxy}, \text{T}_{\text{plot}_i}\right)$ Redefine each interpolation function such that Tls and Tplot data points change between iterations

$\text{CubicSpline}(x,y) \leftarrow$ cubic spline function

$\quad \text{pt} \leftarrow \begin{bmatrix} \frac{x}{x_{dim}} \cdot (N_x + 1) \\ \frac{y}{y_{dim}} (N_y + 1) \end{bmatrix}$

$\quad \text{Temp} \leftarrow \text{interp}\left(\text{coef3}_i, \text{Mxy}, \text{T}_{\text{plot}_i}, \text{pt}\right)$

$\quad$ return Temp

$\text{ParCubSpline}(x,y) \leftarrow$ cubic spline function with parabolic endpoints

$\quad \text{pt} \leftarrow \begin{bmatrix} \frac{x}{x_{dim}} \cdot (N_x + 1) \\ \frac{y}{y_{dim}} (N_y + 1) \end{bmatrix}$

$\quad \text{Temp} \leftarrow \text{interp}\left(\text{coef2}_i, \text{Mxy}, \text{T}_{\text{plot}_i}, \text{pt}\right)$

$\quad$ return Temp

$\text{LinCubSpline}(x,y) \leftarrow$ cubic spline function with linear endpoints

$\quad \text{pt} \leftarrow \begin{bmatrix} \frac{x}{x_{dim}} \cdot (N_x + 1) \\ \frac{y}{y_{dim}} (N_y + 1) \end{bmatrix}$

$\quad \text{Temp} \leftarrow \text{interp}\left(\text{coef1}_i, \text{Mxy}, \text{T}_{\text{plot}_i}, \text{pt}\right)$

$\quad$ return Temp

$\text{Regression3}(x,y) \leftarrow$ 3nd order multiple regression

$\quad n \leftarrow 3$

$\quad \text{Reg} \leftarrow \text{regress}\left(\text{Mreg}, \text{T}_{\text{ls}_i}, n\right)$

$\quad \text{Temp} \leftarrow \text{interp}\left[\text{Reg}, \text{Mreg}, \text{T}_{\text{ls}_i}, \begin{pmatrix} x \\ y \end{pmatrix}\right]$

$\quad$ return Temp

$\text{Regression2}(x,y) \leftarrow$ 2nd order multiple regression

$\quad n \leftarrow 2$

$\quad \text{Reg} \leftarrow \text{regress}\left(\text{Mreg}, \text{T}_{\text{ls}_i}, n\right)$

$\quad \text{Temp} \leftarrow \text{interp}\left[\text{Reg}, \text{Mreg}, \text{T}_{\text{ls}_i}, \begin{pmatrix} x \\ y \end{pmatrix}\right]$

$\quad$ return Temp

Legrange interpolation function

$$\text{Lagrange}(x,y) \leftarrow \sum_{j=1}^{N_y} \sum_{k=1}^{N_x} \left[\text{Lgx}(x,k) \cdot \text{Lgy}\left(y, j \cdot N_x\right) \cdot \left(\text{T}_{\text{plot}_i}\right)_{k,j}\right]$$

if $i = 1$

$\quad \text{ErrorCubic} \leftarrow \text{CalcErr}(\text{InterpGrid}, \text{CubicSpline})$

$\quad \text{ErrorParabolic} \leftarrow \text{CalcErr}(\text{InterpGrid}, \text{ParCubSpline})$

$\quad \text{ErrorLin} \leftarrow \text{CalcErr}(\text{InterpGrid}, \text{LinCubSpline})$

$\quad \text{ErrorReg3} \leftarrow \text{CalcError}(\text{InterpGrid}, \text{Regression3})$

$\quad \text{ErrorReg2} \leftarrow \text{CalcError}(\text{InterpGrid}, \text{Regression2})$

$\quad \text{ErrorLag} \leftarrow \text{CalcErr}(\text{InterpGrid}, \text{Lagrange})$

if $i > 1$

$\quad \text{ErrorCubic} \leftarrow \text{stack}(\text{ErrorCubic}, \text{CalcErr}(\text{InterpGrid}, \text{CubicSpline}))$

$\quad \text{ErrorParabolic} \leftarrow \text{stack}(\text{ErrorParabolic}, \text{CalcErr}(\text{InterpGrid}, \text{ParCubSpline}))$

$\quad \text{ErrorLin} \leftarrow \text{stack}(\text{ErrorLin}, \text{CalcErr}(\text{InterpGrid}, \text{LinCubSpline}))$

$\quad \text{ErrorReg3} \leftarrow \text{stack}(\text{ErrorReg3}, \text{CalcError}(\text{InterpGrid}, \text{Regression3}))$

$\quad \text{ErrorReg2} \leftarrow \text{stack}(\text{ErrorReg2}, \text{CalcError}(\text{InterpGrid}, \text{Regression2}))$

$\quad \text{ErrorLag} \leftarrow \text{stack}(\text{ErrorLag}, \text{CalcErr}(\text{InterpGrid}, \text{Lagrange}))$

return $\begin{pmatrix} \text{ErrorCubic} \\ \text{ErrorParabolic} \\ \text{ErrorLin} \\ \text{ErrorReg3} \\ \text{ErrorReg2} \\ \text{ErrorLag} \end{pmatrix}$

$$\text{InterpolationErrorData} = \begin{pmatrix} \{2,4\} \\ \{2,4\} \\ \{2,4\} \\ \{2,4\} \\ \{2,4\} \\ \{2,4\} \end{pmatrix}$$

Extract Error data

Error data for each interpolation function

ErrorRBF

ErrorCubic := InterpolationErrorData$_1$

ErrorParabolic := InterpolationErrorData$_2$

ErrorLin := InterpolationErrorData$_3$

ErrorReg3 := InterpolationErrorData$_4$

ErrorReg2 := InterpolationErrorData$_5$

ErrorLag := InterpolationErrorData$_6$

Bi-linear inspired method code

This section has the code used for reconstructing with few paths, inspired by the bi-linear method.

Calculates the data points to be used for interpolation using bi-linear inspired approach

```
CalcDataPts(TransPos, RecPos) :=
    NoTrans ← length(TransPos)
    NoRec ← length(RecPos)
    DistMat ← matrix(N_t, N_b, zeroes)
    path ← 0
    for i ∈ 1..NoTrans
        for j ∈ 1..NoRec
            pt1 ← TransPos_i
            pt2 ← RecPos_j
            if pt1_3 ≠ pt2_3
                path ← path + 1
                Start ← submatrix(pt1, 1, 2, 1, 1)
                End ← submatrix(pt2, 1, 2, 1, 1)                    populate path length matrix
                Length_path ← DistPts(Start, End)
                Tpath_path ← (1/B^2) · (Length_path)^2 / (t_path)^2    Calculate temperature of each path
                x_start_path ← Start_1
                y_start_path ← Start_2                              store coordinates for start and ends of paths
                x_end_path ← End_1
                y_end_path ← End_2
    x_mid ← (x_start + x_end)/2                                     calculate midpoints for each path
    y_mid ← (y_start + y_end)/2
    Tdev ← stdev(Tpath)                                             determine standard deviation and mean and max of path temperature data
    Tmean ← mean(Tpath)
    Tmax ← max(Tpath)
    ScalFac ← 2 (Tdev · Tpath)/(Tpath · Tmean) + 1                  calculate the scale factor of each path
    return (x_start, x_mid, x_end, y_start, y_mid, y_end, Tpath, ScalFac, Length)
```

$$\begin{pmatrix} x_{start} \\ x_{mid} \\ x_{end} \\ y_{start} \\ y_{mid} \\ y_{end} \\ Tpath \\ ScalFac \\ Length \end{pmatrix} := CalcDataPts(TransPos, RecPos)$$

$T_{mid} := \overrightarrow{(Tpath \cdot ScalFac)}$

$T_{start} := \overrightarrow{[Tpath \cdot (2 - ScalFac)]}$

Calculate end and middle temperature data points

$T_{end} := T_{start}$

$x_{transmit} := x_{start} \quad y_{transmit} := y_{start}$

$x_{receive} := x_{end} \quad y_{receive} := y_{end}$

Prepare data to remove duplicates of points

$PrepareData(x_{start}, x_{end}, y_{start}, y_{end}, T_{start}, T_{end}) :=$

```
StartData ← augment(x_start, y_start, T_start)
EndData ← augment(x_end, y_end, T_end)
cnt ← 0
for i ∈ 1.. length(TransMat^⟨1⟩)
    Tvec ← 0
    for j ∈ 1.. length(StartData^⟨1⟩)
        if (TransMat_{i,1} = StartData_{j,1}) ∧ (TransMat_{i,2} = StartData_{j,2})
            cnt ← cnt + 1
            Tvec_cnt ← StartData_{j,3}
    cnt ← 0
    NewT_start_i ← mean(Tvec)
for i ∈ 1.. length(RecMat^⟨1⟩)
    Tvec ← 0
    for j ∈ 1.. length(EndData^⟨1⟩)
        if (RecMat_{i,1} = EndData_{j,1}) ∧ (RecMat_{i,2} = EndData_{j,2})
            cnt ← cnt + 1
            Tvec_cnt ← EndData_{j,3}
    cnt ← 0
    NewT_end_i ← mean(Tvec)
return (TransMat^⟨1⟩, RecMat^⟨1⟩, TransMat^⟨2⟩, RecMat^⟨2⟩, NewT_start, NewT_end)
```

$$\begin{pmatrix} xx_{start} \\ xx_{end} \\ yy_{start} \\ yy_{end} \\ TT_{start} \\ TT_{end} \end{pmatrix} := PrepareData(x_{start}, x_{end}, y_{start}, y_{end}, T_{start}, T_{end})$$

$$PredictShape(\varepsilon) := \begin{| \Phi_{fg} \leftarrow RBF(x_i, y_i, \varepsilon) \\ errormat \leftarrow \frac{\left(\Phi_{fg}^{-1} \cdot T_i\right)}{\left(diag\left(\Phi_{fg}^{-1}\right)\right)} \\ Predictor \leftarrow \sqrt{errormat \cdot errormat} \\ return\ \ Predictor}$$

Redefine regression and RBF functions

$BracketMin := 0.02 \qquad BracketMax := 1 \qquad tolerance := 0.001$

$guess := 0.5$

$\varepsilon := GoldenMin(PredictShape, BracketMin, BracketMax, tolerance) = 0.09539$

$\Phi_{fg} := RBF(x_i, y_i, \varepsilon)$

$\omega_{fg} := \Phi_{fg}^{-1} \cdot T_i$

$$TRBF(x, y) := \begin{| T_{rbf} \leftarrow 0 \\ for\ \ i \in 1..(length(x_i)) \\ \quad T_{rbf} \leftarrow T_{rbf} + \omega_{fg_i} \cdot \left[1 + \left[\varepsilon \cdot \left[\sqrt{(x - x_{i_i})^2 + (y - y_{i_i})^2}\right]\right]^2\right]^{-0.5} \\ T_{rbf}$$

$$TRBF(x, y) := \begin{| T_{rbf} \leftarrow 0 \\ for\ \ i \in 1..(length(x_i)) \\ \quad T_{rbf} \leftarrow T_{rbf} + \omega_{fg_i} \cdot \left[1 + \left[\varepsilon \cdot \left[\sqrt{(x - x_{i_i})^2 + (y - y_{i_i})^2}\right]\right]^2\right]^{-0.5} \\ T_{rbf}$$

$Mreg := augment(x_i, y_i)$

$$Regression3(x, y) := \begin{| n \leftarrow 3 \\ Reg \leftarrow regress(Mreg, T_i, n) \\ Temp \leftarrow interp\left[Reg, Mreg, T_i, \begin{pmatrix} x \\ y \end{pmatrix}\right] \\ return\ \ Temp}$$

Error testing is then done as before.

Appendix D. LabView program code

Front panel

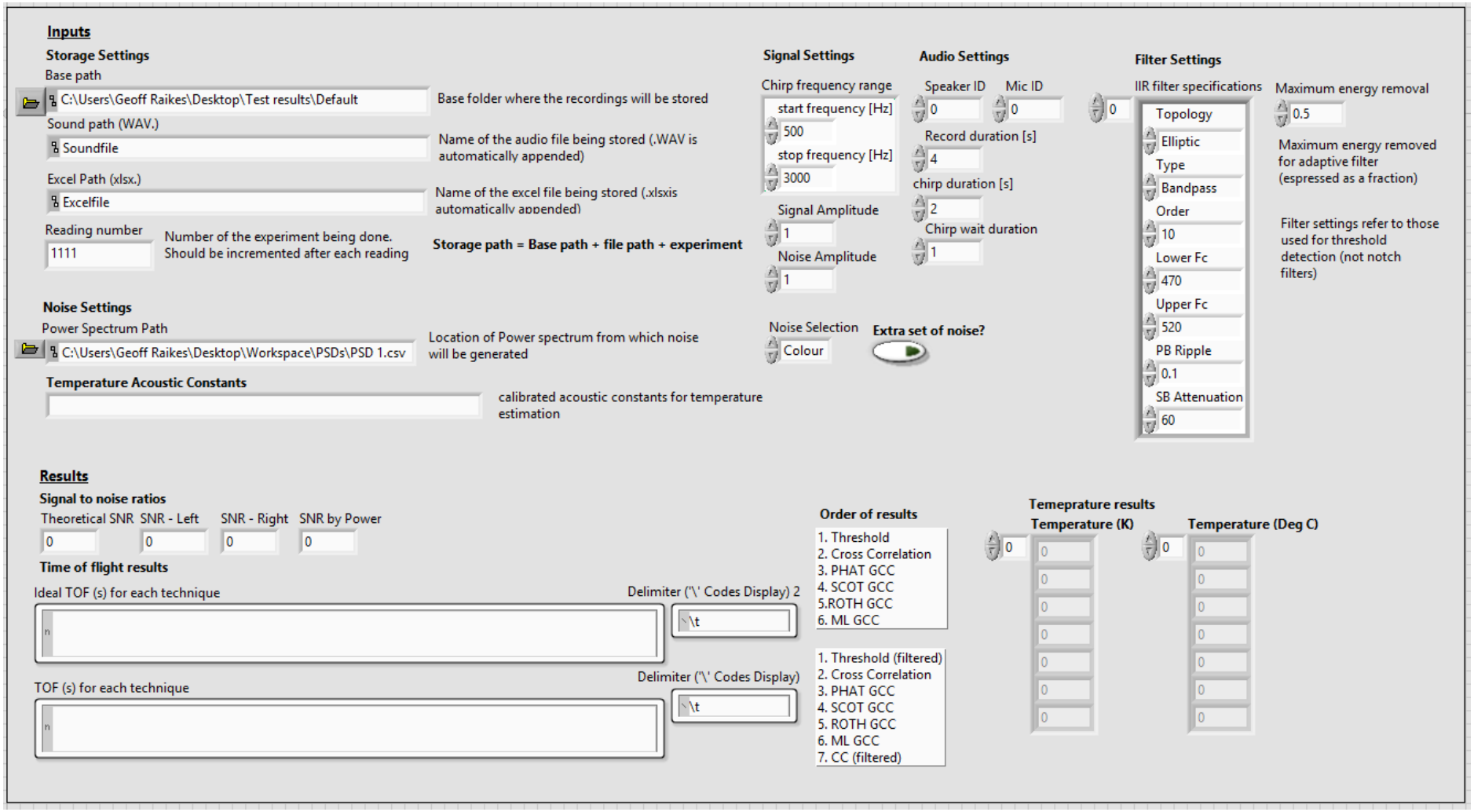

Main Code

This section includes the block diagram of the code running behind the front panel. This VI calls on many SubVIs as denoted by the white blocks. The more integral of these SubVIs will also be included.

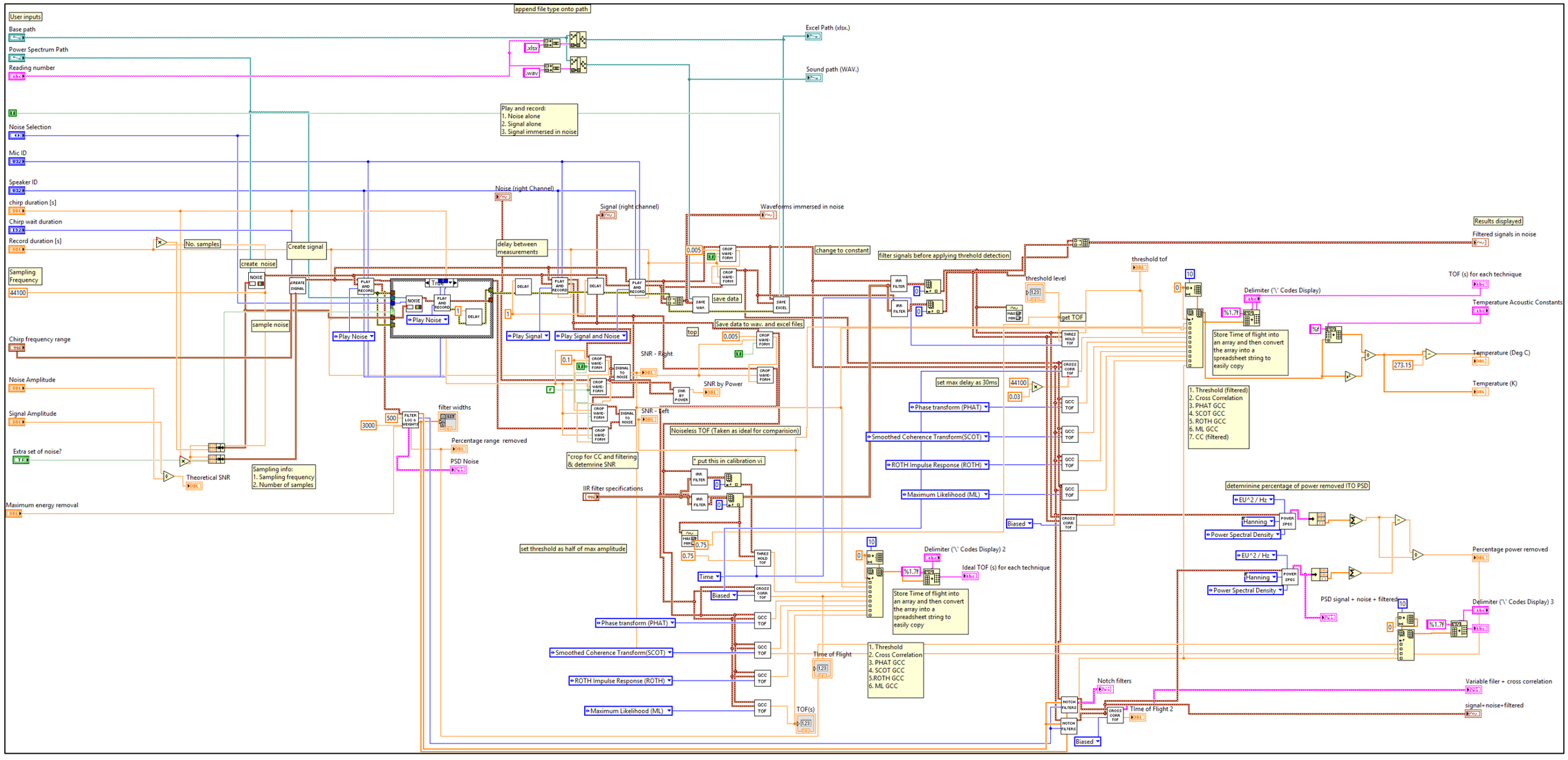

Play and record SubVI block diagram

Block diagram of code responsible for simultaneously recording inputs from the mixer and outputting the generated signals.

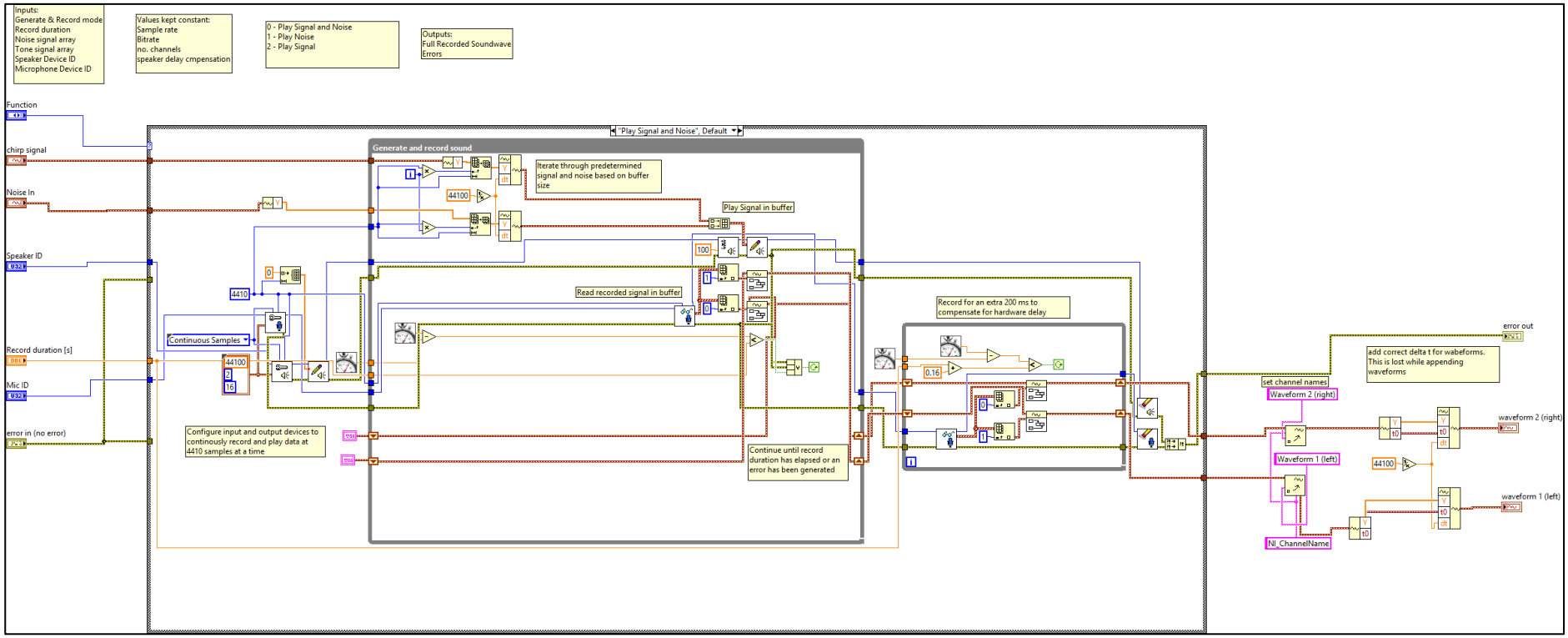

Variable notch filter method – Get filter positions and weights SubVI block diagram

This code determines the dominant frequency components within recorded noise and determines how many filters, where they should be placed and the width of each filter.

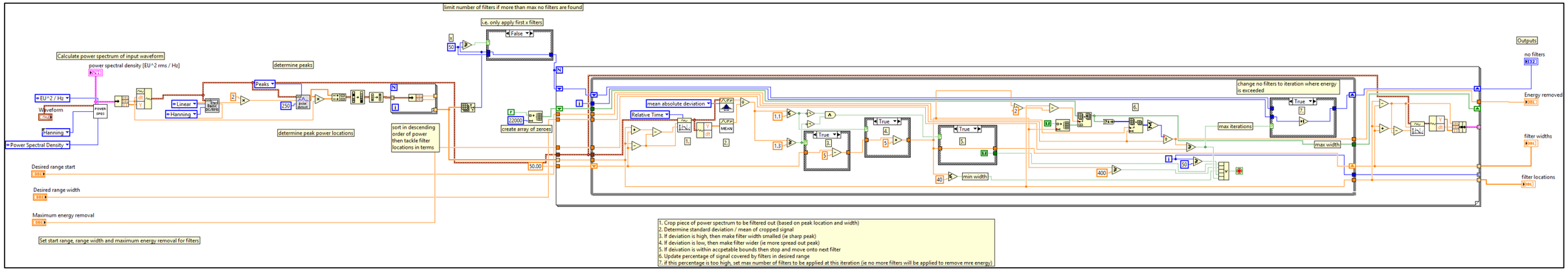

Generalised Cross correlation SubVI

This VI computes the GCC algorithm based on weighting selected. Each weighting will be shown inside the case structure.

PHAT weighting

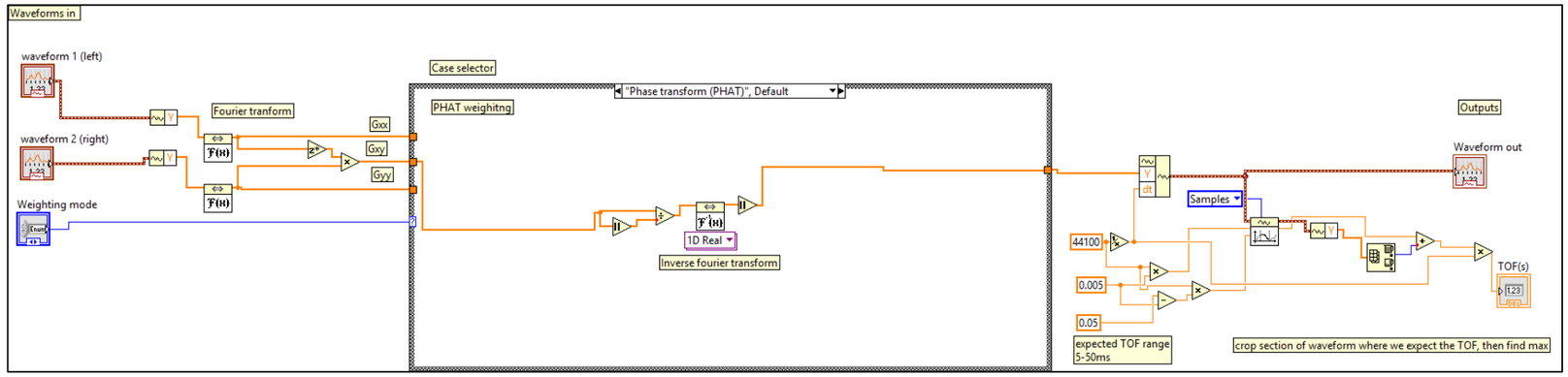

SCOT weighting

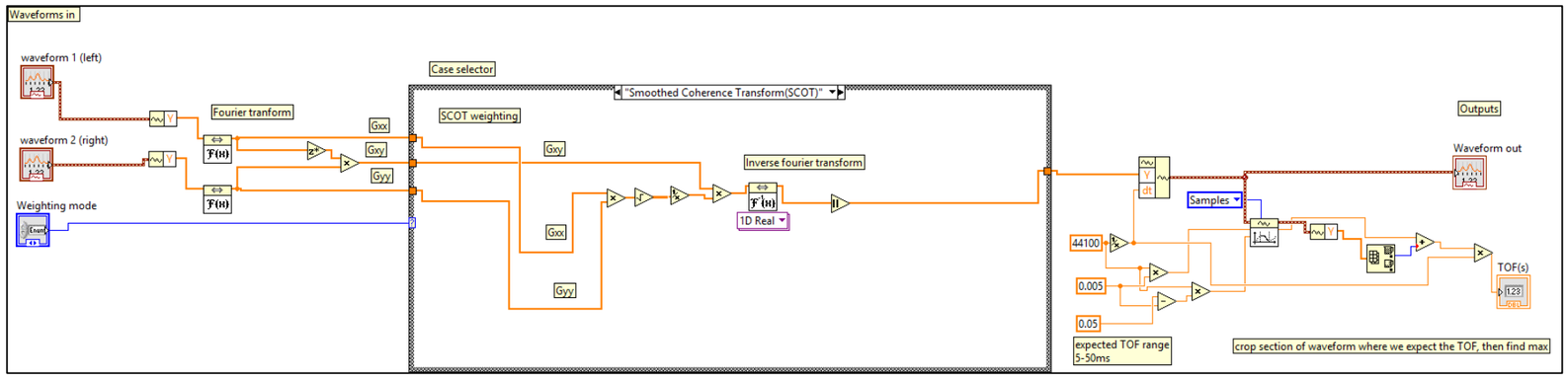

ROTH weighting

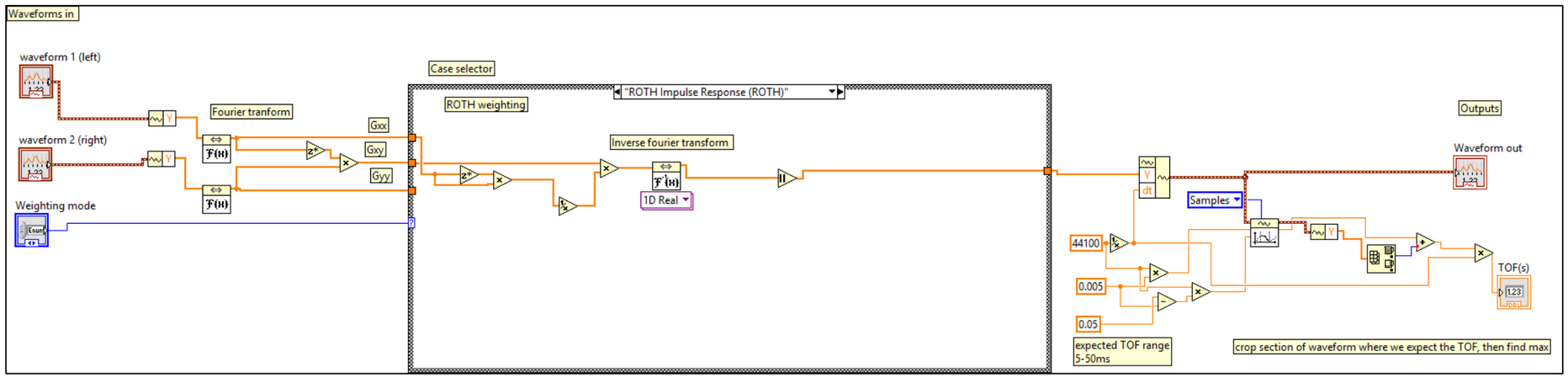

ML weighting

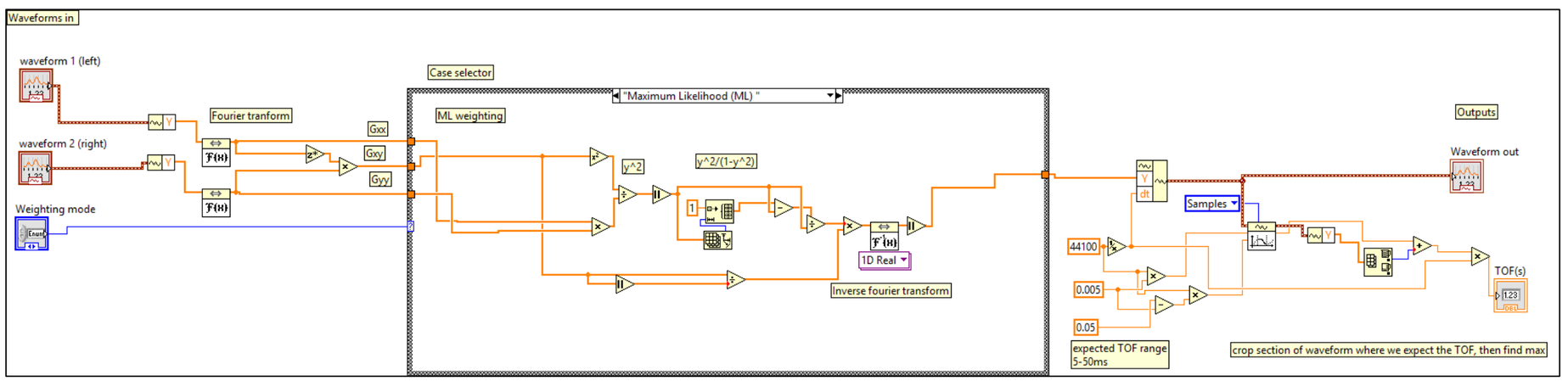

Threshold detection method SubVI

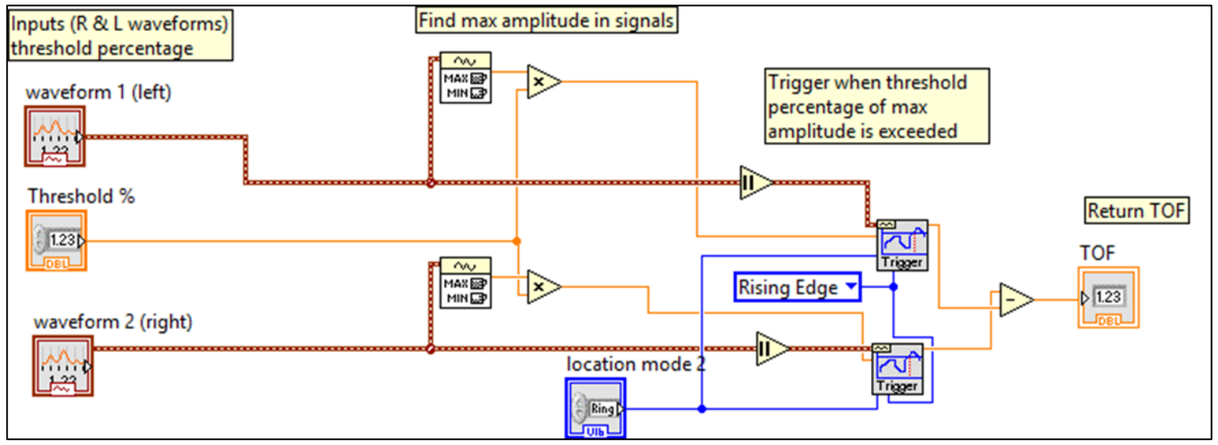

Standard Cross correlation SubVI

Computes the cross correlation of two waveforms based on the advanced signal processing cross correlation VI.

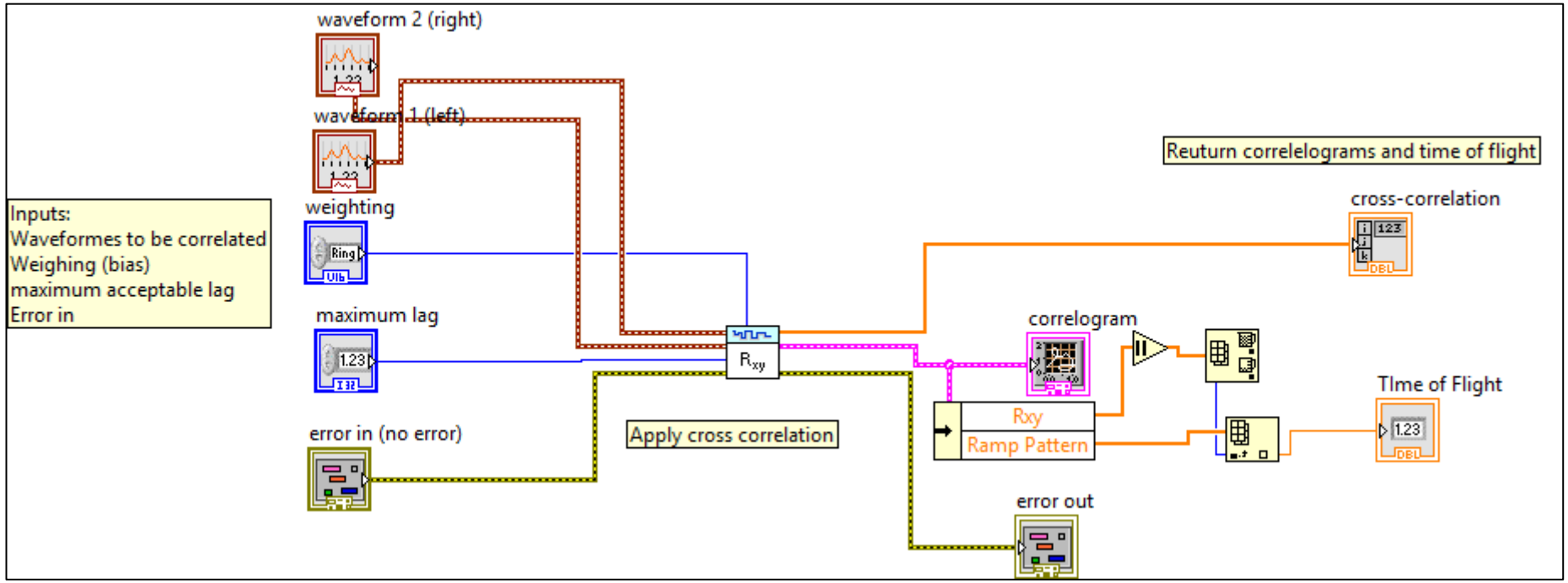

Coloured noise generator SubVI

Adapted from the LabVIEW coloured noise generator VI, this SubVI takes in a power spectrum from a CSV. File and creates a signal fitting that noise profile